

Cross-Equatorial Heat Transports and the Monsoons

A Thesis

Submitted in accordance with
the requirements for the degree of

Doctor of Philosophy

by

MD Rabiul Awal

Supervisors: **Dr. Andrew Turner**
Dr. David Ferreira



Department of Meteorology
University of Reading
United Kingdom

January 8, 2025

Declaration of Authorship

I confirm that this is my own work, and the use of all materials and contents from other sources has been duly credited and acknowledged.

Signed by:

MD Rabiul Awal

Abstract

Monsoons, the lifeline for billions of people, result from the cross-equatorial Hadley circulation (HC), which imports moisture into monsoon regions and exports heat. The inter-annual relationships between cross-equatorial heat transports and monsoons are largely unexplored, which is vital for water resources and climate stability.

Using reanalysis data, it is revealed that increased cross-equatorial atmospheric heat transport (CE-AHT) during JJA weakens the Indian, West African, and North American monsoons by contracting the HC, shifting the subtropical jets and Inter-tropical Convergence Zone (ITCZ) equatorward, weakening the Walker circulation, and inducing El Niño-like conditions. During DJF, the Australian, South African, and South American monsoons strengthen as the HC expands, the ITCZ and subtropical jets move poleward, strengthening the Walker circulation, and promoting La Niña-like conditions. Global monsoon precipitation increases in both JJA and DJF. Conversely, increased cross-equatorial oceanic heat transport (CE-OHT) in JJA and DJF elicits effects opposite to those of CE-AHT.

A few CMIP6 models simulate the historical trends observed in reanalysis for CE-AHT and CE-OHT. However, the relationship between CE-AHT, CE-OHT, and monsoons in most models mirrors reanalysis patterns.

Under the shared socioeconomic pathways 5-8.5 scenario, most CMIP6 models exhibit upward CE-AHT and downward CE-OHT trends in JJA, but these trends are downward and insignificant for DJF. In JJA, all models indicate increases in Indian monsoon precipitation for 2080–2100 compared to 1995–2014, while disagreement arises regarding the West African and North American monsoons. In multi-model space, greater CE-AHT weakens Indian monsoon rainfall, while greater CE-OHT weakens global monsoon rainfall. In DJF, models differ on Australian, South African, and South American monsoon precipitation changes.

This research suggests that changes in CE-AHT and CE-OHT are deeply intertwined with monsoons, and future warming could alter monsoon dynamics and heighten uncertainty in climate modelling and predictions.

Acknowledgements

I am deeply grateful to my supervisors, Dr. Andrew Turner and Dr. David Ferreira, for their invaluable guidance, unwavering support, and encouragement throughout my research journey. Their expertise, insightful feedback, and constant motivation have been instrumental in shaping this work. I am fortunate to have had the opportunity to learn from such esteemed mentors.

I would also like to express my sincere appreciation to the members of my monitoring committee, Dr. Miguel Teixeira and Dr. Remi Tailleux, for their constructive criticism, thoughtful suggestions, and support. Their input has significantly enhanced the quality of this research.

To my family, thank you for your endless love, patience, and encouragement. Your faith in me has been a constant source of strength and inspiration. I am grateful to them for their understanding and sacrifices, which have allowed me to focus on my studies and achieve my goals.

Finally, I extend my heartfelt thanks to my friends and colleagues for their support and for making this journey a memorable experience.

Contents

Authorship Declaration	ii
Abstract	iii
Acknowledgements	iv
List of Figures	vii
List of Acronyms	xxii
1 Introduction	1
1.1 Background and Context	1
1.2 Motivation and Rationale	16
1.3 Aims of this Study	20
1.4 Structure of the Thesis	21
2 Data and Methodology	22
2.1 Introduction	22
2.2 Observation-based Data	23
2.3 CMIP6 Model Data	25
2.4 Methodology	27
2.4.1 Calculation of heat transport using a direct method	27
2.4.2 Calculation of heat transport using an indirect method	32
2.4.3 Estimation of stream-function	34
3 Cross-Equatorial Heat Transport and the Monsoons: Observational Insights	35
3.1 Introduction	35
3.2 Data and Methodology	39
3.3 Results	46
3.3.1 Observation-based atmospheric heat transport	46
3.3.2 Atmospheric Heat Transport and Monsoon Dynamics	51
3.3.3 Observation-based oceanic heat transport	67

3.3.4	Oceanic heat transport relationship with the monsoons	71
3.4	Conclusions	81
4	The Relationship of Cross-Equatorial Heat Transports and the Monsoons in CMIP6 Historical Simulations	84
4.1	Introduction	84
4.2	Data and Methodology	89
4.3	Results	93
4.3.1	Simulated Patterns of Cross-Equatorial Heat Transport	94
4.3.2	Linking heat transports with the monsoons in CMIP6	102
4.3.3	Model Performance Based on Pattern Correlation	128
4.4	Conclusion	132
5	Climate Change effects on the Relationship between Cross-Equatorial Heat Transports and the Monsoons	134
5.1	Introduction	134
5.2	Data and Methodology	137
5.3	Results	139
5.3.1	Climate Change Effects on Heat Transports and the Monsoons	139
5.3.2	Projected Cross-Equatorial Heat Transport	151
5.3.3	Reliability of the ITCZ metric I_{msf}	158
5.3.4	Heat Transport and the Monsoons in the future Climate	159
5.4	Conclusion	163
6	Conclusion	166
6.1	Recap of Scientific Questions	166
6.2	Discussion of Results	167
6.2.1	What relationships exist between cross-equatorial transports of heat in the atmosphere/ocean and the monsoons using reanalysis products?	167
6.2.2	How do the CMIP6 climate models simulate the relationship between cross-equatorial heat transports and monsoons?	173
6.2.3	How do future climate projections alter the cross-equatorial transports, and can this be related to the monsoon response?	176
6.3	Limitations and Constraints	178
6.4	Future Avenues	181
	Bibliography	184

List of Figures

1.1	The global monsoon domain is reproduced and delineated as areas where the difference between local summer (boreal: June-July-August (JJA)) and winter (boreal: December-January-February (DJF)) precipitation exceeds 2 mm per day using GPCP precipitation spanning 1979–2020, as described in earlier studies (Wang and Ding, 2008; Zhou et al., 2008a,b; Wang et al., 2013a; Kitoh et al., 2013; Wang et al., 2014; Yim et al., 2014; Geen et al., 2020). The regions exhibiting JJA season monsoon characteristics, including the North American, North African, and Asian monsoons, are depicted with red shading, while those displaying DJF season monsoon features, such as the Australian, South American, and South African monsoons, are represented with blue shading.	2
1.2	(a) The annual mean net radiation (net incoming – net outgoing) flux (Wm^{-2}) using ERA-5 for the period 1979-2020 at the Top of the Atmosphere (TOA). (b) Zonal mean of ‘(a)’. (c) and (d) are the same as Figures ‘(a)’ and ‘(b)’, respectively, but for the JJA season. (e) and (f) depict Figures ‘(a)’ and ‘(b)’, respectively, but for the DJF season. All the results align with previous findings (Trenberth and Stepaniak, 2004; Trenberth and Caron, 2001; Trenberth and Solomon, 1994).	11

- 1.3 (a) An illustrative diagram depicts the behaviour of the Hadley Circulation (HC) during the JJA season. Wind patterns are depicted by black arrows, mass overturning stream-function by solid and dashed contours for positive (clockwise circulation from east) and negative (anti-clockwise circulation from east) values, respectively. Precipitation distribution is shown by white-blue droplets, and the direction of Cross-equatorial atmospheric heat transport (CE-AHT) is represented by a red arrow at the equator. The cross-equatorial winter-Hadley cell, which symbolises monsoon circulation, transports atmospheric moist-static energy (MSE: green arrow) towards its ascending branch via the lower branch. Concurrently, the upper branch transfers energy from the summer hemisphere to the winter hemisphere as dry static energy (DSE: blue arrow). Midlatitude eddies (orange curved arrows) subsequently distribute heat from this region towards the poles. The ‘EQ’, ‘S’, and ‘N’ refer to the equator (dashed green line), south pole, and north pole, respectively. (b) Same as Figure (a), but for the DJF season. 13
- 1.4 (a) A schematic illustration of near-surface ocean heat transport during the JJA season. Direction of circulation are depicted by black arrows, mass overturning stream-function by solid and dashed contours for positive (clockwise circulation from east) and negative (anti-clockwise circulation from east) values, respectively. The direction of Cross-equatorial oceanic heat transport (CE-OHT) is represented by red arrow at the equator. Heat exchange from the ocean to the atmosphere in mid-latitudes are denoted by the green curved arrows. Furthermore, mid-latitude eddies (orange curved arrows) subsequently distribute heat from this region towards the poles. The ‘EQ’, ‘S’, and ‘N’ refer to the equator (dashed green line), south pole, and north pole, respectively. (b) Same as Figure (a), but for the DJF season. . . 16
- 2.1 Annual-mean zonally integrated AHTs (PW) for January 1979, calculated using ERA-5 vertically integrated northward total energy data (blue solid line). AHTs derived from 6-hourly, 12-hourly, and 24-hourly ERA-5 pressure level data are represented by the cyan, red, and blue (dashed) lines, respectively. 31

- 3.1 The time-averaged yearly mean mid-tropospheric stream function and its derivative are displayed by the red and green solid curves using ERA-5 reanalysis data for the period 1979–2020, respectively. The inter-annual yearly mean mid-tropospheric stream function is shown by grey lines. The annual, zonal-mean AHT and precipitation are shown by the blue and magenta solid curves, respectively. The vertical dashed lines in blue, red, magenta, and green represent the mean latitudinal position of the ITCZ using AHT (zero AHT: Energy flux equator (EFE)), Mid-tropospheric (averaged between 700–300 hPa) stream-function (MTSF) (zero MTSF near equator: Ψ_0), I_{pr} , and derivative of MTSF (I_{dmsf}), respectively. The EFE, Ψ_0 , I_{pr} , and I_{dmsf} metrics have the following units: PW, $1 \times 10^{10} \text{ kg s}^{-1}$, $\text{mm day}^{-1} \text{ rad}^{-1}$, and $0.5 \times 10^{10} \text{ kg s}^{-1} \text{ rad}^{-1}$, respectively. 40
- 3.2 The annual mean mid-tropospheric stream-function and its derivative are displayed by the black and magenta solid curves using ERA-5 reanalysis data for the period 1979–2020, respectively. The vertical dashed lines in magenta and cyan represent the mean southern (HC_s : first zero to the south of Ψ_0 in MTSF) and northern (HC_n : first zero to the north of Ψ_0 in MTSF) edges of the Hadley circulation using MTSF, respectively. The red vertical dashed line is the position of the ITCZ by the derivative of MTSF (I_{dmsf}). The southern (ITCZ_s: first zero to the south of I_{dmsf}) and northern (ITCZ_n: first zero to the north of I_{dmsf}) latitudinal boundaries of the ITCZ are denoted by the blue and green vertical dashed lines, respectively. The units for MTSF and the derivative of MTSF are $1 \times 10^{10} \text{ kg s}^{-1}$, and $1 \times 10^9 \text{ kg s}^{-1} \text{ rad}^{-1}$, respectively. 41
- 3.3 The JJA mean mid-tropospheric stream-function for each year is displayed by the gray solid curve using ERA-5 reanalysis data for the period 1979–2020. The time-averaged zonal mean MTSF (red), AHT (blue), precipitation (magenta), and derivative of MTSF (green) are shown by the solid curves for the JJA season, respectively. The vertical dashed lines in blue, red, magenta, green, represent the location of the ITCZ by the EFE (zero AHT), Ψ_0 , I_{pr} , and I_{dmsf} metrics, respectively. The EFE, Ψ_0 , I_{pr} , and I_{dmsf} metrics have the following units: PW, $1 \times 10^{10} \text{ kg s}^{-1}$, mm day^{-1} , and $10 \times 10^{10} \text{ kg s}^{-1} \text{ rad}^{-1}$, respectively. 42
- 3.4 Same as Figure 3.3 except for the DJF season. 43
- 3.5 The annual mean zonally integrated AHTs (PW) are shown in grey curves using ERA-5 reanalysis data for the period 1979–2020. The time-averaged AHT is represented by the red curve. The blue dashed line denotes the position of the energy flux equator (EFE). 47

- 3.6 The inter-annual AHTs (PW) for (a) DJF, (b) MAM, (c) JJA, and (d) SON are shown in grey lines using ERA-5 reanalysis data for the period 1979–2020. The mean, mean+sd (sd: standard deviation), and mean–sd values are displayed by the red, green, and blue lines, respectively. 48
- 3.7 The standard deviation of AHT (PW) for DJF, MAM, JJA, and SON using ERA5 reanalysis data for the period 1979–2020 is shown on an inter-annual time scale. The standard deviation of AHT for DJF, MAM, JJA, and SON is represented by the red, blue, green, and black lines, respectively. 50
- 3.8 The seasonal cycle of CE-AHT (PW) is displayed using ERA-5 reanalysis data spanning the period 1979–2020. The mean CE-AHT values are marked by blue bars, whereas box-and-whisker plots represent the data distribution and dispersion, indicating the minimum value, 1st quartile, median, 3rd quartile, and maximum value. The outliers, which lie outside of 1.5 times the interquartile range above the upper (3rd) quartile and below the lower (1st) quartile, are denoted as green points. 51
- 3.9 (a) The left panel is the regression slope of upper-tropospheric (200 hPa) winds onto CE-AHT (black vectors; $\text{m s}^{-1} \text{PW}^{-1}$) during JJA using ERA-5 reanalysis data on an inter-annual time scale for the period 1979–2020. The colour shading shows the inter-annual regression slope of 200-hPa zonal winds onto CE-AHT for the same period. The right panel exhibits the regression slope of zonal-mean upper-tropospheric zonal winds (blue) and meridional winds (red) onto CE-AHT for the JJA season. (b) Same as panel ‘a’ except for the DJF season. 52
- 3.10 (a) The time-averaged stream function for the JJA season is displayed by the black curves, using ERA-5 reanalysis data spanning 1979 to 2020. Panels (b) and (c) show the stream function for positive CE-AHT anomalies (the mean JJA stream function plus five times the regression slope of the stream function onto CE-AHT on an inter-annual time scale) and negative CE-AHT anomalies (the mean JJA stream function minus five times the regression slope of the stream function onto CE-AHT on an inter-annual time scale), respectively, indicated by black curves. In (a), (b), and (c), the black dashed and solid curves represent anti-clockwise and clockwise rotation (from east), respectively. The colour shading in (a), (b), and (c) illustrates the meridional derivative (positive: ascent; negative: subsidence) of the stream function, indicating the vertical mass flux. The core position, where the absolute value of mass flux peaks, is shown by the green marker for the climatological HC and the purple marker for the regressed HC. The units of the stream function and its meridional derivative are $10^{10} \text{ kg s}^{-1}$ and $10^{10} \text{ kg s}^{-1} \text{ rad}^{-1}$, respectively. 54
- 3.11 Same as Figure 3.10 except for the DJF season. 55

- 3.12 (a) The derivative of time-averaged MTSF (stream function averaged over 700–300 hPa; red) is displayed using ERA-5 reanalysis data for JJA spanning 1979–2020. The derivatives of MTSF for positive CE-AHT anomalies (the mean JJA MTSF plus five times the regression slope of the MTSF onto CE-AHT on an inter-annual time scale) and negative CE-AHT anomalies (the mean JJA MTSF minus five times the regression slope of the MTSF onto CE-AHT on an inter-annual time scale) are shown by blue and green curves, respectively. The positions ($^{\circ}$) of the ITCZ identified by the I_{dmsf} metric for mean MTSF (red), positive CE-AHT anomalies (blue), and negative CE-AHT anomalies (green) are represented by the vertical lines for the JJA season. (b) Same as panel ‘a’ but for the DJF season. 57
- 3.13 (a) The left panel shows the regression slope of precipitation onto CE-AHT (colour shading in $\text{mm day}^{-1} \text{PW}^{-1}$) using ERA-5 reanalysis on an inter-annual time scale for the JJA season spanning 1979–2020. The solid magenta curves depict mean precipitation (mm day^{-1}). The right panel displays the zonal mean of climatological precipitation (red; $1 \times 10 \text{ mm day}^{-1}$) and its regressed slope onto CE-AHT (blue; $\text{mm day}^{-1} \text{PW}^{-1}$) for the JJA season. (b) Same as panel ‘a’ but for the DJF season. 58
- 3.14 The correlation coefficient between CE-AHT and precipitation is displayed for JJA using ERA-5 reanalysis data on an inter-annual time scale for the period 1979–2020. The red and blue lines exhibit the correlation of global CE-AHT versus precipitation and CE-AHT versus AHT, respectively. The green, blue, and red circles represent the correlation between regional CE-AHT and precipitation over the Indian, West-African, and North-American monsoon domains, respectively. For the Indian, West African, and North American monsoons, CE-AHTs are computed over the domains $45^{\circ}\text{E}–95^{\circ}\text{E}$, $20^{\circ}\text{W}–25^{\circ}\text{E}$, and $60^{\circ}\text{W}–130^{\circ}\text{W}$, respectively. 60
- 3.15 (a) The left panel shows the regression slope, on an inter-annual time scale, of lower-tropospheric (850 hPa) winds onto CE-AHT, represented by vectors for the JJA season using ERA-5 reanalysis data for the period 1979–2020. The colour shading is the slope of the regression of precipitation onto CE-AHT for the same time domain. The right panel depicts regression slopes ($\text{m s}^{-1} \text{PW}^{-1}$) of the zonal mean lower-tropospheric zonal wind (blue) and meridional (red) wind for the JJA season. (b) Same as panel ‘a’ but for the DJF season. 61

- 3.16 (a) On an inter-annual time scale, the regression slope of SST onto CE-AHT ($^{\circ}\text{C PW}^{-1}$) is represented by colour shading for the JJA season using Hadley Centre Sea Ice and Sea Surface Temperature version 1 (HadISST1) reanalysis data spanning 1979–2020. The green curves depict the mean SST during the JJA season for the same time domain. (b) Same as panel ‘a’ but for the DJF season. 62
- 3.17 The regression slope of Ocean potential temperature (OPT) (after taking the meridional mean in between 5°N and 5°S) onto CE-AHT ($^{\circ}\text{C PW}^{-1}$) is displayed by colour shading using ERA-5 reanalysis data for the JJA season on an inter-annual time scale for the period 1979–2020. 64
- 3.18 Same as Figure 3.17 but for the DJF season. 65
- 3.19 A permutation test is conducted between ‘A’ (a 3-month mean non-sliding time series) and ‘B’ (a 3-month mean sliding time series), which extends for four consecutive months forward and backward. (i) The time series ‘A’ and ‘B’ represent CE-AHT and ONI, respectively, for the JJA season during the period 1979–2020. (ii) Same as (i), but for the DJF season. 67
- 3.20 The annual mean oceanic heat transport (OHT; grey) (PW) is represented using ORAS-5 reanalysis for the period 1979–2020. The red curve depicts the climatological mean OHT for the same time period. 67
- 3.21 The inter-annual OHTs (PW) for the (a) DJF, (b) MAM, (c) JJA, and (d) SON seasons are shown in grey lines using ORAS-5 reanalysis data for the period 1979–2020. The mean, mean+sd (sd: standard deviation), and mean–sd values are displayed by the red, green, and blue lines, respectively. 68
- 3.22 The standard deviation of the inter-annual OHT (PW) using ORAS-5 reanalysis data spanning the period 1979–2020 is represented for the DJF (red), MAM (blue), JJA (green), and SON (black) seasons. The standard deviation of annual mean OHT is shown by magenta colour. 69
- 3.23 The seasonal cycle of CE-OHT (PW) is displayed using ORAS-5 reanalysis data spanning the period 1979–2020. The mean CE-OHT values are marked by blue bars, whereas box-and-whisker plots represent the data distribution and dispersion, indicating the minimum value, 1st quartile, median, 3rd quartile, and maximum value. The outliers, which lie outside of 1.5 times the interquartile range above the upper (3rd) quartile and below the lower (1st) quartile, are denoted as green points. 70

- 3.24 (a) The left panel shows the regression slope of upper-tropospheric (200 hPa) u,v-winds onto CE-OHT (black vectors; $\text{m s}^{-1} \text{PW}^{-1}$) during JJA, using ORAS-5 reanalysis data on an inter-annual time scale for the period 1979–2020. The colour shading shows the inter-annual regression slope of 200-hPa zonal winds onto CE-OHT for the same period. The right panel is the zonal mean regression slope of upper-tropospheric zonal winds (blue) and meridional winds (red) onto CE-OHT for the JJA season. (b) Same as panel ‘a’ but for the DJF season. 71
- 3.25 (a) The time-averaged atmospheric stream function for the JJA season is displayed by the black curves using ERA-5 reanalysis data for the period 1979–2020. The stream functions for the positive anomalous CE-OHT (mean JJA stream function plus five times the regression slope of the stream function onto CE-OHT on an inter-annual time scale) and the negative anomalous CE-OHT (mean JJA stream function minus five times the regression slope of the stream function onto CE-OHT on an inter-annual time scale) are depicted in (b) and (c), respectively, by black curves. In (a), (b), and (c), the black dashed and solid curves represent anti-clockwise and clockwise rotation (from east), respectively. The colour shading in (a), (b), and (c) illustrates the meridional derivative (positive: ascent; negative: subsidence) of the stream function, indicating the vertical mass flux. The core position, where the absolute value of mass flux peaks, is shown by the green marker for the climatological HC and the purple marker for the regressed HC. The stream function and its meridional derivative have units kg s^{-1} and $\text{kg s}^{-1} \text{rad}^{-1}$, respectively. 72
- 3.26 Same as the Figure 3.25 but for the DJF season. 73
- 3.27 (a) The derivative (stream function averaged over 700–300 hPa; red) of time-averaged MTSF is displayed using ERA-5 reanalysis data for JJA for the period 1979–2020. The derivatives of MTSF for positive CE-OHT anomalies (the mean JJA MTSF plus five times the regression slope of the MTSF onto CE-OHT on an inter-annual time scale; blue) and negative CE-OHT anomalies (the mean JJA MTSF minus five times the regression slope of the MTSF onto CE-OHT on an inter-annual time scale; green), are shown. The positions ($^{\circ}$) of the ITCZ identified by the I_{dmsf} metric for the mean MTSF (red), positive CE-OHT anomalies (blue), and negative CE-OHT anomalies (green) are represented by the vertical lines for the JJA season. (b) Same as panel ‘a’ but for the DJF season. 74

- 3.28 (a) The left panel is the regression slope of precipitation onto CE-OHT for the JJA (colour shading in $\text{mm day}^{-1} \text{PW}^{-1}$) season using ORAS-5 on an inter-annual time scale for the period 1979–2020. The solid magenta curves depict mean precipitation (mm day^{-1}). The right panel shows the zonal mean of climatological precipitation ($1 \times 10 \text{ mm day}^{-1}$) in a red curve and the regressed precipitation slope onto CE-OHT ($\text{mm day}^{-1} \text{PW}^{-1}$) in a blue curve for the JJA season. (b) Same as panel ‘a’ but for the DJF season. 75
- 3.29 (a) The left panel is the regression slope of lower-tropospheric (850 hPa) winds onto the CE-OHT and has been represented by vectors for the JJA season for the period 1979–2020. The colour shading represents the slope of precipitation regression onto the CE-OHT for the same time domain. The right panel shows the zonal mean of lower-tropospheric zonal wind and meridional wind regression slopes ($\text{m s}^{-1} \text{PW}^{-1}$) in blue and red, respectively, for the DJF season. (b) Same as the Figure ‘a’ but for the DJF season. 76
- 3.30 (a) The regression slope of SST onto CE-OHT ($^{\circ}\text{C PW}^{-1}$) is represented by colour shading for the JJA season for the period 1979–2020. The green curves are the mean SST for the JJA season. (b) Same as ‘a’ but for the DJF season. 77
- 3.31 The regression slope of OPT (after taking the meridional mean in between 5°N and 5°S) onto CE-OHT ($^{\circ}\text{C PW}^{-1}$) is displayed by colour shading using ORAS-5 reanalysis data for the JJA season on an inter-annual time scale for the period 1979–2020. 78
- 3.32 Same as Figure 3.17 but for the DJF season. 79
- 4.1 A monthly time series of cross-equatorial latent heat transport (PW) by direct (vertically integrated: blue) and indirect (evaporation-precipitation: red) methods. Negative and positive values denote southward and northward exports, respectively. 90
- 4.2 A monthly time series of cross-equatorial oceanic heat transport (PW) estimated by the direct method (red: model-estimated; blue: our estimation) is shown. Negative and positive values denote southward and northward exports, respectively. 91
- 4.3 (a) The seasonal cycle of CE-AHT (PW) is displayed for the reanalysis data (black solid line) and various CMIP6 models for the period 1979–2020. (b) Same as panel ‘a’ but for CE-OHT (PW). Here, OBS denotes ERA-5 in (a) and ORAS-5 in (b), and MMM refers to the multi-model mean. 94

4.4	(a) The time series of the five-year running mean CE-AHT (PW) is shown for OBS (ERA-5: black solid line) and various CMIP6 models spanning 1979–2020 for the JJA season. (b) The slopes, calculated using linear regression, of the corresponding CE-AHT time series for the same period (blue dots: statistical significance at the 95% confidence level or higher; red dots: statistically insignificant at the 95% confidence level), measured in PW per decade. MMM refers to the multi-model mean. Negative and positive values denote southward and northward transports, respectively.	95
4.5	Same as in Figure 4.4 but for the CE-OHT, and OBS denotes the ORAS-5.	96
4.6	Same as Figure 4.4 but for the DJF season.	97
4.7	Same as Figure 4.5 but for the DJF season.	98
4.8	Along the horizontal axis, the inter-annual correlation coefficient between CE-AHT and CE-OHT for both the JJA season (blue markers) and DJF season (green markers) spanning the period 1979–2020 for each CMIP6 model and reanalysis data (OBS: ERA-5 and ORAS-5). The vertical axis represents the confidence level. MMM refers to the multi-model mean.	98
4.9	(a) The inter-model relationship between CE-AHT and CE-OHT is depicted for the long-term mean (1979–2020) during the JJA season. The correlation coefficient and the p-value from linear regression analysis on an inter-annual time scale are represented as the first and second entries between the parenthesis. (b) Same as panel ‘a’ but for the DJF season. MMM refers to the multi-model mean, and OBS denotes the reanalysis data (ERA-5 and ORAS-5).	99
4.10	The inter-annual regression slope ($\text{ms}^{-1} \text{PW}^{-1}$) of upper-tropospheric (200 hPa) winds onto CE-AHT is displayed in vectors for the JJA season for the period 1979–2020. The colour shading shows the inter-annual regression slope of 200-hPa zonal winds onto CE-AHT for the same period. OBS denotes ERA-5 reanalysis, and MMM refers to the multi-model mean.	102
4.11	Same as in Figure 4.10 but for the CE-OHT.	103
4.12	Same as Figure 4.10 but for the DJF season.	104
4.13	Same as Figure 4.11 except for the DJF season.	105

- 4.14 The latitudinal position of the ITCZ using zonal mean precipitation (I_{pr} : blue colour) and mid-tropospheric stream function (I_{dmsf} : green colour) is shown for the JJA season in CMIP6 model data and observational data for the period 1979–2020. The whiskers indicate the range of the data, excluding outliers. The lower and upper edges of the box represent the first quartile (Q1) and the third quartile (Q3), respectively. The median is shown as a red line, and the mean is shown as a red star. Outliers are denoted by yellow points. At the bottom, r, c, and e refer to the inter-annual correlation coefficient, confidence level, and RMSE error, respectively, between I_{pr} and I_{dmsf} . For JJA mean, the latitudes of the ITCZ by I_{pr} and I_{dmsf} are given by the top blue and green numbers, respectively. MMM refers to the multi-model mean. 106
- 4.15 Same as Figure 4.14 except for the DJF season. 106
- 4.16 (i) The stream function regressed onto CE-AHT is displayed using the MIROC6 CMIP6 model for the JJA season on an inter-annual time scale spanning 1979–2020. (a) The time-averaged stream function for the JJA season is depicted by the black curves. (b) The stream function for positive CE-AHT anomalies (the mean JJA stream function plus five times the regression slope of the stream function onto CE-AHT on an inter-annual time scale) is represented by black curves. (c) The stream function for negative CE-AHT anomalies (mean JJA stream function minus five times the regression slope of the stream function onto CE-AHT on an inter-annual time scale) is shown by black curves. In (a), (b), and (c), the black dashed curves denote anticlockwise rotation, and the solid black curves denote clockwise rotation (from east). The core position, where the absolute value of mass flux peaks, is shown by the green marker for the climatological HC and the purple marker for the regressed HC. The meridional derivative of the stream function, representing the vertical mass flux, is shown in colour shading. The units of the stream function and its meridional derivative are $10^{10} \text{ kg s}^{-1}$ and $10^{10} \text{ kg s}^{-1} \text{ rad}^{-1}$, respectively. (ii) Same as (i), but for the DJF season. (iii) Same as (i), but for CE-OHT. (iv) Same as (ii), but for CE-OHT. 107
- 4.17 (a) The mean latitudinal position of the HC rising branch is depicted for the JJA season using CMIP6 models and reanalysis data for both the climatological mean and regressed stream function onto CE-AHT on an inter-annual time scale, from 1979 to 2020. Markers denote the position of the rising branch for the climatological mean (black), positive CE-AHT anomalies (red), and negative CE-AHT anomalies (blue). MMM refers to the multi-model mean. (b) Same as panel ‘a’ but for the CE-OHT. 108
- 4.18 Same as Figure 4.17 except for the DJF season 109

4.19	The left panel of each model is the inter-annual precipitation regression onto CE-AHT during JJA on an inter-annual time scale for the period 1979–2020 (colour shading in $\text{mm day}^{-1} \text{PW}^{-1}$). The right panel is the zonal mean of climatological precipitation (blue; scaled down by 10; mm day^{-1}) and the regressed precipitation slope onto CE-AHT (red; $\text{mm day}^{-1} \text{PW}^{-1}$) for the JJA season. MMM refers to the multi-model mean.	110
4.20	Same as in Figure 4.19 but for the CE-OHT.	111
4.21	Same as Figure 4.19 except for DJF season.	112
4.22	Same as Figure 4.20 except for DJF season.	113
4.23	The inter-annual regression slope of lower-tropospheric (850 hPa) winds onto CE-AHT is delineated in vectors for the JJA season during the period 1979–2020 ($\text{ms}^{-1} \text{PW}^{-1}$). The colour shading is the inter-annual regression slope of precipitation onto CE-AHT for the same period. MMM refers to the multi-model mean.	114
4.24	Same as Figure 4.23 but for the CE-OHT.	115
4.25	Same as Figure 4.23 except for the DJF season.	116
4.26	Same as Figure 4.24 except for the DJF season.	117
4.27	The inter-annual SST regression onto CE-AHT is displayed in colour shading for the JJA season over 1979–2020 in CMIP6 models ($^{\circ}\text{C PW}^{-1}$). The right panel shows the zonal mean SST (scaled down by 30; blue) and regressed SST (red curve) for the JJA season.	118
4.28	Same as in Figure 4.27 but for the CE-OHT.	119
4.29	Same as Figure 4.27 except for the DJF season.	120
4.30	Same as Figure 4.28 except for the DJF season.	121
4.31	The pattern correlation between reanalysis and CMIP6 models is shown for JJA (a) and DJF (b), with climatological mean precipitation along the horizontal axis and regressed precipitation (onto CE-AHT in blue and CE-OHT in red) along the vertical axis on an inter-annual time scale for the period 1979–2020. Similarly, the RMSE is displayed in panels (c) and (d).	128
4.32	Same as in Figure 4.31 but for the SST.	129
5.1	Long-term changes in precipitation for good (MIROC6) and bad (CanESM5 and UKESM1-0-LL) models during the JJA season, computed for 2080–2100 with respect to the base period 1995-2014.	140
5.2	Same as Figure 5.1 but for the DJF season.	141

5.3	(i) CE-AHT during the JJA season is represented utilizing reanalysis and CMIP6 model datasets for the historical periods (1995–2014; blue) and future projections (2080–2100; green). Whiskers denote the data range, excluding outliers, while the lower and upper edges of the box signify the first quartile (Q1) and the third quartile (Q3), respectively. The median is depicted by a red line, the mean by a red star, and the outliers by yellow points. MMM refers to the multi-model mean, and OBS represents ERA-5. (ii) Same as ‘(i)’ but for the CE-OHT, and OBS represents ORAS-5.	142
5.4	Same as Figure 5.3 except for the stream-function strength.	143
5.5	Same as in Figure 5.3, but for the DJF season.	144
5.6	The ITCZ location during the JJA season is represented using reanalysis and CMIP6 model datasets for historical (1995–2014; blue) and future projections (2080–2100; green). Whiskers denote the data range, excluding outliers, while the lower and upper edges of the box signify the first quartile (Q1) and the third quartile (Q3), respectively. The median is depicted by a red line, the mean by a red star, and the outliers by yellow points. MMM refers to the multi-model mean.	145
5.7	Same as Figure 5.6 except for the DJF season.	145
5.8	(i) The zonal mean precipitation intensity during the JJA season is represented by utilizing reanalysis and CMIP6 model datasets for historical (1995–2014; blue) and future projections (2080–2100; green). Whiskers denote the data range, excluding outliers, while the lower and upper edges of the box signify the first quartile (Q1) and the third quartile (Q3), respectively. The median is depicted by a red line, the mean by a red star, and the outliers by yellow points. MMM refers to the multi-model mean. (ii) Same as ‘(i)’ except for the DJF season.	146
5.9	(a) Inter-model correlation between zonal mean maximum precipitation changes and CH-AHT changes during the JJA season, computed for 2080–2100 with respect to the base period 1995–2014. The first and second entries in parenthesis represent correlation coefficient and p-value, respectively. (b) Similar analysis for the ITCZ position and CE-AHT. (c) and (d) represent analogous investigations to (a) and (b), respectively, but for CE-OHT. MMM refers to the multi-model mean.	147
5.10	Same as Figure 5.9 except for the DJF season.	147

- 5.11 (a) Inter-model correlation between global monsoon mean precipitation (45°S – 45°N) changes and CH-AHT changes (blue), northern-hemisphere monsoon mean precipitation (0 – 45°N) changes and CH-AHT changes (red), and southern-hemisphere monsoon mean precipitation (45°S – 0) changes and CH-AHT changes (green), during the JJA season, computed for 2080–2100 with respect to the base period 1995–2014. The first and second entries in parenthesis represent the correlation coefficient and p-value, respectively. (b) Similar analysis for the precipitation and CE-OHT during the JJA season. (c) and (d) represent analogous investigations to (a) and (b), respectively, but for the DJF season. MMM refers to the multi-model mean. 148
- 5.12 (a) Inter-model correlation between Indian monsoon mean precipitation (45°S – 45°N) changes and CH-AHT changes (blue), West-African monsoon mean precipitation (0 – 45°N) changes and CH-AHT changes (red), and North-American monsoon mean precipitation (45°S – 0) changes and CH-AHT changes (green), during the JJA season, computed for 2080–2100 with respect to the base period 1995–2014. The first and second entries in parenthesis represent the correlation coefficient and p-value, respectively. (b) Similar analysis for precipitation and CE-OHT during the JJA season. (c) and (d) represent analogous investigations to (a) and (b), respectively, but for the DJF season. MMM refers to the multi-model mean. 149
- 5.13 (a) The seasonal cycle of the CE-AHT (PW) for various CMIP6 models for the period 2021–2100. Positive and negative denote northward and southward transport, respectively. (b) Same as ‘a’ except for CE-OHT. Here, OBS indicates ERA-5 in (a) and ORAS-5 in (b), and MMM refers to the multi-model mean. 152
- 5.14 (a) The time series of five-year running mean CE-AHT (PW) for various CMIP6 models for the JJA season. (b) The slopes, calculated using linear regression, of the corresponding CE-AHT time series for the period 1960–2020 in dots and 2021–2100 in cross markers (blue: statistical significance at the 95% confidence level or higher; red color markers: statistically insignificant at the 95% confidence level), measured in PW per decade. Positive and negative denote northward and southward transport, respectively. Here, OBS indicates ERA-5, and MMM refers to the multi-model mean. 153
- 5.15 As in Figure 5.14 but for CE-OHT, and OBS refers to ORAS-5. 154
- 5.16 Same as Figure 5.14 except for the DJF season. 155
- 5.17 Same as Figure 5.15 except for the DJF season 156

- 5.18 The inter-annual correlation coefficient between CE-AHT and CE-OHT for JJA (blue markers) and DJF (green markers) for 2021–2100 for each CMIP6 model. The vertical axis represents the confidence level. MMM refers to the multi-model mean. The dashed horizontal line (at 0.95) indicates the 95% confidence level. 156
- 5.19 (a) The inter-model relationship between CE-AHT and CE-OHT for the time-averaged JJA season spanning 2021–2100. The correlation coefficient and p-value from linear regression are provided as the first and second entries inside the parenthesis. (b) Same as ‘a’ except for the DJF season. MMM refers to the multi-model mean. 157
- 5.20 The latitudinal position of the ITCZ using zonal mean precipitation (I_{pr} , blue dots) and mid-tropospheric stream function (I_{dmsf} , green dots) for the inter-annual JJA season in the CMIP6 model datasets for the period 2021–2100. The whiskers indicate the range of the data, excluding outliers. The lower and upper edges of the box represent the first quartile (Q1) and the third quartile (Q3), respectively. The median is shown as a red line, and the mean is shown as a red star. Outliers are indicated by yellow dots. At the bottom, ‘r’, ‘c’, and ‘e’ refer to the inter-annual correlation coefficient, confidence level, and RMSE error, respectively, between inter-annual I_{pr} and I_{dmsf} . For JJA mean, the latitudes of the ITCZ by I_{pr} and I_{dmsf} are given by the top blue and green numbers, respectively. MMM refers to the multi-model mean. The I_{pr} and I_{dmsf} metrics are discussed in Chapter 3 and Section 3.2. 158
- 5.21 Same as Figure 5.20 except for the DJF season. 158
- 5.22 (a) The latitudinal position of the Hadley Cell rising branch in the JJA season: regression of the stream-function onto CE-AHT in CMIP6 models data for the period 2060–2100. Marker points are used to indicate the rising branch’s position for the climatological mean (black), positive CE-AHT anomaly (red), and negative CE-AHT anomaly (blue). (b) Same as ‘a’ but for the CE-OHT. MMM refers to the multi-model mean. 160
- 5.23 Same as Figure 5.22 except for the DJF season 161
- 5.24 The inter-annual SST regression onto CE-AHT ($^{\circ}\text{C PW}^{-1}$) is displayed in colour shading during the JJA season over 2080–2100 for good (MIROC6) and bad (CanESM5 and EKESM1-0-LL) models. 162
- 5.25 The inter-annual SST regression onto CE-AHT ($^{\circ}\text{C PW}^{-1}$) is displayed in colour shading during the JJA season over 2080–2100 for good (MIROC6) and bad (CanESM5 and EKESM1-0-LL) models. 163

-
- 6.1 A schematic illustration of outcomes for northward CE-AHT and CE-OHT anomalies in JJA is displayed, showing the winter-Hadley cell (top panel) and zonal mean precipitation (bottom panel). The mean position of the rising branch of the HC is shown by green vectors, while red and blue vectors denote its shift for northward CE-AHT and CE-OHT anomalies, respectively. Similarly, the green dashed line indicates the ITCZ location by zonal mean precipitation, with red and blue dashed lines representing the ITCZ location for northward CE-AHT and CE-OHT anomalies. The black vertical dashed line refers to the equator. 174
- 6.2 Same as Figure 6.1, but for the DJF season. 175

List of Acronyms

A list of utilized acronyms throughout this thesis, with page references directing to their initial usage or definition.

AHT Atmospheric heat transport	28
AMOC Atlantic Meridional Overturning Circulation	182
ASM Asian summer monsoon	181
AUSM Australian summer monsoon	181
BJC Bjerknes compensation	88
CE-AHT Cross-equatorial atmospheric heat transport	viii
CE-OHT Cross-equatorial oceanic heat transport	viii
CMIP6 Climate Model Intercomparison Project Phase Six	22
CPC Climate Prediction Center	39
DJF December-January-February	vii
ECMWF European Centre for Medium Range Weather Forecasts	22

EFE Energy flux equator	ix
ENSO El Niño-Southern Oscillation	39
ERA-5 ECMWF reanalysis 5th generation	22
GM Global monsoon	3
GPCP Global Precipitation Climatology Project	22
HadISST1 Hadley Centre Sea Ice and Sea Surface Temperature version 1	xii
HC Hadley circulation	34
IPO Inter-decadal Pacific Oscillation	182
ITCZ Inter-tropical Convergence Zone	3
JJA June-July-August	vii
LE Latent energy	46
MTSF Mid-tropospheric (averaged between 700-300 hPa) stream-function	ix
NH Northern hemisphere	3
ONI Oceanic Niño Index	39
OPT Ocean potential temperature	xii
SE Standard error	69

SH Southern hemisphere	3
SPCZ South Pacific convergence zone	63
SSP Shared Socio-economic Pathway	26
SST Sea surface temperature	183
STJ Sub-tropical jet	6
TEJ Tropical easterly jet	9
RCP Representative Concentration Pathway	26
OHT Oceanic heat transport	38
ORAS-5 Ocean reanalysis system 5	22
TOA Top of the atmosphere	27

1

Introduction

1.1 Background and Context

Monsoons are blessings to several regions of the world, and monsoonal precipitation contributes about 31% of the total global rainfall (Wang and Ding, 2008). Many densely populated countries get the majority of their rainfall during the summer monsoon. For instance, in the regions north of 20°S in Australia, more than 80% of the total rainfall occurs during the December-March period (Suppiah, 1992), whereas the South Asian Monsoon regions, during June to September, receive a significant portion of the annual rainfall, exceeding 75% (Turner and Annamalai, 2012; Masson-Delmotte et al., 2021). Monsoonal rainfall is vital for plantations, crop growth, and water resources (Wang et al., 2011). Thus, monsoons play a critical role in the economies of those agriculture-dependent regions (Webster et al., 1998). Monsoonal rainfall exhibits high temporal as well as spatial variations; for example, the In-

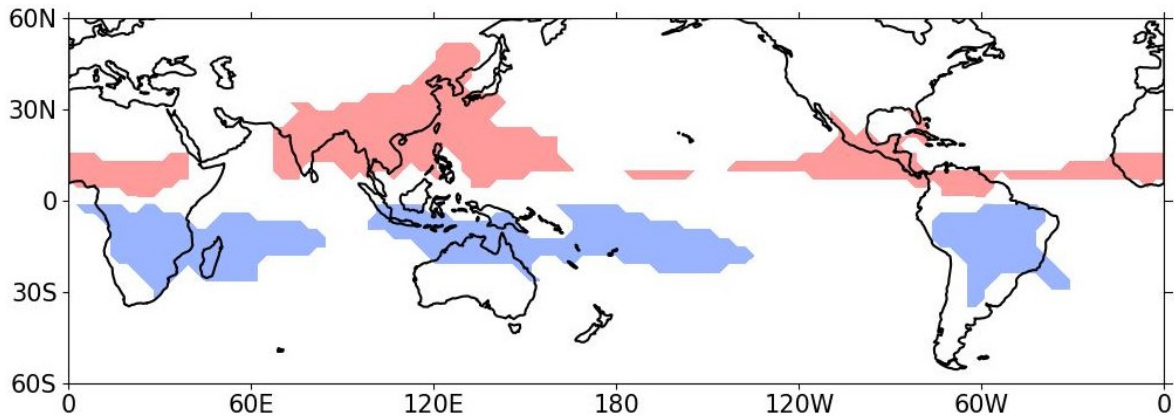


Figure 1.1: The global monsoon domain is reproduced and delineated as areas where the difference between local summer (boreal: JJA) and winter (boreal: DJF) precipitation exceeds 2 mm per day using GPCP precipitation spanning 1979–2020, as described in earlier studies (Wang and Ding, 2008; Zhou et al., 2008a,b; Wang et al., 2013a; Kitoh et al., 2013; Wang et al., 2014; Yim et al., 2014; Geen et al., 2020). The regions exhibiting JJA season monsoon characteristics, including the North American, North African, and Asian monsoons, are depicted with red shading, while those displaying DJF season monsoon features, such as the Australian, South American, and South African monsoons, are represented with blue shading.

dian monsoon rainfall varies spatially, ranging from 160 to 1800 mm/year (Kishore et al., 2016). As a result, a lack of monsoon rainfall can lead to drought, water scarcity, crop failures, and food shortages. Monsoons can also cause heavy rainfall and floods, which can lead to damage to infrastructure and homes and the loss of life. Therefore, we need to understand variations in monsoons on interannual, decadal, multi-decadal, or climate time scales in order to make better forecasts or for infrastructure planning and water, energy, and food security (Turner and Annamalai, 2012).

The root of the term ‘monsoon’ is the Arabian word ‘Mausam’, which means ‘season’ (Wang et al., 2014). A monsoon has been defined in terms of temperature gradient, wind, atmospheric circulation, and precipitation. Monsoons typically occur in tropical and subtropical regions and are associated with large-scale changes in atmospheric pressure and temperature. According to the classical definition of the monsoon, the reversal of the prevailing surface wind direction is attributed to the differential heating of the ocean and land during solstice seasons (Halley, 1686). So, land-sea differential heating and the resulting pressure gradients drive monsoons. However, the land-sea thermal contrast is neither essential nor solely responsible for monsoon occurrence; the annual variation of solar radiation

is crucial (Wang et al., 2012a). Therefore, the modern definition states that monsoon is a seasonal wind system that blows from a cold to a warm direction, and it is characterised by a significant contrast in wind direction, wind intensity, and precipitation between rainy and dry seasons (Webster, 1987; Wang and Ding, 2006; Wang et al., 2014, 2017).

Rainfall influences atmospheric circulation, the hydrological cycle, and connects radiative forcing to atmospheric circulation (Wang et al., 2012a; Dixit, 2020). Global monsoon (GM) rainfall, the largest component of the global water and energy cycles, drives atmospheric circulation (Wang et al., 2012b, 2014). During boreal summer (JJA), Northern hemisphere (NH) monsoons undergo a summer rainy season with south-westerly winds, while the Southern hemisphere (SH) experiences a localized winter monsoon characterized by below-normal rainfall with an equatorward displacement (Wang et al., 2014). As a result, moisture transport from the winter to the summer hemisphere takes place. Conversely, during NH winter, precipitation anomalies reverse sign, and surface winds change direction. A view of the global monsoon domain, which includes all major regional monsoons, is displayed in Figure 1.1 (Wang and Ding, 2008; Zhou et al., 2008a,b; Wang et al., 2013a; Kitoh et al., 2013; Wang et al., 2014; Yim et al., 2014; Geen et al., 2020).

It is imperative to identify the defining features of the GM, which encompasses both summer and winter monsoons (Wang et al., 2012b), for a better understanding of the monsoon's regional and global aspects. GM has been characterized in multiple manners, and a few are discussed here. The GM is defined as a planetary-scale seasonal reversal of the three-dimensional monsoon circulation, which is linked to the movement of rainfall within the monsoon trough and the Inter-tropical Convergence Zone (ITCZ) (Wang et al., 2014). Trenberth et al. (2000) provided a definition of the global monsoon, characterising it as a persistent, year-round atmospheric circulation spanning the tropics and subtropics on a planetary scale. Chao and Chen (2001) redefined the concept of a monsoon as the trade winds converging ITCZ situated significantly away from the equator, typically more than 10 degrees, and the presence of the ITCZ does not necessarily depend on land-sea contrasts. According to Geen et al. (2021), the global monsoon is the annual north-south migration of

the tropical rain band, which spans the globe by a low-latitude rainfall band and circulation of the yearly cycle.

GM is a response to the annual variation of solar radiation (Wang et al., 2012a), while the variations observed among regional monsoon systems predominantly stem from specific surface features such as land-sea distribution, topography, and oceanic circulations (Wang et al., 2017). Despite a broad range of factors between global and regional monsoons, the key common feature is the low-level cross-equatorial component of flow into the summer hemisphere, driven by seasonal pressure and temperature differences. **Atmospheric circulation can be categorised into rotational and divergent components, where the divergent atmospheric circulation refers to the horizontal outflow of air from a region, which typically leads to subsidence (downward motion) in high-pressure zones or upward motion in low-pressure areas.** By analysing the divergent components of meridional circulation on a height-latitude plane, Trenberth et al. (2000) identified six regional monsoon domains. Those monsoon sectors are Africa, Australia-Asia, North America, South America, and the Pacific and Atlantic Oceans. Wang et al. (2011) has discussed about seven regional monsoon systems, namely: the South Asian monsoon, East Asian monsoon, Australian monsoon, North African monsoon, South African monsoon, North American monsoon, and South American monsoon. The existence of two different sets of monsoon domains can be attributed to variations in the criteria and methodologies used by different studies. Trenberth et al. (2000) have emphasized the divergent elements of meridional circulation, whereas Wang et al. (2011) have employed precipitation distributions and wind patterns. Moreover, Trenberth et al. (2000) grouped larger areas together, whereas Wang et al. (2011) distinguished them as separate monsoon systems. For instance, Trenberth et al. (2000) merged the South Asian and East Asian monsoons into an ‘Australia-Asia’ region, whereas Wang et al. (2011) considered them distinct systems.

However, a more comprehensive understanding of the formation mechanisms of monsoons would not only enrich our knowledge of the global monsoon (GM) phenomenon but also enhance our insights into the dynamics and characteristics of regional monsoons.

Following the classical notion, as mentioned in many studies (Halley, 1686; Meehl, 1992; Gadgil, 2018), a thermal low is formed over the land region because of the lower heat capacity, whereas the reverse pattern is observed over the ocean, leading to a pressure gradient directed from the ocean towards the land. As a result, the surface wind changes its direction, blows from the ocean towards the land, and brings a large amount of moisture from the surrounding oceans towards the land. Imported moisture-laden warm air rises and condenses over the land, leading to precipitation. Another significant mechanism of precipitation formation is orographic lifting. When moist air encounters mountain ranges (such as the Western Ghats in India) or elevated terrain (the Himalayas and Tibetan Plateau), it is forced to rise. As the air ascends, it cools and condenses, leading to enhanced rainfall on the windward side of the mountains. Conversely, in winter, radiative cooling and heating over the land and ocean lead to a thermal high and low, respectively, which induces a reversed pressure gradient, inverses the wind direction, and initiates the onset of the winter monsoon. So, the switching of radiative heating and temperature gradients between land and adjacent oceans following the solar cycle drives the monsoon by reversing the surface wind direction, atmospheric circulation, and associated precipitation.

However, the complex interactions between ocean and land in global circulation are simplified in aquaplanet model simulations, challenging the classical understanding of monsoon behaviour. In an aquaplanet model setup, a monsoon can develop over large bodies of water, even in the absence of landmasses or continents, with its onset attributed to large-scale extra-tropical eddy momentum fluxes (Bordoni and Schneider, 2008). Topography, land-sea contrasts, and other surface irregularities contribute to the intricate structure of monsoons, including the asymmetric onset and end of monsoons (Bordoni and Schneider, 2008). Chao and Chen (2001) have shown, using a global circulation model, that the presence of a continental-scale land-sea contrast during both summer and winter monsoons is not a prerequisite for their occurrence. They found that the monsoon persists even when the Asian, Australian, and Maritime Continent land masses are replaced by high sea surface temperatures (SST). The land-sea contrast helps determine the monsoonal flow pattern and longitudinal

position of the ITCZ (Chao, 2000). Additionally, Gadgil (2018) documented a departure from the traditional monsoon theory for the Indian summer monsoon, revealing that surface temperatures peak over land in the northwestern part of the monsoon zone, where rainfall is minimal.

Hence, a monsoon used to be considered a planetary-scale land-sea breeze due to the differential heating of land and ocean for more than 300 years. However, this traditional view of the monsoonal driving force has been challenged, as monsoons have been observed to occur even in the absence of land masses (Chao and Chen, 2001; Geen et al., 2020). Let's delve into the tropical circulations and their connection with the monsoon.

One of the dominant atmospheric circulations in the tropics is the Hadley circulation (HC) (Hadley, 1735), which is coupled with monsoon circulation (Tanaka et al., 2004; Geen et al., 2020) and tropical precipitation (Seidel et al., 2008). The key features of the HC involve air rising up to the tropopause over the tropics (a height of approximately 12–15 km) (Nguyen et al., 2013). This upward motion occurs due to buoyancy, and at higher altitudes, there is a divergence of air towards the poles (Johanson and Fu, 2009; Wallace and Hobbs, 2006). However, the ascent is constrained by the presence of the tropopause. Subsequently, air descends into the subtropics due to upper-level mass convergence, followed by an equatorward return flow near the surface induced by the Coriolis effect (Seidel et al., 2008; Johanson and Fu, 2009; Nguyen et al., 2013). The boundaries of the Hadley cell, which delineate the tropics, are defined by the poleward reach of subsidence in the subtropical dry zones and by the positions of the Sub-tropical jet (STJ) (Fu et al., 2006; Seidel et al., 2008; Johanson and Fu, 2009; Nguyen et al., 2013). As a consequence of subsidence, most of the deserts of the world lie over subtropical regions, and the mechanism is known as the Rodwell–Hoskins mechanism (Rodwell and Hoskins, 1996; Chou and Neelin, 2003). However, during the solstice seasons (JJA and DJF), a single cross-equatorial HC cell dominates, whereas during the equinoctial seasons, an individual HC cell is visible on either side of the equator and spans from the tropics to the subtropics (Oort and Yienger, 1996; Geen et al., 2018, 2020).

The ITCZ is interlinked with the HC and plays a significant role in controlling the tropical climate by regulating temperature, moisture, and rainfall patterns. The ITCZ, a planetary-scale narrow tropical rain belt having increased convective cloud and coincident with the ascending branch of the HC, arises from the convergence of south-easterly winds from the southern hemisphere and north-easterly winds from the northern hemisphere (Schneider et al., 2014; Adam et al., 2016a,b; Geen et al., 2020). The ITCZ can be categorised into the monsoon trough zones, which are predominant over the global monsoon domains, including both land and oceans, and the trade wind convergence zones, primarily found over the central Pacific and Atlantic Oceans (Wang, 1994). The ITCZ shows a north-south movement relative to the equator, and its latitudinal position, width, and area have a great impact on precipitation (Byrne et al., 2018). For example, in boreal summer, the northern extreme of the ITCZ is prominent over India, influenced by the intense warming of the Eurasian landmass and the heating effect of the Tibetan Plateau (Yanai and Wu, 2006), whereas the southern extreme lies near Madagascar during austral summer, driven by the strong southward cross-equatorial flow originating from the NH winter monsoon and the associated Iranian High (Wang et al., 2014). Overall, the ITCZ oscillates more widely over the Indian monsoon domain between the typical latitudes of 20°N and 8°S (Schneider et al., 2014; Lashkari and Jafari, 2021).

The above discussion outlines very evidently that the HC, ITCZ, and monsoon circulation are strongly coupled tropical phenomena with different driving forces (Tanaka et al., 2004; Geen et al., 2020). The ITCZ and monsoon circulation are integral parts of the HC, considering the concept of convergence zone (rising branch of the HC) (Geen et al., 2020). During the seasonal cycle, the Hadley circulation rapidly swings between an equatorially symmetric state and a cross-equatorial state (equatorially asymmetric) (Lindzen and Hou, 1988). When the convergence zone is located at or near the Equator, the HC is primarily influenced by eddies, and the convergence zone resembles the ITCZ (Geen et al., 2020). Conversely, when the convergence zone is distant from the Equator, the thermally driven HC represents monsoons, with its strength primarily determined by energetic constraints. The shift from an equatorially symmetric to an equatorially asymmetric Hadley circulation oc-

occurs when the convergence zone moves beyond approximately 7 degrees from the equator (Geen et al., 2018, 2019). In aquaplanet models, recent research has also investigated the maximum extent of the convergence zone's migration away from the Equator; it does not extend beyond 25 degrees, even when the maximum moist static energy is located at the poles, due to Earth's rotation rate and weak temperature gradients (Faulk et al., 2017).

However, the close proximity of the ITCZ and the peaks of the Hadley circulation during solstice seasons have been noted (Dima and Wallace, 2003). Moreover, during solstice seasons, the summer-Hadley cell extends towards the pole more than the winter-Hadley cell due to a greater deviation from angular momentum conservation (Kang and Lu, 2012). This deviation weakens upper-level zonal winds, allowing the Hadley cell to expand poleward before becoming baroclinically unstable. Moreover, the Hadley cell's poleward extent is influenced by the displacement of the ITCZ away from the equator, resulting in a greater poleward extension during solstices compared to equinoxes (Kang and Lu, 2012).

To sum up, the HC variations manifest regional monsoons (Webster, 2004), and the rising branch of the HC is collocated with the ITCZ. Unlike monsoons, the ITCZ is not confined to a fixed position, and its propagation towards monsoon regions has significant implications. Integrating discussions about the GM, regional monsoons, the HC, and the ITCZ within a single thread is essential given their interconnected nature. These atmospheric phenomena influence each other and collectively play a crucial role in shaping global climate patterns.

An inter-annual weakening trend of GM precipitation over land is observed during the period 1948-2003 and is attributed to the decrease of NH monsoon precipitation (Wang and Ding, 2006; Zhou et al., 2008b) and NH summer monsoon circulation (Jiang and Zhou, 2019). The suppression of North-African and South-Asian monsoons due to a decrease in both rainfall intensity and monsoon area induces that decline in NH land monsoon precipitation (Zhou et al., 2008b). However, an increasing trend of GMP is observed for the period 1979-2008 due to a significant increasing trend of NHSM precipitation (Wang et al., 2012a). The increase in Indian monsoon rainfall is attributed to intensification and northward movement of the ITCZ, typically located over the southern equatorial Indian Ocean during boreal

winter (Gadgil, 2018), and strengthening of the HC (Hari et al., 2020). A separated and northward-extended ITCZ branch induces heavy rains in the southern half of Iran and the countries of the Arabian Peninsula (Jafari and Lashkari, 2020). The inter-annual variation of the East Asian summer monsoon is linked to the local Hadley circulation variation (Sun and Zhou, 2014). Likewise, the Australian summer monsoon (AUSM) originates from the southward migration of the ITCZ and the shift of the Hadley circulation during the austral summer, as noted by (Gadgil, 2018). The intensification and southward shift of the local HC have led to heavy precipitation over northern Australia from 1930 to 2014 (Fahrenbach et al., 2024).

On an inter-annual time scale, the ENSO impacts both GM and regional monsoons. Inter-annually, global land monsoon precipitation shows a strong correlation with the ENSO (Wang et al., 2017), driven primarily by oceanic forcing (Zhou et al., 2008a). GM precipitation declines due to the warming of the central-eastern Pacific and western tropical Indian Ocean (Zhou et al., 2008a; Wang et al., 2017). ENSO exerts a greater impact on the NH summer monsoon (NHSM) compared to the SH summer monsoon (SHSM) (Wang et al., 2012a). Moreover, the Asian Pacific Oscillation is positively correlated with boreal summer monsoon rainfall across all major NH land on an inter-annual scale (Yim et al., 2014).

However, all regional summer monsoons, except for the Australian monsoon, exhibit a non-stationary relationship with ENSO (Yim et al., 2014). The connections between ENSO and the regional summer monsoons of the western North Pacific, Northern Africa, North America, and South America intensified but weakened for the Indian summer monsoon (with a recovery in the late 1990s) (Yim et al., 2014). For instance, the Tropical easterly jet (TEJ) has been identified as a connecting mechanism between ENSO and the Indian monsoon (Pattanaik and Satyan, 2000). During La Niña, the TEJ strengthens and induces heavy monsoon rainfall over India, whereas the opposite is true for El Niño (Pattanaik and Satyan, 2000). Moreover, following an El Niño event, basin-wide warming is observed over the tropical Indian Ocean, peaking in late boreal winter and early spring and persisting through boreal summer, resulting in an increase in precipitation across most of the Asian monsoon basins (Yang et al., 2007). Nonetheless, the connection between ENSO and Australian monsoon

rainfall is non-linear (Power et al., 2006; Cai et al., 2010; King et al., 2015). La Niña typically corresponds closely to substantially increased rainfall. Conversely, the extent of drying in Australia is less directly linked to the magnitude of El Niño (Power et al., 2006).

From an energy budget perspective, because of the tilt of the Earth, atmospheric composition, the angle of the incident solar radiation, and the Earth-Sun varying relative distance from the tropics to the poles, the lower latitudinal regions are a source of energy. Hence, the annual mean difference between absorbed and outgoing solar radiation is positive in low-latitude regions and negative in high-latitude regions (Trenberth and Solomon, 1994). In the annual mean, the net energy is positive and symmetric over the equatorial regions, as shown in Figure 1.2(a & b). During solstice seasons, equator-pole energy contrast is asymmetric and tends to be inter-hemispheric as well (Figure 1.2(c, d, e, & f)) (Gill, 1980). As a result, poleward and cross-equatorial hemispheric energy redistribution emerges as a crucial mechanism for regulating the Earth's climate.

In the model study, equatorial heating results in two narrower and weaker Hadley cells (Gill, 1980; Lindzen and Hou, 1988). However, the off-equatorial heating during solstice seasons triggers monsoon-like circulation in a simplified equatorial plane defined by longitude and latitude following the solution of (Gill, 1980). The solution of (Gill, 1980) states that upward motion will align with the prescribed heating along the 0 longitude, slightly north of the Equator. This heating induces adjustments in low-level zonal (u) and meridional (v) winds, resulting in convergence at the Equator and cyclonic circulations to the north, resembling monsoonal patterns. Surface pressure maintains an approximate geostrophic balance with near-surface winds in response to the heating (Gill, 1980). However, heating away from the equator leads to a stronger cross-equatorial cell, accompanied by a weaker cell in the summer hemisphere (Lindzen and Hou, 1988).

In the atmosphere, heat transport primarily occurs through the mean meridional overturning circulations in low latitudes, namely the Hadley circulation, and transient eddies in middle and high latitudes (Trenberth and Stepaniak, 2003b,a, 2004; He et al., 2019). Additionally, stationary eddies contribute to heat transport in the Northern Hemisphere (Oort and

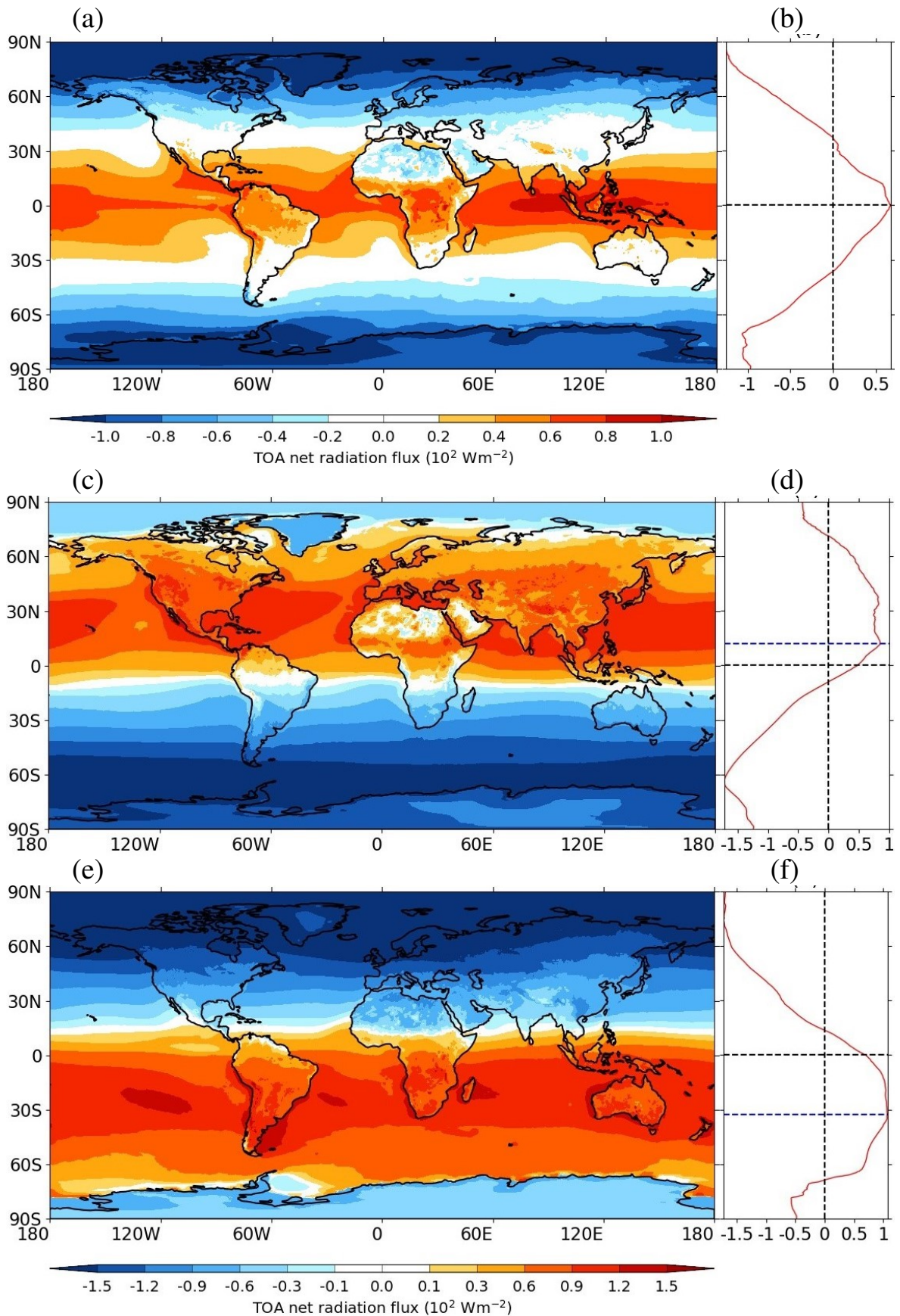


Figure 1.2: (a) The annual mean net radiation (net incoming – net outgoing) flux (Wm^{-2}) using ERA-5 for the period 1979-2020 at the Top of the Atmosphere (TOA). (b) Zonal mean of ‘(a)’. (c) and (d) are the same as Figures ‘(a)’ and ‘(b)’, respectively, but for the JJA season. (e) and (f) depict Figures ‘(a)’ and ‘(b)’, respectively, but for the DJF season. All the results align with previous findings (Trenberth and Stepaniak, 2004; Trenberth and Caron, 2001; Trenberth and Solomon, 1994). Page 11 of 214

Peixóto, 1983; Magnúsdóttir and Saravanan, 1999).

The net energy divergence and convergence are substantial in the rising and sinking branches of the Hadley cell, resulting in adiabatic cooling and heating, respectively (Oort, 1971; Trenberth and Stepaniak, 2003b). The low-level cross-equatorial HC branch imports latent heat in the form of moisture towards the rising branch (Lionello et al., 2024). The convection of imported moisture occurs because of existing thermal lows there. As a result, moisture condenses and falls down as precipitation, releasing latent heat or energy (LE) that intensifies the thermal contrast and brings more moist air towards that region. The released latent heat is subsequently converted into internal energy (IE), followed by its transformation into potential energy (PE), resulting in a cooling of the air. Internal and potential energy undergo a partial conversion into kinetic energy (KE) to sustain atmospheric circulation. Upon reaching higher altitudes, the relatively cold air is conveyed back to the subtropics via the upper branch of the Hadley cell, where it warms again in the descending branch. Here, its potential energy is converted back into internal energy.

The total atmospheric energy or heat (AHT) refers to the collective atmospheric energy (LE+IE+PE+KE) within a column (Trenberth and Stepaniak, 2004). Dry static energy (DSE) is the sum of enthalpy and potential energy, while moist static energy comprises DSE and LE (Trenberth and Solomon, 1994; Trenberth and Stepaniak, 2003a,b). During the solstice season, the subsiding branch of the dominating winter-Hadley cell lies in the winter hemisphere, but its rising branch is in the summer hemisphere (Oort and Yienger, 1996; Trenberth and Stepaniak, 2003b). This implies that the net CE-AHT occurs towards the winter hemisphere (Lionello et al., 2024). The energy cycle by the HC seems to effectively cool the atmosphere near the rising branch of the summer hemisphere and warm it in the subtropics of the winter hemisphere through adiabatic processes (Oort, 1971; Trenberth and Stepaniak, 2003b). Therefore, the width, strength, or intensity, and extent of the HC are significant for the redistribution of heat. A schematic view of HC and its associated heat transport is displayed in Figure 1.3.

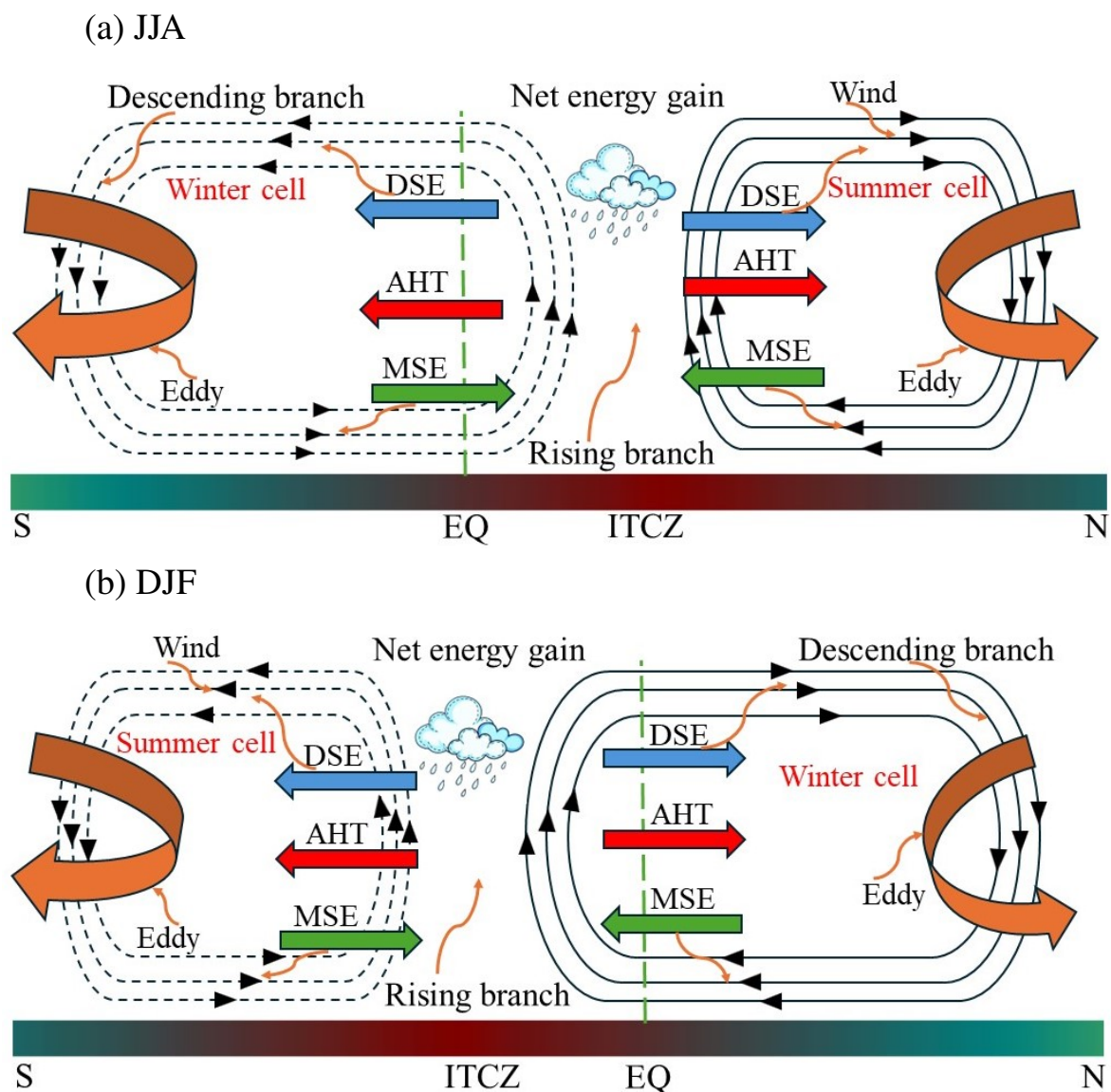


Figure 1.3: (a) An illustrative diagram depicts the behaviour of the Hadley Circulation (HC) during the JJA season. Wind patterns are depicted by black arrows, mass overturning stream-function by solid and dashed contours for positive (clockwise circulation from east) and negative (anti-clockwise circulation from east) values, respectively. Precipitation distribution is shown by white-blue droplets, and the direction of CE-AHT is represented by a red arrow at the equator. The cross-equatorial winter-Hadley cell, which symbolises monsoon circulation, transports atmospheric moist-static energy (MSE: green arrow) towards its ascending branch via the lower branch. Concurrently, the upper branch transfers energy from the summer hemisphere to the winter hemisphere as dry static energy (DSE: blue arrow). Midlatitude eddies (orange curved arrows) subsequently distribute heat from this region towards the poles. The ‘EQ’, ‘S’, and ‘N’ refer to the equator (dashed green line), south pole, and north pole, respectively. (b) Same as Figure (a), but for the DJF season.

In short, the winter-Hadley cell of the HC transports heat towards the winter hemisphere during the solstice seasons. Consequently, the HC acts to establish inter-hemispheric energy equilibrium by adiabatically cooling and warming the summer and winter hemispheres, re-

spectively. However, since oceans cover approximately 71% of the Earth's surface, it would be worthy of exploring the ocean's role in exporting heat (Trenberth and Stepaniak, 2004).

The overall heat content of the atmosphere is generally negligible compared to the ocean, owing to water's substantial capacity to store heat (Trenberth and Stepaniak, 2004). Furthermore, oceans account for 99.99% of the total water in the climate system (Hartmann, 2016). Thus, oceans act as a heat sink for the atmosphere over the tropics by absorbing and storing a large amount of excess heat from the sun and redistributing it around the globe through ocean currents. In the ocean, the subtropical cells (Klinger and Marotzke, 2000), which are the oceanic equivalent of the Hadley Cell's mean meridional overturning circulation, play a dominant role in heat transport at low latitudes (Zheng and Giese, 2009; Frierson et al., 2013). Ocean and atmosphere exchange momentum, water vapor, heat, and radiation at the sea surface (Hall and Bryden, 1982), particularly from the subtropics and high latitudes (Webster, 1994). Increasing ocean heat transport raises global near-surface temperatures and diminishes equator-to-pole temperature gradients (Rose and Ferreira, 2012). This increase in oceanic heat transport leads to a decline in atmospheric heat transport by weakening the HC (Knietzsch et al., 2015). Conversely, if the MOC and oceanic poleward heat transport are reduced, the atmosphere compensates by enhancing its northward transport transport (Vellinga and Wu, 2008). **Figure 1.4 shows a schematic representation of near-surface oceanic circulation and its corresponding heat transport. This circulation and heat transport are directly related to the atmospheric conditions. However, most of the oceanic heat transport occurs through deep oceanic circulation, particularly in the Atlantic Ocean.**

However, the meridional heat transport in the ocean is contributed by both the zonally averaged meridional overturning circulation (MOC) and the gyre circulation (Bryden, 1993). The overturning component of the meridional ocean heat transport (OHT) over the Atlantic Ocean accounts for the majority of the total when compared with the contribution from the gyre (Johns et al., 2011). Though both high-latitude convection and winds influence the heat transport associated with deep North Atlantic overturning circulations, the heat transport in the Pacific and Indian Oceans is associated with tropical and subtropical wind-driven gyres

(Ferrari and Ferreira, 2011). Unlike the peak atmospheric heat transport, which moves from the tropical periphery to middle and high latitudes (Oort and Yienger, 1996; Trenberth and Stepaniak, 2003b,a), oceanic heat transport is predominant within the deep tropics, typically within 10-15° of the equator (Ganachaud and Wunsch, 2003). However, if there is no alteration in both the net radiation flux at the top of the atmosphere (TOA) and the oceanic heat storage, the changes in atmospheric heat transport (AHT) and the changes in oceanic heat transport (OHT) are expected to occur in opposite directions as a compensatory response (Bjerknes, 1964; Zhao et al., 2016; Yang et al., 2016).

In the annual mean, the ocean's meridional overturning circulation plays a vital role in redistributing heat northward across the equator, contributing to the hemispheric asymmetry in tropical rainfall by transporting heat from the Southern Hemisphere to the Northern Hemisphere (Frierson et al., 2013; Lionello et al., 2024). The variability in this ocean heat transport is primarily driven by the strength of the meridional overturning circulation (Zheng and Giese, 2009). Observational records reveal a considerable decline in the Atlantic Meridional Overturning Circulation (AMOC) due to freshwater flux, leading to a reduction in northward oceanic heat transport (Bryden et al., 2005; Zheng and Giese, 2009; Bryden et al., 2020; Caesar et al., 2018, 2021). This reduction warms the equatorial ocean, which weakens the Walker circulation and results in an El Niño-like condition (Zhang and Delworth, 2005; Timmermann et al., 2005). In turn, these changes contribute to a weakening of the regional land-sea thermal gradient, a weakening of the regional Hadley circulation and monsoon circulation over the South Asian region, and an increase in northward atmospheric heat transport (Lu and Dong, 2008; Heaviside and Czaja, 2013; Sandeep et al., 2020).

Hence, atmospheric and oceanic circulations transport heat or energy from tropical regions and control the distribution of water vapour, clouds, and precipitation on both global and regional scales. This study aims to investigate the interactions between cross-equatorial (atmospheric and oceanic) transports of heat and the monsoon systems for the JJA and DJF seasons.

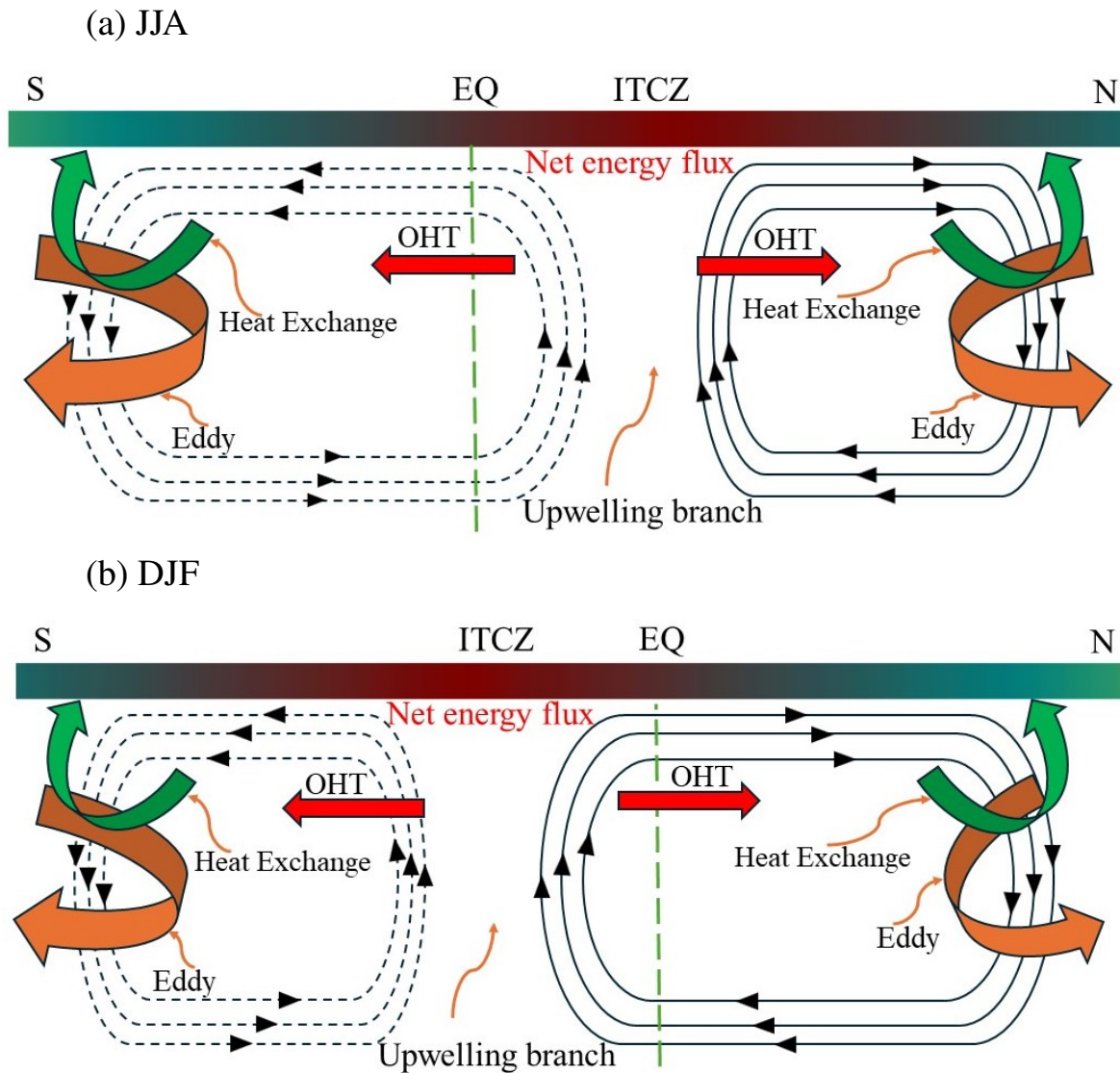


Figure 1.4: (a) A schematic illustration of near-surface ocean heat transport during the JJA season. Direction of circulation are depicted by black arrows, mass overturning stream-function by solid and dashed contours for positive (clockwise circulation from east) and negative (anti-clockwise circulation from east) values, respectively. The direction of CE-OHT is represented by red arrow at the equator. Heat exchange from the ocean to the atmosphere in mid-latitudes are denoted by the green curved arrows. Furthermore, mid-latitude eddies (orange curved arrows) subsequently distribute heat from this region towards the poles. The ‘EQ’, ‘S’, and ‘N’ refer to the equator (dashed green line), south pole, and north pole, respectively. (b) Same as Figure (a), but for the DJF season.

1.2 Motivation and Rationale

Monsoonal precipitation varies greatly and has a connection with energy circulation (Wang and Ding, 2008). While typically situated north of the equator on average (Gruber, 1972; Marshall et al., 2014; Schneider et al., 2014; Bischoff and Schneider, 2014, 2016; Adam et al., 2016a,b), the annual position of the ITCZ is influenced by complex interactions

between the ocean and atmosphere, inter-hemispheric heating contrast (Green et al., 2019), as well as coastal-continental surface patterns (Philander et al., 1996). Notably, the northward CE-OHT, particularly in the Atlantic Ocean, plays a significant role in determining the ITCZ's location (Marshall et al., 2014; Lu and Dong, 2008; Vellinga and Wood, 2002). Moreover, in the Indian monsoon domain, the ITCZ position exhibits substantial fluctuations and is inversely correlated with cross-equatorial atmospheric heat transport (CE-AHT) (Bischoff and Schneider, 2014). Specifically, stronger southward CE-AHT tends to push the ITCZ farther northward from the equator (Schneider et al., 2014; Liu et al., 2021). Despite these insights, there remains a gap in understanding the precise mechanisms governing the interaction between CE-AHT, CE-OHT, and the latitudinal variability of the ITCZ during solstice seasons (JJA and DJF). Therefore, this study seeks to fill this gap by investigating how the ITCZ position relative to the equator varies with CE-AHT and CE-OHT during the JJA and DJF seasons.

The connection between northern hemisphere summer precipitation and Hadley circulation intensity on a decadal scale has been documented (Wang et al., 2013a). **Observations from reanalyses indicate a significant poleward expansion of the HC by approximately 2 to 5 degrees over the past few decades (Lionello et al., 2024; Johanson and Fu, 2009).** This poleward migration is associated with the descending branch of the Hadley Cell, which induces a poleward shift of large-scale atmospheric circulation systems, such as jet streams and storm tracks (Fu et al., 2006; Seidel et al., 2008; Nguyen et al., 2013), and consequently leads to the expansion of subtropical dry zones towards the poles (Fu et al., 2006; Seager et al., 2007; Johanson and Fu, 2009; Hu et al., 2018). One plausible explanation for the HC expansion is the increase in tropospheric static stability (Seager et al., 2007). This increased stability serves to stabilize the subtropical jet streams, effectively suppressing baroclinic instability at the poleward flank of the Hadley Cell (Seager et al., 2007). Consequently, the Hadley Cell extends poleward, amplifying the vertical wind shear at its edge, until reaching a new latitude where this shear effectively compensates for the diminished baroclinic instability caused by the rising static stability.

Positive sea surface temperature (SST) anomalies over the Eastern Pacific Ocean strengthen and contract the HC, while the opposite effect occurs with negative SST anomalies on the yearly mean inter-annual time scale (Hu et al., 2018; Nguyen et al., 2013; Lau et al., 2006; Stachnik and Schumacher, 2011). During El Niño years, the anomalously warm tongue along the Pacific equator generates stronger and more concentrated ascent motion in the deep tropics, thereby causing the descent branch of the HC to also concentrate towards the equator (Hu et al., 2018). The influence of the El Niño Southern Oscillation (ENSO) on the HC during solstice seasons has been emphasized in previous studies (Oort and Yienger, 1996; Quan et al., 2004) and observed the same response. Given the integral roles of the ITCZ and monsoon circulation in the Hadley circulation, it is necessary to investigate the connection between cross-equatorial heat transport and the Hadley circulation during the JJA and DJF monsoon periods. Therefore, investigating how variations in cross-equatorial atmospheric and oceanic heat transport (CE-AHT and CE-OHT) influence the Hadley circulation during JJA and DJF seasons would provide valuable insights into these dynamics.

The effects of cross-equatorial atmospheric and oceanic heat transport (CE-AHT and CE-OHT) variations on monsoonal circulation and precipitation patterns during the solstice seasons remain largely unexplored. Therefore, the question arises: What are the implications of variations in CE-AHT and CE-OHT on monsoonal precipitation patterns during the solstice seasons (JJA and DJF)?

Coupled Model Intercomparison Project 6 (CMIP6) simulations reveal a substantial advancement in capturing the historical behaviour of the Hadley circulation (Wang et al., 2023) and sea surface temperature (SST) (Li et al., 2023). Similar to observations, climate model simulations exhibit a significant poleward expansion of the HC (Lionello et al., 2024; Johanson and Fu, 2009). In aquaplanet model simulations, global mean temperature and the pole-to-equator temperature gradient are identified as the driving factors for the HC expansion (Frierson et al., 2007). As surface temperatures rise, the static stability of the subtropical regions increases due to the higher moisture content in the atmosphere, which pushes the onset of baroclinic instability poleward. Moreover, simulations of global monsoon precip-

itation and intensity in the CMIP6 models are better compared to CMIP5 models (Wang et al., 2021). The skill of CMIP6 in simulating observational precipitation patterns has been discussed for JJA and DJF seasons and found consistent with observations (Du et al., 2022). However, the capability of CMIP6 models in simulating the relationship between cross-equatorial atmospheric and oceanic heat transport (CE-AHT, CE-OHT) and monsoon systems remains an open question.

However, (Hwang and Frierson, 2010) predicted a rise in poleward energy transport at 40°N and 40°S within the atmosphere as a consequence of global warming using the CMIP3 climate models. The primary reason for the rise in transport is attributed to the increased atmospheric moisture content, while the variability is predominantly accounted for by alterations in the radiation budget caused by cloud dynamics (Hwang and Frierson, 2010). In a warming climate, CE-AHT is anti-correlated with the precipitation intensity resulting from a narrowed ITCZ (Byrne et al., 2018). The ITCZ narrowing results from equatorward propagation of midlatitude eddies in response to the unstable baroclinic behaviour of the subtropical jets (Watt-Meyer and Frierson, 2019). However, if the meridional overturning circulation weakens in the future due to global warming, it could lead to southward shift the ITCZ (Frierson et al., 2013; Vellinga and Wood, 2002; Zhang and Delworth, 2005). Climate model projections reveal that AMOC weakening will cause a reduction in northward oceanic heat transport resulting a southward shift of the ITCZ relative to the equator (Sandeep et al., 2020; Frierson et al., 2013; Caesar et al., 2018).

Factors that contribute to the Hadley cell width changes include global warming (Frierson et al., 2007; Seager et al., 2007; Lu et al., 2007; Johanson and Fu, 2009; Kushner et al., 2001), the meridional SST gradient (Frierson et al., 2007; Lu et al., 2007), warming of the west Pacific (Johanson and Fu, 2009), or cooling of the polar stratosphere (Johanson and Fu, 2009; Williams, 2006; Lorenz and DeWeaver, 2007; Polvani and Kushner, 2002; Haigh et al., 2005). Under global warming, the middle and upper tropospheres experience greater warming compared to the lower troposphere in subtropical regions, which widens the HC (Hu et al., 2018). Concurrently, the subtropical dry zones exhibit a poleward expansion in

alignment with the movement of the HC (Lu et al., 2007). Poleward expansion of the Hadley cell is observed in all seasons with global warming, and the expansion is more strong when the ITCZ shifts further away from the equator (Kang and Lu, 2012).

Moreover, the NHSM rainfall intensity increases by 9.5% per degree of warming (Wang et al., 2013a). NHSM land rainfall declined from 1950 to 1980 but rebounded after the 1980s due to a combination of internal climate variability and radiative forcing Wang et al. (2021). Over the Indian monsoon domain, similar patterns were observed (Huang et al., 2020); global warming, aerosol effects, and deforestation were identified as factors contributing to the decline.

In a warming climate scenario, particularly during the boreal summer (JJA), it can be hypothesized that the northward and southward CE-AHT will increase and decrease, respectively. This southward decrease is attributed to the weakening of the HC. As a compensation, the southward CE-OHT is expected to be stronger. Consequently, it is anticipated that the ITCZ will shift northward in response to warming as the southward CE-OHT will increase. As the ITCZ shifts, it may alter the distribution of rainfall and atmospheric moisture transport, further influencing the northward CE-AHT. These hypotheses are based on our understanding of the mechanisms governing atmospheric and oceanic dynamics and their responses to climate change, as discussed earlier. However, the role of CE-AHT and CE-OHT in changing the HC, ITCZ, and monsoonal precipitation during solstice seasons remains uncertain under climate change. Addressing this research gap is essential for enhancing our understanding of the impacts of climate change on both global and regional scales.

1.3 Aims of this Study

The main purpose of this thesis is to explore the impact of cross-equatorial atmospheric and oceanic heat transport on monsoonal precipitation (global and regional) and circulation. Hence, the scientific questions of this study are:

- ▶ What relationships exist between cross-equatorial transports of heat in the atmosphere/ocean and the monsoons in observation-based reanalysis?

- ▶ How do the CMIP6 climate models simulate the relationship between cross-equatorial heat transports and monsoons?
- ▶ How do future climate projections alter the cross-equatorial transports, and can this be related to the monsoon response?

1.4 Structure of the Thesis

Datasets and methodology for computing CE-AHT, CE-OHT, and stream-function are discussed in Chapter 2. Subsequently, the relationship between CE-AHT, CE-OHT, and monsoons for reanalysis datasets is investigated in Chapter 3. Then, the performance of the CMIP6 models in simulating the relationship is documented in Chapter 4. Later on, the impact of climate change on CE-AHT, CE-OHT, and the relationship with the monsoons are detailed in Chapter 5. Finally, all the results and findings are reviewed, considering constraints and limitations, including future avenues of research, and compiled as a conclusion in Chapter 6.

2

Data and Methodology

2.1 Introduction

This chapter serves as the foundation upon which the subsequent analyses and interpretations are built. In this chapter, I provide a comprehensive overview of the data sources and methodological approaches utilised in the investigation of atmospheric and oceanic dynamics. The key data sources are: reanalysis data from the European Centre for Medium Range Weather Forecasts (ECMWF) (ECMWF reanalysis 5th generation (ERA-5) ; Ocean reanalysis system 5 (ORAS-5)), rainfall data from the Global Precipitation Climatology Project (GPCP) Version 2.3, SST data from the HadISST1, and data from the Climate Model Intercomparison Project Phase Six (CMIP6) models. **The GPCP is widely used for model evaluation because it offers comprehensive global coverage and has been collecting data for more than 40 years. In the comparison of ERA-5 and ERA-Interim reanalyses with GPCP,**

ERA-5 exhibited lower bias and unbiased root-mean squared error, along with higher correlation coefficients compared to ERA-Interim, particularly in the tropics and mid-latitude regions (Nogueira, 2020). The primary objective is to leverage these datasets to calculate stream-function and assess atmospheric and oceanic heat exports, shedding light on the relationship between cross-equatorial heat exports and monsoons. Reanalysis and climate model datasets are discussed in Section 2.2 and Section 2.3, whereas methodological approaches are provided in Section 2.4. Finally, the conclusion of this chapter is drawn in Section ??.

2.2 Observation-based Data

The GPCP Version 2.3 monthly mean rainfall data from 1979–2020 is used in this study and collected from the Physical Science Laboratory (Adler et al., 2018). The GPCP product is an integrated analysis that combines precipitation estimates from low-orbit satellite microwave data, geosynchronous-orbit satellite infrared data, and surface rain gauge observations (Adler et al., 2003). The microwave estimates are derived from Special Sensor Microwave Imager data from the Defence Meteorological Satellite Programme satellites, which operate in sun-synchronous low-Earth orbits. The infrared precipitation estimates are primarily obtained from geostationary satellites operated by the United States, Europe, and Japan, and secondarily from polar-orbiting satellites. Additional precipitation estimates are based on Television and Infrared Observation Satellite Operational Vertical Sounder and outgoing long-wave radiation (OLR) measurements. Rain gauge data are collected, quality controlled, and analysed to enhance the analysis over land. Datasets from all sources have been merged to estimate monthly rainfall on a 2.5-degree global grid from 1979 to the present.

The ERA-5 dataset is a comprehensive reanalysis from 1950 to near-real time that assimilates many observations from the upper air and near surface (note: the dataset now extends back to 1940) (Hersbach et al., 2020). However, uncertainty in ERA-5 is relatively higher during the pre-satellite era due to notable gaps in observational data coverage (Hersbach et al., 2020; Simmons et al., 2021). This dataset assimilates a vast array of observational data

from satellites, weather stations, and other sources and uses advanced 4D-Var data assimilation techniques. The ECMWF Integrated Forecast System (IFS) CY41R2 model forecasts (Váňa et al., 2017) and 4D-Var data assimilation (Rabier and Liu, 2003) are used to construct ERA-5, which has 137 hybrid sigma/pressure (model) levels in the vertical and a top level at 0.01 hPa. The dataset provides atmospheric data on these levels, along with interpolation to 37 pressure, 16 potential temperature, and 1 potential vorticity level(s).

Monthly atmospheric internal energy, latent energy, and stream function have been calculated using temperature, specific humidity, and meridional wind datasets, respectively. The meridional and zonal wind datasets are used for the estimation of kinetic energy. The monthly mean vertical integral of northward total energy flux ($\text{Jm}^{-1}\text{s}^{-1}$) ERA-5 data is the northward flow rate of total energy, extending from the surface of the Earth to the top of the atmosphere. Positive values indicate a flux from south to north as conventional. Total northward atmospheric energy is made up of northward internal, potential, kinetic, and latent energy. All the ERA-5 datasets considered for this study have a spatial resolution of $0.25^\circ \times 0.25^\circ$.

The ORAS-5, a state-of-the-art ocean reanalysis system developed by the ECMWF, uses a combination of ocean observations and a numerical ocean model to produce a consistent and accurate representation of the ocean state over the past several decades (Zuo et al., 2019). It uses the Nucleus for European Modelling of the Ocean (NEMO) model and the Ocean Regional Coupled Atmosphere (ORCA) grid resolution, which has a spatial resolution of about $1/4$ degree in the horizontal and about 75 levels in the vertical. The eddy-permitting ORCA grid is tripolar, with poles located over Antarctica, Central Asia, and North Canada. In addition to NEMO, ORAS-5 also uses a number of other models to represent the ocean state. The Louvain-la-Neuve sea-ice model version 2 (LIM2) is used to simulate sea ice dynamics and thermodynamics (Fichefet and Maqueda, 1997). A data assimilation system, NEMOVAR (3D-Var FGAT), that combines the ocean model with observations to produce the best estimate of the ocean state (Mogensen et al., 2012). The ORAS-5 ocean potential temperature and meridional velocity are used in this research and accessible from 1958 to the present day (Zuo et al., 2019).

SST is crucial in the climate system, weather prediction, and atmospheric model simulations, as it provides critical information on ocean-atmosphere interactions. SST influences pressure, wind speeds, and ocean circulation, which have the potential to change weather and climate patterns on global and regional scales. The HadISST1 SST dataset is derived from in situ sea surface observations and satellite-derived estimates (Rayner et al., 2003). The HadISST1 SST is available from 1870 to date on a 1-degree latitude-longitude grid.

Since the GPCP precipitation dataset is available from 1979 onwards, we maintain consistency among all variables by selecting the period from 1979 to 2020 for all analyses.

2.3 CMIP6 Model Data

Models enable scientists to explore potential future scenarios by projecting how the Earth system might respond to changes in various factors like greenhouse gas emissions, land use, and atmospheric composition. This predictive capability is essential for policy-makers and stakeholders to make informed decisions and develop effective strategies for mitigating and adapting to climate change and other environmental challenges.

Additionally, model studies help improve our understanding of observed phenomena by comparing model simulations with real-world observations. This process allows scientists to identify discrepancies between model outputs and observational data, leading to model refinement and enhancement.

Atmosphere-Ocean General Circulation Models (AOGCMs) in CMIP historical experiments are crucial because they provide a comprehensive representation of the Earth's climate by simulating interactions between the atmosphere and the ocean. AOGCMs allow for better understanding and prediction of how ocean currents and atmospheric conditions influence each other, which is essential for making reliable long-term climate forecasts and assessing past climate change impacts. In this study, historical simulations of the CMIP6 models (Eyring et al., 2016) are used to assess their performance in simulating observed climate conditions and the interplay between cross-equatorial heat transport and monsoons. A list of

the CMIP6 models for this study is given in Table 1.

Table 1: A table of CMIP6 Models used in this study

Model Name (Institute)	Atmosphere (Ocean) Resolution (°) (lon×lat)	Reference
CanESM5 (Canadian Centre for Climate Modelling and Analysis, Canada)	2.8°×2.8°(1°×1°)	(Swart et al., 2019)
CNRM-CM6-1 (Centre National de Recherches Meteorologiques, France)	1.4°×1.4°(1°×1°)	(Voldoire, 2019)
CNRM-ESM2-1 (Centre National de Recherches Meteorologiques, France)	1.4°×1.4°(1°×1°)	(Seferian, 2018)
EC-Earth3 (Swedish Meteorological and Hydrological Institute, Sweden)	0.7°×0.7°(1°×1°)	(EC-Earth Consortium (EC-Earth), 2019)
FGOALS-g3 (Chinese Academy of Sciences, China)	2°×2.25°(1°×1°)	(Li, 2019)
GISS-E2-1-G (Goddard Institute for Space Studies, USA)	2.5°×2°(1°×1°)	(NASA Goddard Institute for Space Studies (NASA/GISS), 2018)
HadGEM3-GC31-LL (Met Office Hadley Centre, UK)	1.875°×1.25° (1°×1°)	(Ridley et al., 2019a)
HadGEM3-GC31-MM (Met Office Hadley Centre, UK)	0.83°×0.55° (0.25°×0.25°)	(Ridley et al., 2019b)
IPSL-CM6A-LR (Institut Pierre Simon Laplace, France)	2.5°×1.25°(1°×1°)	(Boucher et al., 2018)
MIROC6 (Japan Agency for Marine-Earth Science and Technology, Japan)	1.4°×1.4°(1°×1°)	(Tatebe and Watanabe, 2018)
MPI-ESM1-2-HR (Max Planck Institute for Meteorology, Germany)	0.94°×0.94° (0.4°×0.4°)	(Jungclaus et al., 2019)
MPI-ESM1-2-LR (Max Planck Institute for Meteorology, Germany)	1.875°×1.875° (1.5°×1.5°)	(Wieners et al., 2019)
MRI-ESM2-0 (Meteorological Research Institute, Japan)	1.125°×1.125° (1°×0.5°)	(Yukimoto et al., 2019)
UKESM1-0-LL (Met Office Hadley Centre, UK)	1.875°×1.25°(1°×1°)	(Tang et al., 2019)

The CMIP6 future scenario experiments are characterized by two frameworks: a Shared Socio-economic Pathway (SSP) and a Representative Concentration Pathway (RCP). These frameworks are indicated by the three digits in the experiment's name. The first digit denotes the SSP storyline, reflecting socio-economic challenges related to mitigation and adaptation. The second and third digits signify the RCP climate forcing of the experiment (O'Neill et al., 2014). For instance, the SSP2-4.5 experiment corresponds to SSP2, which involves moderate mitigation and adaptation challenges, and RCP4.5, which results in a radiative forcing of 4.5

Wm^{-2} by 2100. There are five main SSP scenarios, and these are used in climate modelling to understand how global societal trends such as population growth, economic development, and technological advancements might evolve and influence greenhouse gas emissions and climate change (O'Neill et al., 2014).

However, the SSP5-8.5 scenario represents the high end of plausible future forcing pathways, leading to a radiative forcing of 8.5 Wm^{-2} by 2100. This scenario envisions a world with rapid economic growth driven by fossil fuels, resulting in high greenhouse gas emissions. Therefore, future projections from the CMIP6 models are examined to understand the potential impact of climate change under SSP5-8.5 scenario, with detailed findings presented in Chapter 5.

2.4 Methodology

This section aims to present a comprehensive overview of the methodologies employed throughout this thesis. Subsection 2.4.1 delves into the processes involved in estimating the atmospheric and oceanic heat transport by vertical integration techniques (direct method), while Subsection 2.4.2 elaborates on the estimation using the energy budgets and residuals at the surface and Top of the atmosphere (TOA) (indirect method). Additionally, Subsection 2.4.3 outlines the methodology employed for calculating stream-function.

2.4.1 Calculation of heat transport using a direct method

Energy transport by the atmospheric and oceanic circulations is crucial to the Earth's climate system and has drawn significant scholarly attention. The prevailing method for quantifying energy transport involves directly computing atmospheric energy transport by vertical integration through the utilisation of in situ measurements encompassing atmospheric temperature, humidity, geopotential, and wind velocity (Oort and Yienger, 1996; Oort, 1971; Trenberth et al., 2002; Chiodo and Haimberger, 2010; Trenberth and Stepaniak, 2003a; Mayer and Haimberger, 2012).

The mathematical expression used for the mass-weighted vertical integral of a property 'M' is (Oort and Yienger, 1996; Trenberth et al., 2002; Trenberth and Stepaniak, 2003a):

$$\widetilde{M} = \int_0^{\infty} \rho M dz = \frac{1}{g} \int_{p_t}^{p_s} M dp \quad (2.1)$$

where, ρ (kg m^{-3}) is the density, g ($=9.8 \text{ m s}^{-2}$) is the gravitational acceleration, p (Pa) is the pressure, z (m) is the altitude, p_s is the surface pressure, and p_t is the pressure at the TOA.

The total heat or energy per unit mass of air in the atmosphere comprises four primary elements: enthalpy or sensible energy (SE), latent heat (LE), potential energy (PE), and kinetic energy (KE), as mentioned in the previous chapter. These components are characterized as, $SE = c_p T$, $LE = L_v q$, $PE = gz$, and $KE = 0.5 * (u^2 + v^2)$ (Trenberth and Solomon, 1994; Trenberth et al., 2002; Trenberth and Stepaniak, 2003a; Fasullo and Trenberth, 2008a; Trenberth and Fasullo, 2018; Liu et al., 2020b). Here, c_p ($=1004 \text{ J kg}^{-1} \text{ K}^{-1}$) is the specific heat capacity of dry air for constant pressure, T is the temperature of air in kelvin (K), L_v ($=2500 \text{ kJ kg}^{-1}$) is the specific heat of vaporisation or condensation, q is the specific humidity (kg kg^{-1}), u is the zonal wind velocity (m s^{-1}), and v is meridional wind velocity (m s^{-1}). **Moreover, dry static energy (DSE) is the sum of specific enthalpy or sensible heat ($SE = c_p T$) and PE, and moist static energy is given by DSE+LE.**

In pressure coordinates with the use of equation 2.1, the vertically integrated northward total atmospheric energy (\widetilde{T}_a) flux can be written as (Mayer et al., 2017; Trenberth and Fasullo, 2018; Liu et al., 2020b):

$$\widetilde{T}_a = \frac{1}{g} \int_{p_t}^{p_s} [(1 - q)c_p T + L_v q + gz + 0.5 * (u^2 + v^2)] v dp \quad (2.2)$$

The contribution of kinetic energy is negligible in comparison to moist static energy in the annual mean (Trenberth et al., 2002), but crucial in the energetics of general circulation, as it links and redistributes other forms of energy across the globe (Oort and Peixóto, 1983). The zonal integration of total northward atmospheric energy is termed the Atmospheric heat transport (AHT), and the mathematical expression is (Oort and Yienger, 1996):

$$[\widetilde{T}_a] = 2\pi R \cos(\phi) \int_0^{2\pi} \widetilde{T}_a d\lambda \quad (2.3)$$

where R (m), ϕ ($^\circ$) and λ ($^\circ$) represent radius of the earth, latitude and longitude, respectively.

However, the rate of change of vertically integrated mass \widetilde{M} can be expressed as:

$$\frac{\partial \widetilde{M}}{\partial t} + \int_{p_t}^{p_s} \frac{1}{g} \nabla \cdot M \mathbf{V} dp = S$$

where, \mathbf{V} is the horizontal velocity and S is the source minus sink of \widetilde{M} .

The total mass of the atmosphere within a column, denoted as \widetilde{m} , comprises the sum of dry air mass (\widetilde{m}_d) and water vapour or precipitable water (w), expressed as $\widetilde{m} = \widetilde{m}_d + w = p_s/g$, hence, $\widetilde{m}_d = (p_s/g) - w$. Ideally, we should consider the presence of liquid and ice phases of water as well, but their quantities are typically negligible (Trenberth, 1991; Trenberth and Fasullo, 2018). However, it's crucial to acknowledge their presence, especially regarding precipitation, which removes mass from the atmosphere, although mass can be restored through evaporation (Trenberth and Fasullo, 2018). The mass of dry air is conserved, therefore

$$\frac{\partial \widetilde{m}_d}{\partial t} + \nabla \cdot \int_{p_t}^{p_s} \frac{1}{g} (1 - q) \mathbf{V} dp = 0 \quad (2.4)$$

Mass and moisture conservation are essential for all budget studies, but several factors contribute to the violation of mass conservation on pressure coordinates in global reanalysis (Trenberth, 1991; Trenberth and Solomon, 1994; Trenberth et al., 1995; Trenberth, 1997; Trenberth et al., 2002; Trenberth and Fasullo, 2018; Liu et al., 2015; Mayer et al., 2017; Liu et al., 2020b). For instance, factors include the post-processing of variables onto pressure surfaces from native model grids, data assimilation, the complexities of addressing the lower boundary and introducing an artificial atmosphere below ground level, and the diurnal pressure fluctuations associated with the semi-diurnal tide, along with the timing and spatial distribution of observational data (Boer, 1982; Trenberth, 1991; Trenberth et al., 2002, 1995; Trenberth, 1997; Trenberth et al., 2002; Liu et al., 2020b). If the conservation of mass is violated, then the above equation 2.4, using equation 2.1 and $m_d = 1 - q$, can be expressed as (Mayer et al., 2021):

$$\frac{1}{g} \frac{\partial}{\partial t} \int_{p_t}^{p_s} (1 - q) dp + \nabla \cdot \int_{p_t}^{p_s} \frac{1}{g} (1 - q) \mathbf{V}^* dp = R_e \quad (2.5)$$

where \mathbf{V}^* is assumed to be the original velocity and R_e is the spurious residual. In this computation, W is estimated using moisture following (Liu et al., 2020b), since significant uncertainties have been identified in the estimates of precipitation within global reanalyses (Graversen et al., 2007).

It's widely acknowledged that the primary uncertainty and the leading source of inaccuracies in global reanalysis stem from the divergent wind component, the second term of the equation 2.4 (Boer, 1982; Trenberth, 1991; Trenberth et al., 1995), as it involves the dry air and the first term is negligible. As a result, the approach to assessing and rectifying the overall mass balance involves assuming that any discrepancies lie within the divergent wind (Trenberth, 1991; Mayer et al., 2017; Liu et al., 2020b). A barotropic correction is applied to the wind velocity, and let \mathbf{V}^c be the correction of \mathbf{V}^* , which does not depend on pressure. Therefore, the corrected velocity field \mathbf{V} can be written as,

$$\mathbf{V} = \mathbf{V}^* - \mathbf{V}^c$$

then

$$\int_{p_t}^{p_s} (1 - q) \mathbf{V}^c dp = \mathbf{V}^c (p_s - p_t - gw)$$

Since it is assumed that all the errors stem from the second term of the equation 2.5,

$$\nabla \cdot \mathbf{V}^c (p_s - p_t - gw) = R_e$$

Let us define a potential function X^c such that $R_e = \nabla^2 X^c$, then $\mathbf{V}^c = \nabla X^c / (p_s - p_t - gw)$, where w is the water vapour or precipitable water. Since all errors originate from the divergence of dry air, the corrected velocity field adheres to the dry air convergence equation 2.4 and R_e approaches zero. Although truncation errors prevent the exact satisfaction of the dry mass convergence equation due to the finite resolution of data and the significant spatial variability of surface pressure associated with terrain, any remaining discrepancy primarily consists of small-scale structures and is of minimal magnitude (Trenberth, 1991; Trenberth

and Solomon, 1994).

Figure 2.1 shows the estimation of AHT using different temporal resolutions compared to AHT derived from ERA-5 monthly vertically integrated northward total energy flux data for January 1979. The 6-hourly pressure level data provides a better approximation than the 12-hourly and 24-hourly data. Consequently, steps related to mass convergence have been omitted. For the period 1979-2020, AHT estimation is performed using ERA-5 monthly vertically integrated northward total energy flux data instead of 6-hourly pressure level data.

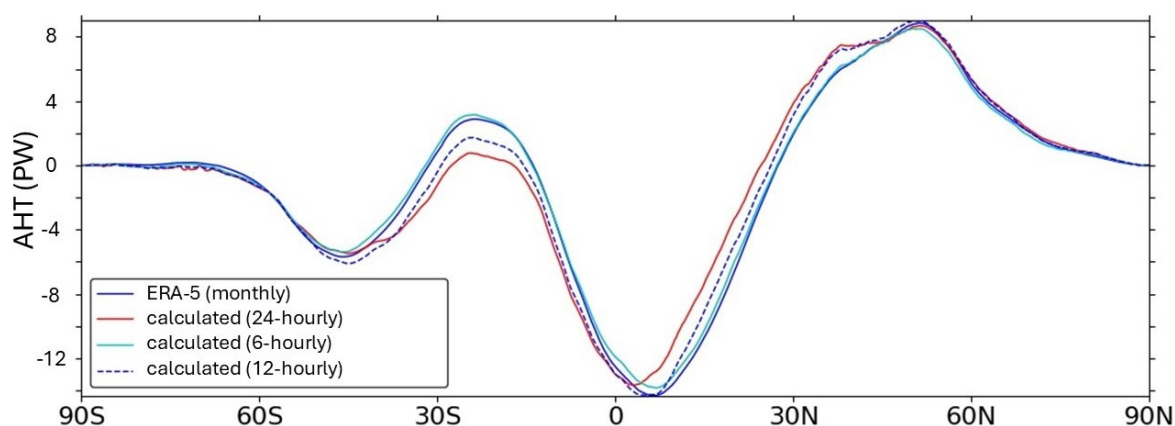


Figure 2.1: Annual-mean zonally integrated AHTs (PW) for January 1979, calculated using ERA-5 vertically integrated northward total energy data (blue solid line). AHTs derived from 6-hourly, 12-hourly, and 24-hourly ERA-5 pressure level data are represented by the cyan, red, and blue (dashed) lines, respectively.

In contrast to the atmosphere, energy transport within the ocean can be effectively described by its internal energy. The oceanic heat transport at any latitude can be computed using the following mathematical equation (Bryan, 1962; Hall and Bryden, 1982; Böning and Herrmann, 1994; Liu et al., 2020b),

$$[\tilde{T}_o] = \int_0^{2\pi} \int_{-H}^0 \rho_o c_{po} \theta v_o \cos(\phi) dz d\lambda \quad (2.6)$$

where, θ ($^{\circ}\text{C}$) is seawater potential temperature, v_o (m s^{-1}) is the meridional current velocity, z (m) is the vertical coordinate, c_{po} ($=3987 \text{ J kg}^{-1} \text{ }^{\circ}\text{C}$) is the specific heat capacity of seawater, ρ_o ($=10^3 \text{ kg m}^{-3}$) is the seawater density, and H (m) is the depth in the ocean.

The calculation of OHT encounters a slight mass discrepancy, for instance, stemming

from differences between precipitation and evaporation (Mayer et al., 2017).

2.4.2 Calculation of heat transport using an indirect method

The total mean transport for the entirety of the atmosphere-ocean system is inferred from the net radiative flux at the TOA (Oort and Yienger, 1996; Masuda, 1988; Trenberth and Caron, 2001). In the indirect method, the AHT is estimated from the net radiative energy input into the atmosphere, which is obtained by subtracting net surface energy and atmospheric energy storage from the net radiative flux at the TOA. Oceanic energy transport is subsequently discerned by deducting atmospheric energy transport from the total transport (Oort and Vonder Haar, 1976; Masuda, 1988; Trenberth and Solomon, 1994; Trenberth and Caron, 2001). However, the indirect estimation process of meridional atmospheric and oceanic heat transport is discussed below from the perspective of the global energy budget.

In a column, let \tilde{E} be the vertically integrated total energy of the Earth-climate system, then the rate of change of \tilde{E} can be expressed as (Oort and Vonder Haar, 1976; Zhang and Rossow, 1997)

$$\frac{\partial \tilde{E}}{\partial t} = \tilde{S}_a + \tilde{S}_o + \tilde{S}_l + \tilde{S}_{is} = R_{ta} - \nabla \cdot \mathbf{V}_a \tilde{T}_a - \nabla \cdot \mathbf{V}_o \tilde{T}_o \quad (2.7)$$

where, \tilde{S}_a , \tilde{S}_o , \tilde{S}_l , and \tilde{S}_{is} represent the rates of energy storage in the atmosphere, ocean, land, and ice-snow, respectively. R_{ta} is the net radiation energy flux at TOA (incoming shortwave – reflected shortwave – outgoing longwave; positive downward). \tilde{T}_a and \mathbf{V}_a stand for the vertically integrated total energy and horizontal velocity in the atmosphere, respectively, while \tilde{T}_o and \mathbf{V}_o represent those for the ocean. $\nabla \cdot \mathbf{V}_a \tilde{T}_a$ and $\nabla \cdot \mathbf{V}_o \tilde{T}_o$ denote the total atmospheric and oceanic energy divergences, respectively, where positive values indicate sources and negative values indicate sinks.

Equation 2.7 can be partitioned into atmospheric and oceanic branches of energy budgets, such as,

$$\textbf{Atmospheric: } \tilde{S}_a = R_{ta} - \nabla \cdot \mathbf{V}_a \tilde{T}_a - F_s \quad (2.8)$$

$$\textbf{Oceanic: } \tilde{S}_o + \tilde{S}_l + \tilde{S}_{is} = F_s - \nabla \cdot \mathbf{V}_o \tilde{T}_o \quad (2.9)$$

Here, F_s (positive downward) is the net energy flux at the surface, i.e., F_s is the summation of net radiative energy (net incoming – net outgoing) and net turbulent energy (sensible + latent). To simplify, \tilde{S}_{is} , which is positive (accumulation of heat) during local summer and negative (release of heat) during local winter, and \tilde{S}_l , which contributes minimally compared to oceanic heat storage, have been disregarded (Oort and Vonder Haar, 1976; Zhang and Rossow, 1997; Hwang and Frierson, 2010). Then equations 2.8 and 2.9 can be organised as:

$$\text{Atmospheric: } \nabla \cdot \mathbf{V}_a \tilde{T}_a = R_{ta} - \tilde{S}_a - F_s \quad (2.10)$$

$$\text{Oceanic: } \nabla \cdot \mathbf{V}_o \tilde{T}_o = F_s - \tilde{S}_o \quad (2.11)$$

The meridional heat transport in the atmosphere involves integrating the right-hand side of the equation 2.10 over both zonal and meridional directions. The same procedure applies to the ocean using equation 2.11. The northward and southward transports are considered positive and negative, respectively. In this process, the uncertainties in atmospheric and oceanic energy transfers stem from uncertainties in both the TOA and surface energy exchanges and predominantly pertain to surface radiative fluxes and latent heat exchanges (Zhang and Rossow, 1997).

The rationale behind employing a hybrid methodology, which amalgamates direct calculations for atmospheric storage and transports with indirect inference for surface energy flux or oceanic storage and transports (Zhang and Rossow, 1997), stems from the absence of comprehensive global measurements of current velocity, temperature, and salinity in the oceans (Oort and Vonder Haar, 1976; Trenberth and Solomon, 1994). The CE-AHT and CE-OHT are the heat transports at the equator by the atmosphere and ocean, respectively. The CE-AHT and CE-OHT are determined by linear interpolation at the equator for both the JJA and DJF seasons.

2.4.3 Estimation of stream-function

The HC, a fundamental large-scale atmospheric overturning circulation pattern, is crucial for understanding global climate patterns. The HC was comprehensively studied and interpreted through stream function analysis (Stachnik and Schumacher, 2011; Xian et al., 2021; Chemke, 2022). The stream function in fluid dynamics provides a tangible representation of fluid flow patterns in two-dimensional systems. Physically, the stream function embodies the concept of mass conservation, where the difference in stream function values between two streamlines corresponds to the flow rate per unit depth. It relates directly to the velocity components in the flow, facilitating an understanding of how fluid motion evolves over space.

The meridional stream-function in latitude (ϕ) - pressure (p) plane, denoted by $\Psi(\phi, p)$, is obtained by the vertically integrated zonal-mean meridional wind component, which measures the zonal-mean atmospheric mass circulation in kilogrammes per second. The mathematical representation of stream-function using the meridional wind component is (Oort and Yienger, 1996; Hari et al., 2020; Chemke, 2022; Mayer et al., 2023):

$$\Psi(\phi, p) = \frac{2\pi R}{g} \int_0^{p_s} [v] \cos(\phi) dp \quad (2.12)$$

Here, ϕ , p , p_s , R , g , and v have the same physical meaning and units as discussed above. The '['] symbol refers to the zonal mean. The positive and negative values indicate a clockwise and anti-clockwise circulation, respectively, from the east. For conservation of mass, the stream-function values are initialized as zero at the uppermost boundary of the atmosphere, while adjustments are made to ensure that the stream function equates to zero at the lower boundary (Stachnik and Schumacher, 2011).

The stream-functions for the JJA and DJF seasons will be analysed to find how the rising branch and the Hadley circulation (HC) change with the rise of CE-AHT and CE-OHT on an inter-annual time scale.

3

Cross-Equatorial Heat Transport and the Monsoons: Observational Insights

3.1 Introduction

Energy absorbed in the tropics is redistributed by the atmosphere and ocean. Understanding this transport is essential for comprehending global energy balance and climate dynamics. This energy transport significantly impacts weather patterns, ocean currents, and the overall stability of the climate system.

In observations, the distribution of annual mean transport by the atmosphere-ocean system across latitudes demonstrates significant symmetry between the hemispheres, with peak poleward transport of 5.9 PW occurring around 35 degrees latitude north and south (Stone, 1978; Masuda, 1988; Fasullo and Trenberth, 2008b). At those latitudes, atmospheric trans-

port contributes 78% of the total heat transport in the northern hemisphere and 92% in the southern hemisphere (Trenberth and Caron, 2001). The inter-annual variability ranges by ± 0.3 PW in the Northern Hemisphere and ± 0.5 PW in the Southern Hemisphere (Fasullo and Trenberth, 2008b). Atmospheric and oceanic contributions to total heat transport exhibit significant differences between the hemispheres. Notably, in the subtropical regions of the northern hemisphere, the ocean carries more heat poleward compared to the same latitudes in the southern hemisphere (Masuda, 1988; Trenberth and Solomon, 1994; Trenberth and Stepaniak, 2004; Fasullo and Trenberth, 2008b).

Ocean-atmosphere interactions play a pivotal role in controlling Earth's climate, primarily through heat transport by the atmosphere and ocean. Atmospheric heat transport is crucial for moderating the equator-to-pole temperature gradient and for the hydrologic cycle, such as monsoons and storm tracks. Furthermore, changes in atmospheric heat transport can have significant impacts on climate variability, such as shifts in the position of precipitation patterns and alterations to regional climate conditions.

The annual mean AHT peaks in the mid-latitudes (roughly between 35° – 50° latitudes) in both hemispheres, though the maximum transport occurs in the northern hemisphere (Trenberth and Caron, 2001; Mayer and Haimberger, 2012; Fajber et al., 2023; Masuda, 1988; Marshall et al., 2014; Mayer et al., 2021). The peak AHT value reaches ≈ 5.1 PW in the northern hemisphere and ≈ 4.9 PW in the southern hemisphere, accompanied by variability ranges of ± 0.5 PW and ± 0.2 PW, respectively (Fasullo and Trenberth, 2008b; Trenberth and Caron, 2001). The atmosphere dominates the mid-latitude heat transport, as both latent and dry static heat transports are poleward and reinforce each other, predominantly driven by eddy components (Yang et al., 2015). In the annual mean, changes in latent heat transport are often offset by changes in dry static energy transport of the opposite sign (Magnusdottir and Saravanan, 1999). As a result, cross-equatorial atmospheric heat transport is minimal near the tropics. The CE-AHT ranges between 0.22–0.43 PW with a variability ranging between ± 0.02 PW to ± 0.6 PW (Loeb et al., 2016; Stephens et al., 2016; Liu et al., 2017a; Mayer et al., 2017; Trenberth et al., 2019; Liu et al., 2020a).

In the JJA season, the southern hemisphere transports more atmospheric heat poleward from mid-latitudes than the northern hemisphere, whereas the opposite occurs in the DJF season (Fasullo and Trenberth, 2008b). As dry static energy transport dominates over latent heat transport outside of low latitudes, particularly in midlatitudes, this is primarily driven by a significant rise in transient transport (Magnusdottir and Saravannan, 1999). At low latitudes during JJA and DJF seasons, there's a significant cancellation between dry static and latent heat transports (Magnusdottir and Saravannan, 1999). Consequently, the CE-AHT is approximately -2 PW and 1.18 PW in JJA and DJF seasons, respectively (Heaviside and Czaja, 2013).

Similar to the atmosphere, oceans redistribute energy from the equator towards the poles, helping to regulate global temperatures and weather patterns. For example, warm ocean currents like the Gulf Stream transport heat from tropical regions to higher latitudes, which warms up the atmosphere and supplies moisture, and the variability in Gulf Stream transport leads to changes in European temperature, precipitation, and storm activity (Palter, 2015).

The annual mean oceanic heat transport exhibits dominance over the tropical regions. The highest average global ocean transport occurs at $\approx 15^\circ\text{N}$ with 1.7 PW and at $\approx 11^\circ\text{S}$ with 1.2 PW, where the associated variability ranges are ± 0.3 PW and ± 0.5 PW, respectively (Fasullo and Trenberth, 2008b; Trenberth and Caron, 2001). Relatively small poleward transport in the Southern Hemisphere stems from the cancellation of the northward transport in the South Atlantic, juxtaposed with the net southward transport in the combined Indo-Pacific Oceans (Ganachaud and Wunsch, 2003). Both the OHT and its divergence over the Indian Ocean, Atlantic Ocean, and Pacific Ocean are southward, northward, and poleward, respectively (Trenberth and Solomon, 1994), but the OHT over the Pacific Ocean is stronger (Forget and Ferreira, 2019). The annual mean OHT in the Pacific is almost symmetric about the equator, with northward and southward OHT peaks at 20°N and 10°S , respectively (Forget and Ferreira, 2019), where the contribution from the deep water circulation is very negligible (Bryden, 1993). In the annual mean, the heat transport at each latitude over the Indian and Atlantic Oceans is southward and northward, respectively (Trenberth and Caron, 2001; Trenberth et al., 2019). The global CE-OHT fluctuates between 0.22 – 0.53 PW, with variability

spanning from ± 0.1 PW to ± 0.6 PW (Loeb et al., 2016; Stephens et al., 2016; Liu et al., 2017a; Mayer et al., 2017; Trenberth et al., 2019; Liu et al., 2020a).

Similar to the atmosphere, the ocean in the southern hemisphere tropics exports a larger amount of heat towards the pole in comparison to the northern hemisphere tropics during the JJA season, and the reverse is observed in the DJF season (Fasullo and Trenberth, 2008b). The CE-OHT during the solstice seasons has not been extensively studied. However, the rise of low-latitude Oceanic heat transport (OHT) transport warms mid- to high-latitudes mean surface temperature and decreases the equator-to-pole temperature gradient (Rose and Ferreira, 2012). Thus, the oceanic heat transport modifies the atmospheric Hadley circulation, which in turn not only brings a huge amount of moisture towards the rising branch but also drives ocean heat transport (Trenberth and Stepaniak, 2003b).

However, the variability range in CE-AHT and CE-OHT underscores the significant dynamism and variability inherent in atmospheric and oceanic heat transport processes, influenced by factors such as atmospheric conditions, oceanic currents, and seasonal changes. The adjustment between CE-AHT and CE-OHT is achieved by shifting the HC and oceanic circulation and consequently shifting ITCZ meridionally relative to the equator (Liu et al., 2017b). For instance, the northward shift of the mean ITCZ in the coupled simulations is attributed to an enhanced northward ocean heat transport across the equator, which necessitates a compensating southward atmospheric energy transport across the equator. On the other hand, 1 petawatt (PW) change in the CE-AHT leads to about a 3° shift in the position of the ITCZ (Schneider et al., 2014). Thus, the CE-AHT and CE-OHT, by influencing the HC and ITCZ, impact monsoonal circulation and precipitation. Therefore, the scientific questions for this chapter are outlined below:

- ▶ What are the observed cross-equatorial atmospheric heat transport (CE-AHT) and oceanic heat transport (CE-OHT) in reanalysis during the solstice seasons?
- ▶ How do cross-equatorial atmospheric heat transports affect monsoons during solstice seasons by influencing the Hadley Circulation and ITCZ, in observation-based reanal-

ysis?

- ▶ How do cross-equatorial oceanic heat transports impact monsoons by affecting the Hadley Circulation and ITCZ in reanalysis data during solstice seasons?

This chapter is structured as follows: Section 3.2 provides an overview of the datasets and methodology employed for this chapter. The relationship between cross-equatorial heat transport and the monsoons using observational-based datasets is offered in Section 3.3. Finally, the conclusion is drawn in Section 3.4.

3.2 Data and Methodology

In this chapter, I use GPCP (precipitation), ERA-5 (zonal and meridional winds, surface pressure, air temperature, geopotential, and specific humidity), ORAS-5 (ocean potential temperature and meridional velocity), and HadISST1 (SST) datasets as observations. All these datasets have been discussed in detail in Chapter 2. By analysing these datasets, I evaluate CE-AHT and CE-OHT, their historical trends, variability, and correlations, and their connection to monsoon dynamics. Therefore, it is first required to understand the monsoons in terms of the HC and ITCZ during solstice seasons.

The Oceanic Niño Index (ONI) is crucial for monitoring and predicting the El Niño-Southern Oscillation (ENSO) phenomena, which significantly impacts global weather patterns through teleconnections (Latif et al., 1998). The ONI index is calculated by averaging sea surface temperature anomalies over the Niño-3.4 region (5°N to 5°S and 170°W to 120°W) with a 3-month sliding mean following the methodology of the Climate Prediction Center (CPC) of the National Oceanic and Atmospheric Administration. To address the significant warming trend in the Niño-3.4 region since 1950, these anomalies are typically computed relative to a 30-year base period which is updated every 5 years. The CPC used Extended Reconstructed Sea Surface Temperature Version 5 (Huang et al., 2017) for the calculation of the ONI, whereas I have used the HadISST1 data.

For causality analysis, a non-parametric statistical method called the permutation test is used to test hypotheses by re-sampling data. If A and B are time series, then null hypothesis assumes no relationship between A and B, and any observed correlation is purely due to chance. A null distribution is created by randomly permuting B multiple times and calculating correlations for each permutation. If the observed correlation falls outside the confidence interval, it is statistically significant.

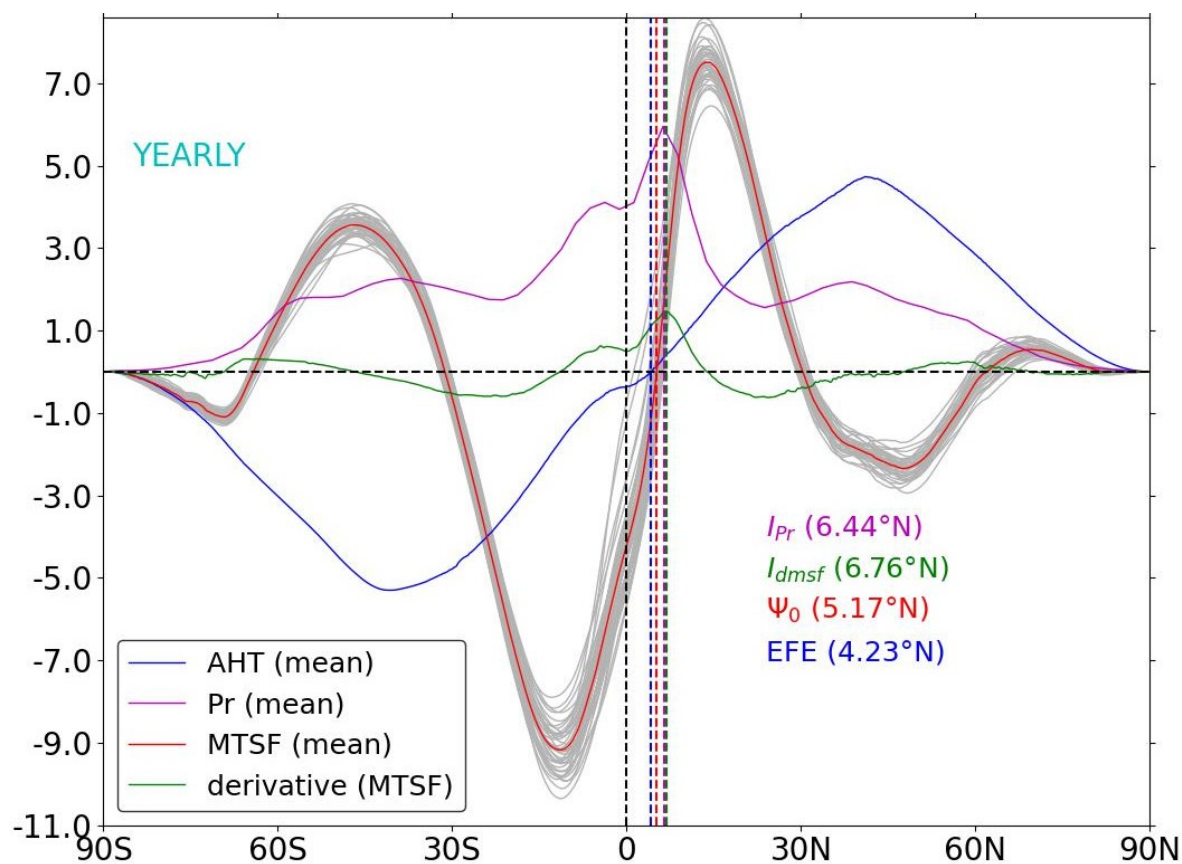


Figure 3.1: The time-averaged yearly mean mid-tropospheric stream function and its derivative are displayed by the red and green solid curves using ERA-5 reanalysis data for the period 1979–2020, respectively. The inter-annual yearly mean mid-tropospheric stream function is shown by grey lines. The annual, zonal-mean AHT and precipitation are shown by the blue and magenta solid curves, respectively. The vertical dashed lines in blue, red, magenta, and green represent the mean latitudinal position of the ITCZ using AHT (zero AHT: EFE), MTSF (zero MTSF near equator: Ψ_0), I_{Pr} , and derivative of MTSF (I_{dmsf}), respectively. The EFE, Ψ_0 , I_{Pr} , and I_{dmsf} metrics have the following units: PW, $1 \times 10^{10} \text{ kg s}^{-1}$, $\text{mm day}^{-1} \text{ rad}^{-1}$, and $0.5 \times 10^{10} \text{ kg s}^{-1} \text{ rad}^{-1}$, respectively.

The stream function as a metric has been used in many studies to determine the HC-associated indices like width, strength, intersection, and poleward edges or extents of the HC. The width of the HC has been defined as the distance between the equator and the latitude at which the 500 hPa stream function is equal to zero (Frierson et al., 2007). Having

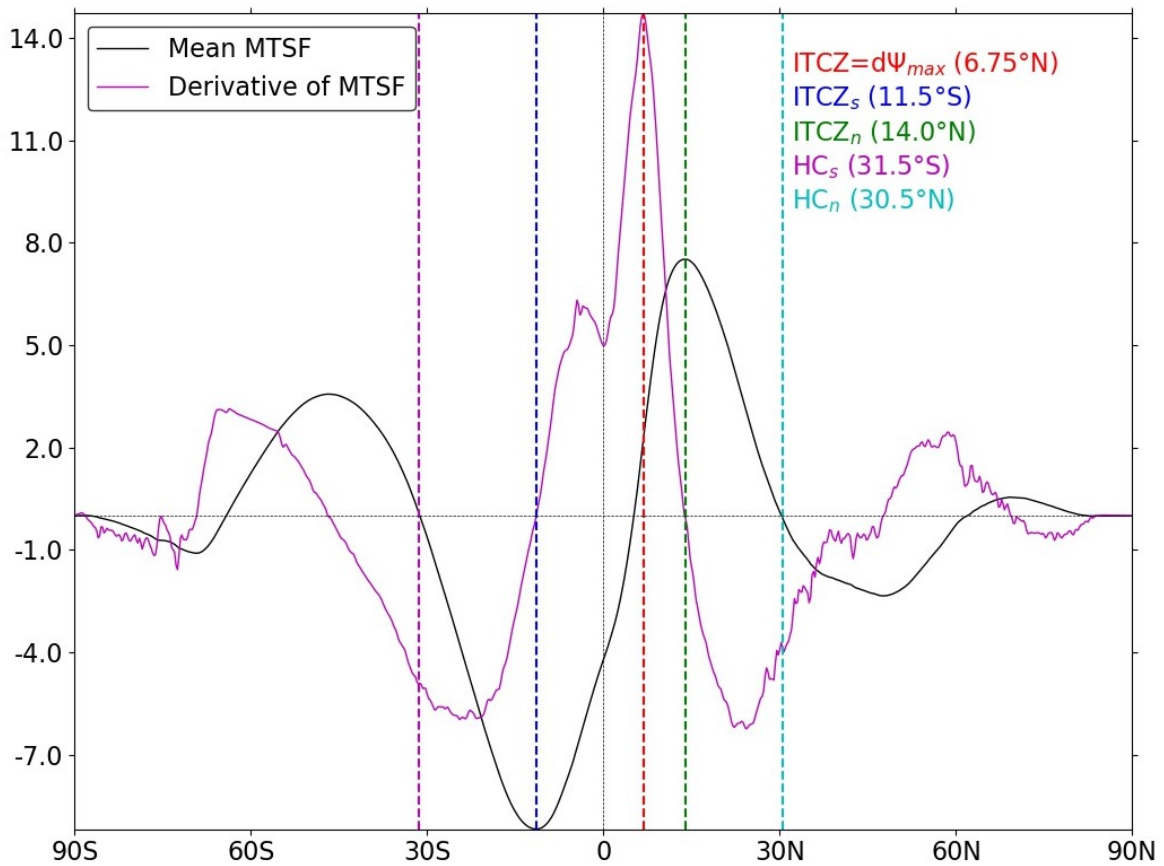


Figure 3.2: The annual mean mid-tropospheric stream-function and its derivative are displayed by the black and magenta solid curves using ERA-5 reanalysis data for the period 1979–2020, respectively. The vertical dashed lines in magenta and cyan represent the mean southern (HC_s : first zero to the south of Ψ_0 in MTSF) and northern (HC_n : first zero to the north of Ψ_0 in MTSF) edges of the Hadley circulation using MTSF, respectively. The red vertical dashed line is the position of the ITCZ by the derivative of MTSF (I_{dmsf}). The southern ($ITCZ_s$: first zero to the south of I_{dmsf}) and northern ($ITCZ_n$: first zero to the north of I_{dmsf}) latitudinal boundaries of the ITCZ are denoted by the blue and green vertical dashed lines, respectively. The units for MTSF and the derivative of MTSF are $1 \times 10^{10} \text{ kg s}^{-1}$, and $1 \times 10^9 \text{ kg s}^{-1} \text{ rad}^{-1}$, respectively.

determined the absolute maximum value of the stream function, the edges of the HC are determined as the first poleward latitude of the maximum value where the stream function reaches zero at 500 hPa (Lu et al., 2007). Another metric to identify the edges of the HC is the first poleward latitude where the value of the stream function, averaged over 700–400 hPa, equals zero, away from the location of the absolute maximum stream function in each hemisphere (Stachnik and Schumacher, 2011). The extents or edges of the HC can also be found by averaging the stream function over 600–400 hPa, whereas the intersection of Hadley cells is the latitude at which the stream function changes its sign or becomes zero near the equator (Nguyen et al., 2013). The maximum value of the stream function is an

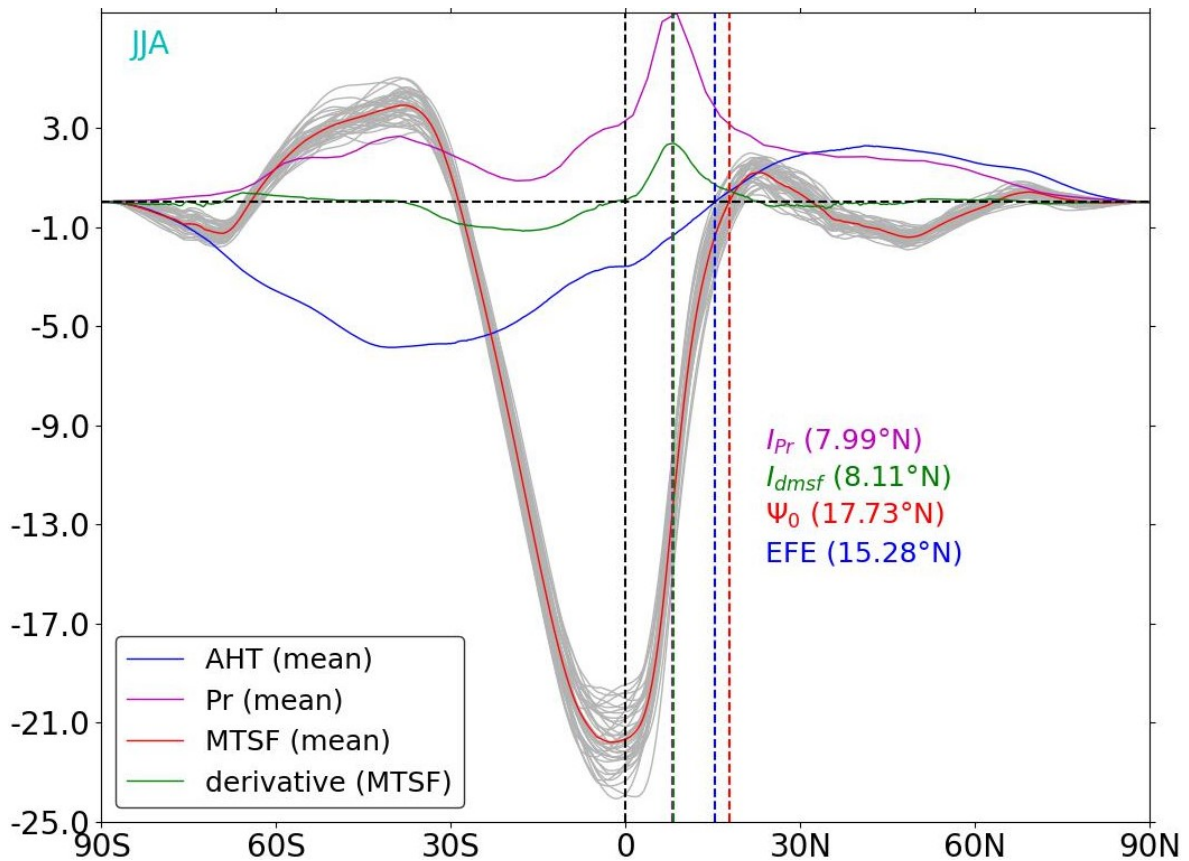


Figure 3.3: The JJA mean mid-tropospheric stream-function for each year is displayed by the gray solid curve using ERA-5 reanalysis data for the period 1979–2020. The time-averaged zonal mean MTSF (red), AHT (blue), precipitation (magenta), and derivative of MTSF (green) are shown by the solid curves for the JJA season, respectively. The vertical dashed lines in blue, red, magenta, green, represent the location of the ITCZ by the EFE (zero AHT), Ψ_0 , I_{pr} , and I_{dmsf} metrics, respectively. The EFE, Ψ_0 , I_{pr} , and I_{dmsf} metrics have the following units: PW, $1 \times 10^{10} \text{ kg s}^{-1}$, mm day^{-1} , and $10 \times 10^{10} \text{ kg s}^{-1} \text{ rad}^{-1}$, respectively.

index to measure the strength or intensity of the HC (Oort and Yienger, 1996), although the peak value of the stream function, having been vertically averaged over 900–200 hPa, is also used as an intensity index (Nguyen et al., 2013).

In this study, the MTSF is used to find the HC-associated indices by defining it as the average of stream-function between 700–300 hPa. The MTSF is zero (Ψ_0) around the equator in the annual mean and it is assumed the intersection of both the winter and summer Hadley cells. The latitude of first zero in MTSF away from Ψ_0 is identified in order to determining the northern and southern edges of the HC. The very first latitude of zero mass transport to the north and south of Ψ_0 in the MTSF is termed as HC-northern edge (HC_n)

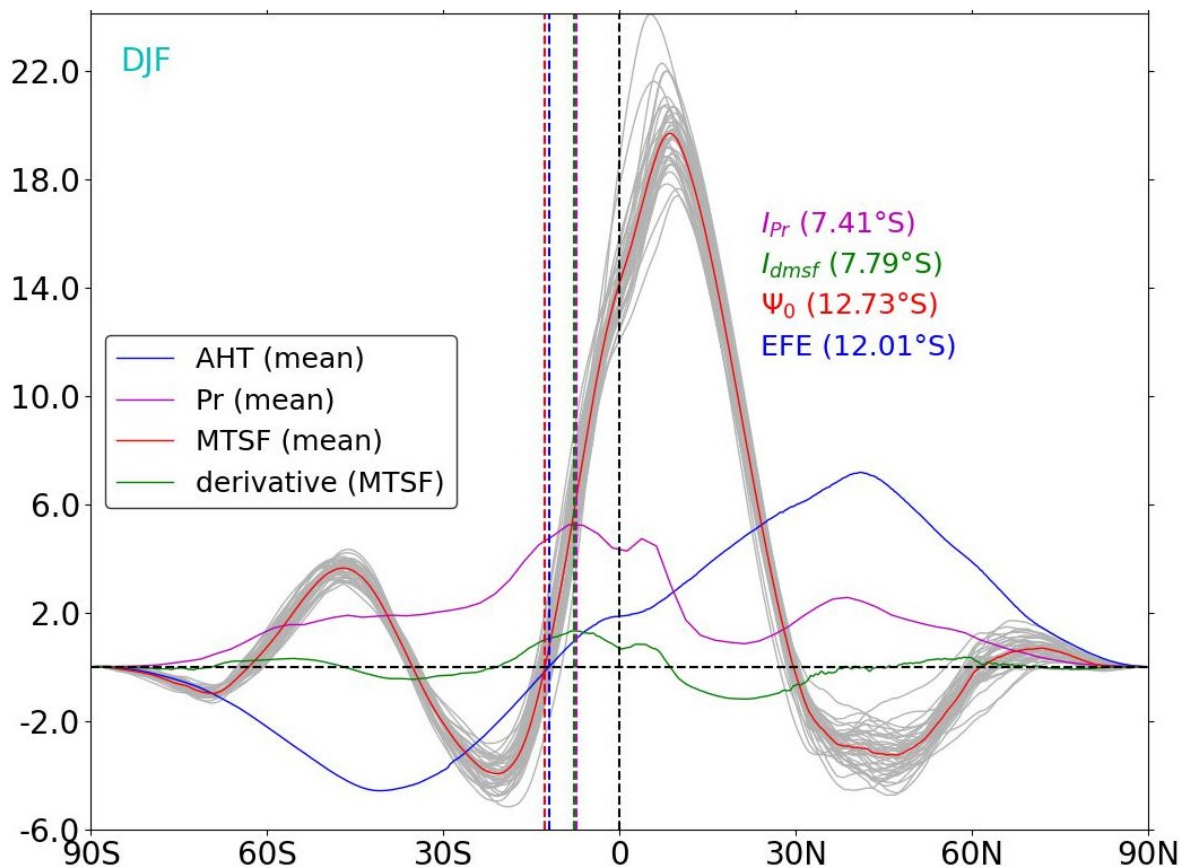


Figure 3.4: Same as Figure 3.3 except for the DJF season.

and HC-southern edge (HC_s), respectively. The width of the each HC cell is the difference between the position (Ψ_0) and HC edge (HC_n) or (HC_s). The width of the HC is the difference between (HC_n) and (HC_s). The maximum value of MTSF, Ψ_{max} , is used to find the intensity of the clockwise Hadley cell, whereas, the intensity of the anti-clockwise Hadley cell is determined using the minimum value of MTSF denoted by Ψ_{min} .

Various metrics are used to identify the meridional position of the ITCZ because its latitudinal position, intensity, width, and variability influence the rainfall distribution. The SST, precipitation, and stream function have been used frequently as metrics in past studies to determine the ITCZ location. For instance, Marshall et al. (2014) used the latitude of maximum zonal mean precipitation as the mean position of the ITCZ. Moreover, Donohoe et al. (2013) has identified the latitude of the ITCZ using the median of the zonal average precipitation from 20°S to 20°N. The characteristics of the ITCZ, like mean position, width, and strength, are measured with the help of stream-function (Byrne et al., 2018). Byrne et al. (2018) employed Ψ_0 to determine the position of the ITCZ, for the annual mean time scale. More-

over, the location of the ITCZ is identified using the EFE, which is the latitude where the atmospheric heat transport is zero near the equator, (Bischoff and Schneider, 2014; Adam et al., 2016a,b; Schneider, 2017). Mathematically, the location of maximum value is the point where the first derivative is zero. Therefore, the latitude at which the first meridional derivative of the zonal-mean precipitation becomes zero is used as the metric to identify the ITCZ position, denoted as I_{pr} (Kang et al., 2008).

In this study, from a dynamical perspective, the latitude where the first meridional derivative of the MTSF maximises is used as the metric to identify the ITCZ position and is denoted by I_{dmsf} . Because the maximum meridional derivative of MTSF indicates the exact location where air is rising. On the other hand, the zero of MTSF gives an idea of where the HC is changing its sign, and the EFE (zero AHT) describes the latitude from which the meridional integration of energy to each pole will be equal to the other. The ITCZ, defined by the precipitation maximum, is not always co-located with the zero of the atmospheric energy flux or mass flux (Bischoff and Schneider, 2014; Adam et al., 2016a,b; Schneider, 2017). Therefore, the ITCZ location is determined by the meridional derivative of the mass flux stream function instead of where the stream function or the energy flux vanishes. However, I_{dmsf} is considered to be maximum between 30°S and 30°N for the annual mean, from the equator to 30°N for the JJA season, and from 30°S to the equator for the DJF season. So, the latitude having the maximum in the derivative of MTSF is the core position ($ITCZ_c$) of the ITCZ. The very first latitudes to the north and south of $ITCZ_c$, where the derivative of MTSF equals zero, are defined as the northern ($ITCZ_n$) and southern ($ITCZ_s$) edges of the ITCZ, respectively. The width of the ITCZ is the difference between the northern and southern edges of the ITCZ, that is, ($ITCZ_n - ITCZ_s$). The maximum of the derivative of MTSF is used to estimate the intensity of the ITCZ.

However, I employ the Ψ_0 , EFE, I_{pr} , and I_{dmsf} metrics to identify the ITCZ. The ITCZ positions identified by Ψ_0 , EFE, and I_{dmsf} are juxtaposed with I_{pr} for the annual mean time scale and then for the solstice seasons. This approach will help to determine which metric performs consistently on different time scales.

The ITCZ dominates the spatial distribution of rainfall oscillating about the equator seasonally, and its latitudinal position is vital for identifying the location of intense precipitation. The latitude determined by the I_{pr} metric is considered the original location of the ITCZ, as the I_{pr} metric is based on the precipitation.

Figure 3.1 illustrates the location of the ITCZ identified by the I_{pr} , Ψ_0 , EFE, and I_{dmsf} metrics for the period 1979–2020 on the annual mean time scale. The ITCZ by the I_{pr} , Ψ_0 , EFE, and I_{dmsf} metrics is located at 6.44°N, 5.17°N, 4.23°N, and 6.76°N in the annual mean (Adler et al., 2003; Marshall et al., 2014; Bischoff and Schneider, 2014, 2016). The I_{dmsf} is a better metric to determine the latitude of the ITCZ, as both Ψ_0 and EFE metrics underestimate the latitudinal position of the ITCZ and exhibit larger errors.

Figure 3.2 displays the latitudinal boundaries of the HC and the ITCZ spanning the period 1979–2020 on the annual mean time scale. The intersection of the HC occurs at 5.17°N. The southern edge and northern edge of the HC are at 31.5°S and 30.5°N, respectively. The southern-hemisphere Hadley cell is wider than its counterpart. However, the derivative of MTSF is positive around the equator, and the interval of latitude is the width of the ITCZ (Byrne et al., 2018). The southern and northern edges of the ITCZ are located at 11.5°S and 14.0°N, respectively, where the derivative of the MTSF vanishes.

Hence, on the annual mean time scale, the metric I_{dmsf} outperforms other metrics in identifying the ITCZ location relative to I_{pr} . For the JJA and DJF seasons, it would be useful to compare other metrics to I_{pr} to see which one identifies the ITCZ more accurately.

Figure 3.3 depicts the location of the ITCZ determined by the I_{pr} , Ψ_0 , EFE, and I_{dmsf} metrics for the JJA season spanning 1979–2020. On an inter-annual time scale, the JJA mean location of the ITCZ is at $7.99 \pm 0.06^\circ\text{N}$, $17.73 \pm 0.22^\circ\text{N}$, $15.28 \pm 0.15^\circ\text{N}$, and $8.11 \pm 0.09^\circ\text{N}$ by the I_{pr} , Ψ_0 , EFE, and I_{dmsf} metrics, respectively. The RMSE values are 9.83° (I_{pr} versus Ψ_0), 7.37° (I_{pr} versus EFE), and 0.39° (I_{pr} versus I_{dmsf}). Moreover, the correlation coefficient between I_{pr} and I_{dmsf} is 0.77 (p-value < 0.01), whereas for other metrics the correlation coefficients are below 0.3 and not statistically significant on an inter-annual time scale.

Thus, the I_{dmsf} metric more accurately approximates the location of the ITCZ than the other metrics Ψ_0 and EFE for the JJA season.

In contrast to JJA, Figure 3.4 shows the ITCZ position identified by the I_{pr} , Ψ_0 , EFE, and I_{dmsf} metrics for the DJF season spanning 1979-2020. In DJF, the ITCZ sits at $7.41 \pm 0.27^\circ\text{S}$ (by I_{pr}), $12.73 \pm 0.16^\circ\text{S}$ (by Ψ_0), $12.01 \pm 0.13^\circ\text{S}$ (by EFE), and $7.41 \pm 0.34^\circ\text{S}$ (by I_{dmsf}), on an inter-annual time scale. The RMSE values are 5.23° (I_{pr} versus Ψ_0), 4.69° (I_{pr} versus EFE), and 1.41° (I_{pr} versus I_{dmsf}). Moreover, the correlation coefficients of I_{pr} with Ψ_0 , EFE, and I_{dmsf} are 0.63, 0.32, and 0.76, respectively, and statistically significant on an inter-annual time scale.

Hence, for the DJF season, the metric I_{dmsf} more accurately identifies the location of the ITCZ compared to the metrics Ψ_0 and EFE.

Briefly, the metric I_{dmsf} shows consistency in identifying the ITCZ location in both annual and seasonal time scales. So, I_{dmsf} is employed in parallel with I_{pr} to determine the zonal mean position of the ITCZ in the rest of the study, while I_{pr} is based on precipitation and I_{dmsf} uses the stream function.

3.3 Results

This section outlines observation-based cross-equatorial heat transport from the atmosphere and ocean and their relationships with the monsoons. Section 3.3.1 discusses AHT, CE-AHT, and their variation during the solstice seasons. Following this, Section 3.3.2 highlights the relationship between CE-AHT and monsoon systems for both the JJA and DJF seasons. Section 3.3.3 covers OHT and CE-OHT, while the impacts of CE-OHT on monsoons are provided in Section 3.3.4.

3.3.1 Observation-based atmospheric heat transport

Figure 3.5 depicts the annual mean AHTs spanning 1979–2020. Latent energy (LE) is abundant in the lower troposphere, and the lower branch of the HC exports LE towards the

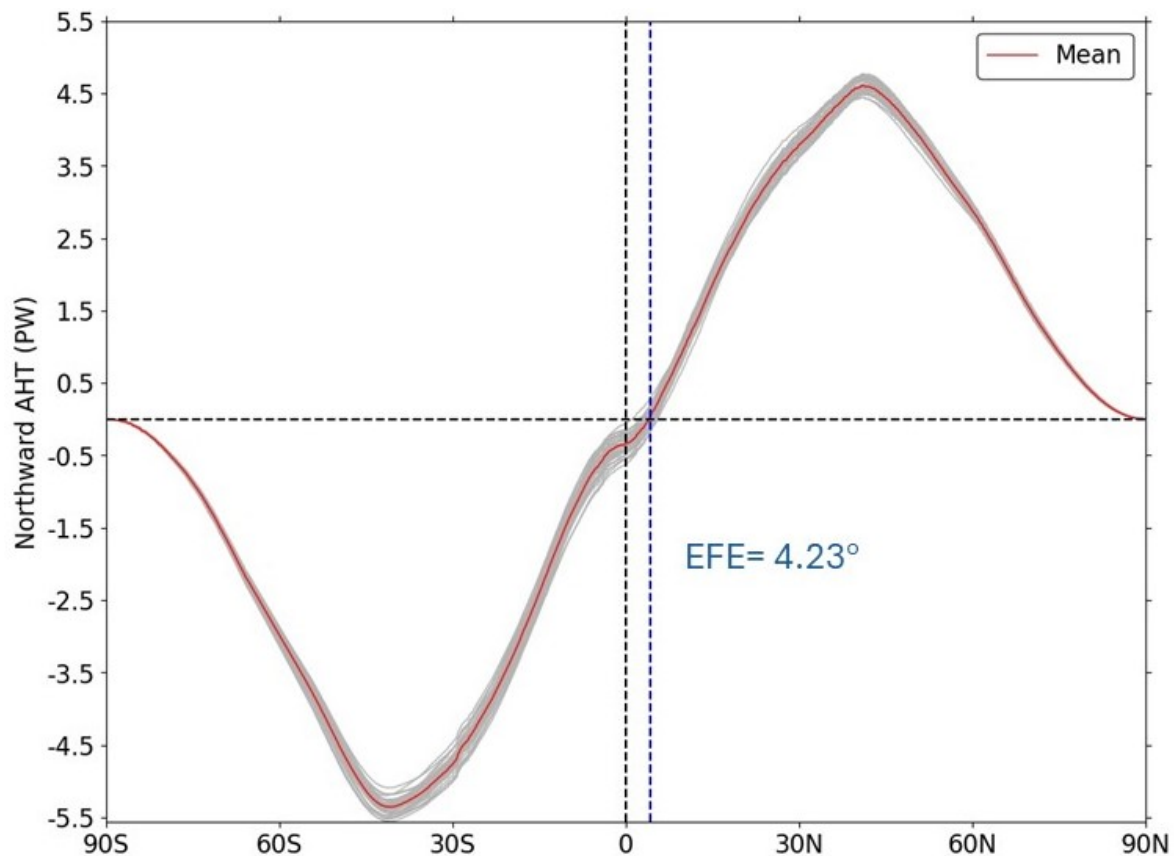


Figure 3.5: The annual mean zonally integrated AHTs (PW) are shown in grey curves using ERA-5 reanalysis data for the period 1979–2020. The time-averaged AHT is represented by the red curve. The blue dashed line denotes the position of the energy flux equator (EFE).

acitcz or HC rising branch. Moist air converges, rises, and diverges as cooler and drier air masses aloft from the ITCZ regions towards the poles. So, the direction of LE in moist air mass and the dry static energy in dry air mass are opposite to one another (Magnusdottir and Saravanan, 1999). As a result, the latent heat energy and dry static energy cancel each other out, leading to a moderate AHT in the tropics (Trenberth and Stepaniak, 2003a). Therefore, the annual mean CE-AHT is southward, approximately -0.3 PW (Donohoe et al., 2013; Marshall et al., 2014; Loeb et al., 2016; Stephens et al., 2016; Liu et al., 2017a; Mayer et al., 2017; Liu et al., 2020a; Trenberth et al., 2019). This cross-equatorial heat transport may result from excess solar insolation heating the northern hemisphere relative to the annual mean. Since the HC plays a major role in heat distribution over the tropics and subtropics (Trenberth and Stepaniak, 2003b,a, 2004; He et al., 2019), inter-hemispheric energy transport is connected to the HC.

The maximum southward AHT and northward AHT are at 40.75°S and 41°N (Trenberth

and Caron, 2001; Masuda, 1988; Mayer and Haimberger, 2012; Marshall et al., 2014; Mayer et al., 2021), respectively, and are associated with a large evaporation from those regions due to the relatively clear sky, resulting in ample absorption of solar energy. Apart from this, both the latent and dry static energies are poleward over the subtropics (Trenberth and Stepaniak, 2003a; Yang et al., 2015). Also, the eddy energy flux asymmetries at the edges of the HC cause the large AHT. The maximum southward and northward AHT is estimated at 5.4 PW and 4.6 PW, respectively (Masuda, 1988; Fasullo and Trenberth, 2008b; Trenberth and Caron, 2001).

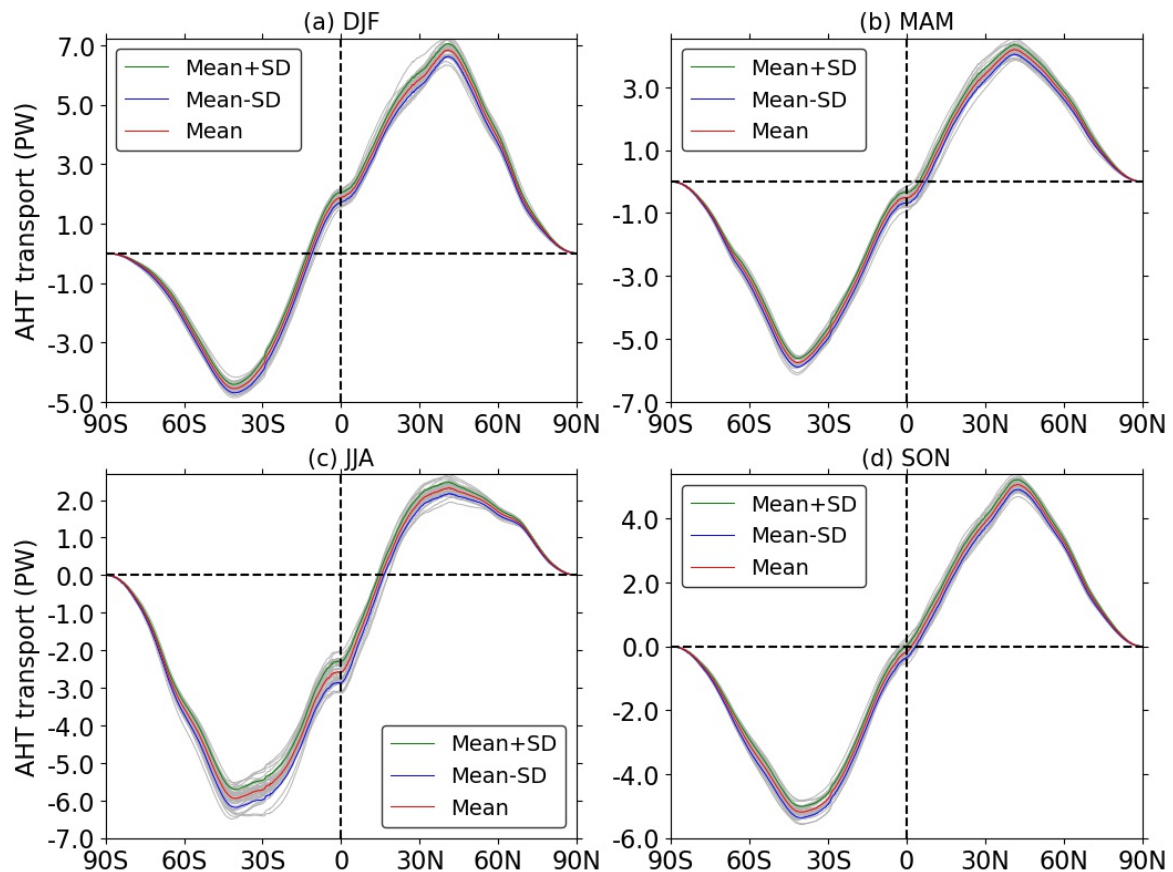


Figure 3.6: The inter-annual AHTs (PW) for (a) DJF, (b) MAM, (c) JJA, and (d) SON are shown in grey lines using ERA-5 reanalysis data for the period 1979–2020. The mean, mean+sd (sd: standard deviation), and mean–sd values are displayed by the red, green, and blue lines, respectively.

On an inter-annual time scale, the AHTs are shown in Figure 3.6 for the JJA, DJF, MAM, and SON seasons. The EFE clearly shows a cycle, and it reaches its southern and northern meridional limits during the DJF (Figure 3.6a) and JJA (Figure 3.6c) seasons, respectively.

During the solstice seasons, the AHT is larger and transports more heat from the winter hemisphere (DJF: Figure 3.6a & JJA: Figure 3.6c) than the summer hemisphere does (Fasullo and Trenberth, 2008b). The reason is that the rising branch of the HC cell reaches the extrema in a meridional direction, and the meridional temperature gradient peaks in the winter hemisphere, which causes stronger energy transport by stronger meridional HC, baroclinic eddies, and stationary waves (Fasullo and Trenberth, 2008b). As a result, the absolute maximum of northward and southward transports also occurs during the DJF (Figure 3.6a) and JJA (Figure 3.6c) seasons, respectively. The cooling in the subtropics is greatly dominated by transient eddies associated with energy transport, with a small contribution from the HC subsidence (Trenberth and Stepaniak, 2003b). During the equinoctial season, the inter-hemispheric energy asymmetry almost vanishes (MAM: Figure 3.6b & SON: Figure 3.6d), and an individual HC cell exists in each hemisphere.

To identify how AHT is changing with time, it is worthwhile to know the standard deviation over time. Figure 3.7 describes inter-annual AHT variations for DJF, MAM, JJA, and SON seasons. The inter-annual AHT variations are comparatively larger during solstice seasons. The AHT variation peaks during JJA in the southern vicinity of the equator and has relatively higher values over the subtropics and mid-latitudes, especially in the southern hemisphere. In DJF, the AHT variation is maximum in the northern hemisphere subtropics. Subsidence from monsoonal circulations contributes to the inter-annual variation of AHT over the subtropics and mid-latitudes in the northern and southern hemispheres during DJF and JJA, respectively. The peak of the variation during solstitial seasons (DJF & JJA) lies in the winter hemisphere (Figure 3.7), where maximum AHT also occurs (Figure 3.6 a & c) (Fasullo and Trenberth, 2008b). During the equinoctial season, the variation in AHT is almost symmetric about the equator because of the symmetric global energy transport by the symmetric HC about the equator. It is a bit strange, as the Asian monsoon is in the NH, that much of the variation is happening in the SH, perhaps due to the subsiding region of the Asian monsoon HC. This is a good motivation, as the variation is dominant during the solstice seasons, for studying the JJA and DJF seasons in particular.

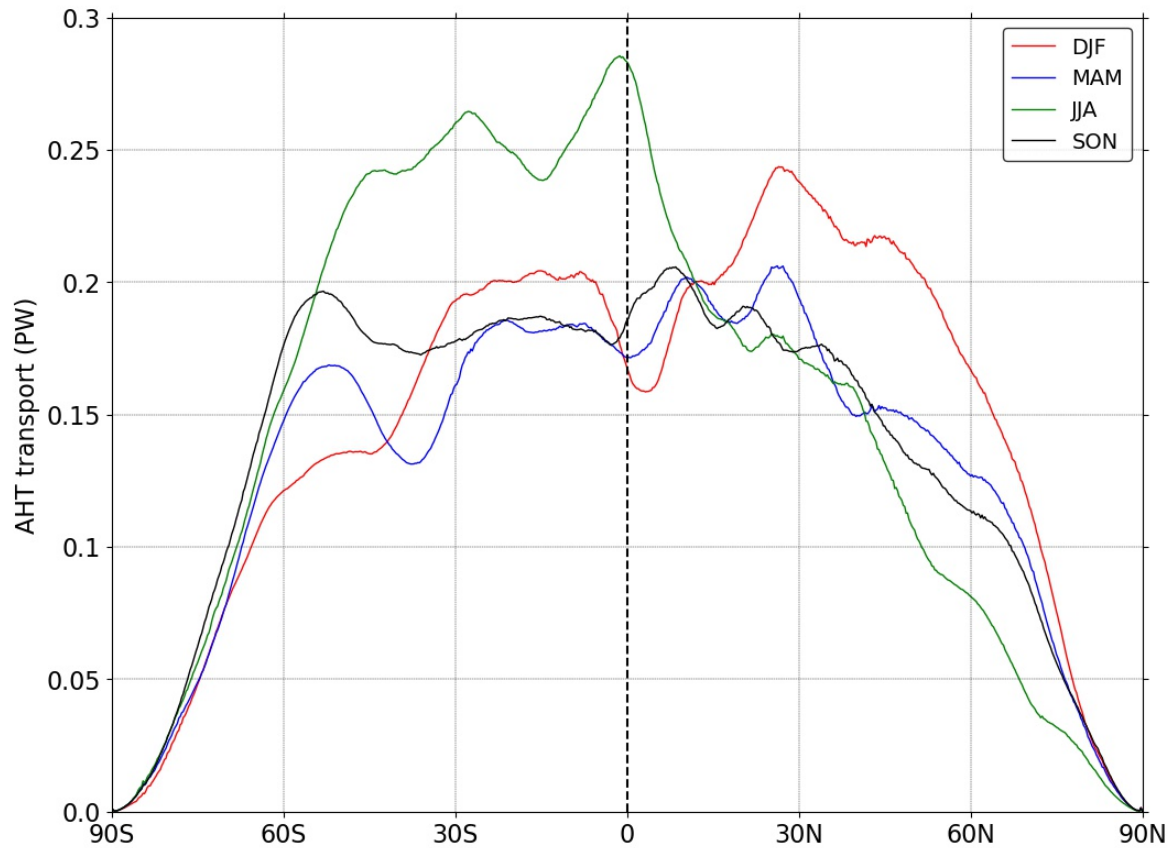


Figure 3.7: The standard deviation of AHT (PW) for DJF, MAM, JJA, and SON using ERA5 reanalysis data for the period 1979–2020 is shown on an inter-annual time scale. The standard deviation of AHT for DJF, MAM, JJA, and SON is represented by the red, blue, green, and black lines, respectively.

From standard deviation, it is found that the JJA and DJF seasons have significant inter-annual variation. The AHT crossing the equator will give an insight into how CE-AHT varies seasonally. The seasonal cycle of the CE-AHT analysis clearly shows how the CE-AHT changes its sign when the equinoctial to solstitial transition occurs in Figure 3.8. The northward CE-AHT (2.2 PW) peaks in January, whereas the southward CE-AHT (−2.7 PW) peaks in July. The winter-Hadley cell in boreal summer with a rising branch in the northern hemisphere is stronger than the Austral summer winter-Hadley cell (Oort and Yienger, 1996), which is consistent with the maximum CE-AHT in July relative to the CE-AHT in January. The time-averaged CE-AHT is -2.59 ± 0.04 PW and 1.86 ± 0.03 PW for the JJA and DJF seasons, respectively (Heaviside and Czaja, 2013). **However, the amount of heat stored in the atmosphere is relatively small compared to other components of the Earth system. Approximately 1% of the excess heat from the Earth’s energy imbalance is stored in**

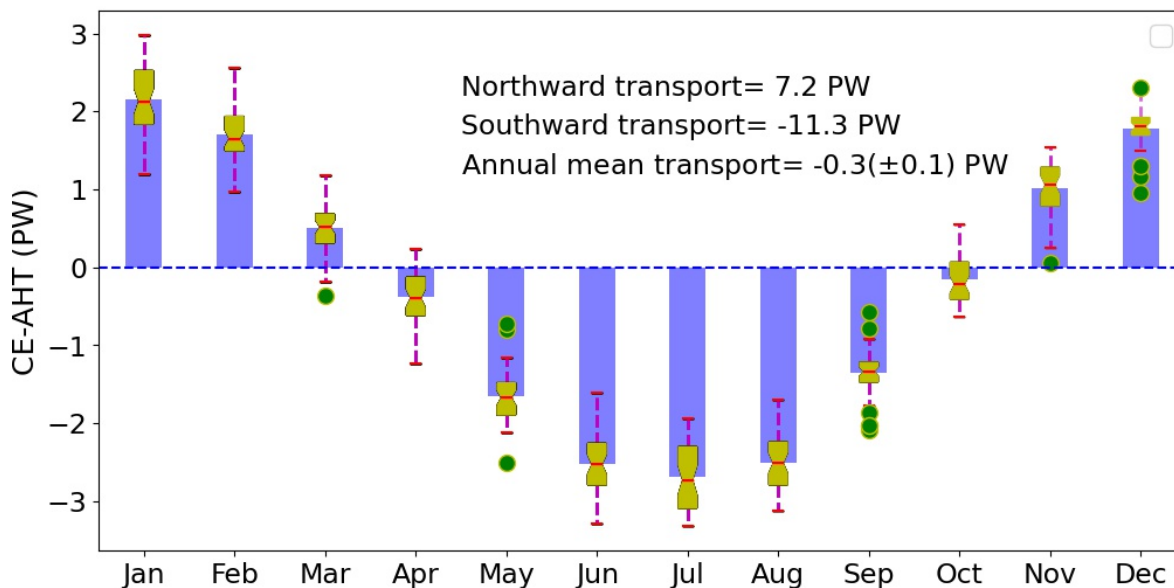


Figure 3.8: The seasonal cycle of CE-AHT (PW) is displayed using ERA-5 reanalysis data spanning the period 1979–2020. The mean CE-AHT values are marked by blue bars, whereas box-and-whisker plots represent the data distribution and dispersion, indicating the minimum value, 1st quartile, median, 3rd quartile, and maximum value. The outliers, which lie outside of 1.5 times the interquartile range above the upper (3rd) quartile and below the lower (1st) quartile, are denoted as green points.

the atmosphere (Von Schuckmann et al., 2023).

3.3.2 Atmospheric Heat Transport and Monsoon Dynamics

Figure 3.9 illustrates the impact of CE-AHT on upper-tropospheric (200 hPa) winds during solstice seasons on an inter-annual time scale spanning the period 1979–2020.

During JJA, the STJ usually sits at $\approx 32^\circ\text{S}$ (Zolotov et al., 2018; Maher et al., 2020) in the northern hemisphere and $\approx 40^\circ\text{N}$ (Du et al., 2016; Maher et al., 2020) in the southern hemisphere in the climatological mean. The right panel of Figure 3.9a shows that increased CE-AHT strengthens anomalous westerly winds over the subtropics in both hemispheres, an equatorward shift of the STJs. In the left panel of Figure 3.9a, the increase of CE-AHT strengthens and moves the anomalous STJs towards the equator, consistent with the right panel. The equatorward movement of the STJs indicates a contraction of the HC, as the upper tropospheric branch of the HC is the main driver of the STJs (Held and Hou, 1980; Schneider, 1977). The contraction of the HC results in an equatorward displacement of the

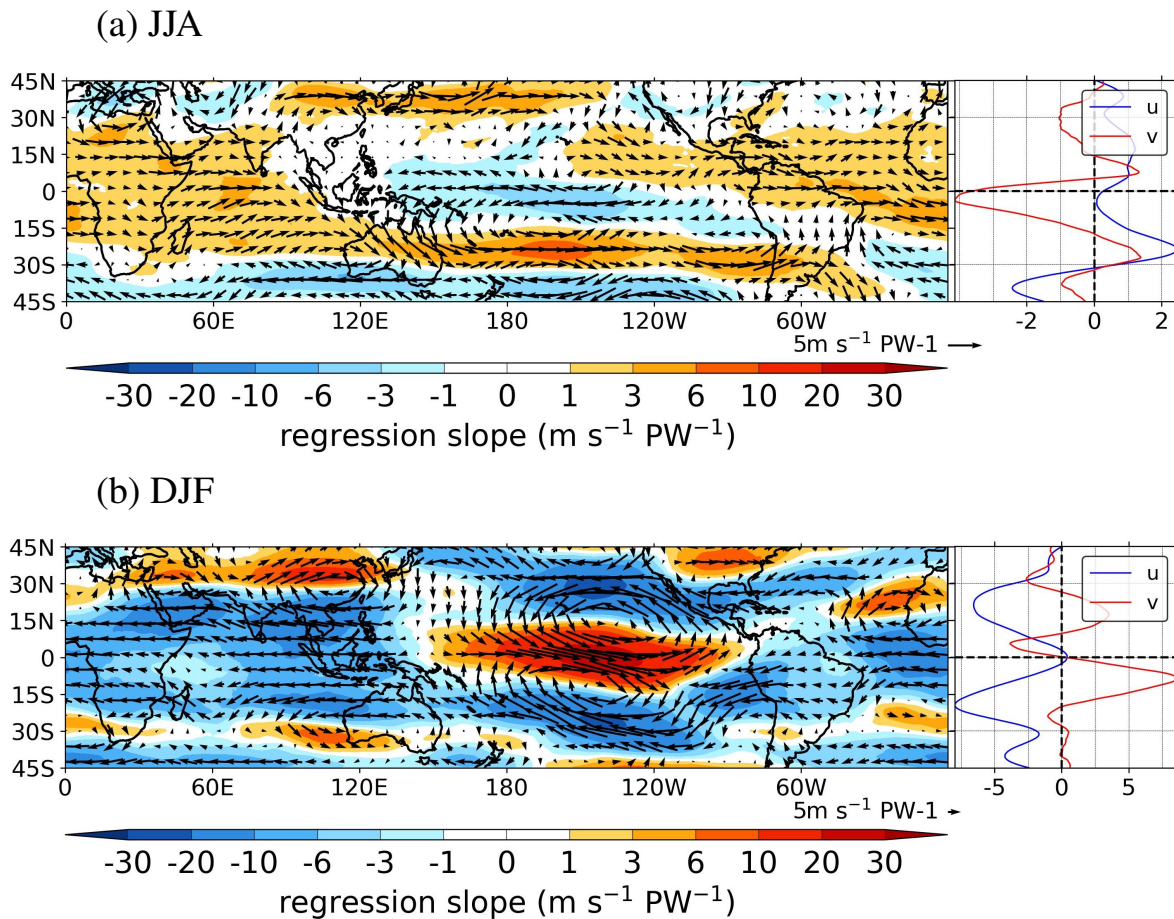


Figure 3.9: (a) The left panel is the regression slope of upper-tropospheric (200 hPa) winds onto CE-AHT (black vectors; $\text{m s}^{-1} \text{PW}^{-1}$) during JJA using ERA-5 reanalysis data on an inter-annual time scale for the period 1979–2020. The colour shading shows the inter-annual regression slope of 200-hPa zonal winds onto CE-AHT for the same period. The right panel exhibits the regression slope of zonal-mean upper-tropospheric zonal winds (blue) and meridional winds (red) onto CE-AHT for the JJA season. (b) Same as panel ‘a’ except for the DJF season.

ITCZ. Moreover, the increased CE-AHT induces anomalous upper-level convergence over the Indian monsoon domain and weakens the TEJ. The upper-level convergence and weakening of the TEJ imply a decrease in the Indian monsoon (Madhu et al., 2014), as found for anomalously warm surface water over the eastern and central equatorial Pacific (Chen and van Loon, 1987; Pattanaik and Satyan, 2000). Additionally, anomalous upper-level convergence over the Maritime Continent and divergence over the Eastern Pacific Ocean evidence a weaker Walker-like circulation linked to El Niño-like conditions, consequently a weaker monsoon (Wang et al., 2017).

On the other hand, during the DJF climatological mean, the southern hemisphere’s STJ is

typically located around $\approx 44^\circ\text{S}$ (Yang and Webster, 1990; Zolotov et al., 2018; Maher et al., 2020), while in the northern hemisphere, it is positioned around $\approx 30^\circ\text{N}$ (Yang and Webster, 1990; Luna-Niño et al., 2021; Maher et al., 2020). In DJF, anomalous easterly winds strengthen over the subtropics in both hemispheres with the increase of CE-AHT, implying a poleward shift of the STJs (right panel of Figure 3.9b). The left panel of Figure 3.9b also exhibits the poleward shift of the STJs, which leads to an expansion of the HC and consequently an equatorward shift of the ITCZ. In the upper-level, strong easterly wind anomalies over the equatorial Indian Ocean and strong westerly wind anomalies over the equatorial Pacific Ocean form a divergence over the Maritime Continent. This upper-level divergence symbolises a strong Walker-like circulation or La Niña-like conditions, typically connected to strong monsoonal precipitation (Wang et al., 2017).

In short, in JJA, increased CE-AHT shifts the STJs towards the equator, contracts the HC, displaces the ITCZ equatorward, weakens the TEJ and Walker-like circulation, and leads to decreased monsoon circulation. Conversely, in DJF, the responses are opposite for increased CE-AHT, such as pushing the STJs poleward, expanding the HC, shifting the ITCZ away from the equator, strengthening the TEJ and Walker-like circulation, and resulting in strong monsoon circulation.

However, it is necessary to examine the association between CE-AHT and the HC during the solstice seasons to determine whether the results obtained from upper-level winds are consistent. To achieve this, the regression slope of the stream function onto CE-AHT has been subtracted from and added to the time-averaged JJA stream function.

In Figure 3.10(a), the time-averaged JJA HC (black lines) exports moisture and latent energy crossing the equator to the northern hemisphere by the lower branch of the HC, while the opposite occurs by the upper branch. The rising branch (red shadings) and the subsiding branch (blue shadings) lie in the northern and southern hemispheres, respectively (Seo et al., 2023; Quan et al., 2004; Hoskins et al., 2020; Feng et al., 2018). The winter-Hadley cell is broader and more intensified than the summer-Hadley cell during the JJA season (Figure 3.10a) (Oort and Yienger, 1996).

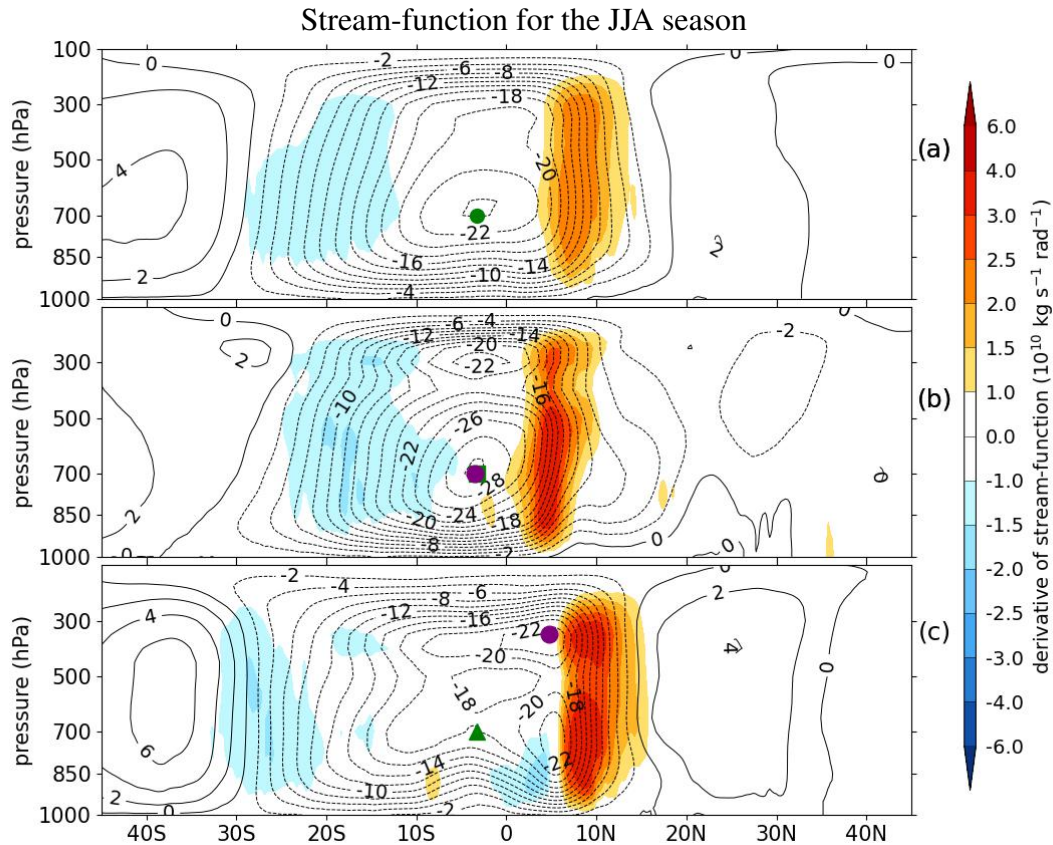


Figure 3.10: (a) The time-averaged stream function for the JJA season is displayed by the black curves, using ERA-5 reanalysis data spanning 1979 to 2020. Panels (b) and (c) show the stream function for positive CE-AHT anomalies (the mean JJA stream function plus five times the regression slope of the stream function onto CE-AHT on an inter-annual time scale) and negative CE-AHT anomalies (the mean JJA stream function minus five times the regression slope of the stream function onto CE-AHT on an inter-annual time scale), respectively, indicated by black curves. In (a), (b), and (c), the black dashed and solid curves represent anti-clockwise and clockwise rotation (from east), respectively. The colour shading in (a), (b), and (c) illustrates the meridional derivative (positive: ascent; negative: subsidence) of the stream function, indicating the vertical mass flux. The core position, where the absolute value of mass flux peaks, is shown by the green marker for the climatological HC and the purple marker for the regressed HC. The units of the stream function and its meridional derivative are $10^{10} \text{ kg s}^{-1}$ and $10^{10} \text{ kg s}^{-1} \text{ rad}^{-1}$, respectively.

Figures 3.10(b) and 3.10(c) illustrate the stream function for northward and southward CE-AHT anomalies, respectively, during the JJA season.

In Figure 3.10(b), for anomalous northward CE-AHT, the HC contracts relative to the climatological HC, particularly at the upper-level, due to the equatorward movement of the STJs as observed in upper-level wind analysis. However, the contraction of the HC aligns with El Niño-like conditions (Hu et al., 2018; Nguyen et al., 2013; Lau et al., 2006; Stachnik and Schumacher, 2011). The anomalous northward CE-AHT strengthens the inter-

hemispheric energy imbalance; in compensation, the summer-Hadley cell weakens, the core of the winter-Hadley cell shifts towards the southern hemisphere, and the rising and subsiding branches of the HC shift towards the equator. The core of the circulation is the location where the absolute maximum mass flux occurs. On the other hand, for southward CE-AHT anomalies, the expansion of the HC results from the poleward movement of the STJs (Figure 3.10b). The rising and subsiding branches of the HC shift away from the equator. As a result, the ITCZ moves away from the equator.

Therefore, in JJA, the width of the HC, especially the winter-Hadley cell, decreases with the anomalous northward CE-AHT, whereas the southward CE-AHT anomaly increases the width. As a result, the ITCZ appears towards the equator for positive CE-AHT anomalies, and the opposite movement of the ITCZ occurs for negative anomalies.

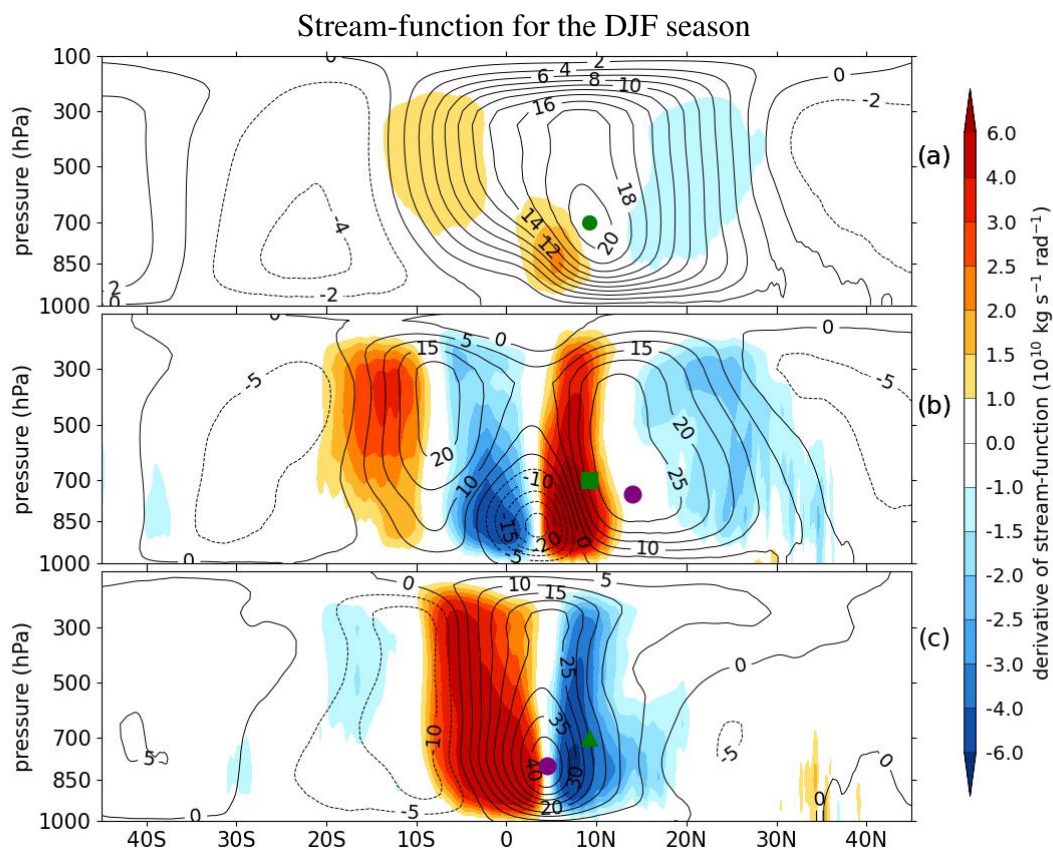


Figure 3.11: Same as Figure 3.10 except for the DJF season.

Figure 3.11(a) displays the climatological mean DJF HC by the black curves, whereas the red and blue shadings indicate the rising and subsiding branches of the HC. The winter-Hadley cell is broader and more intensified than the summer-Hadley cell during the DJF

season as well (Figure 3.11a) (Oort and Yienger, 1996).

In Figure 3.11(b), increased CE-AHT bifurcates the winter-Hadley cell and widens the HC. The bifurcation of the winter-Hadley cell comes from an anomalous anti-clockwise circulation in the deep tropics that moves the ascending and descending branches of the winter-Hadley cell in a poleward direction. The expansion of the HC is consistent with the poleward movement of the STJs and agrees with the La Niña-like conditions during the DJF season (Hu et al., 2018). The anomalous anti-clockwise circulation promotes a salient second rising branch to the north of the equator. The double-rising branch in the HC might be associated with the double ITCZ-like pattern. In contrast, Figure 3.11(c) shows that southward CE-AHT anomalies shrink the HC as the STJs moves towards the equator. Therefore, the rising and subsiding branches of the HC are displaced towards the equator. The width of the winter-Hadley cell decreases with the anomalous northward CE-AHT.

Hence, in DJF, the width of the HC, particularly the winter Hadley cell, increases with northward CE-AHT anomalies, while the opposite is true for southward CE-AHT anomalies. Consequently, the ITCZ shifts away from the equator for northward CE-AHT anomalies and moves in the opposite direction for southward anomalies.

Figure 3.12 shows the derivative of MTSF and the ITCZ location for climatological mean, positive, and negative CE-AHT anomalies. The ITCZ is determined using the I_{dmsf} metric. In JJA, northward CE-AHT anomalies move the ITCZ towards the equator, while southward CE-AHT anomalies shift it away from the equator. Conversely, during DJF, the movement of the ITCZ is opposite, such as poleward and equatorward shifts for northward and southward anomalies, respectively. The direction of the ITCZ fluctuation identified by the I_{dmsf} metric is consistent with the results of the stream function.

The relationship between CE-AHT and precipitation is investigated to understand changes in monsoonal precipitation. It will also help to link the changes in precipitation with the ITCZ movement.

Figure 3.13(a) highlights the relationship between CE-AHT and precipitation for the JJA season. On an inter-annual time scale, a regression analysis confirms that the global

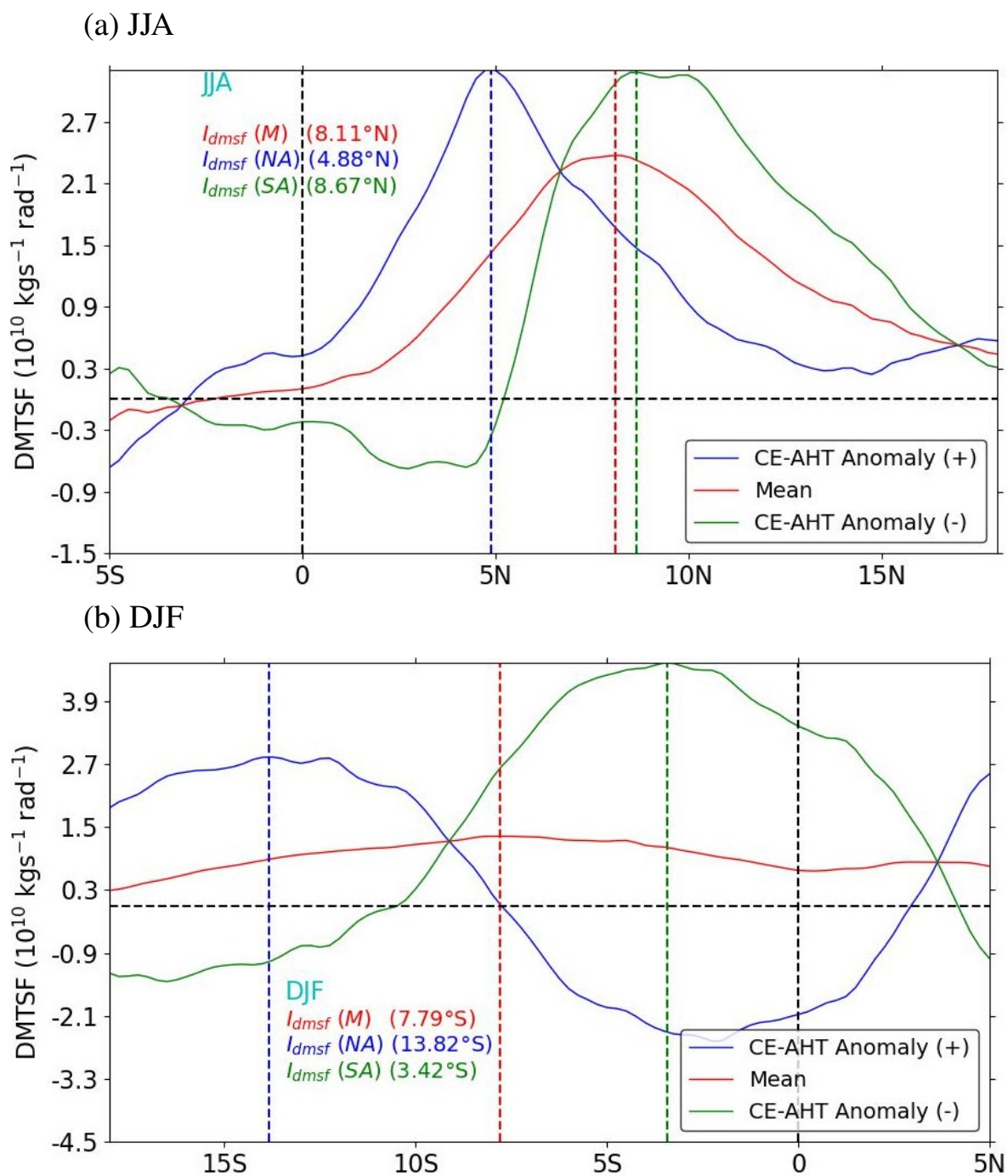


Figure 3.12: (a) The derivative of time-averaged MTSF (stream function averaged over 700–300 hPa; red) is displayed using ERA-5 reanalysis data for JJA spanning 1979–2020. The derivatives of MTSF for positive CE-AHT anomalies (the mean JJA MTSF plus five times the regression slope of the MTSF onto CE-AHT on an inter-annual time scale) and negative CE-AHT anomalies (the mean JJA MTSF minus five times the regression slope of the MTSF onto CE-AHT on an inter-annual time scale) are shown by blue and green curves, respectively. The positions ($^{\circ}$) of the ITCZ identified by the I_{dmsf} metric for mean MTSF (red), positive CE-AHT anomalies (blue), and negative CE-AHT anomalies (green) are represented by the vertical lines for the JJA season. (b) Same as panel ‘a’ but for the DJF season.

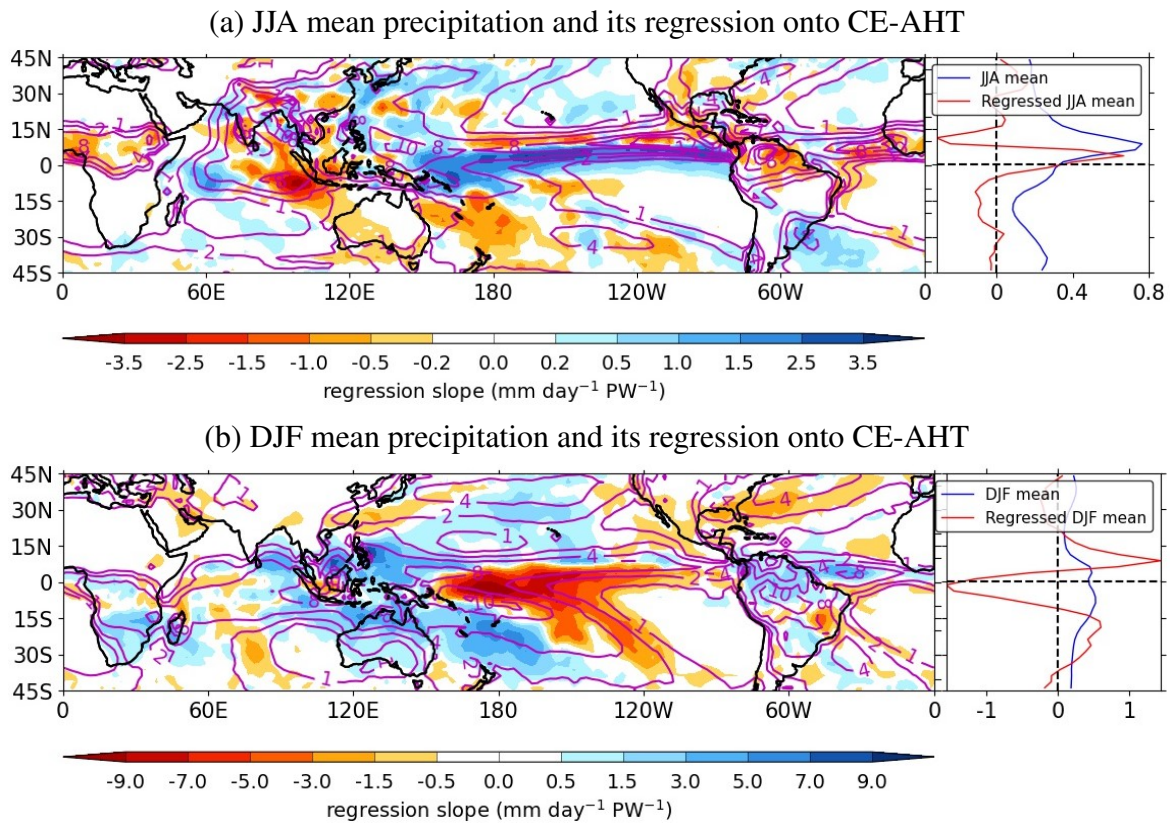


Figure 3.13: (a) The left panel shows the regression slope of precipitation onto CE-AHT (colour shading in $\text{mm day}^{-1} \text{PW}^{-1}$) using ERA-5 reanalysis on an inter-annual time scale for the JJA season spanning 1979–2020. The solid magenta curves depict mean precipitation (mm day^{-1}). The right panel displays the zonal mean of climatological precipitation (red; $1 \times 10 \text{ mm day}^{-1}$) and its regressed slope onto CE-AHT (blue; $\text{mm day}^{-1} \text{PW}^{-1}$) for the JJA season. (b) Same as panel ‘a’ but for the DJF season.

ITCZ shifts southward when the cross-equatorial AHT is anomalously large, although we demonstrate this mainly happens over the Pacific Ocean. Our findings support the inverse relationship between the ITCZ shift and CE-AHT investigated by (Donohoe et al., 2013) and are also consistent with previous findings (Figure 3.10b). Outside of the Pacific sector, that is, over the Indian and African regions, the relationship between CE-AHT and JJA precipitation is more complex. For the West African monsoon region, greater northward CE-AHT is related to weaker rainfall along the Gulf of Guinea coast, while there is stronger rainfall in the Atlantic Ocean ITCZ. In the Indian sector, anomalous northward CE-AHT is associated with a weak monsoon, marked by strong decreases in precipitation on the western coast of India and the southern flank of the Himalayas. **Strong and weak Indian monsoons are identified by a 10% departure of rainfall from the climatological mean value (Raju et al., 2002). The monsoon signal along the western coast of India and the southern flank of the**

Himalayas shows a decrease in precipitation of more than 10% for each PW of northward CE-AHT (Figure 3.13(a)). The North-American monsoonal precipitation also gets reduced with the large export of CE-AHT, perhaps because of the regional HC and ITCZ patterns. A strong positive CE-AHT is strongly correlated with a pattern consistent with a positive Indian Ocean dipole (IOD). As a result, a strong decrease in precipitation is observed over the Maritime Continent, especially over the Sumatra and Borneo islands.

Figure 3.13(b) is the representation of precipitation regression on the CE-AHT for the DJF season on an inter-annual time scale. A strong, well-established double-ITCZ pattern is evident with each ITCZ lying on either side of the equator, especially over the east Indian and west Pacific Oceans when the CE-AHT is anomalously large, which is consistent with the bifurcation of the HC (Brown et al., 2020). Zhang (2001) reported that the double-ITCZ pattern appears when La Niña conditions prevail over the Pacific Ocean, as indicated by the analysis of upper-level winds. However, the ITCZ, lying in the northern hemisphere, causes a strong rise in precipitation over Sri Lanka, the southern Bay of Bengal, and the Philippines. The whole equatorial and south-eastern Pacific Oceans show a strong decrease in precipitation with the increase of the northward CE-AHT. The greater northward cross-equatorial AHT facilitates stronger rainfall over the South American equatorial regions and the West Atlantic Ocean. Strong monsoons are observed over the North African and Australian monsoon domains because of the anomalous northward CE-AHT.

As highlighted in Figure 3.14, it shows the correlations of global CE-AHT versus precipitation and regional CE-AHT versus monsoonal precipitation for the Indian, West African, and North American monsoons. Over the deep tropics, the correlations of global CE-AHT versus precipitation and global CE-AHT versus AHT are positive. So, precipitation is proportional to global CE-AHT in the deep tropics. In the subtropics, the relationship between precipitation and global CE-AHT is inversely proportional. The correlation coefficients of Indian monsoon precipitation versus CE-AHT over the Indian Ocean, North-American monsoon precipitation versus CE-AHT over the Atlantic Ocean, and West-African monsoon precipitation versus CE-AHT over the Pacific Ocean are -0.72 , -0.66 , and -0.51 , respectively.

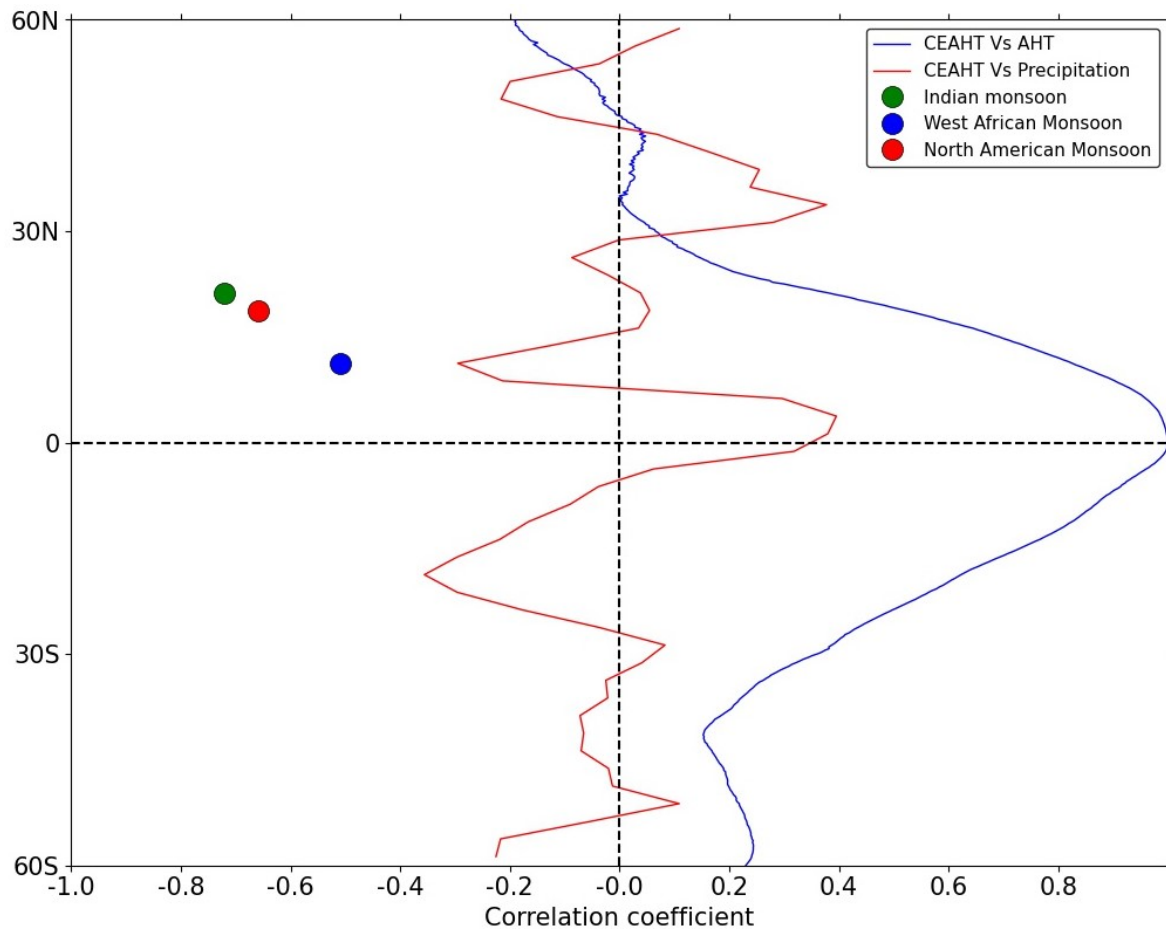


Figure 3.14: The correlation coefficient between CE-AHT and precipitation is displayed for JJA using ERA-5 reanalysis data on an inter-annual time scale for the period 1979–2020. The red and blue lines exhibit the correlation of global CE-AHT versus precipitation and CE-AHT versus AHT, respectively. The green, blue, and red circles represent the correlation between regional CE-AHT and precipitation over the Indian, West-African, and North-American monsoon domains, respectively. For the Indian, West African, and North American monsoons, CE-AHTs are computed over the domains 45°E – 95°E , 20°W – 25°E , and 60°W – 130°W , respectively.

The more southward CE-AHT occurs, the stronger the Indian, West-African, and North-American monsoons become. It is worthy of mention that the decomposing heat transport into the rotational and divergent components is not performed before conducting the correlation.

The relationship between CE-AHT and lower-tropospheric winds has been analysed to elucidate Figures 3.13a and 3.13b and to understand the dynamical reasons.

As shown in Figure 3.15(a), increased CE-AHT in JJA weakens trade winds over the Pacific Ocean and strengthens the Indian Ocean. Over the Pacific Ocean, anomalous weak trade

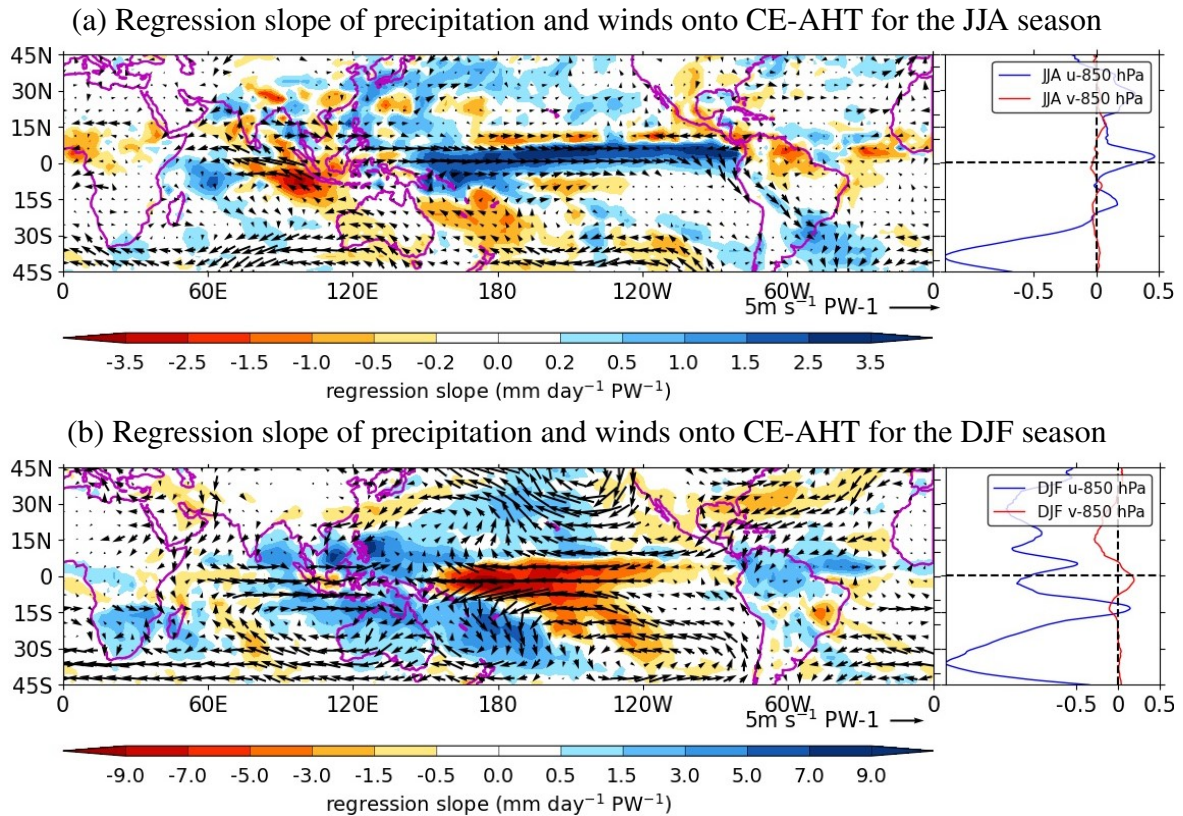


Figure 3.15: (a) The left panel shows the regression slope, on an inter-annual time scale, of lower-tropospheric (850 hPa) winds onto CE-AHT, represented by vectors for the JJA season using ERA-5 reanalysis data for the period 1979–2020. The colour shading is the slope of the regression of precipitation onto CE-AHT for the same time domain. The right panel depicts regression slopes ($\text{m s}^{-1} \text{PW}^{-1}$) of the zonal mean lower-tropospheric zonal wind (blue) and meridional (red) wind for the JJA season. (b) Same as panel ‘a’ but for the DJF season.

winds are converging along the equator, and that converging wind band coincides with the maximum precipitation region. So, the southward shift of that convergent region of lower-tropospheric winds causes the shift of the ITCZ towards the equator during the JJA season with the increase of northward CE-AHT. Moreover, the anti-cyclonic circulation over the north-western Pacific Ocean, which normally facilitates moisture supplies towards the Asian monsoon domain (Yang et al., 2007; Wang et al., 2013b), is diminished and contributes to the decrease in precipitation. Furthermore, south-westerly winds towards the Indian monsoon domain weaken due to prevailing north-easterly wind anomalies over the Arabian Sea and Bay of Bengal, leading to a weaker Somali jet. As a result, moisture supply to the Indian monsoon domain decreases, resulting in a weak monsoon with less southward energy export crossing the equator. An anomalous divergence and convergence of winds over the East Indian and West Indian Oceans are responsible for the positive IOD-like pattern. **During**

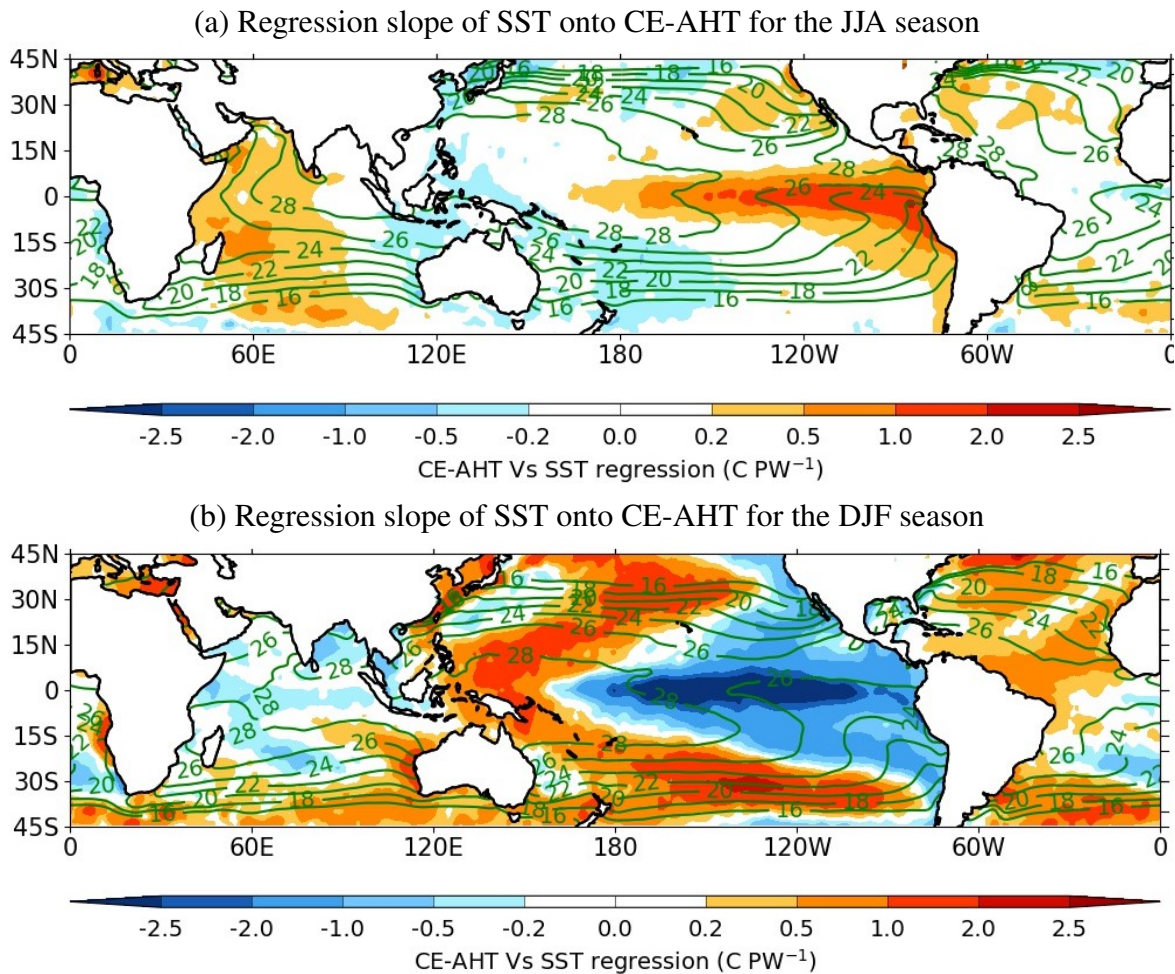


Figure 3.16: (a) On an inter-annual time scale, the regression slope of SST onto CE-AHT ($^{\circ}\text{C PW}^{-1}$) is represented by colour shading for the JJA season using HadISST1 reanalysis data spanning 1979–2020. The green curves depict the mean SST during the JJA season for the same time domain. (b) Same as panel ‘a’ but for the DJF season.

a positive IOD phase, warmer sea surface temperatures are observed in the western Indian Ocean, while the eastern Indian Ocean experiences cooler temperatures (Saji et al., 1999). Moreover, an anomalous divergence over the Maritime Continent implying weaker Walker-like circulation aligns with the results obtained from upper-level winds. Similar suppression patterns in precipitation over the Indian monsoon domain are mainly associated with El Niño-like conditions (Sandeep and Ajayamohan, 2015; Wang et al., 2013b; Pattanaik and Satyan, 2000).

In contrast to JJA, Figure 3.15(b) shows that trade winds are easterly over the Pacific Ocean and westerly over the Indian Ocean, with an increase in northward CE-AHT for the DJF season. However, anomalous westerly trade winds blowing from the Indian Ocean are

stronger than the easterly trade winds of the Pacific Ocean to the north of the equator. As a consequence, an anomalous anti-clockwise rotation of winds causes a low pressure system and precipitates over the north-western Pacific Ocean and adjacent land masses, such as the Philippines. Additionally, an anomalous convergence is induced over the Maritime Continent, denoting a strong Walker-like circulation, similar to the analysis of upper-level winds, resulting in strong precipitation over the Maritime Continent (Wang et al., 2017). But the strong Walker-like circulation suppresses precipitation over the central and eastern Pacific Oceans. The opposite happens to the south of the equator, where easterly trade winds from the Pacific Ocean are stronger and form a low pressure system over the south-western Pacific Ocean and Australian land mass. The strengthening of easterly winds over the equatorial Pacific Ocean suggests the appearance of a double-ITCZ pattern (Zhang, 2001). Moreover, an anomalous anti-cyclone over the south-western Pacific Ocean supplies moisture towards the South Pacific convergence zone (SPCZ) and Australian monsoon areas, leading to a positive precipitation signal over there. Therefore, two anomalous zonal bands of precipitation form the double-ITCZ, straddling the equator. Moist air also converges over the equatorial American land mass and the South African land mass and causes rainfall over those regions.

Winds are caused by pressure differences, which result from surface temperature gradients except for the Earth's own rotation. In an inverted manner, winds can cause surface temperature gradients through the advection and convection of heat by controlling upwelling. The functioning of the SST with the CE-AHT is investigated with the help of regression analysis for both the JJA and DJF seasons, as shown in Figures 3.16a and 3.16b, respectively.

In Figure 3.16(a), the increased northward CE-AHT causes a westerly wind anomaly along the equator, and that westerly wind reduces the equatorial and coastal upwelling of cold water in the Eastern Pacific Ocean, resulting in El Niño-like conditions during the JJA season. In response, trade winds become weak and make the equatorial Eastern Pacific Ocean warmer by relaxing the push of water towards the West Pacific. The positive IOD pattern (Saji et al., 1999) is also present in the SST analysis, and this is formed by the convergence and divergence of winds over the West and East Indian Oceans, respectively. As a consequence, a positive IOD-like pattern is observed in precipitation as well.

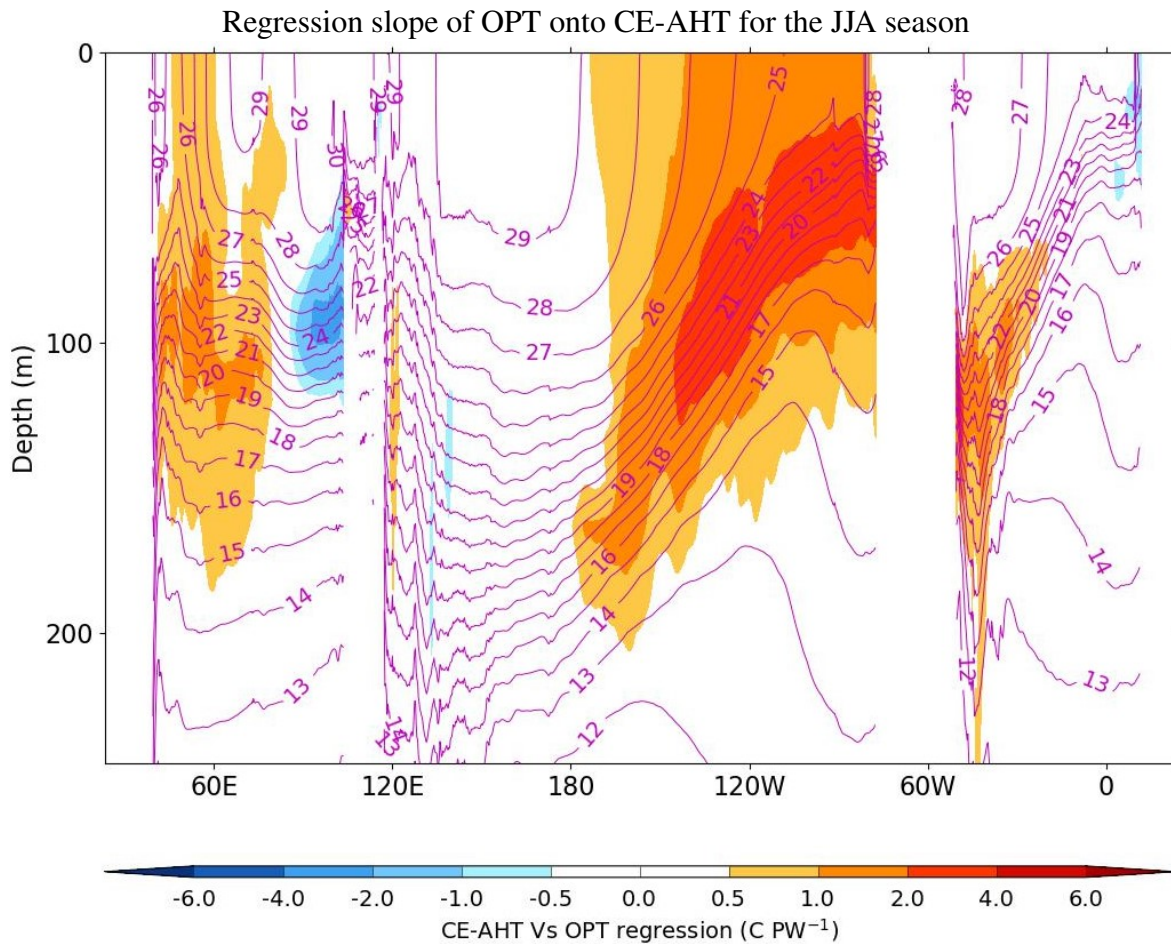


Figure 3.17: The regression slope of OPT (after taking the meridional mean in between 5°N and 5°S) onto CE-AHT ($^{\circ}\text{C PW}^{-1}$) is displayed by colour shading using ERA-5 reanalysis data for the JJA season on an inter-annual time scale for the period 1979–2020.

Conversely, during the DJF season, Figure 3.15(b) illustrates that anomalously positive CE-AHT warms up the Western Pacific Ocean and cools down the Eastern Pacific Ocean, favouring La Niña-like conditions because of stronger easterly wind anomalies over the Pacific Ocean for increased CE-AHT. As a result, in turn, easterly winds strengthen over the equatorial Pacific Ocean, and upwelling increases in the eastern part of the Pacific Ocean. Interestingly, the western Pacific Ocean does not warm up evenly about the equator in the DJF season. The tropical western Pacific region to the north of the equator is comparatively warmer than its southern counterpart, as the anomalous cyclonic system over the northern parts of the western Pacific Ocean is stronger than its counterpart over the south-western Pacific Ocean. Moreover, the double-ITCZ pattern observed in precipitation and stream function coincides with La Niña-like conditions over the Pacific Ocean (Zhang, 2001).

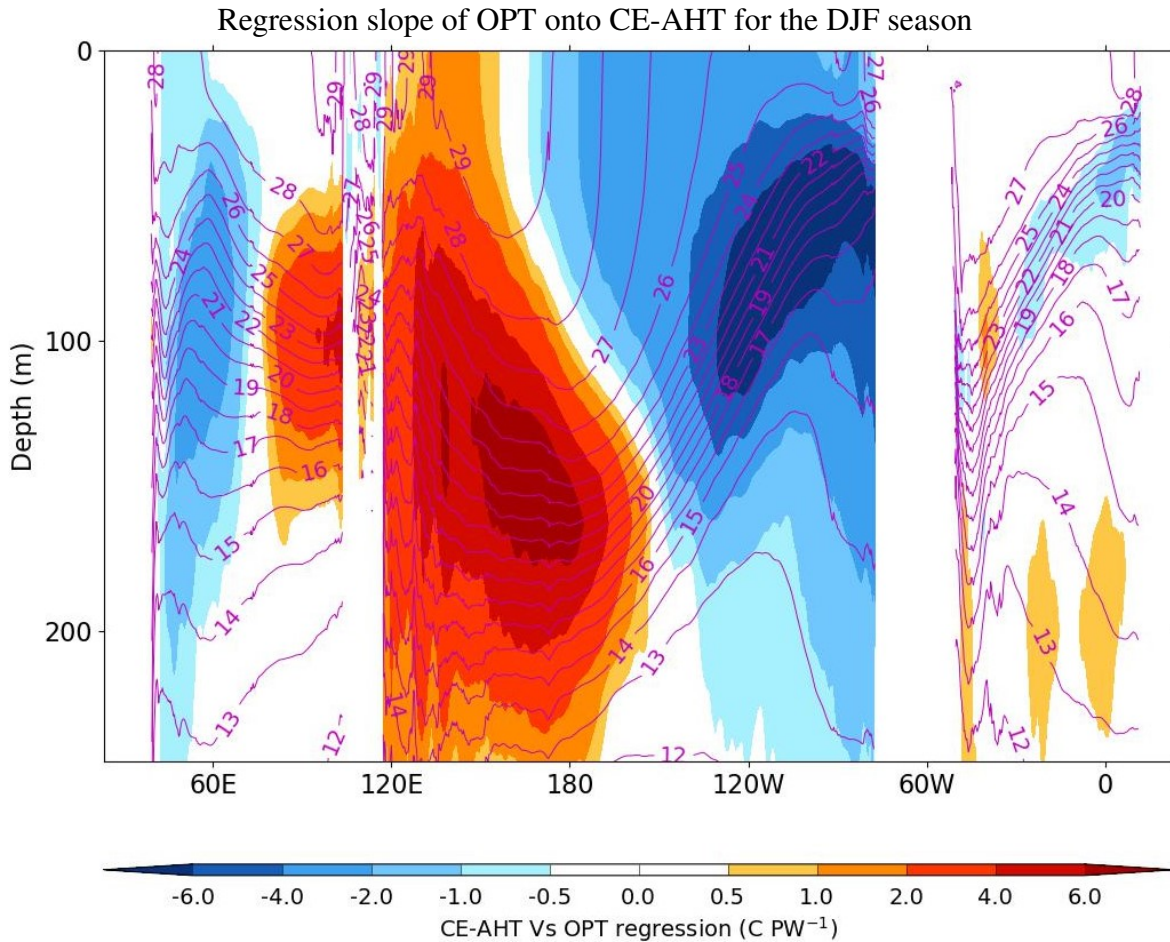


Figure 3.18: Same as Figure 3.17 but for the DJF season.

The skin temperature of the ocean surface water is the SST, and temperature under the surface of the ocean is crucial in displaying the vertical structure temperature. So, the interaction of ocean potential temperature (OPT) in the mixed layer with the CE-AHT is also vital for understanding how the vertical temperature profile changes. As depicted in Figure 3.17, El Niño-like conditions prevail in the mixed layer of the Eastern-Pacific Ocean with the northward export of CE-AHT during the JJA season. At the same time, a positive IOD-like pattern also appears in the mixed layer of the Indian Ocean. These patterns are consistent with the earlier results obtained from upper-level winds, lower-level winds, and SST. In contrast to JJA, during the DJF season, Figure 3.18 shows that an anomalously large northward CE-AHT favours warming and cooling of the western and eastern parts of the Pacific Ocean, respectively. La Niña-like conditions over the Pacific Ocean and negative IOD-like pattern over the Indian Ocean are observed.

The global-scale teleconnections associated with ENSO events are investigated in Figure 3.19 using a permutation test that considers CE-AHT and ONI time series. The null hypothesis assumes no relationship between CE-AHT and ONI, with any observed correlation arising purely by chance. The ONI time series is constructed as a sliding 3-month average and permuted for 1000 times. In Figure 3.19(i), multiple significant correlation coefficients are observed for negative, zero, and positive lags, suggesting a persistent lead-lag relationship and reinforcing the evidence of causality or a strong association between CE-AHT and ONI. Rejecting the null hypothesis at a negative lag implies ONI leads, whereas a positive lag implies CE-AHT leads. A zero lag indicates a contemporaneous or shared relationship between CE-AHT and ONI. The strongest correlation occurs in Figure 3.19(i) at lag=-1, rejecting the null hypothesis and suggesting that ONI leads CE-AHT. This implies that changes in ONI during AMJ (April-May-June) are most strongly associated with changes in CE-AHT during JJA.

Similarly, Figure 3.19(ii) demonstrates a persistent lag-lead relationship rejecting the null hypothesis at multiple lags. However, the maximum correlation at lag=4 for the DJF season indicates changes in CE-AHT lead by 4 months than changes in ONI.

Therefore, the regression analysis patterns are not solely dominated by El Niño or La Niña episodes. In JJA, the ONI appears to dominate inter-annual variability with a month lead, whereas the changes in CE-AHT lead by 4 months in the DJF season. Overall, both CE-AHT and the ONI have shown lag-lead property for the JJA and DJF seasons, indicating a bidirectional influence and a complex interplay between atmospheric heat transport and oceanic variability.

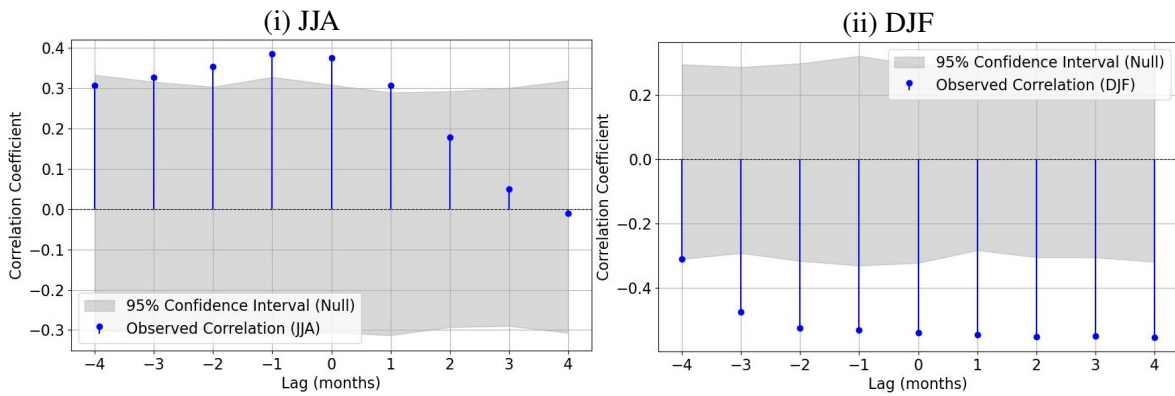


Figure 3.19: A permutation test is conducted between ‘A’ (a 3-month mean non-sliding time series) and ‘B’ (a 3-month mean sliding time series), which extends for four consecutive months forward and backward. (i) The time series ‘A’ and ‘B’ represent CE-AHT and ONI, respectively, for the JJA season during the period 1979–2020. (ii) Same as (i), but for the DJF season.

3.3.3 Observation-based oceanic heat transport

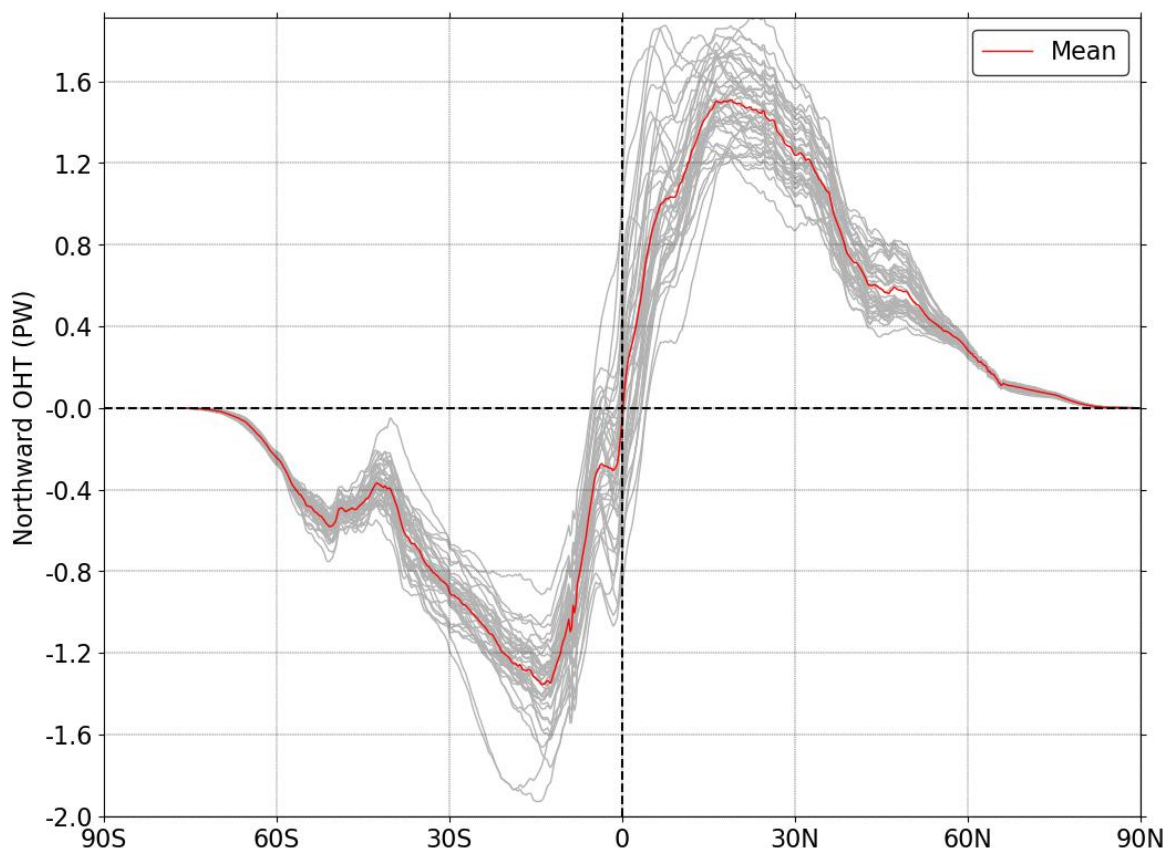


Figure 3.20: The annual mean oceanic heat transport (OHT; grey) (PW) is represented using ORAS-5 reanalysis for the period 1979–2020. The red curve depicts the climatological mean OHT for the same time period.

Monsoons are ocean-atmosphere-coupled phenomena, so oceanic heat transport might be

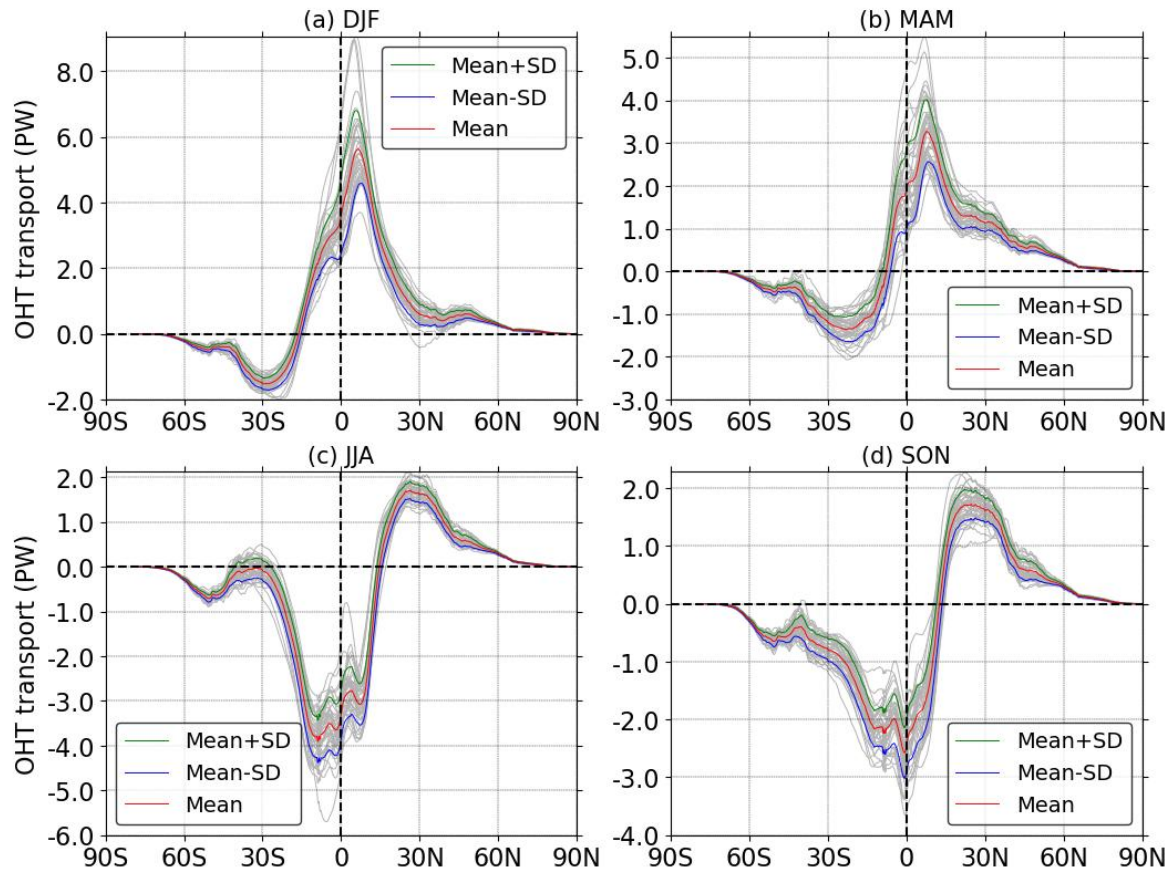


Figure 3.21: The inter-annual OHTs (PW) for the (a) DJF, (b) MAM, (c) JJA, and (d) SON seasons are shown in grey lines using ORAS-5 reanalysis data for the period 1979–2020. The mean, mean+sd (sd: standard deviation), and mean–sd values are displayed by the red, green, and blue lines, respectively.

linked with monsoons. Before investigating the relationship between oceanic heat transport and monsoons, it is essential to understand the properties of oceanic heat transport.

Figure 3.20 outlines the annual mean OHT on an inter-annual time scale and its climatological mean spanning 1979–2020. The northward and southward global OHT peaks at 1.5 PW (18.9°N) and –1.4 PW (13.9°S), respectively (Fasullo and Trenberth, 2008b; Forget and Ferreira, 2019; Trenberth and Caron, 2001). The OHT is dominating over the tropics, and maximum poleward heat transport occurs from the northern hemisphere. The time averaged CE-OHT is northward approximately 0.1 PW with a variability of 0.4 PW.

Figure 3.21 illustrates OHT for the DJF (Figure 3.21a), MAM (Figure 3.21b), JJA (Figure 3.21c), and SON (Figure 3.21d) seasons on an inter-annual time scale.

The southward (negative) OHTs dominate the JJA and SON seasons, contributing –3.9

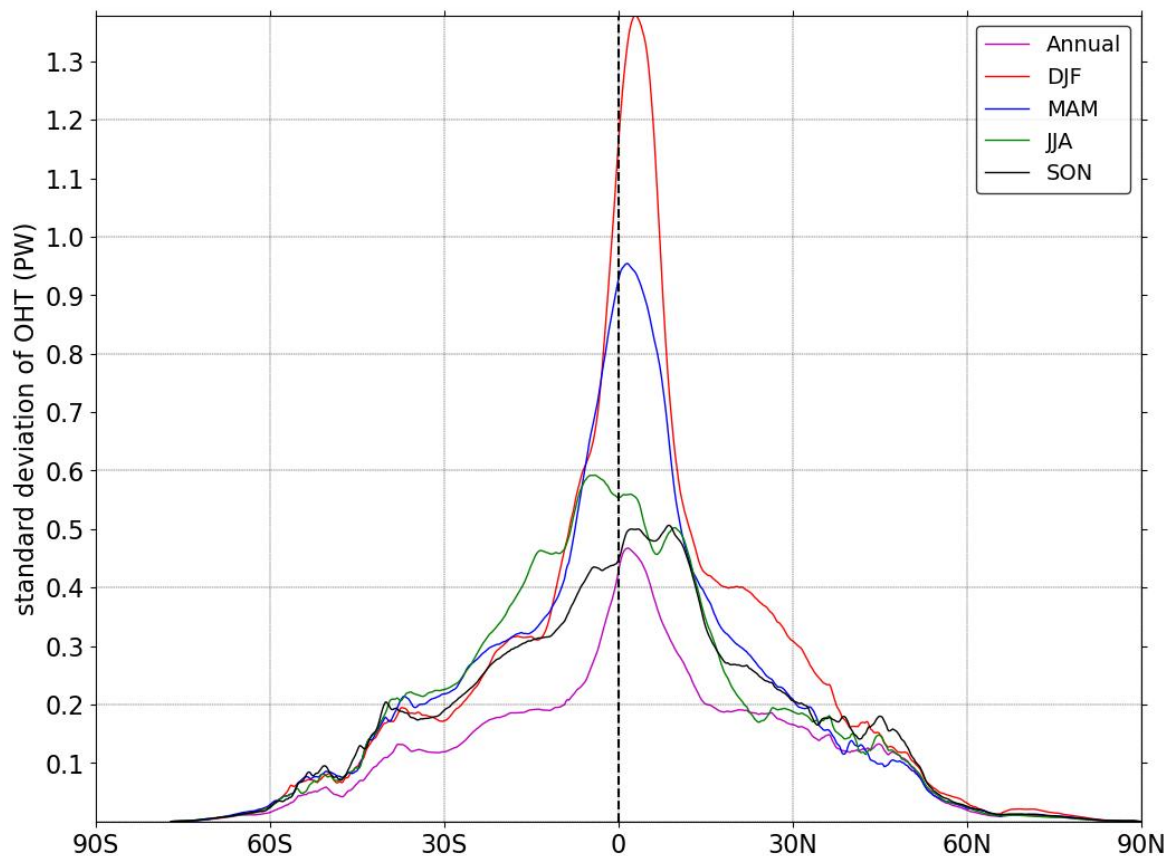


Figure 3.22: The standard deviation of the inter-annual OHT (PW) using ORAS-5 reanalysis data spanning the period 1979–2020 is represented for the DJF (red), MAM (blue), JJA (green), and SON (black) seasons. The standard deviation of annual mean OHT is shown by magenta colour.

PW at 8.7°S and -2.6 PW at 0.7°S , respectively. Conversely, during the DJF and MAM seasons, the northward (positive) OHTs are dominating, with magnitude 5.6 PW at 6.5°N and 3.3 PW at 7.7°N , respectively. Peak northward OHT occurs in DJF from the northern hemisphere, while peak southward OHT is in JJA from the southern hemisphere, near the location of the winter-Hadley cell rising branch (Fasullo and Trenberth, 2008b). The CE-OHTs for the DJF, MAM, JJA, and SON seasons are 3.6 PW (Standard error (SE)= ± 0.2 PW), 1.9 (SE= ± 0.1 PW), -3.3 PW (SE= ± 0.1 PW), and -2.5 PW (SE= ± 0.1 PW), respectively. The maximum southward and northward CE-OHTs occur during the JJA and DJF seasons, respectively. So, CE-OHT occurs in the opposite direction of surface wind stress, which is northward and southward in the vicinity of the equator during JJA and DJF seasons, respectively. The relative higher heat transport in JJA and DJF may be associated with the monsoons.

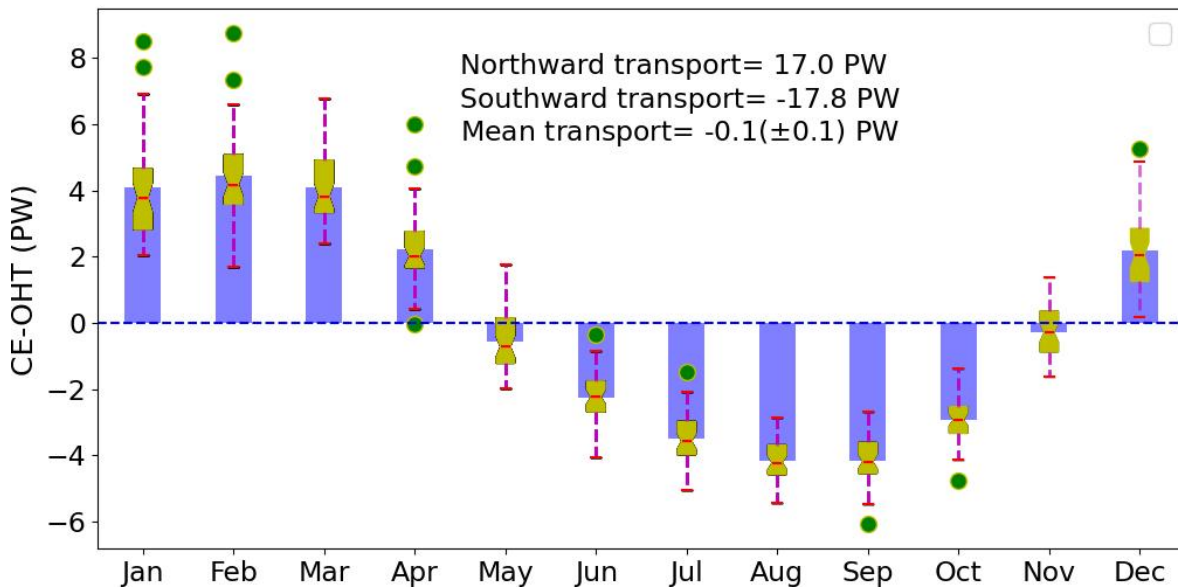


Figure 3.23: The seasonal cycle of CE-OHT (PW) is displayed using ORAS-5 reanalysis data spanning the period 1979–2020. The mean CE-OHT values are marked by blue bars, whereas box-and-whisker plots represent the data distribution and dispersion, indicating the minimum value, 1st quartile, median, 3rd quartile, and maximum value. The outliers, which lie outside of 1.5 times the interquartile range above the upper (3rd) quartile and below the lower (1st) quartile, are denoted as green points.

Figure 3.22 outlines the standard deviation of the OHT along the latitudinal axis for the DJF, MAM, JJA, and SON seasons for the period 1979–2020. The peak standard deviation for each season occurs to the north of the equator. The standard deviation of the OHT is higher for solstice seasons, but the value is highest for the DJF season. During solstice seasons, a similar pattern of standard deviation is also observed for CE-AHT, but comparatively higher for CE-OHT.

Figure 3.23 displays the seasonal cycle of CE-OHT. The CE-OHT cycle changes its sign following the transition from equinoctial to solstitial seasons. The highest northward and southward CE-OHT take place in the months of February (4.25 PW) and September (−3.84 PW), respectively.

A cross-correlation analysis between CE-AHT and CE-OHT reveals an interesting pattern. The CE-OHT exhibits a one-month lag in its seasonal cycle compared to the CE-AHT, explaining the occurrence of southward CE-OHT peaks in September instead of July and

northward CE-OHT peaks in February instead of January. So, the CE-OHT is following the CE-AHT in the seasonal cycle. Please note that the corresponding figure illustrating this analysis is not shown here, as the figure does not reveal any other insights except the lag between CE-AHT and CE-OHT.

3.3.4 Oceanic heat transport relationship with the monsoons

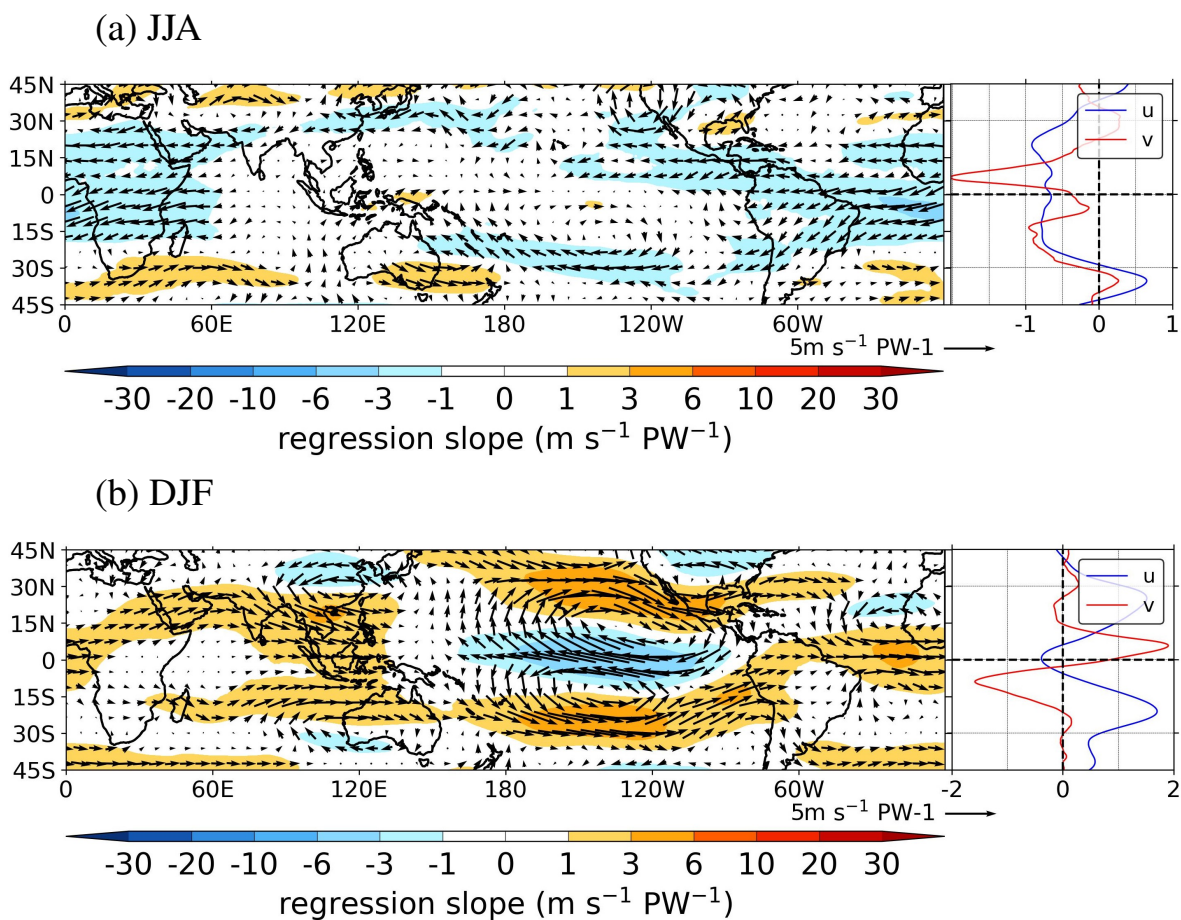


Figure 3.24: (a) The left panel shows the regression slope of upper-tropospheric (200 hPa) u,v-winds onto CE-OHT (black vectors; $\text{m s}^{-1} \text{PW}^{-1}$) during JJA, using ORAS-5 reanalysis data on an inter-annual time scale for the period 1979–2020. The colour shading shows the inter-annual regression slope of 200-hPa zonal winds onto CE-OHT for the same period. The right panel is the zonal mean regression slope of upper-tropospheric zonal winds (blue) and meridional winds (red) onto CE-OHT for the JJA season. (b) Same as panel ‘a’ but for the DJF season.

Northward CE-OHT peaks in DJF, and southward CE-OHT peaks in JJA, with peak variations near the equator during these seasons. The aim is to investigate CE-OHT’s impact on atmospheric circulation and monsoons.

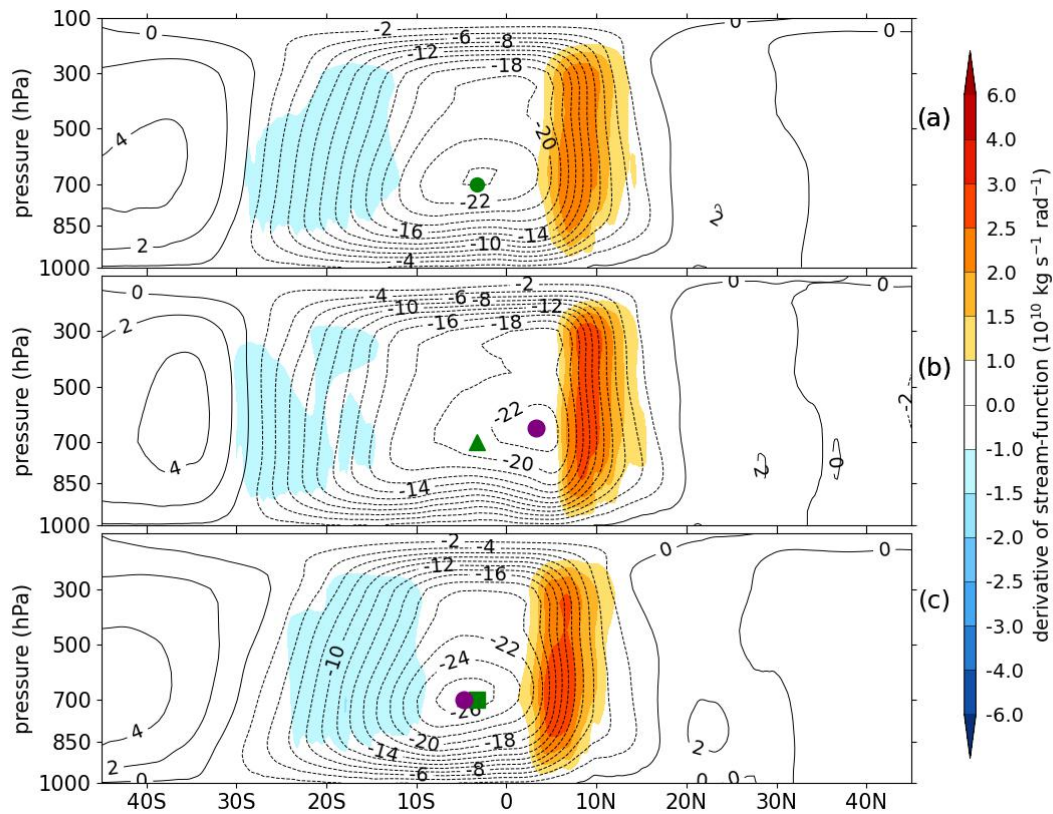


Figure 3.25: (a) The time-averaged atmospheric stream function for the JJA season is displayed by the black curves using ERA-5 reanalysis data for the period 1979–2020. The stream functions for the positive anomalous CE-OHT (mean JJA stream function plus five times the regression slope of the stream function onto CE-OHT on an inter-annual time scale) and the negative anomalous CE-OHT (mean JJA stream function minus five times the regression slope of the stream function onto CE-OHT on an inter-annual time scale) are depicted in (b) and (c), respectively, by black curves. In (a), (b), and (c), the black dashed and solid curves represent anti-clockwise and clockwise rotation (from east), respectively. The colour shading in (a), (b), and (c) illustrates the meridional derivative (positive: ascent; negative: subsidence) of the stream function, indicating the vertical mass flux. The core position, where the absolute value of mass flux peaks, is shown by the green marker for the climatological HC and the purple marker for the regressed HC. The stream function and its meridional derivative have units kg s^{-1} and $\text{kg s}^{-1} \text{rad}^{-1}$, respectively.

Figure 3.24 shows the association of CE-OHT on upper-tropospheric (200 hPa) winds, while Figure 3.24a and Figure 3.24b represent the JJA and DJF seasons, respectively.

In JJA, the increase of CE-OHT pushes the STJs poleward, opposite to the effect of CE-AHT, which moves the STJs towards the equator. The right panel of Figure 3.24a depicts the poleward shifting more clearly in the zonal mean, as observed in the left panel of Figure 3.24a. The poleward shift of the STJs implies an expansion of the HC. Moreover, the TEJ strengthens with the increase of CE-OHT, which is an indication of a strong Indian monsoon (Madhu et al., 2014). The strengthening of the TEJ is associated with La Niña-like

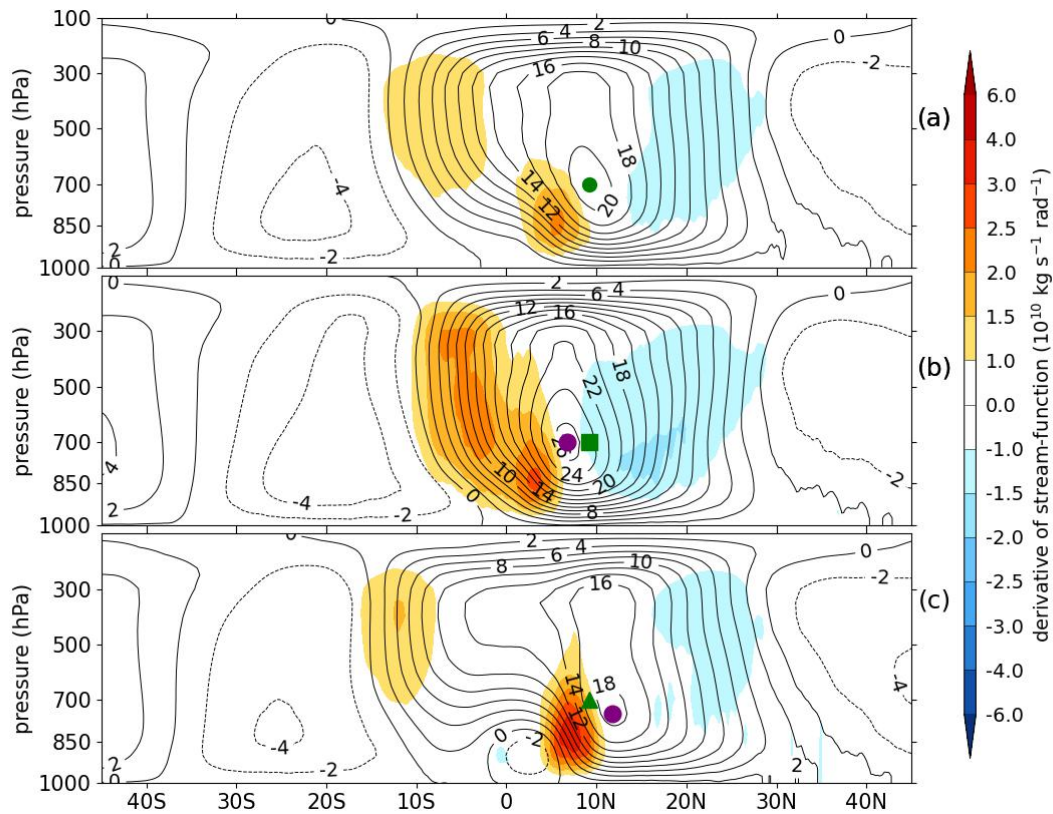


Figure 3.26: Same as the Figure 3.25 but for the DJF season.

conditions over the Pacific Oceans (Chen and van Loon, 1987; Pattanaik and Satyan, 2000). Anomalous divergence over the Maritime Continent and convergence over the central Pacific Ocean are observed, similar to stronger Walker-like circulations.

During DJF, the increase of CE-OHT displaces the STJs towards the equator, and both the left and right panels of Figure 3.24a exhibit a consistent result. The equatorward shift of the STJs indicates shrinking of the HC. Therefore, an equatorward shift of the ITCZ is expected. Anomalous winds converge over the Maritime Continent, denoting weaker Walker-like circulation over the equatorial Pacific Ocean.

Hence, all responses of upper-level winds to CE-OHT are opposite to the effects of CE-AHT in both JJA and DJF. CE-OHT influences upper-level winds, suggesting a stronger monsoon with a poleward shift of the ITCZ widening the HC in JJA and a weaker monsoon with an equatorward shift of the ITCZ contracting the HC in DJF.

Figure 3.25 illustrates how CE-OHT influences the HC for the JJA season. The clima-

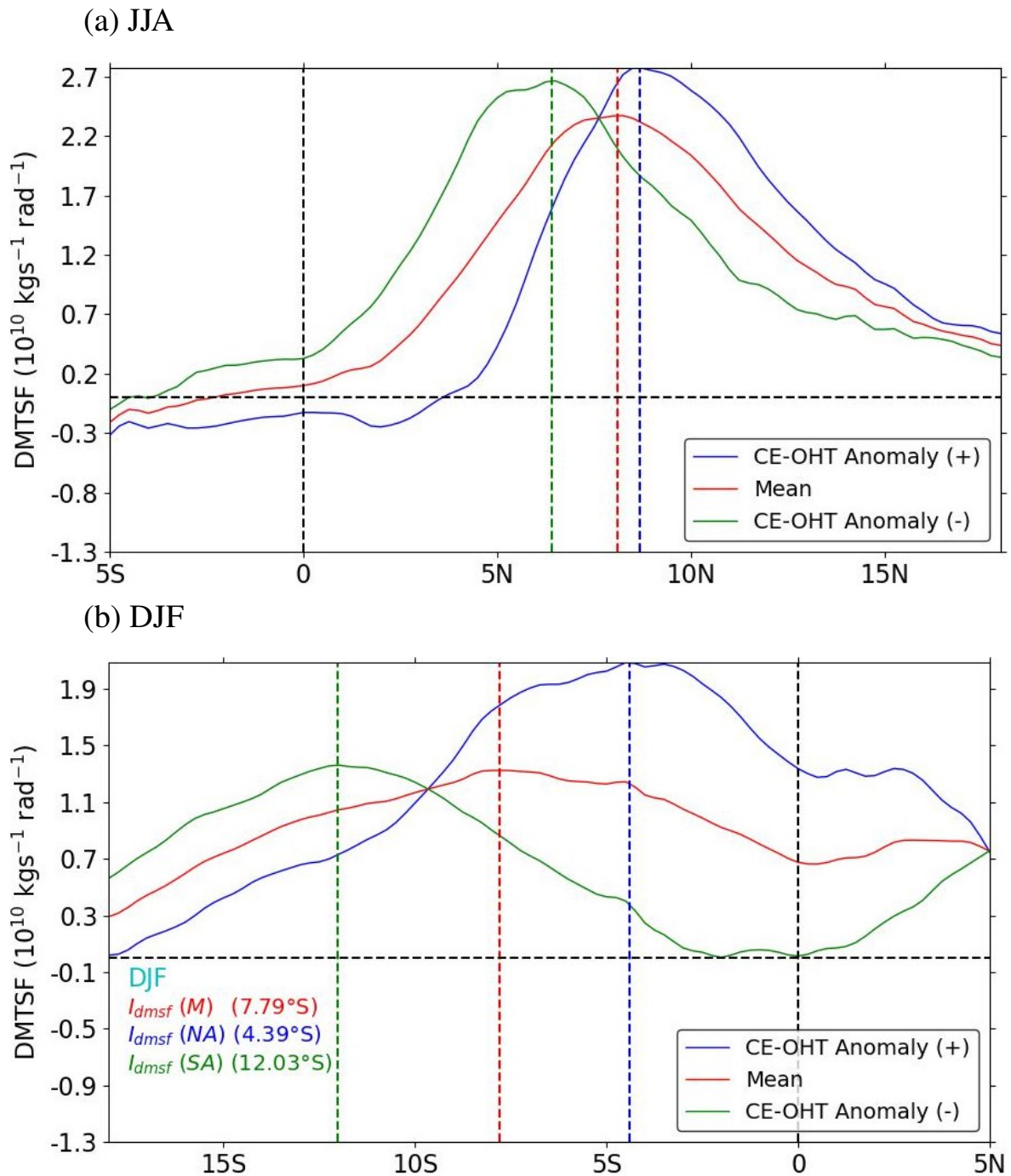


Figure 3.27: (a) The derivative (stream function averaged over 700–300 hPa; red) of time-averaged MTSF is displayed using ERA-5 reanalysis data for JJA for the period 1979–2020. The derivatives of MTSF for positive CE-OHT anomalies (the mean JJA MTSF plus five times the regression slope of the MTSF onto CE-OHT on an inter-annual time scale; blue) and negative CE-OHT anomalies (the mean JJA MTSF minus five times the regression slope of the MTSF onto CE-OHT on an inter-annual time scale; green), are shown. The positions ($^{\circ}$) of the ITCZ identified by the I_{dmsf} metric for the mean MTSF (red), positive CE-OHT anomalies (blue), and negative CE-OHT anomalies (green) are represented by the vertical lines for the JJA season. (b) Same as panel ‘a’ but for the DJF season.

tological HC, with its rising and subsiding branches, is shown in Figure 3.25a, while Figures 3.25b and 3.25c represent corresponding properties of the HC for northward and south-

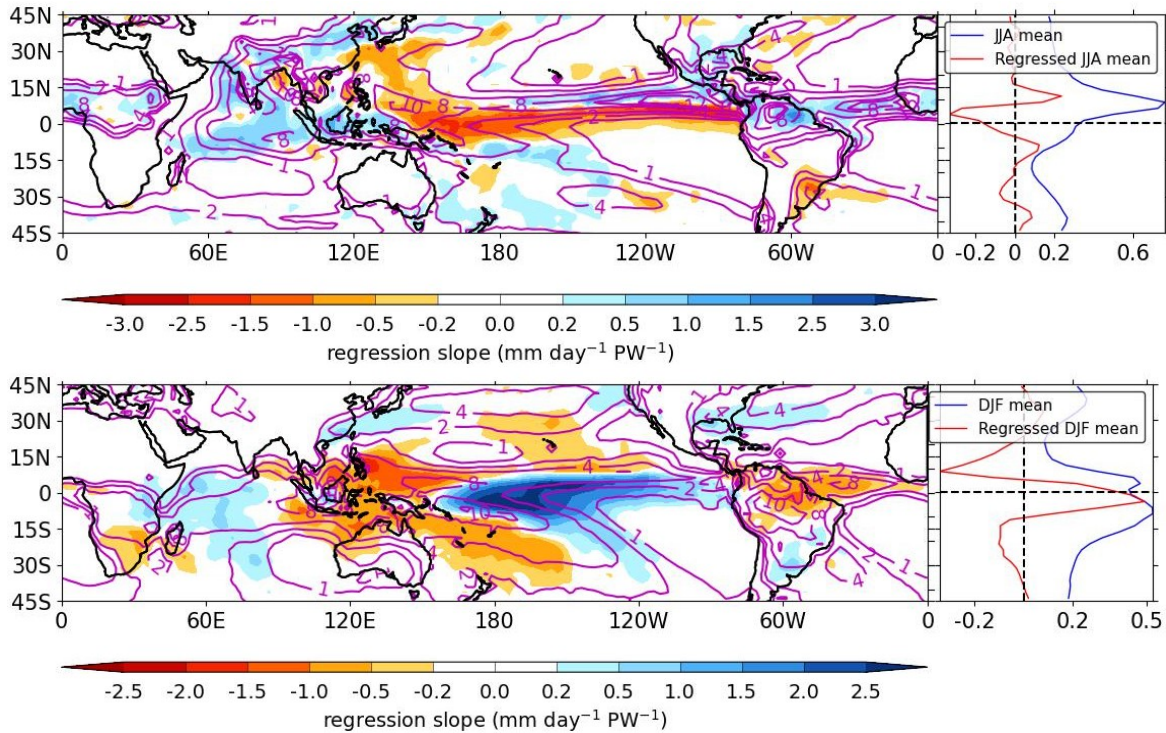


Figure 3.28: (a) The left panel is the regression slope of precipitation onto CE-OHT for the JJA (colour shading in mm day⁻¹ PW⁻¹) season using ORAS-5 on an inter-annual time scale for the period 1979–2020. The solid magenta curves depict mean precipitation (mm day⁻¹). The right panel shows the zonal mean of climatological precipitation (1×10 mm day⁻¹) in a red curve and the regressed precipitation slope onto CE-OHT (mm day⁻¹ PW⁻¹) in a blue curve for the JJA season. (b) Same as panel ‘a’ but for the DJF season.

ward CE-OHT anomalies, respectively. Figure 3.25a is already discussed in Section 3.3.2, so the focus is on Figures 3.25b and 3.25c.

Indeed, southward CE-OHT anomalies contract the HC, while northward anomalies expand the HC, in agreement with the movement of the STJs at the upper-tropospheric level. The contraction and expansion of the HC are related to El Niño and La Niña conditions, respectively (Hu et al., 2018; Nguyen et al., 2013; Lau et al., 2006; Stachnik and Schumacher, 2011). A northward CE-OHT anomaly moves the winter Hadley cell’s rising branch away from the equator, while a southward CE-OHT anomaly shifts it towards the equator during the JJA season, as displayed in Figures 3.25b and 3.25c, respectively. Concurrently, the ITCZ moves away from the equator with northward CE-OHT anomalies and towards the equator with southward CE-OHT anomalies (Marshall et al., 2014; Lu and Dong, 2008; Vellinga and Wood, 2002).

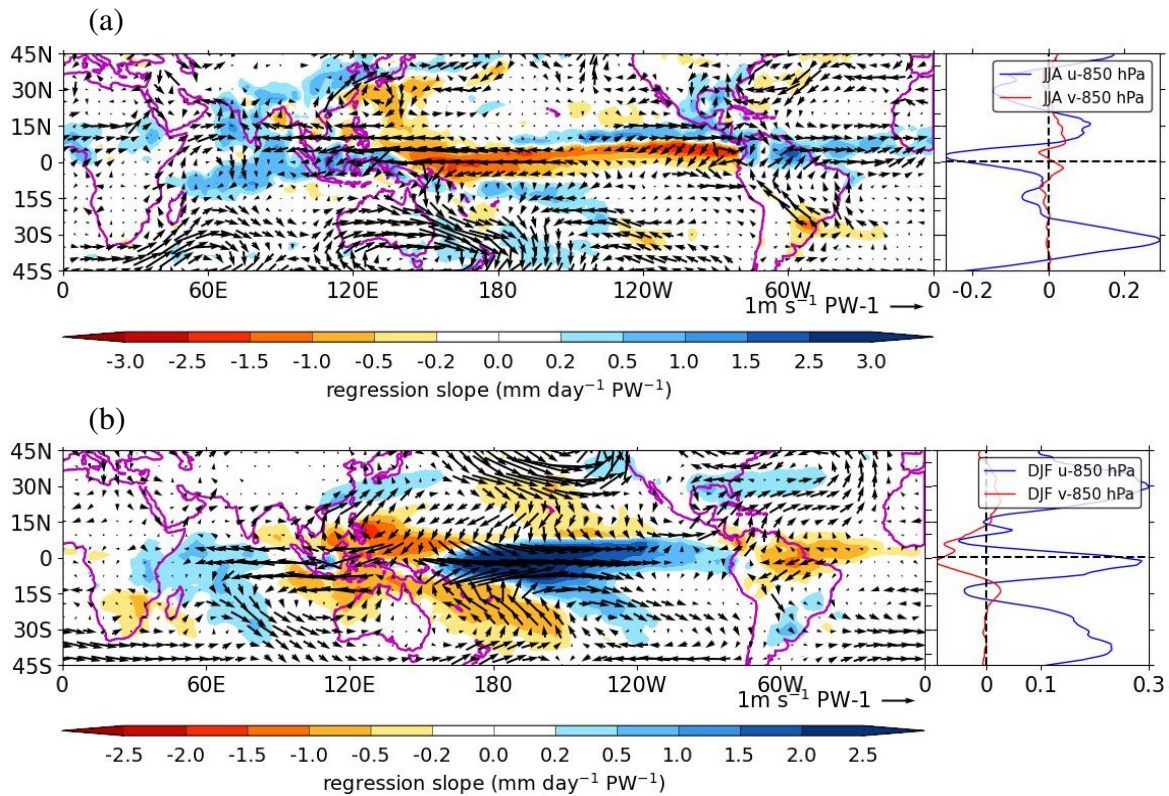


Figure 3.29: (a) The left panel is the regression slope of lower-tropospheric (850 hPa) winds onto the CE-OHT and has been represented by vectors for the JJA season for the period 1979–2020. The colour shading represents the slope of precipitation regression onto the CE-OHT for the same time domain. The right panel shows the zonal mean of lower-tropospheric zonal wind and meridional wind regression slopes ($\text{m s}^{-1} \text{PW}^{-1}$) in blue and red, respectively, for the DJF season. (b) Same as the Figure ‘a’ but for the DJF season.

In contrast to JJA, Figure 3.26 demonstrates the effect of CE-OHT on the HC during the DJF season. The focus is on Figures 3.26b and 3.26c, which depict the HC for northward and southward CE-OHT anomalies, respectively.

Figure 3.26b outlines that the increase of northward CE-OHT unifies the rising branch of the winter Hadley, which was bifurcated for northward CE-AHT anomalies. The HC, particularly the summer-Hadley cell, is contracted, as expected from the equatorward displacement of the STJs in the upper-level winds. Conversely, Figure 3.26c describes that a southward CE-OHT anomaly widens the HC. Moreover, the increase of southward CE-OHT causes the double-rising branch of the winter-Hadley cell by an anticlockwise transient circulation at the equatorial lower-tropospheric level (Zhang, 2001).

Thus, the expansion and contraction of the HC for northward CE-OHT anomalies in the JJA and DJF seasons, respectively, agree with the upper-level winds. Remarkably, the responses of CE-OHT on the HC contrast with the effects of CE-AHT in both JJA and DJF

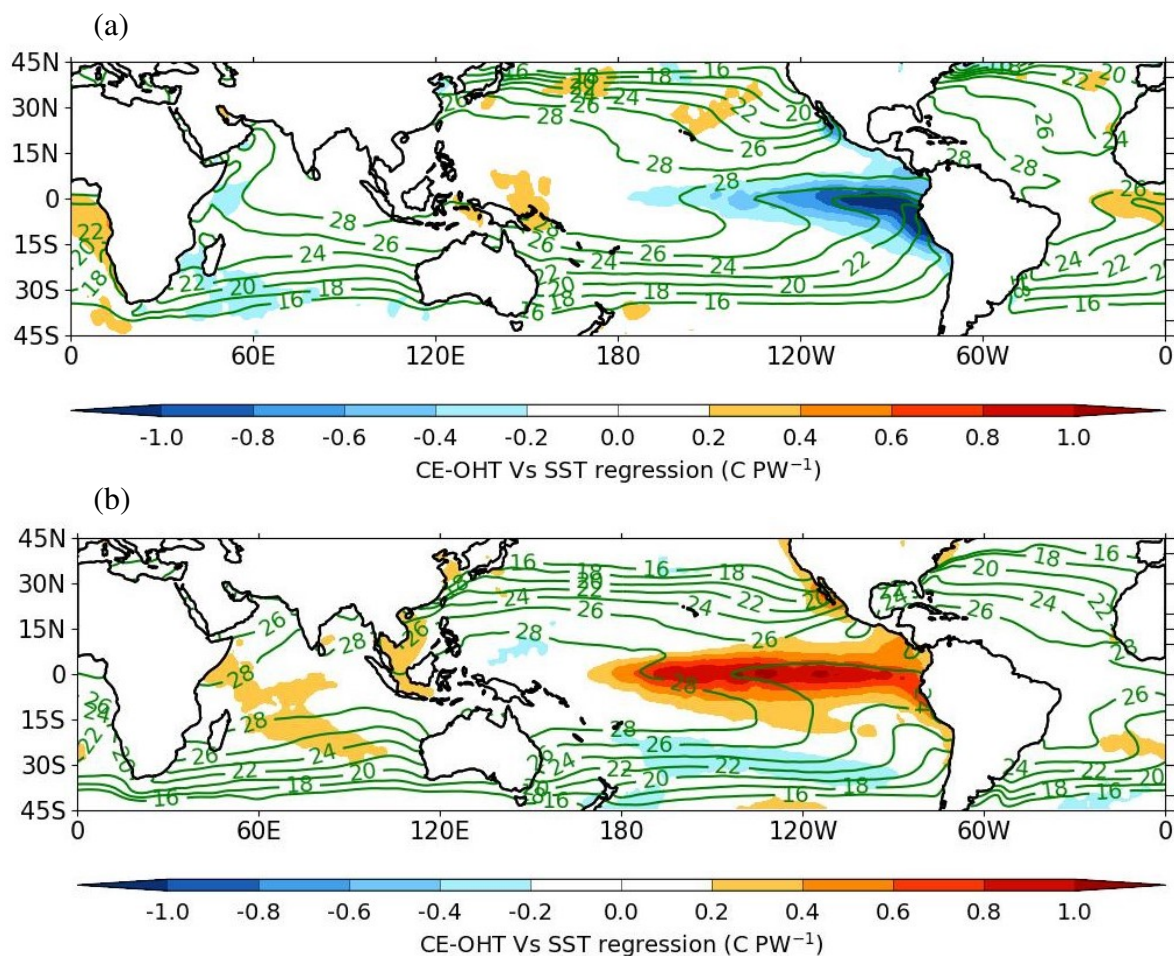


Figure 3.30: (a) The regression slope of SST onto CE-OHT ($^{\circ}\text{C PW}^{-1}$) is represented by colour shading for the JJA season for the period 1979–2020. The green curves are the mean SST for the JJA season. (b) Same as ‘a’ but for the DJF season.

seasons.

The ITCZ movement using the I_{dmsf} metric is displayed in Figure 3.27 for positive and negative CE-OHT anomalies. Figure 3.27(a) for JJA and Figure 3.27(b) for DJF. In JJA, for northward CE-OHT anomalies, the ITCZ moves away from the equator and its climatological position, whereas the ITCZ shifts in the opposite direction for southward CE-OHT anomalies. Conversely, during DJF, the ITCZ is displaced towards the equator from its climatological position for northward CE-OHT anomalies, whereas the ITCZ is pushed poleward for southward CE-OHT anomalies. The movement of the ITCZ is dominated by southward CE-OHT anomalies, whereas northward anomalies are dominant for CE-AHT in both JJA and DJF seasons.

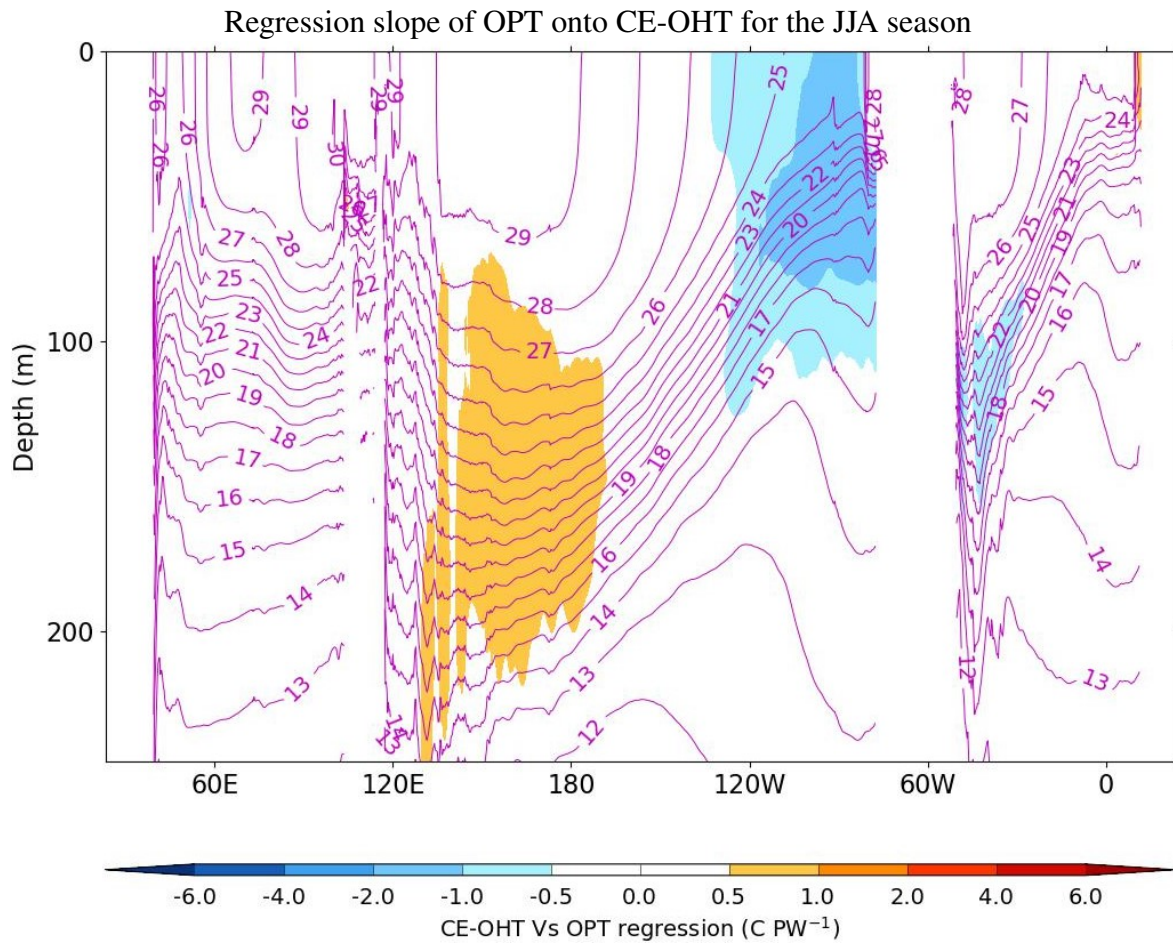


Figure 3.31: The regression slope of OPT (after taking the meridional mean in between 5°N and 5°S) onto CE-OHT ($^{\circ}\text{C PW}^{-1}$) is displayed by colour shading using ORAS-5 reanalysis data for the JJA season on an inter-annual time scale for the period 1979–2020.

Precipitation is a crucial metric for determining a strong or weak monsoon. Therefore, the impacts of CE-OHT on monsoonal precipitation are explored.

Figure 3.28(a) highlights the connection between CE-OHT and monsoonal precipitation for the JJA season. During the JJA season, the right panel of Figure 3.28(a) shows a clear shift of the ITCZ away from the equator and its climatological position, an indication of a strong monsoon. The poleward shift of the ITCZ in terms of precipitation is consistent with that of the HC. Similarly, the left panel of Figure 3.28(a) illustrates that the increase in northward CE-OHT causes heavy precipitation over the Maritime Continent, North African, Indian, and North American monsoon domains. The reduction of precipitation along the equator is observed over the Pacific Ocean, maybe due to the strengthening of the Walker-like circulation as found in the upper-level winds. Therefore, the CE-OHT is acting in the opposite direction as the CE-AHT does.

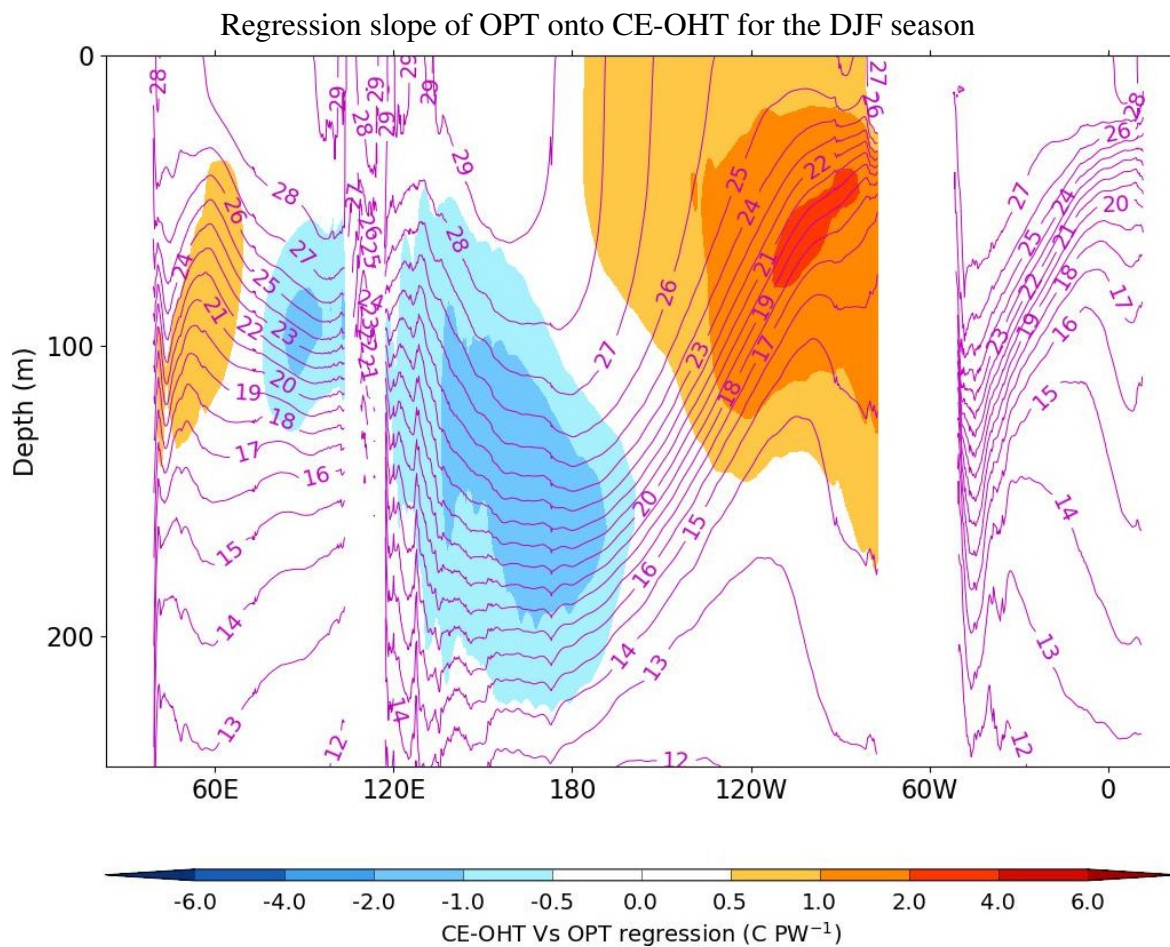


Figure 3.32: Same as Figure 3.17 but for the DJF season.

On the contrary, Figure 3.28(b) depicts the impacts of CE-OHT on monsoonal precipitation for the DJF season. The ITCZ relating to precipitation moves towards the equator with the increase of CE-OHT, as observed from the right panel of Figure 3.28(b). Interestingly, both the left and right panels of Figure 3.28(b) show that for northward CE-OHT anomalies, a single ITCZ pattern is observed in precipitation, similar to the HC, which is opposite for CE-AHT. This single ITCZ indicates an appearance of El Niño-like conditions over the Pacific Ocean, as consistent with the upper-level winds (Zhang, 2001). The northward increment of the CE-OHT reduces precipitation over the Maritime Continent, Australian, South American, and South American monsoon domains during the DJF season. But intense precipitation mostly occurs over the tropical Western Indian and central-eastern Pacific Oceans.

In summary, the increase of CE-OHT strengthens monsoonal precipitation over the Indian, North American, and West African monsoon domains in JJA but suppresses precipita-

tion over the Maritime Continent, Australian, South American, and South American monsoon domains in DJF. CE-OHT alters precipitation in a way that opposes the changes caused by CE-AHT in both JJA and DJF.

The dynamical aspect is analysed using the lower tropospheric winds (850 hPa). The impacts of northward CE-OHT anomalies on lower tropospheric winds are shown for JJA in Figure 3.29(a) and for DJF in Figure 3.29(b).

Figure 3.29(a) displays that northward CE-OHT anomalies in JJA induce anomalous convergence over the Indian monsoon domain, strengthen the Somali jet, and increase south-westerly winds. As a result, a positive signal of precipitation is observed over the Indian monsoon domain. Moreover, convergence over the Maritime Continent, a stronger Walker-like circulation, increases precipitation over there.

On the other hand, in Figure 3.29(b), easterly and westerly wind anomalies prevail over the tropical Indian and Pacific Oceans, respectively, for positive CE-OHT anomalies in DJF. An anomalous divergence of lower-tropospheric winds over the Maritime Continent is observed. This divergence symbolises weaker Walker-like circulation, as found in the upper-level winds, which suppresses precipitation over the Maritime Continent and Australian monsoon domain. As a result, precipitation strengthens over the equatorial Pacific Ocean. Moreover, precipitation is reduced over the South African and South American monsoon domains.

With the increase of CE-OHT, all responses of lower-tropospheric winds align with the results of upper-tropospheric winds but differ from those of CE-AHT in both JJA and DJF seasons.

The connection of SST anomalies with the increase in CE-OHT is explored in Figure 3.30. Figure 3.30(a) shows the effects of northward CE-OHT anomalies on SST for JJA, and Figure 3.30(b) for DJF.

Figure 3.30(a) illustrates that positive CE-OHT anomalies promote La Niña-like conditions over the eastern Pacific Ocean, and it is consistent with all earlier analysis for the JJA season. Conversely, during DJF season, the negative CE-OHT anomalies induce El Niño-like

conditions over the eastern Pacific Ocean, as aligned with other findings.

In essence, the increase of CE-OHT produces La Niña-like conditions in JJA and El Niño-like conditions in DJF, while the opposite pattern is observed for CE-AHT in each corresponding season.

OPT is analysed on the latitude-depth plane to understand its response to increased CE-OHT. The impacts of northward CE-OHT anomalies on OPT are shown in Figure 3.31 for JJA and Figure 3.32 for DJF.

Similar to the results of SST, the OPT exhibits La Niña-like conditions in JJA and El Niño-like conditions in DJF, while CE-AHT displays the reverse pattern in each corresponding season.

3.4 Conclusions

Peak southward AHT and OHT occur in the winter hemisphere during the JJA season, with CE-AHT and CE-OHT also reaching their southward maxima. On an inter-annual time scale in JJA, the peak standard deviation of CE-AHT and CE-OHT is near the equator. Conversely, during DJF, northward AHT and OHT dominate the winter hemisphere, with northward CE-AHT and CE-OHT prevailing and showing peak variation around the equator on an inter-annual time scale. In the seasonal cycle, CE-OHT follows CW-AHT, lagging behind by a month. Peak CE-AHT and CE-OHT and their corresponding highest variabilities imply an atmosphere-ocean-coupled connection of heat transport with the monsoons during solstice seasons.

The increase of CE-AHT in JJA shifts the STJs equatorward and weakens the TEJ and Walker-like circulation. Furthermore, the HC shrinks and the ITCZ is displaced towards the equator, reducing precipitation over the Indian, West African, and North American monsoon domains and revealing El Niño-like conditions in the eastern Pacific Ocean. On the other hand, CE-OHT induces effects opposite to those of CE-AHT: STJs move poleward, the TEJ and Walker-like circulation strengthen, the HC widens, and the ITCZ moves away

from the equator leading to increased Indian, West African, and North American monsoonal precipitation, indicative of La Niña-like conditions.

During DJF, northward CE-AHT anomalies push the STJs away from the equator and strengthen the Walker-like circulation, denoting La Niña-like conditions. Moreover, the HC expands, moving the ITCZ poleward, which, in turn, increases precipitation over the Maritime Continent, Australian, South American, and South African monsoon domains. In contrast to CE-AHT, the increase of CE-OHT reveals that the STJs are displaced towards the equator and the Walker-like circulation is weakened. As a consequence, the HC contracts and the ITCZ moves in the equatorward direction, reducing precipitation over the Maritime Continent, Australian, South American, and South African monsoon domains.

It is noteworthy to mention that all responses to CE-AHT contrast the effects of CE-OHT in both JJA and DJF seasons on an inter-annual time scale. Thus, atmospheric and oceanic cross-equatorial heat transports affect the subtropical jet streams (STJs), which then influence the Hadley and Walker circulations. Consequently, the Intertropical Convergence Zone (ITCZ) fluctuates meridionally and alters monsoon rainfall patterns.

Therefore, the observation-based reanalysis datasets indicate that cross-equatorial heat transports are intricately linked to monsoonal circulations and significantly impact the distribution of monsoonal rainfall during solstice seasons. This connection highlights the importance of understanding how variations in heat transport can influence weather patterns dynamically and thermodynamically. In a warming climate, how these relationships evolve remains unexplored, which is crucial for rainfall distribution patterns, water budgets, and climate modelling.

However, to gain a more comprehensive understanding, it is essential to investigate how well climate models, especially those used in the latest phase of the Coupled Model Intercomparison Project (CMIP6), simulate this observed relationship. Since these models are critical for predicting future climate scenarios and informing policy decisions, their accuracy in capturing the dynamics of cross-equatorial heat transport and its effects on monsoons is crucial.

Studying the performance of CMIP6 models in this context would involve comparing

their simulations against reanalysis data to assess their ability to reproduce the observed patterns of heat transport, monsoonal rainfall, and the relationship between heat transport and monsoons. This analysis could help identify any biases or limitations in the models and provide insights into potential improvements. Understanding these dynamics in climate models is vital for improving their reliability and accuracy in projecting future changes in monsoonal systems under various climate change scenarios.

4

The Relationship of Cross-Equatorial Heat Transports and the Monsoons in CMIP6 Historical Simulations

4.1 Introduction

Global climate models simulate the past and present climate in order to predict potential future climate changes, vulnerabilities, and consequential hazards. But limitations arising from complex feedback processes among land, atmosphere, and ocean, as well as uncertainties in measuring and specifying climate forcing, impact the models' predictive capabilities (Karl and Trenberth, 2003). Also, coarse resolutions, imperfect initial and boundary conditions, poor parametrizations, and systematic model biases have the potential to limit the

performance of climate models. The state-of-the-art CMIP6 climate models, consisting of a set of Diagnostic, Evaluation, and Characterization of Klima (known as DECK) experiments, have become a pivotal global tool to assess climate change (Eyring et al., 2016).

CMIP6 models feature improved spatial resolution for both atmosphere and ocean in contrast to CMIP5 (Simpkins, 2017). For example, the EC-Earth global model for HighResMIP is one of the finest models with an atmospheric resolution of ~ 16 km and an oceanic resolution of $1/12^\circ$ (~ 8 km) (Moreno-Chamarro et al., 2024). CMIP6 integrates advanced and intricate mechanisms, such as enhanced land surface processes, ice sheet dynamics, permafrost behaviour, biogeochemical cycles, and other complex systems (Eyring et al., 2019; Simpkins, 2017). Furthermore, in comparison to CMIP5, CMIP6 models used improved forcing field data, including greenhouse gases, solar irradiance, ozone, volcanic aerosols, and aerosol optical properties (Eyring et al., 2016; Meinshausen et al., 2017; Matthes et al., 2017).

The variability of precipitation has great potential to damage social development, especially in vulnerable agrarian-based developing economies. Over a billion people depend on Indian monsoon rainfall for their livelihood and economic well-being. Many studies have been conducted to assess the performance of the CMIP6 models in reproducing historical precipitation and SST, considering various horizontal and temporal scales. For example, the CMIP6 models perform better in simulating the JJA precipitation than the DJF precipitation on a global scale, except for mountainous regions (Huang et al., 2023). Additionally, Du et al. (2022) demonstrated that the CMIP6 models exhibit improved accuracy in simulating precipitation patterns over global land compared to the CMIP5 models over multi-year timescales for both annual and seasonal means.

Despite advancements, the annual mean precipitation still exhibits the double-ITCZ bias, an extra zonal band of precipitation to the south of the equator, particularly over the Pacific Ocean, in CMIP6 (Zhang et al., 2021; Tian and Dong, 2020; Ma et al., 2023). Even in Chapter 3, a double-ITCZ-like pattern emerged when precipitation and stream function were regressed onto CE-AHT during the DJF season. With an increase in CE-AHT, both ITCZ-

like patterns shifted poleward in their respective hemispheres. This made it challenging to identify which one represented the actual ITCZ. This issue was addressed by considering only the ITCZ-like pattern in the southern hemisphere, where the ITCZ typically resides during DJF. However, the surface convergence bias resulting from the meridional pattern of biases in SST has been reported as the dominant cause (Zhou et al., 2020). The double-ITCZ bias can be mitigated by enhancing model resolutions (Song and Zhang, 2020) and convective parametrizations (Zhang et al., 2019a) in climate models, such as adjusting the entrainment rate, raindrop re-evaporation, and convection triggering function (Zhang et al., 2021). The CMIP6 models are successful in simulating the climatological annual mean HC (Wang et al., 2023), particularly regarding its spatial distribution, outperforming the CMIP5 models (Li et al., 2023). Nonetheless, the CMIP6 model simulations display biases in both the intensity and spatial extent of the Hadley circulation cells (Li et al., 2023).

In the regional case, the simulation of the annual mean climatology of dry or wet months and trends of precipitation over North Africa are satisfactory when compared with the observation (Babaousmail et al., 2021). In spite of the prevailing cold bias and wet bias over the Tibetan Plateau, temperature and precipitation simulations in CMIP6 have a pattern correlation exceeding 0.75 on the annual mean time scale (Zhu and Yang, 2020). Spatially and temporally, the Indian monsoon displays highly heterogeneous behaviour. The spatial distribution of the Indian monsoon rainfall (JJAS), including the Western Ghats and North-East foothills of the Himalayas (Gusain et al., 2020), is well captured by the CMIP6 models (Rajendran et al., 2022; Dutta et al., 2022; Choudhury et al., 2022), regardless of the vast physiographic variations across the monsoon domain (Mitra, 2021). The CMIP6 models also reproduce the inter-annual variability of Indian monsoon rainfall (Rajendran et al., 2022; Choudhury et al., 2022). However, the CMIP6 models show a narrow region of dry bias over central India (Dutta et al., 2022) and wet bias over the surrounding oceans (Rajendran et al., 2022).

The distribution of energy balance on the annual mean time scale, particularly noticeable at the surface and top of the atmosphere, exhibits a slight imbalance, which manifests as a surplus of energy in the southern hemisphere and a deficit in the northern hemisphere

in CMIP5 (Loeb et al., 2016). CMIP6 models show a tendency for higher intake or less loss of energy over northern hemisphere land, southern hemisphere ocean, and high latitudes (Li et al., 2023). The CMIP6 models fail to capture reflected solar radiation changes over low-cloud-dominating regions, which contributes to the energy discrepancies in the models (Loeb et al., 2020). **Despite energy flux uncertainty in regions such as Eurasia, the North Atlantic, and Indian Oceans, CMIP6 outperforms CMIP5 in the energy balance aspect on a regional scale (Li et al., 2023).**

The partitioning of total meridional heat transport, arising from the net energy imbalance at the top of the atmosphere, into atmospheric and oceanic heat transports has been challenging in climate models. **The net energy imbalance at the top of the atmosphere is primarily due to the difference between incoming solar radiation and outgoing terrestrial radiation (Loeb et al., 2018). Human activities, particularly the emission of greenhouse gases, have increased the amount of heat trapped in the Earth's system, leading to a positive energy imbalance. According to the Earth Radiation Budget Experiment (ERBE) and other studies, this imbalance is a critical indicator of climate change, with recent estimates showing a heating rate of approximately 0.76 Wm^{-2} from 2006 to 2020 (Von Schuckmann et al., 2020). In climate models, errors in representing energy imbalance stem from uncertainties in radiative forcing estimates, oversimplified feedback mechanisms (e.g., cloud-aerosol interactions), and inadequate resolution of oceanic and atmospheric processes (Taylor et al., 2007).** The CMIP6 climate models consistently exhibit an underestimation of oceanic heat transport and an overestimation of atmospheric heat transport compared to observations (Donohoe et al., 2023). For example, Loeb et al. (2016) found a considerable variation in CE-AHT across all CMIP5 models, with a standard deviation of 0.2 PW. Donohoe et al. (2023) reported that the biases remain unchanged regardless of the datasets used to measure actual heat transfers across three successive generations of climate models (CMIP3, CMIP5, and CMIP6). They found a pattern of higher-than-observed surface evaporation in the tropics, which increases atmospheric heat transfer but diminishes oceanic heat transfer. In the CMIP5 multi-model mean, CE-AHT and CE-OHT are 0.03 PW and 0.40 PW, respectively, in the annual mean for the period 1980–2004 (Loeb et al., 2016).

Bjerknes compensation (BJC) is the balancing mechanism between atmospheric and oceanic heat transport to maintain stable total meridional heat transport (Bjerknes, 1964). Bjerknes compensation is typically studied in mid- to high-latitudes, where the interactions between atmospheric and oceanic heat transport are most prominent due to strong meridional temperature gradients and active thermohaline circulation (Van der Swaluw et al., 2007; Rose and Ferreira, 2012; Outten et al., 2018). Theoretical studies by Liu et al. (2016) and Yang et al. (2016) confirm that the energy constraint is a prerequisite in a coupled system for the occurrence of Bjerknes compensation, while local climate feedback governs the manner in which it takes place. Yang et al. (2016) highlights energy conservation as the core mechanism underlying BJC and establishes a direct connection between radiative feedback and the extent of compensation. It also suggests a strong relationship between the top-of-atmosphere energy balance and ocean thermohaline dynamics. For instance, local climate feedback such as the asymmetric thermohaline circulation results in stronger BJC in the northern hemisphere compared to the southern hemisphere (Shi and Yang, 2021). The investigation will focus on whether the CMIP6 models exhibit BJC at the equator during the solstice seasons.

In the previous Chapter 3, the impacts of cross-equatorial atmospheric and oceanic heat transports on monsoons were discussed using reanalysis datasets. Building upon this exploration, the present investigation turns its focus towards the evaluation and analysis of the CMIP6 climate models, aiming to discern their efficiency in capturing the intricate interplay between cross-equatorial heat dynamics and monsoonal patterns. This chapter seeks to provide valuable insights into the models' performance, offering a comprehensive understanding of their ability to simulate the observed relationships. Therefore, all queries that will be addressed in Chapter 4 are:

- ▶ What are the simulated patterns of cross-equatorial heat transport in CMIP6?
- ▶ How are cross-equatorial heat transports linked with the monsoons in CMIP6?
- ▶ How does model performance vary based on pattern correlation?

The datasets of the CMIP6 models and methodologies are outlined in Section 4.2. The results are presented in Section 4.3, while the conclusion is provided in Section 4.4.

4.2 Data and Methodology

Table 1: A table of CMIP6 Models used in this study

Model Name (Institute)	Atmosphere (Ocean) Resolution (°) (lon×lat)	Reference
CanESM5 (Canadian Centre for Climate Modelling and Analysis, Canada)	2.8°×2.8°(1°×1°)	(Swart et al., 2019)
CNRM-CM6-1 (Centre National de Recherches Meteorologiques, France)	1.4°×1.4°(1°×1°)	(Voldoire, 2019)
CNRM-ESM2-1 (Centre National de Recherches Meteorologiques, France)	1.4°×1.4°(1°×1°)	(Seferian, 2018)
EC-Earth3 (Swedish Meteorological and Hydrological Institute, Sweden)	0.7°×0.7°(1°×1°)	(EC-Earth Consortium (EC-Earth), 2019)
FGOALS-g3 (Chinese Academy of Sciences, China)	2°×2.25°(1°×1°)	(Li, 2019)
GISS-E2-1-G (Goddard Institute for Space Studies, USA)	2.5°×2°(1°×1°)	(NASA Goddard Institute for Space Studies (NASA/GISS), 2018)
HadGEM3-GC31-LL (Met Office Hadley Centre, UK)	1.875°×1.25° (1°×1°)	(Ridley et al., 2019a)
HadGEM3-GC31-MM (Met Office Hadley Centre, UK)	0.83°×0.55° (0.25°×0.25°)	(Ridley et al., 2019b)
IPSL-CM6A-LR (Institut Pierre Simon Laplace, France)	2.5°×1.25°(1°×1°)	(Boucher et al., 2018)
MIROC6 (Japan Agency for Marine-Earth Science and Technology, Japan)	1.4°×1.4°(1°×1°)	(Tatebe and Watanabe, 2018)
MPI-ESM1-2-HR (Max Planck Institute for Meteorology, Germany)	0.94°×0.94° (0.4°×0.4°)	(Jungclaus et al., 2019)
MPI-ESM1-2-LR (Max Planck Institute for Meteorology, Germany)	1.875°×1.875° (1.5°×1.5°)	(Wieners et al., 2019)
MRI-ESM2-0 (Meteorological Research Institute, Japan)	1.125°×1.125° (1°×0.5°)	(Yukimoto et al., 2019)
UKESM1-0-LL (Met Office Hadley Centre, UK)	1.875°×1.25°(1°×1°)	(Tang et al., 2019)

The present study utilizes monthly precipitation, sea surface temperature, winds, and oceanic heat transport data from 14 models sourced from the CMIP6 (Eyring et al., 2016) archive, as outlined in Table 1. These selected CMIP6 models provide data for both historical periods (ranging from either 1850 or 1950 to 2014) and the SSP5-8.5 scenario (spanning from 2015 to 2100). Notably, the inclusion of model-calculated and offered OHT is a primary criterion in the selection of these 14 models. Due to data availability constraints, different combinations of realizations, initializations, physics, and forcing are employed for

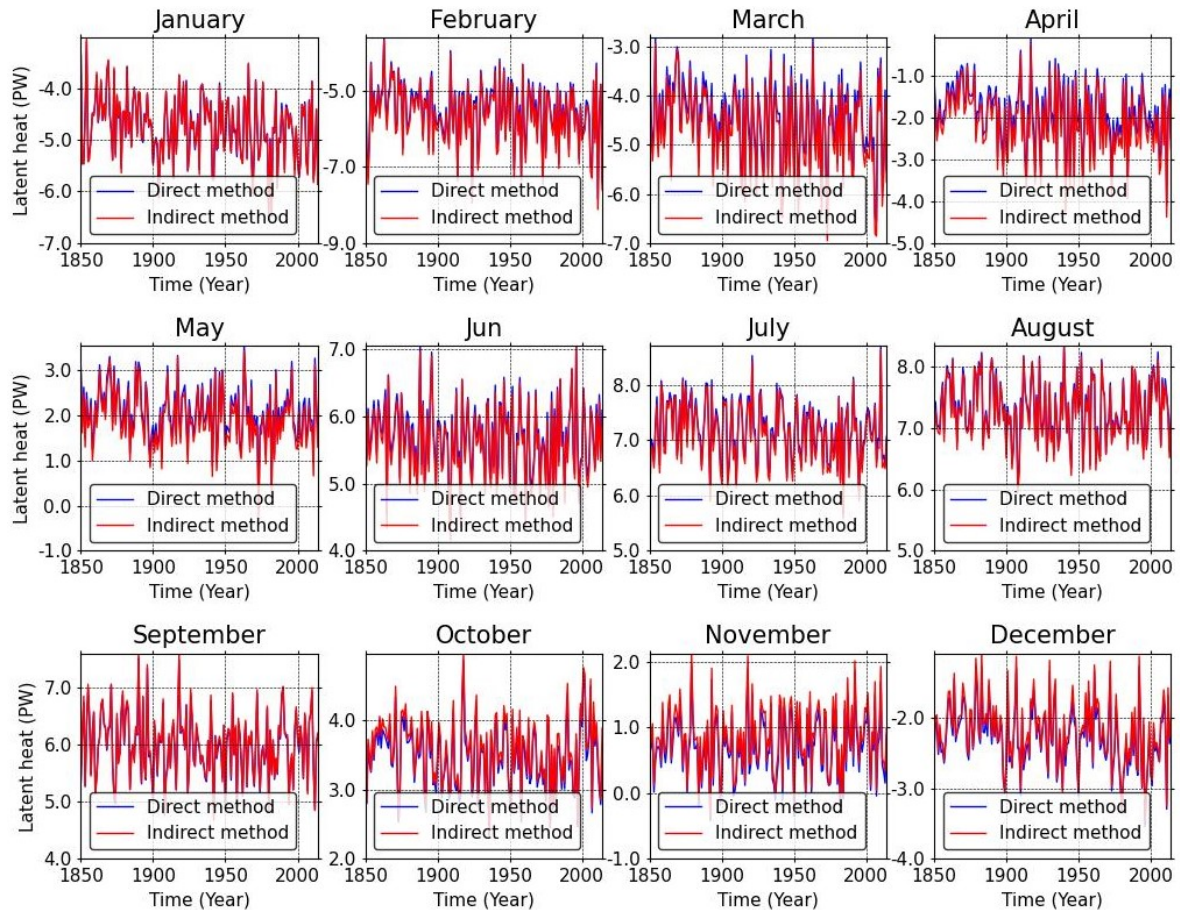


Figure 4.1: A monthly time series of cross-equatorial latent heat transport (PW) by direct (vertically integrated: blue) and indirect (evaporation-precipitation: red) methods. Negative and positive values denote southward and northward exports, respectively.

each model in the historical experiments.

The calculation process of stream function in the CMIP6 models is similar to how I calculated it for the reanalysis data, which is discussed in subsection 2.4.3. In the previous chapter (Chapter 3), I also discussed various metrics for identifying the ITCZ, particularly focusing on zonal mean precipitation and the DMTSF (derivative of mid-tropospheric stream function). I employ both the I_{pr} and I_{dmsf} metrics to identify the ITCZ in the CMIP6 models and compare how accurately the I_{dmsf} metric captures the location of the ITCZ identified by I_{pr} .

The computation of CE-AHT differs between reanalysis data and CMIP6. The direct method (through vertical integration as in subsection 2.4.1) is used for the reanalysis data, and the indirect method (using energy balance at the TOA and surface as in subsection 2.4.2)

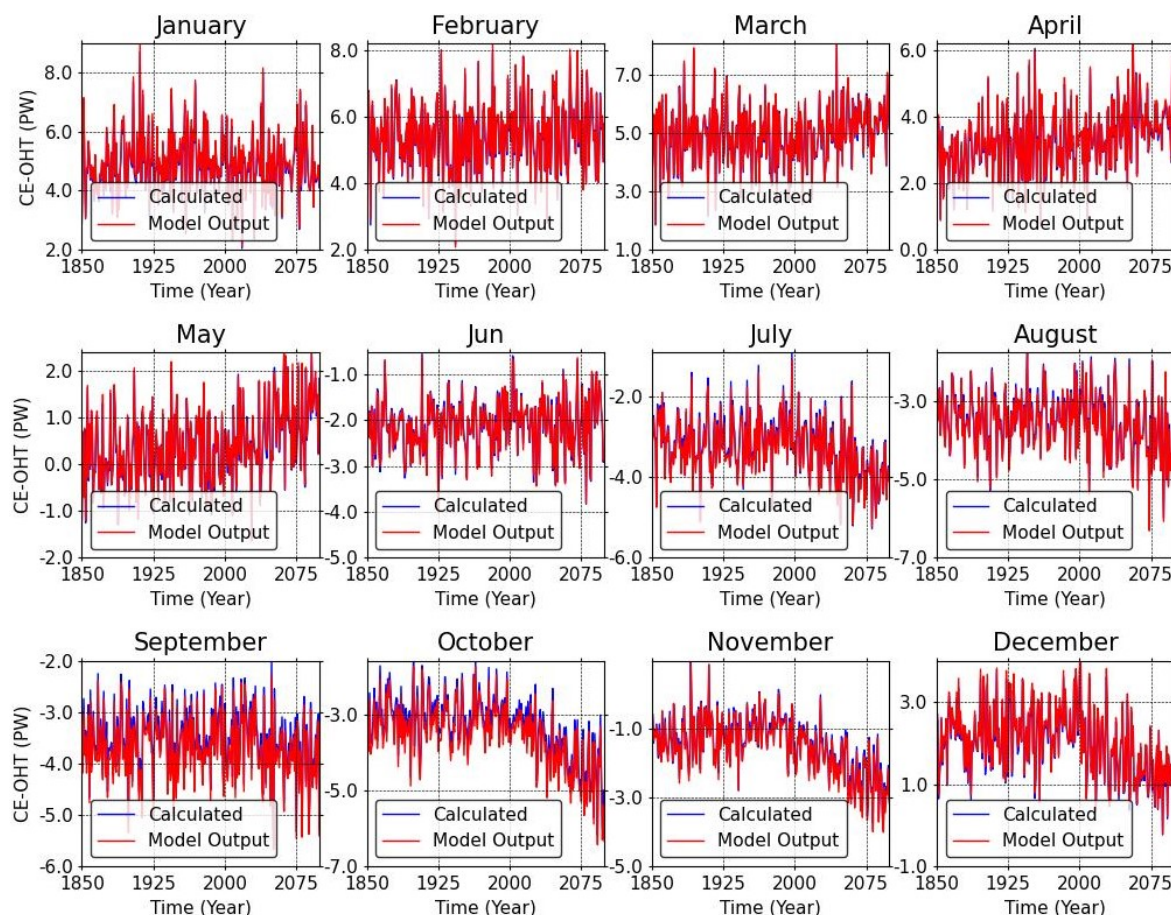


Figure 4.2: A monthly time series of cross-equatorial oceanic heat transport (PW) estimated by the direct method (red: model-estimated; blue: our estimation) is shown. Negative and positive values denote southward and northward exports, respectively.

is employed in the CMIP6 models. For estimating OHT in CMIP6, I use the direct method, similar to the reanalysis data, as discussed in subsection 2.4.1).

The accurate estimation of CE-AHT via the indirect method relies on the energy balance at the top of the atmosphere, whereas the spatial, vertical, and temporal resolutions are crucial in the direct estimation process. It has been documented that 1 Wm^{-2} energy imbalance at the TOA corresponds to 0.51 PW heat transport (Fasullo and Trenberth, 2008a). Wild (2020) reported annual mean energy imbalances in CMIP6 models ranging from 0.2 to 4.6 Wm^{-2} , with a multi-model mean of 1.1 Wm^{-2} .

Figure 4.1 illustrates the reliability of using the indirect method to compute CE-AHT. The HadGEM3-GC31-LL model-provided cross-equatorial latent heat transport is compared with the computed latent heat transport by the indirect method using evaporation minus precipitation. A very strong correlation coefficient ($p\text{-value} < 0.001$) on the inter-annual

time scale is noted in the seasonal cycle (Figure 4.1). Likewise, the comparison between the HadGEM3-GC31-LL model-given CE-OHT and calculated CE-OHT (using the direct method) for the same model is displayed in Figure 4.2. An extremely strong correlation coefficient with an extreme confidence level is found for each month in the seasonal cycle (Figure 4.2).

I employ the boxplot, also known as a box-and-whisker plot, as a graphical representation to visualize the distribution of a dataset and identify potential outliers. It consists of a rectangular box spanning from the first quartile (Q1) to the third quartile (Q3), representing the interquartile range ($IQR=Q3 - Q1$) of the data, encompassing the middle 50% of the data. The length of the box indicates the spread of this central portion of the dataset. ‘Whiskers’ extend from the box to the furthest data points within a certain distance from the quartiles. Boxplots are commonly employed in statistical analysis and data visualization due to their ability to provide a concise summary of the data distribution and highlight any extreme values or outliers. In a boxplot, any data points beyond the whiskers are considered outliers. Mathematically, outliers are identified as the data points that fall below $Q1 - 1.5 * IQR$ or above $Q3 + 1.5 * IQR$. These outliers, if present, are displayed individually on the plot, allowing for easy identification and further investigation of potentially anomalous data points.

For assessing the ability of climate models in simulation, lots of metrics have been proposed in numerous studies, encompassing aspects from capturing the spatial distribution of the climatological mean state to temporal variability. Bias is the difference between the modelled and observed climatological mean field, where smaller values signify better model performance. It is commonly used for the evaluation of the spatial distribution of model climatology against observations. Furthermore, root mean square error (RMSE, representing the square root of the average of the squared differences between the modelled and observed values, with smaller values indicating better model simulation performance) and pattern correlation (P_{cor} , indicating the correlation between the patterns of the modelled and observed climatological mean field) are frequently used to serve the same purpose (Nishant et al., 2022). In P_{cor} , larger values signify improved model simulation performance. The equations

for bias, RMSE, and P_{cor} (Cohen et al., 2009), considering a variable in model simulations (X_m) and observational datasets (X_o) with ‘N’ number of entries, are as follows:

$$\text{Bias} = \frac{1}{N} \sum_{i=1}^N (X_{m,i} - X_{o,i}) \quad (4.1)$$

$$\text{RMSE} = \sqrt{\frac{1}{N} \sum_{i=1}^N (X_{m,i} - X_{o,i})^2} \quad (4.2)$$

$$P_{cor} = \frac{\sum_{i=1}^N (X_{m,i} - \overline{X_m}) \times (X_{o,i} - \overline{X_o})}{\sqrt{\sum_{i=1}^N (X_{m,i} - \overline{X_m})^2} \times \sqrt{\sum_{i=1}^N (X_{o,i} - \overline{X_o})^2}} \quad (4.3)$$

All analyses conducted on historical simulations are juxtaposed with results from reanalysis datasets. It is noteworthy that reanalysis datasets cover a comparatively shorter time-frame, starting from the satellite era (1979–2020). Prior to model comparison, all analysed datasets are regridded to a common regular (64×128) grid using bilinear interpolation.

4.3 Results

To begin with, the seasonal cycle and trends of the CE-AHT and CE-OHT are discussed to highlight their respective values and patterns. The relationship between the CE-AHT or CE-OHT and monsoon in each CMIP6 model is then investigated by regression on various variables, such as precipitation, SST, stream function, and winds (850 hPa and 200 hPa). Eventually, with the help of Bias, P_{cor} , and RMSE, the performance of CMIP6 models in simulating the existing relationship between the CE-AHT or CE-OHT and monsoon is investigated.

The seasonal cycle, trend, and mutual interaction of CE-AHT and CE-OHT are discussed in subsection 4.3.1. The I_{pr} metric, the I_{dmsf} metric, and the relationship of cross-equatorial heat transports with the Hadley circulation, ITCZ movement, precipitation, winds, and SST are given in subsection 4.3.2. The model performance based on pattern correlation in simulating the seasonal means and the relationship between the cross-equatorial heat transports and the monsoons is highlighted in subsection 4.3.3.

4.3.1 Simulated Patterns of Cross-Equatorial Heat Transport

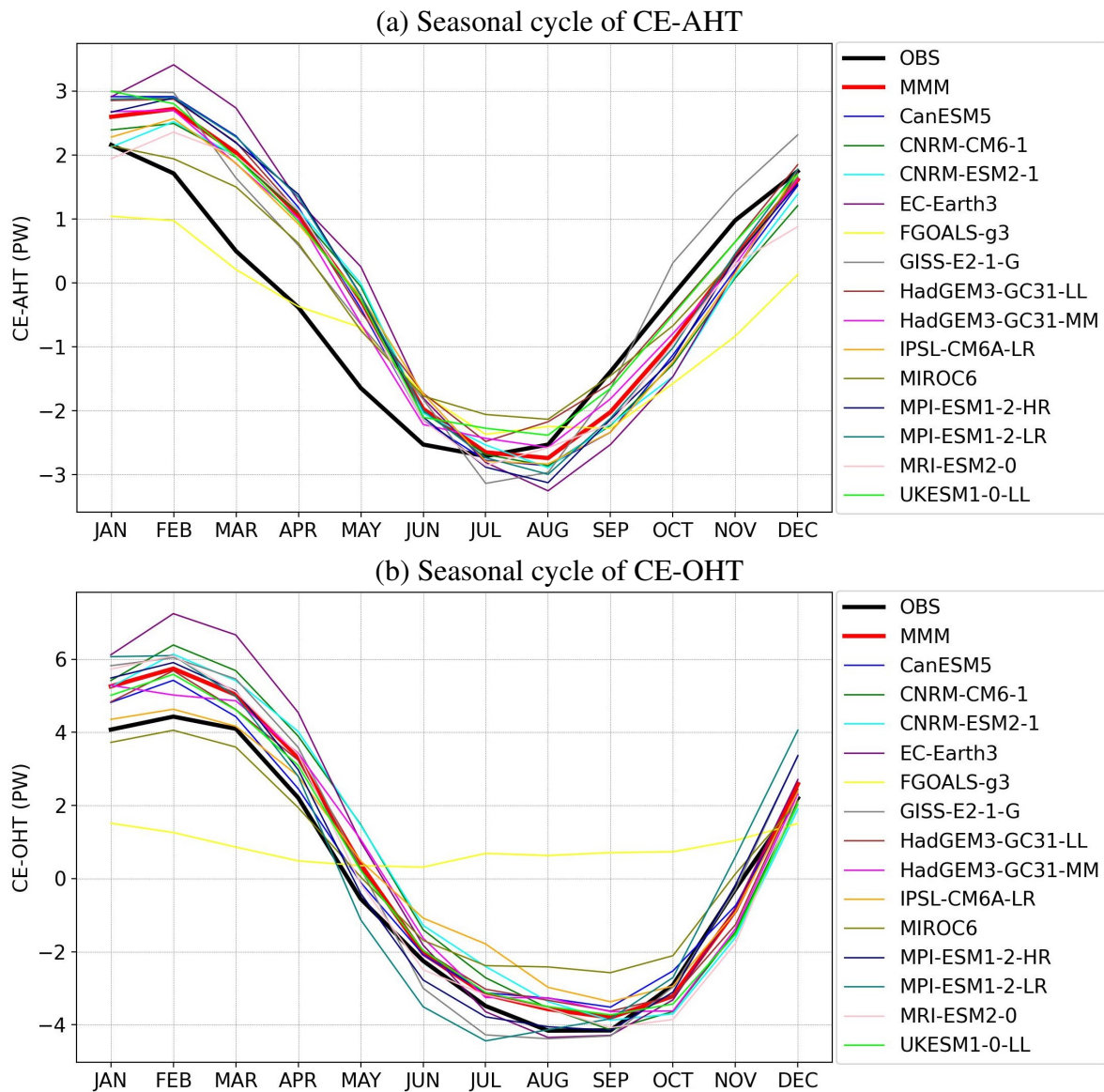


Figure 4.3: (a) The seasonal cycle of CE-AHT (PW) is displayed for the reanalysis data (black solid line) and various CMIP6 models for the period 1979–2020. (b) Same as panel ‘a’ but for CE-OHT (PW). Here, OBS denotes ERA-5 in (a) and ORAS-5 in (b), and MMM refers to the multi-model mean.

The seasonal cycles of CE-AHT and CE-OHT are illustrated in Figures 4.3a and 4.3b, respectively. The positive or northward CE-AHT indicates the export of atmospheric heat from the southern hemisphere to the northern hemisphere by the Hadley circulation in both JJA and DJF seasons, and vice versa. The CE-OHT exhibits a similar pattern, driven by oceanic circulations. In Figure 4.3a, a very few models agree with reanalysis in capturing the maximum and minimum atmospheric energy exports in January (FGOALS-g3, MIROC6, and

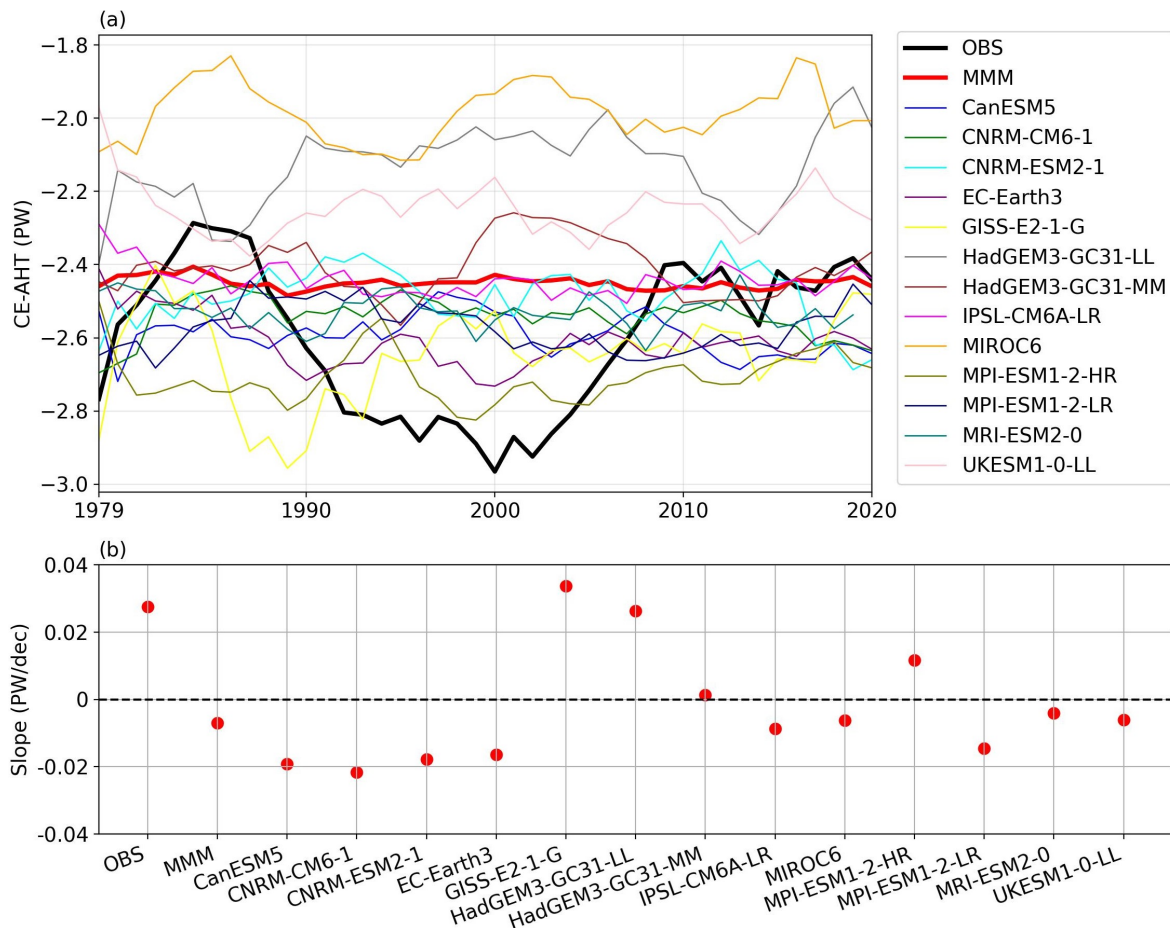


Figure 4.4: (a) The time series of the five-year running mean CE-AHT (PW) is shown for OBS (ERA-5: black solid line) and various CMIP6 models spanning 1979–2020 for the JJA season. (b) The slopes, calculated using linear regression, of the corresponding CE-AHT time series for the same period (blue dots: statistical significance at the 95% confidence level or higher; red dots: statistically insignificant at the 95% confidence level), measured in PW per decade. Negative and positive values denote southward and northward transports, respectively.

UKESM1-0-LL) and July (FGOALS-g3, GISS-E2-1-G, HadGEM3-GC31-LL, MRI-ESM2-0, and UKESM1-0-LL), respectively. In the rest of the models, the atmospheric energy peak occurs in February and the minimum in August (Figure 4.3a). On the other hand, most of the models (except FGOALS-g3 and HadGEM3-GC31-MM) have an oceanic energy peak in February, similar to reanalysis (Figure 4.3b). With the exception of the EC-Earth3 and MPI-ESM1-2-LR models (where it's in August and July, respectively), the maximum southward CE-OHT is generally found in September as the reanalysis (Figure 4.3b). Interestingly, the FGOALS-g3 exhibits a northward heat export in the seasonal cycle of CE-OHT, which is inconsistent with reanalysis and other CMIP6 models.

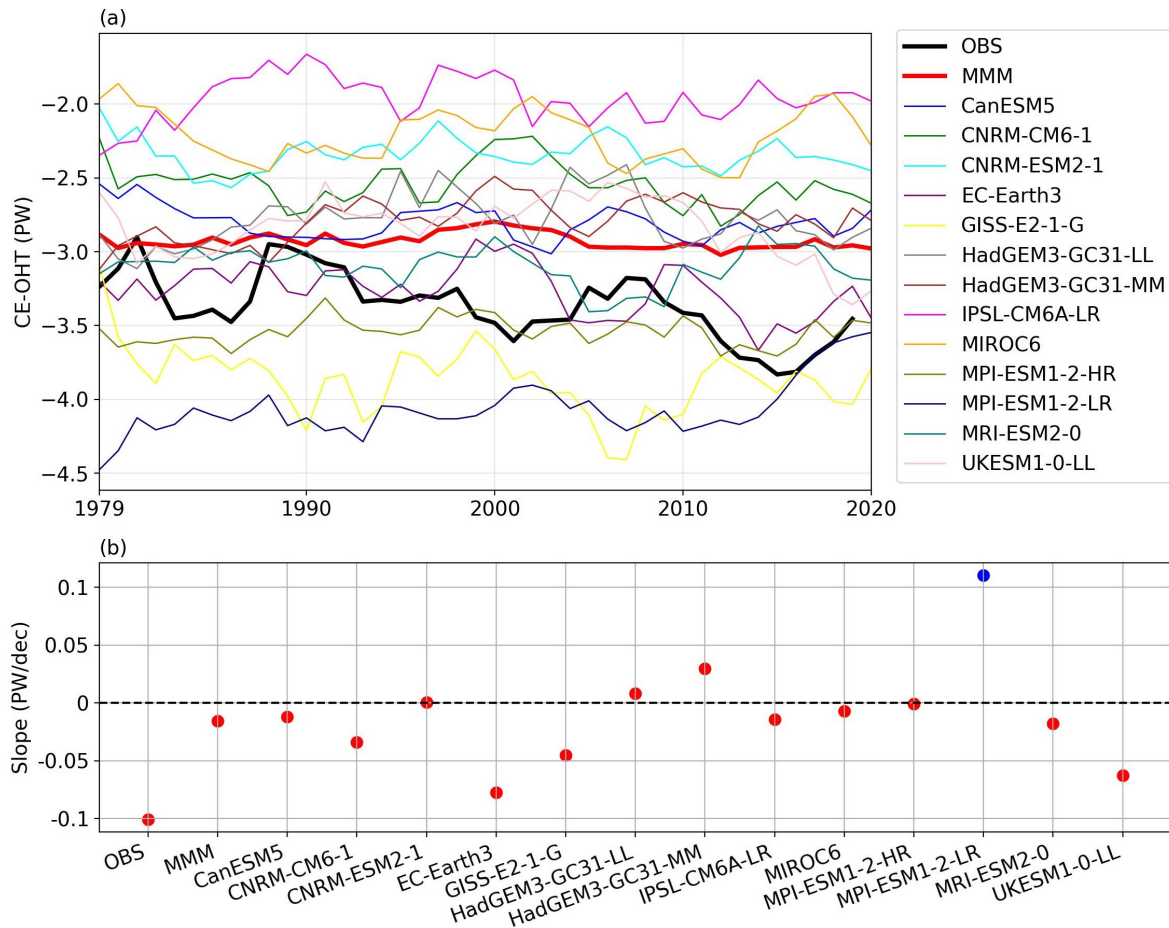


Figure 4.5: Same as in Figure 4.4 but for the CE-OHT, and OBS denotes the ORAS-5.

The discernible discrepancy of up to 1.5 PW (Feb-Jun) between reanalysis and CMIP6 models may stem from the energy imbalance at the top of the atmosphere in the CMIP6 models, as shown in Figure 4.3a (Wild, 2020). Energy imbalances exist in CMIP6 models (Wild, 2020) and may explain the inter-model discrepancies in CE-AHT and CE-OHT (Figures 4.3a and 4.3b). Additionally, according to (Donohoe et al., 2023), an abundance of surface evaporation found in the CMIP6 models is a contributing factor to the bias in AHT and OHT. Since surface evaporation controls the heat transport carried out by the atmosphere by increasing moisture, which releases energy to the atmosphere through condensation (Fajber et al., 2023).

Furthermore, the ERA-5 reanalysis itself may contribute to the discrepancy of CE-AHT arising from observational uncertainty, the background model, and the data assimilation process. Primary sources of uncertainty in the ERA-5 reanalysis include changes in the observing system over time (Hersbach et al., 2020), particularly in earlier decades when observational coverage, especially over oceans and remote regions, was sparse (Simmons et al.,

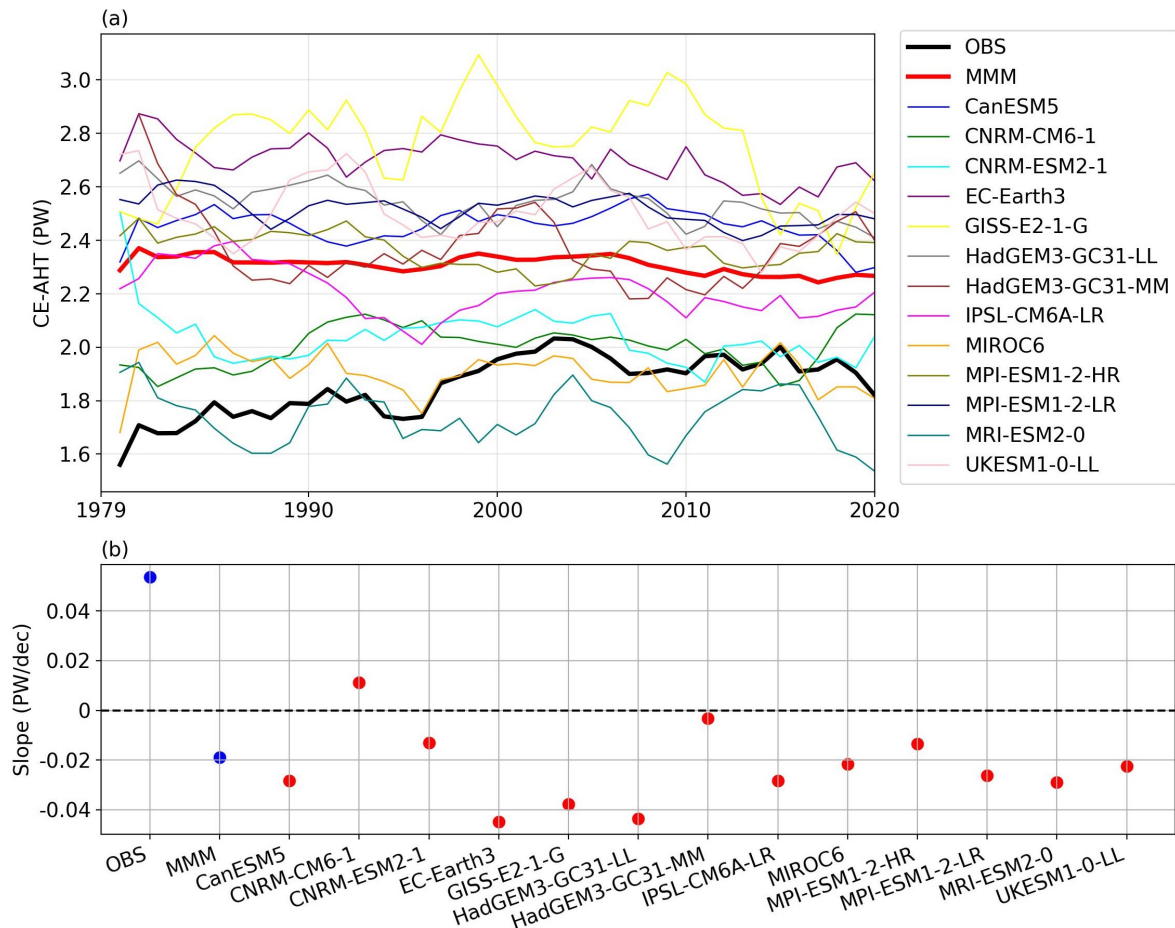


Figure 4.6: Same as Figure 4.4 but for the DJF season.

2021). ERA-5 uses the Integrated Forecasting System CY41R2 model forecast (Váňa et al., 2017), operational since 2016, and the 4D-Var data assimilation system (Rabier and Liu, 2003), which can be sensitive to observation quality and distribution (Hersbach et al., 2020).

The erratic behaviour of the CE-AHT and CE-OHT in the FGOALS-g3 model may arise from the TOA and surface energy balance (see Figures 4.3a and 4.3b). Because, the energy balance at the TOA and surface plays a crucial role in determining the Earth's climate system's overall energy budget (Zhang and Rossow, 1997). Models that emphasize the accurate representation of the energy balance at the TOA and surface are likely to provide more realistic simulations of climate variability and change. They may better capture feedback mechanisms associated with changes in surface temperature, cloud cover, and radiative forcing, which in turn can influence atmospheric and oceanic circulations and associated heat transports. In contrast to many other CMIP6 models, where the energy balance at the TOA and the surface was a priority, the FGOALS-G3 model did not consider this aspect (Li et al.,

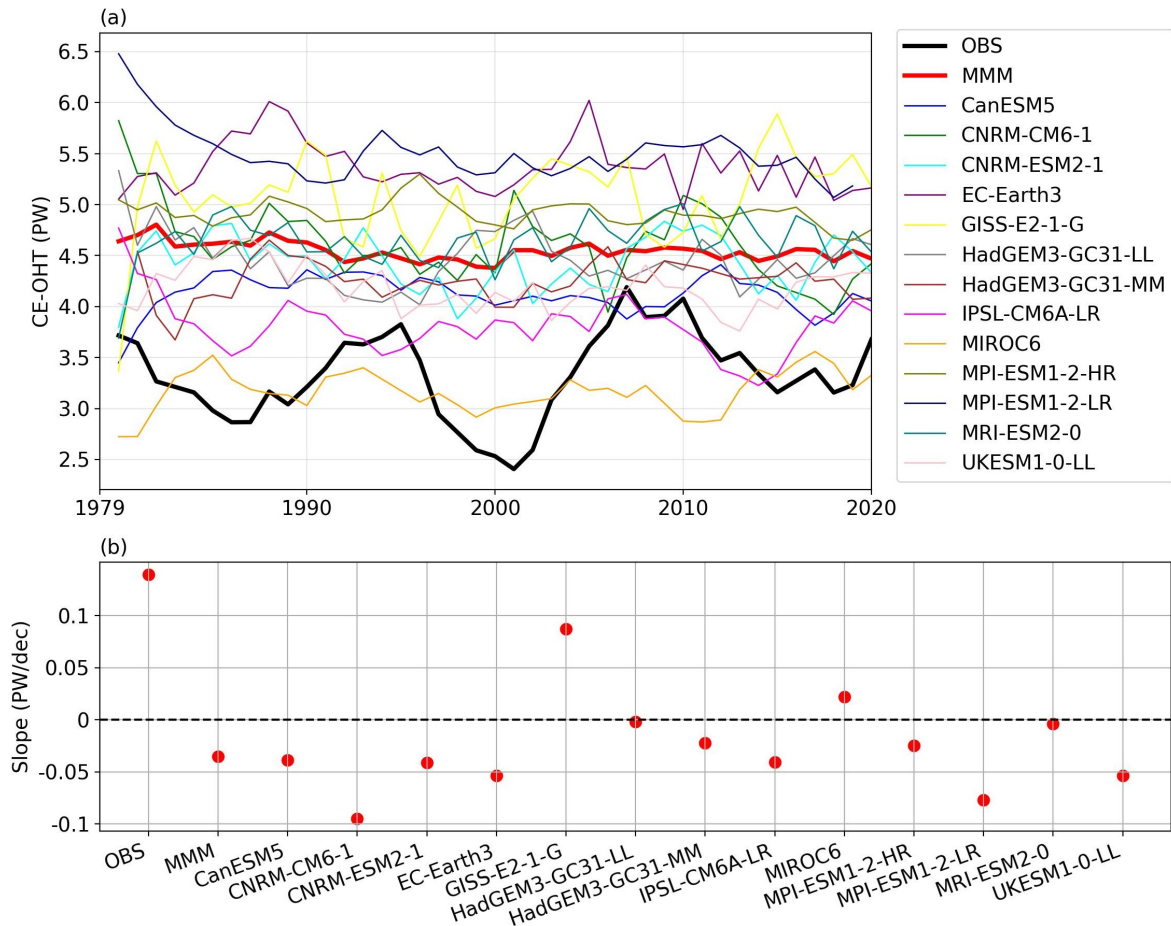


Figure 4.7: Same as Figure 4.5 but for the DJF season.

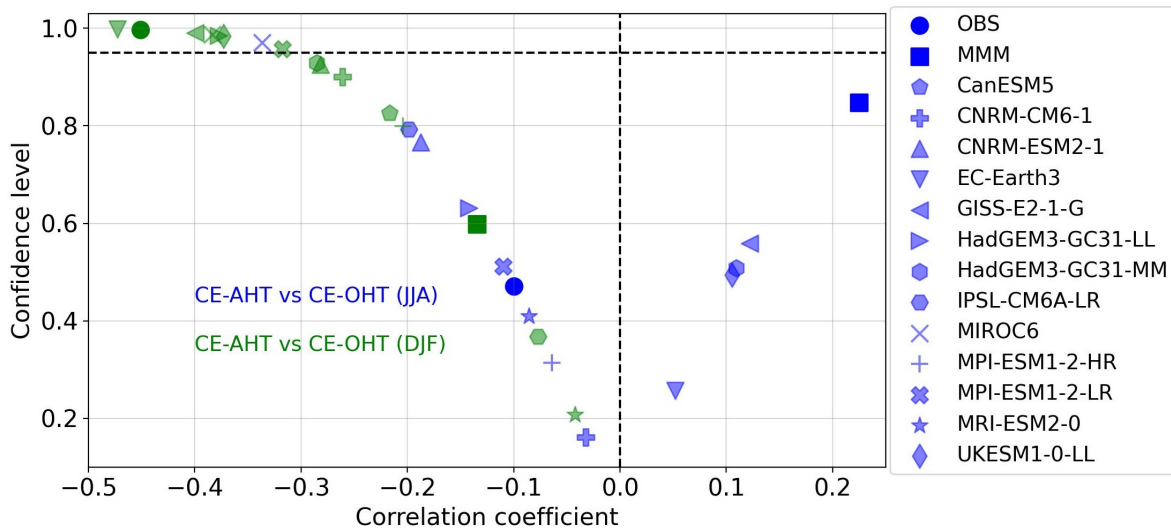


Figure 4.8: Along the horizontal axis, the inter-annual correlation coefficient between CE-AHT and CE-OHT for both the JJA season (blue markers) and DJF season (green markers) spanning the period 1979–2020 for each CMIP6 model and reanalysis data (OBS: ERA-5 and ORAS-5). The vertical axis represents the confidence level. MMM refers to the multi-model mean.

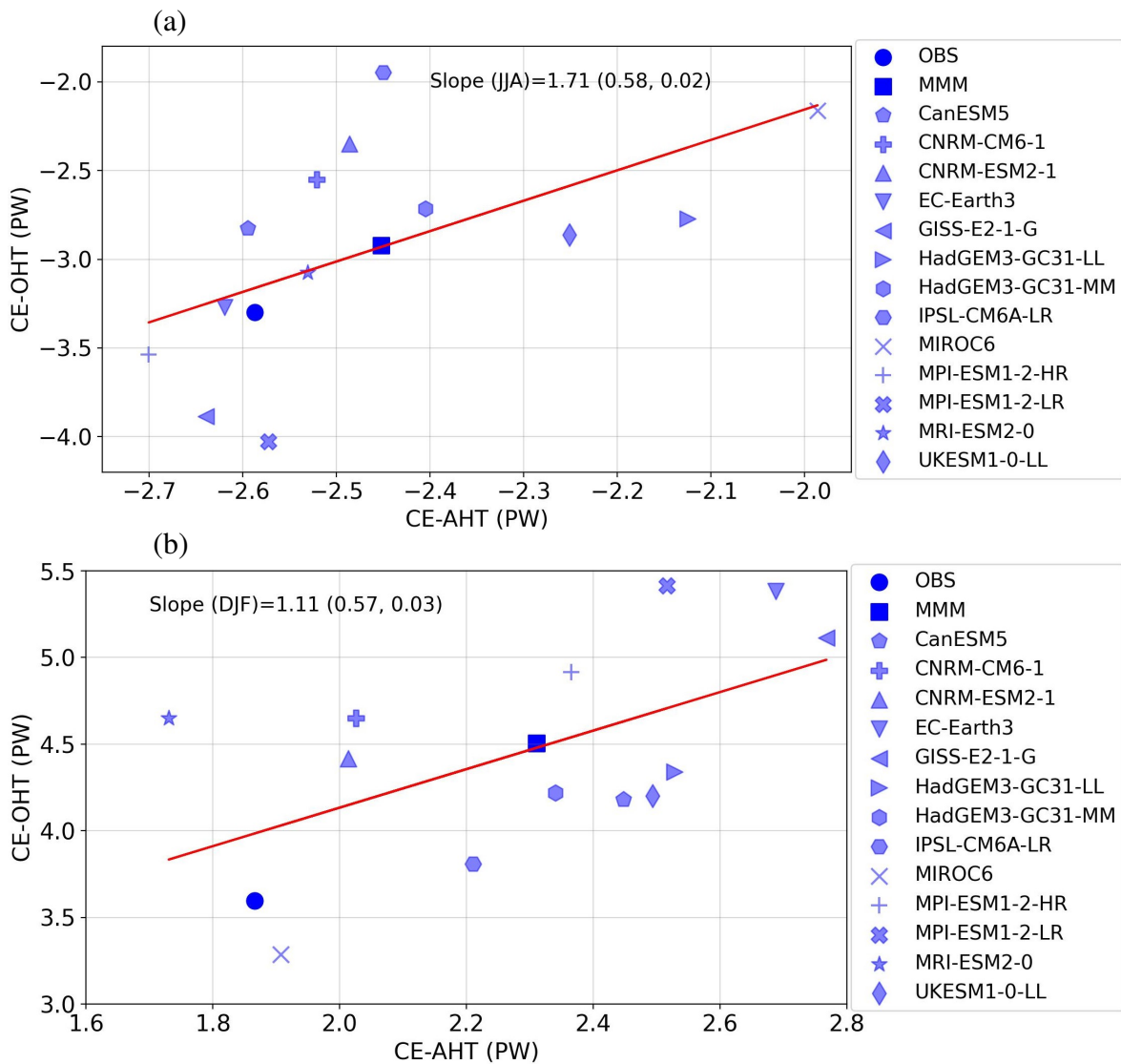


Figure 4.9: (a) The inter-model relationship between CE-AHT and CE-OHT is depicted for the long-term mean (1979–2020) during the JJA season. The correlation coefficient and the p-value from linear regression analysis on an inter-annual time scale are represented as the first and second entries between the parenthesis. (b) Same as panel ‘a’ but for the DJF season. MMM refers to the multi-model mean, and OBS denotes the reanalysis data (ERA-5 and ORAS-5).

2020). This difference may have implications for the representation of energy exchange processes between the atmosphere and the ocean, which may affect atmospheric and oceanic heat transport in the FGOALS-g3 model. Due to inconsistencies of the FGOALS-g3 model’s CE-AHT and CE-OHT with other models as well as reanalysis data, no further analysis will be conducted on this model.

Extreme southward and northward cross-equatorial heat transports occur in the JJA and DJF seasons in reanalysis (from Chapter 3), respectively, in both the atmosphere and the

ocean. To evaluate long-term trends and inter-annual changes in cross-equatorial heat transports for the JJA and DJF seasons in CMIP6, time series analysis is conducted.

As shown in Figure 4.4a, the CE-AHT values exhibit a southward heat export pattern in both reanalysis and CMIP6 climate models during the JJA season. This pattern is attributed to the dominant anticlockwise rotation of the cross-equatorial winter Hadley cell when observed from the east, which leads to the export of mass and heat towards the southern hemisphere. Small fluctuations in the time series may arise from inter-annual variability, whereas larger fluctuations may be attributed to decadal variability.

The trends of the CE-AHT in JJA are displayed in Figure 4.4b for the period 1979–2020. In reanalysis, the slope is positive, approximately 0.03 PW/dec, and statistically insignificant. However, all the CMIP6 models have a slope that is statistically indistinguishable from zero. A few models show a positive slope, aligning with the observed trend in ERA-5. The positive slope of CE-AHT in JJA season indicates weaker seasonal heat transport by the Hadley circulation towards the southern hemisphere, and vice versa.

Just as the CE-AHT showcases southward directed heat transport, the CE-OHT also follows suit in reanalysis and CMIP6 models, for the JJA season (Figure 4.5a). Most of the models are able to capture the trend of ERA-5. But only one models has a significant slope, indicating that others are not different from zero (Figure 4.5b). The negative trend describes that cross-equatorial southward oceanic heat transports are increasing from year to year, whereas the positive trend indicates a decrease in southward transport and an increase in northward transport.

In clear opposition to CE-AHT's and CE-OHT's southward exports during the JJA season, both the CE-AHT and CE-OHT, in reanalysis and CMIP6 climate models, reveal a prevailing northward flow of energy in the DJF season (Figures 4.6a and 4.7a). In DJF, most of the models fail to capture the trend of ERA-5 and ORAS-5. Figure 4.6b shows the trends of CE-AHT for the 1979–2020 period, where only the MMM model displays a statistically significant negative trend. Interestingly, the CE-OHT exhibits a statistically insignificant trend across all CMIP6 models and reanalysis for the DJF season (Figure 4.7b).

In the context of the coupled behaviour of the atmosphere and ocean, changes in oceanic heat transport can be offset by changes in atmospheric heat transport, and vice versa. For example, if there is an increase in oceanic heat transport due to changes in ocean currents, it may lead to adjustments in atmospheric circulation patterns to balance the overall heat budget of the Earth's climate system. This compensation mechanism, known as Bjerknes compensation (Bjerknes, 1964), helps maintain equilibrium in the distribution of heat energy between the atmosphere and the ocean. In JJA season, only the MIROC6 model exhibits a relatively strong and significant Bjerknes compensation aligning with the reanalysis on an inter-annual time scale (Figure 4.8). Insignificant compensation in JJA season is noticed in the CNRM-ESM2-1, HadGEM3-GC31-LL, IPSL-CM6A-LR, MPI-ESM1-2-LR, MRI-ESM2-0, and UKESM1-0-LL (Figure 4.8). On the other hand, they all have the correct (negative) sign, but only a few are significant in DJF season (Figure 4.8).

The long-term mean inter-model relationship between CE-AHT and CE-OHT is illustrated in Figure 4.9a and Figure 4.9b for the JJA and DJF seasons, respectively. A model with larger CE-AHT has larger CE-OHT, that is, 1 PW CE-AHT changes are compensated by 1.7 PW and 1.1 PW CE-OHT for the time averaged JJA season (Figure 4.9a) and DJF season (Figure 4.9b), respectively. The long-term mean positive correlation coefficient is strong and statistically significant for the DJF season, whereas it is weak and significant for the JJA season. On long-term time scales, it can be viewed as the weak associations among the models during the JJA season and stronger associations for the DJF seasons due to their design, parameterizations, or resolution, likely due to differences in their design, parameterizations, or resolution.

Altogether, the maximum northward and southward cross-equatorial heat exports occur in DJF and JJA in the atmosphere and ocean in CMIP6, respectively, implying that the models are correctly simulating seasonality. In almost all the CMIP6 models, the trends of CE-AHT and CE-OHT are statistically insignificant, and they fail to capture them. On the inter-annual time scale, the Bjerknes compensation prevails significantly only in a few models. 1 PW CE-AHT changes are compensated by 1.7 PW and 1.1 PW CE-OHT in the JJA

and DJF seasons, respectively.

4.3.2 Linking heat transports with the monsoons in CMIP6

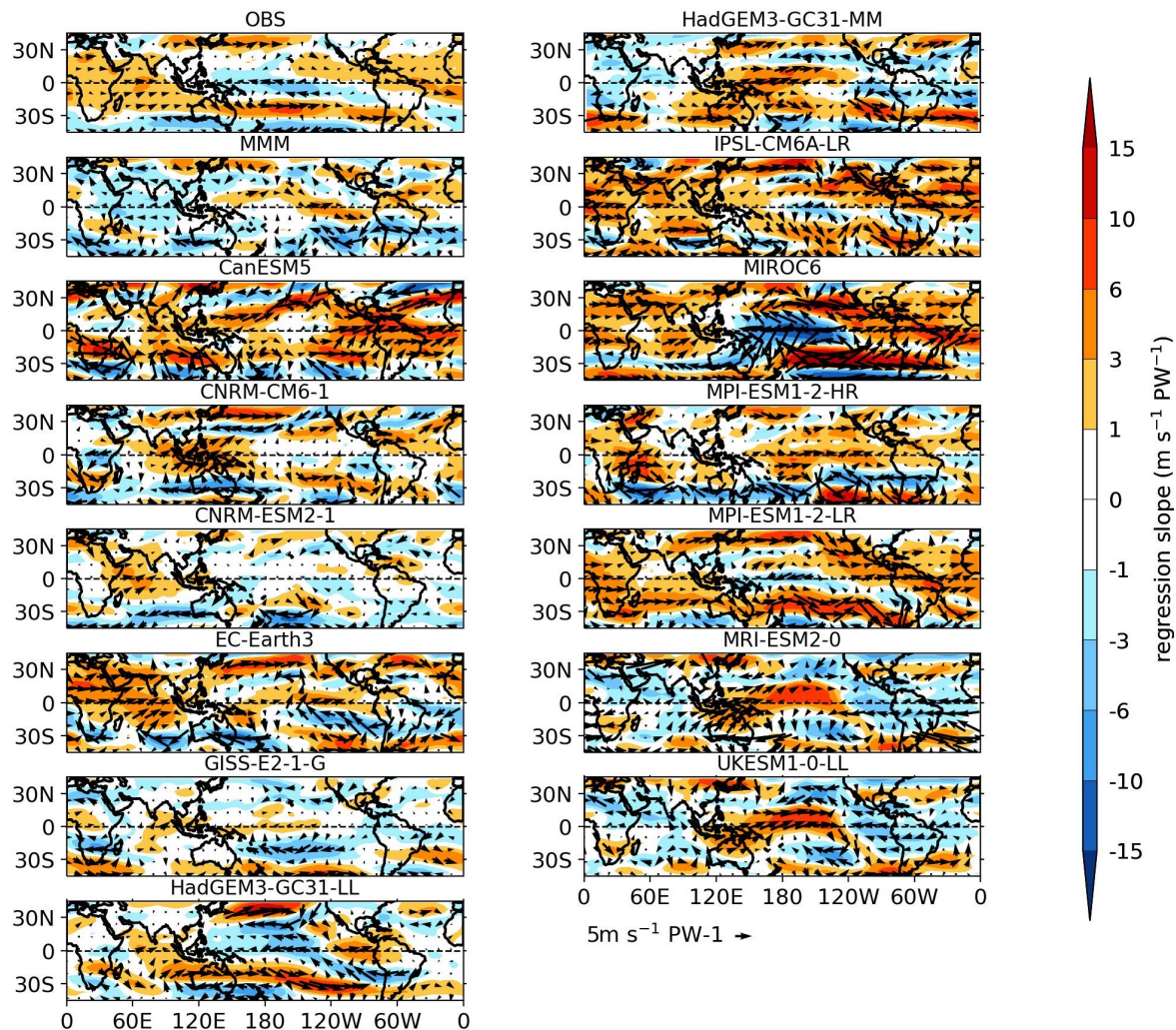


Figure 4.10: The inter-annual regression slope ($\text{ms}^{-1} \text{PW}^{-1}$) of upper-tropospheric (200 hPa) winds onto CE-AHT is displayed in vectors for the JJA season for the period 1979–2020. The colour shading shows the inter-annual regression slope of 200-hPa zonal winds onto CE-AHT for the same period. OBS denotes ERA-5 reanalysis, and MMM refers to the multi-model mean.

In Chapter 3, the analysis focused on the influence of the CE-AHT and CE-OHT on the stream function representing the Hadley circulation, with particular emphasis on the solstitial seasons (DJF and JJA) within the reanalysis data. In order to understand the influence of cross-equatorial heat transport on the stream function, a sensitivity analysis was conducted. This analysis was designed to quantify how the inter-annual variability of the stream function is affected by cross-equatorial heat transport. Therefore, a metric was employed that

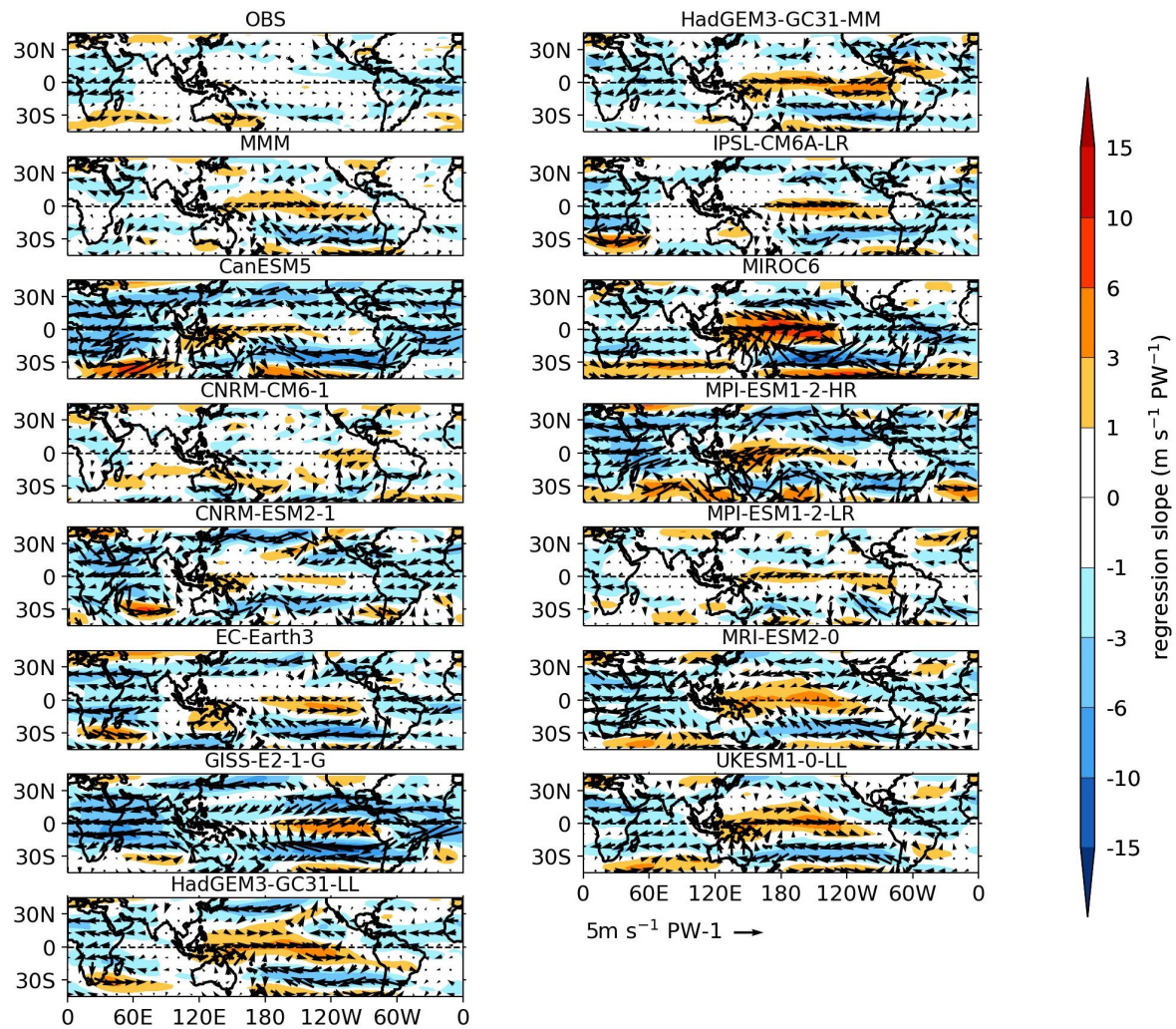


Figure 4.11: Same as in Figure 4.10 but for the CE-OHT.

incorporated both the mean stream function and five times the regression slope of the stream function onto CE-AHT or CE-OHT. This approach enabled us to discern the effects associated with anomalies in both the northward (mean + five times slope) and southward (mean – five times slope) directions. Furthermore, investigation extends beyond reanalysis data to encompass CMIP6 climate models. Within this context, likewise, regression analyses of the stream function on CE-AHT and CE-OHT were conducted with the goal of elucidating the intricate relationship between cross-equatorial heat transport and the monsoon dynamics within the CMIP6 framework. This research not only advances our understanding of the Earth’s tropical climate system but also offers valuable insights into the potential implications of these interactions on future climate scenarios and variability.

Upper tropospheric winds (200 hPa) drive large-scale atmospheric circulation patterns

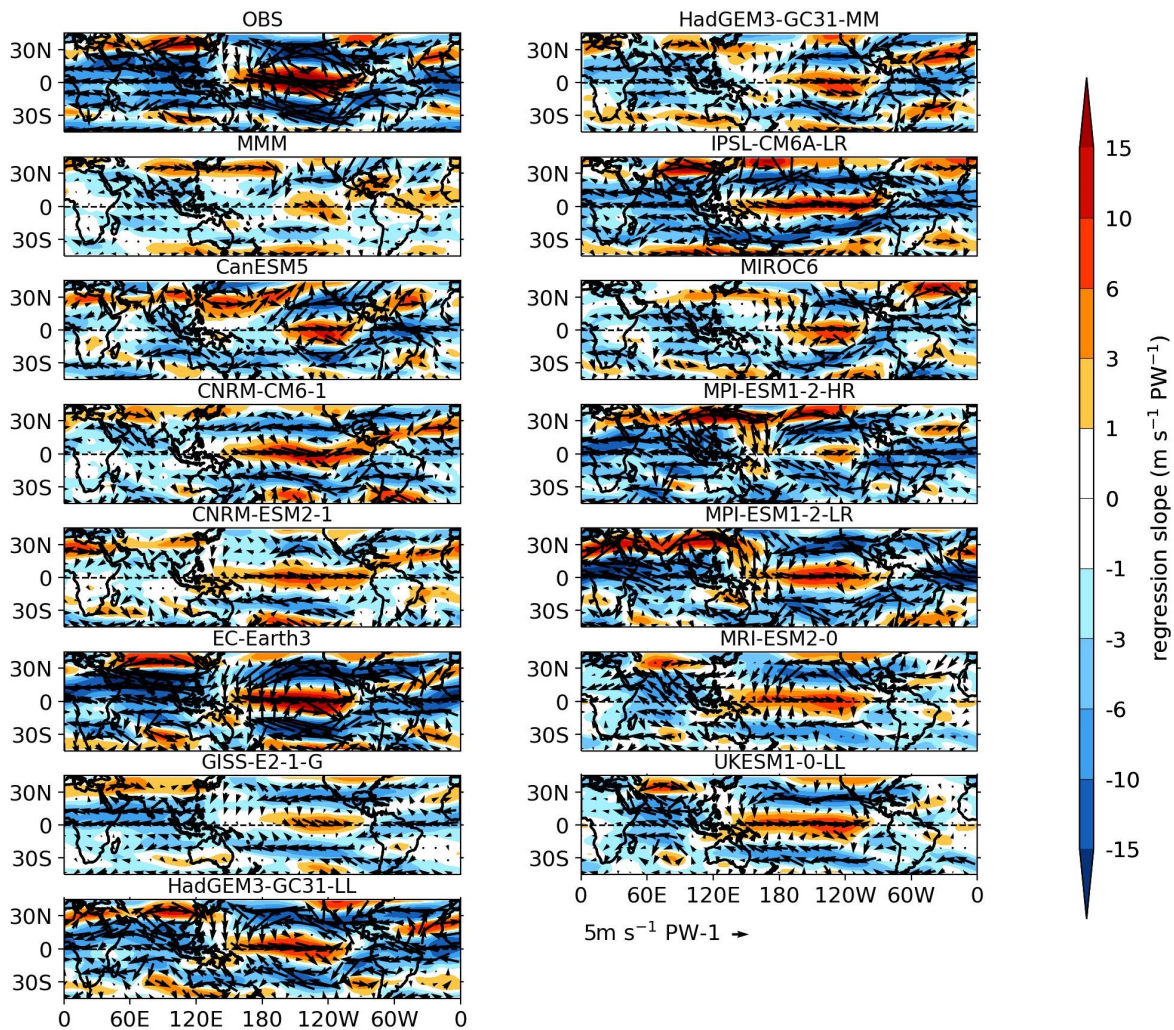


Figure 4.12: Same as Figure 4.10 but for the DJF season.

and influence surface weather conditions by transporting heat and shaping weather systems. Regression analysis of these winds onto cross-equatorial heat transport anomalies in CMIP6 models would help to assess their impact on atmospheric dynamics and climate variability.

Figure 4.10 illustrates the impact of upper tropospheric winds (200 hPa) during northward CE-AHT anomalies in JJA season across CMIP6 models. The STJs migrate towards the equator in a few models, as in reanalysis, implying El Niño-like conditions over the Pacific Ocean (Manney et al., 2021). A few models exhibit anomalous convergence over the Maritime Continent, indicating a weaker Walker-like circulation, similar to reanalysis. Additionally, the westerly wind anomaly weakens the TEJs (Koteswaram, 1958), which is closely linked to the ENSO and Indian monsoon (Pattanaik and Satyan, 2000) through Hadley circulation (Dima and Wallace, 2003). The intensity of the Walker and Hadley circulations is strongly associated with the ENSO phenomenon (Oort and Yienger, 1996; Nguyen et al.,

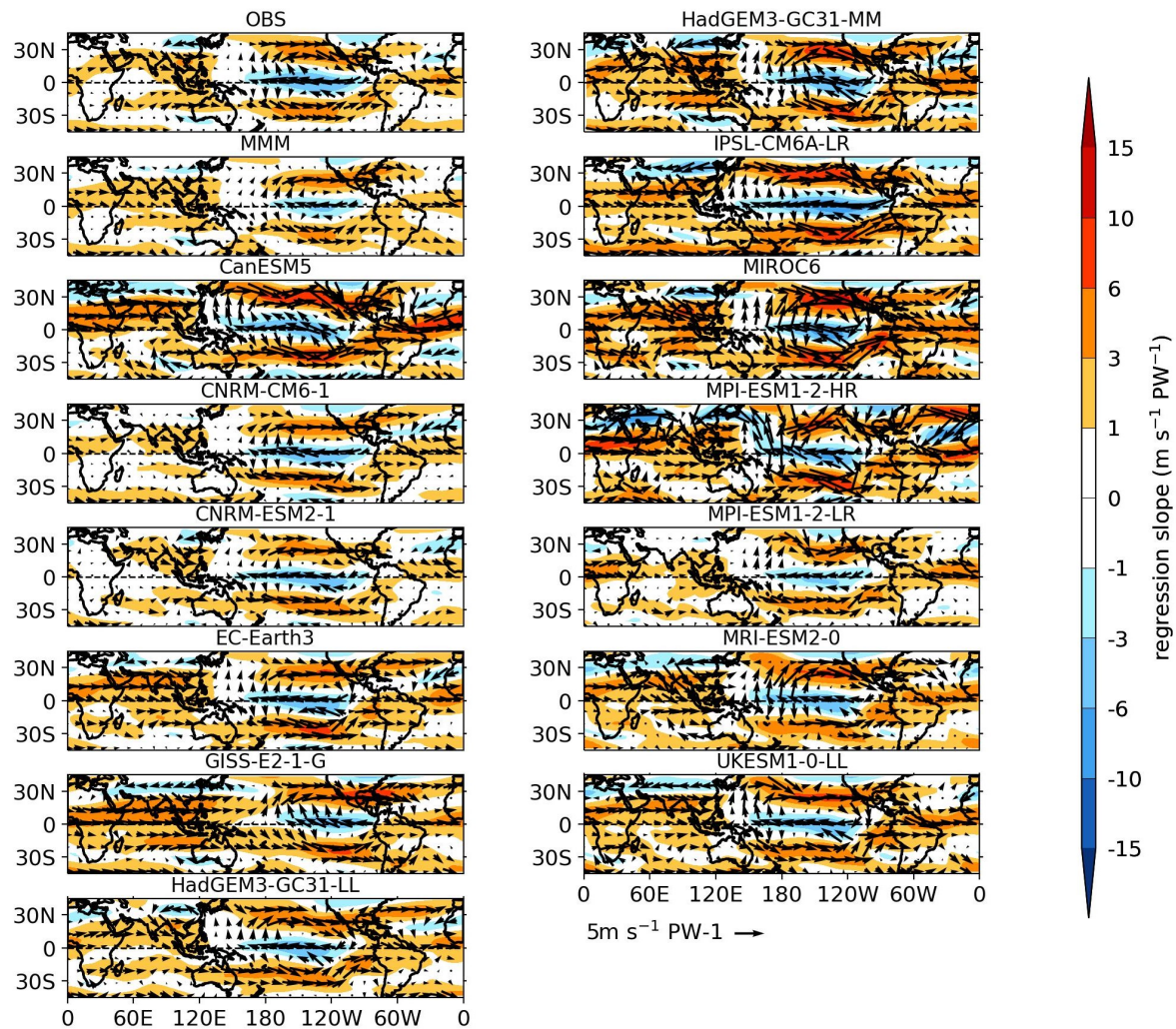


Figure 4.13: Same as Figure 4.11 except for the DJF season.

2013; Quan et al., 2004).

Conversely, the increase of CE-OHT pushes the STJs poleward in most of the models, as consistent with the reanalysis, which denotes La Niña-like conditions in the equatorial Pacific Ocean (Manney et al., 2021). An anomalous divergence occurs over the Maritime Continent during northward CE-OHT anomalies in most models, indicating a strong Walker-like circulation. It has been found that strong TEJ-like and La Nina-like phenomena are connected with strong Indian monsoons (Abish et al., 2013; Athira et al., 2023).

For northward CE-AHT anomalies in the DJF season, Figure 4.12, consistent with the reanalysis, illustrates a poleward shift of the STJs and an anomalous divergence over the Maritime Continent and western Pacific Ocean in most of the CMIP6 models, indicating a strong Walker-like circulation over the Pacific Ocean. On the contrary, the positive CE-OHT anomalies in DJF season cause an upper-level anomalous convergence over the Maritime

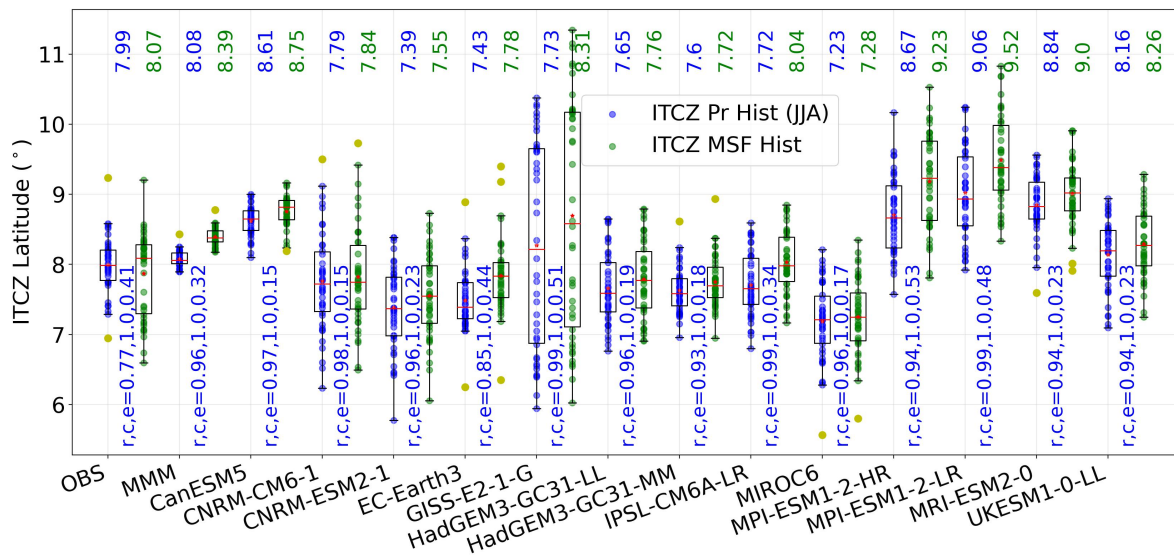


Figure 4.14: The latitudinal position of the ITCZ using zonal mean precipitation (I_{pr} : blue colour) and mid-tropospheric stream function (I_{dmsf} : green colour) is shown for the JJA season in CMIP6 model data and observational data for the period 1979–2020. The whiskers indicate the range of the data, excluding outliers. The lower and upper edges of the box represent the first quartile (Q1) and the third quartile (Q3), respectively. The median is shown as a red line, and the mean is shown as a red star. Outliers are denoted by yellow points. At the bottom, r , c , and e refer to the inter-annual correlation coefficient, confidence level, and RMSE error, respectively, between I_{pr} and I_{dmsf} . For JJA mean, the latitudes of the ITCZ by I_{pr} and I_{dmsf} are given by the top blue and green numbers, respectively. MMM refers to the multi-model mean.

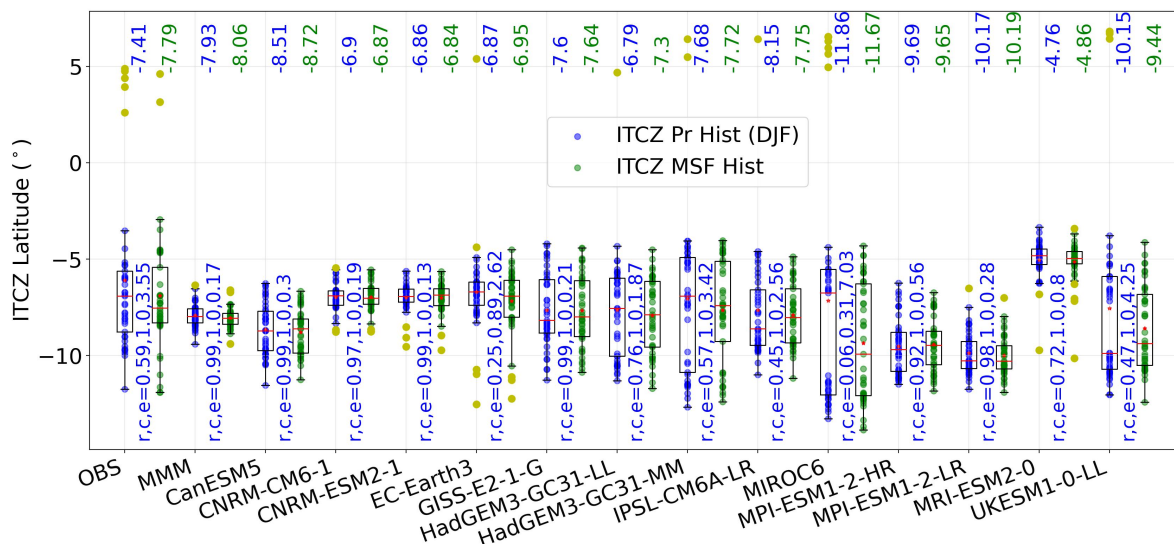


Figure 4.15: Same as Figure 4.14 except for the DJF season.

Continent (Figure 4.13) and equatorward movement of the STJs, which indicates a weakened Walker-like circulation. A strong Walker circulation strengthens the Australian monsoon, whereas the opposite occurs for a weak Walker circulation (Power et al., 2006; Cai et al., 2010; King et al., 2015).

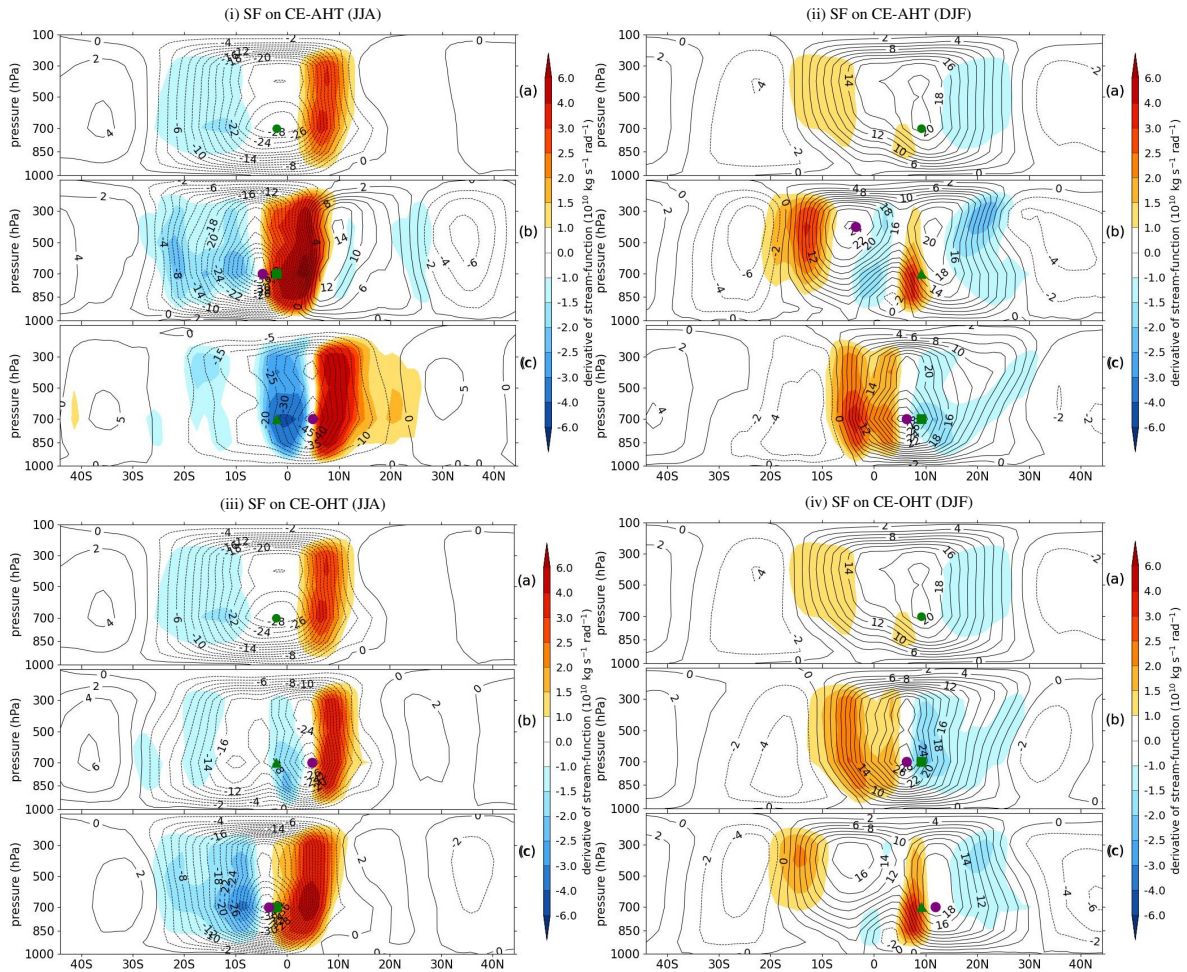


Figure 4.16: (i) The stream function regressed onto CE-AHT is displayed using the MIROC6 CMIP6 model for the JJA season on an inter-annual time scale spanning 1979–2020. (a) The time-averaged stream function for the JJA season is depicted by the black curves. (b) The stream function for positive CE-AHT anomalies (the mean JJA stream function plus five times the regression slope of the stream function onto CE-AHT on an inter-annual time scale) is represented by black curves. (c) The stream function for negative CE-AHT anomalies (mean JJA stream function minus five times the regression slope of the stream function onto CE-AHT on an inter-annual time scale) is shown by black curves. In (a), (b), and (c), the black dashed curves denote anticlockwise rotation, and the solid black curves denote clockwise rotation (from east). The core position, where the absolute value of mass flux peaks, is shown by the green marker for the climatological HC and the purple marker for the regressed HC. The meridional derivative of the stream function, representing the vertical mass flux, is shown in colour shading. The units of the stream function and its meridional derivative are $10^{10} \text{ kg s}^{-1}$ and $10^{10} \text{ kg s}^{-1} \text{ rad}^{-1}$, respectively. (ii) Same as (i), but for the DJF season. (iii) Same as (i), but for CE-OHT. (iv) Same as (ii), but for CE-OHT.

In essence, the increase of CE-AHT and CE-OHT in the JJA season dislocates the STJs equatorward and poleward, respectively. Moreover, northward CE-AHT and CE-OHT anomalies in the JJA season yield weaker and stronger Walker-like circulations, respectively. Conversely, during the DJF season, the opposite of JJA occurs for both CE-AHT and CE-OHT.

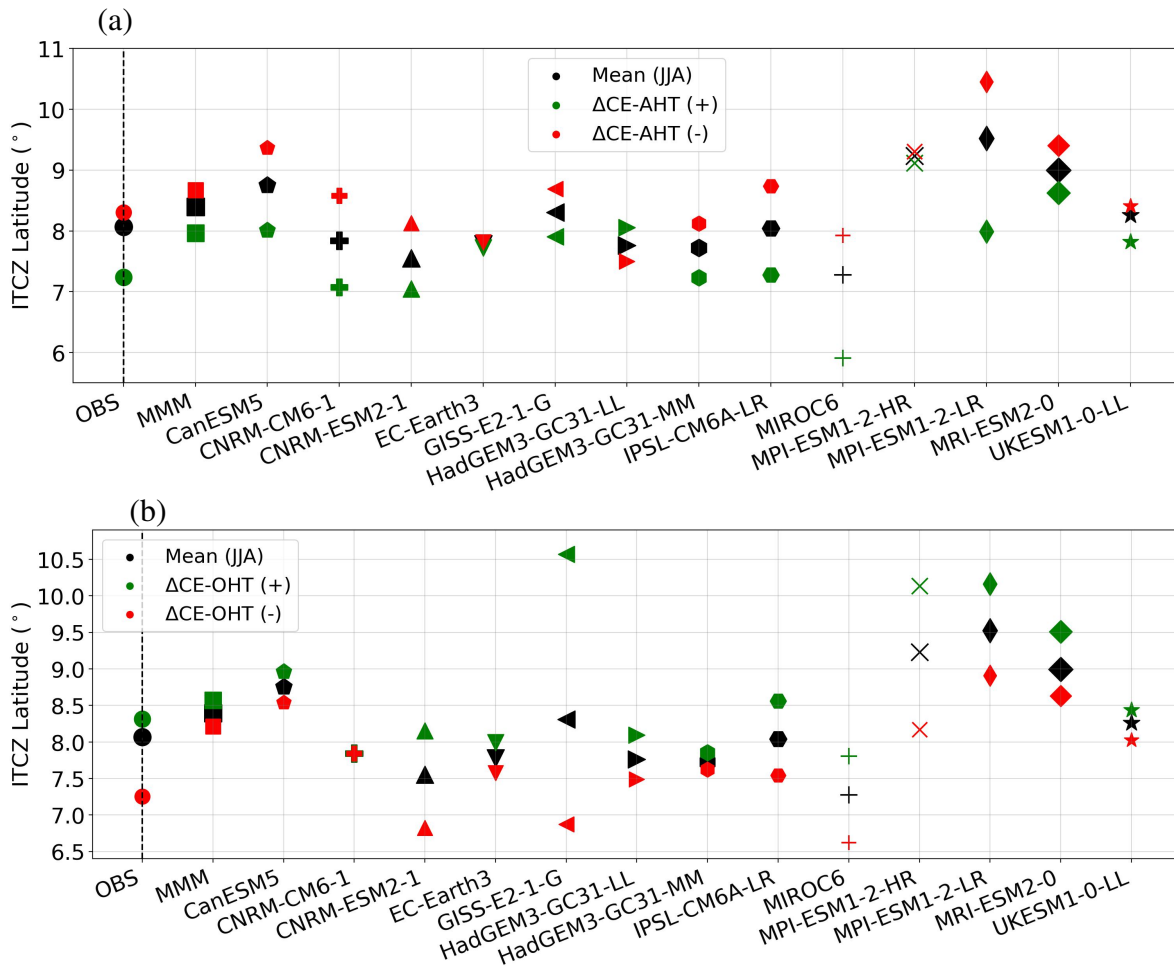


Figure 4.17: (a) The mean latitudinal position of the HC rising branch is depicted for the JJA season using CMIP6 models and reanalysis data for both the climatological mean and regressed stream function onto CE-AHT on an inter-annual time scale, from 1979 to 2020. Markers denote the position of the rising branch for the climatological mean (black), positive CE-AHT anomalies (red), and negative CE-AHT anomalies (blue). MMM refers to the multi-model mean. (b) Same as panel ‘a’ but for the CE-OHT.

Before conducting analysis on lower tropospheric winds, it would be insightful to find the link between ITCZ movement and cross-equatorial transports. So, prior to utilizing the stream-function-associated ITCZ metric to estimate the latitudinal location of the ITCZ, I need to verify its reliability across all CMIP6 models. Apart from that, it is also crucial to find out how the CMIP6 models perform to identify the position of the ITCZ from the zonal mean perspective using both the I_{pr} and I_{dmsf} metrics.

For the JJA season, the ITCZ location is displayed in Figure 4.14, showing that the ITCZ is located in the northern hemisphere across all CMIP6 models, and that is aligned with the observation (Quan et al., 2004; Hoskins et al., 2020; Feng et al., 2018). The I_{dmsf} performs

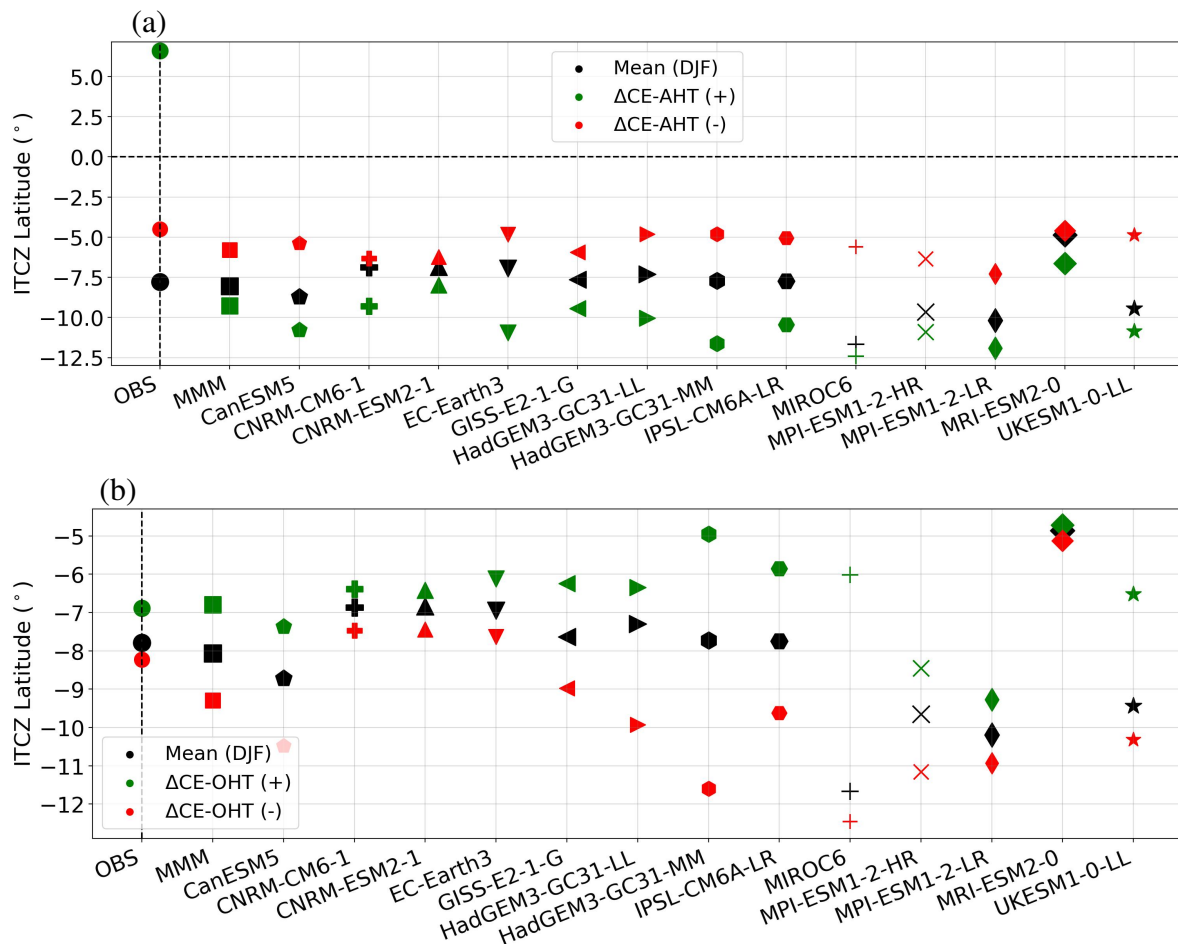


Figure 4.18: Same as Figure 4.17 except for the DJF season

well in locating the ITCZ, as identified by I_{pr} , on both time-averaged and inter-annual time scales. The I_{pr} and I_{dmsf} exhibit a strong correlation ($P\text{-value} \leq 0.001$; Figure 4.14), and the RMSE of the ITCZ position identified by the I_{pr} and I_{dmsf} metrics ranges from 0.15° to 0.53° across all CMIP6 models. However, the I_{dmsf} has a poleward tendency for the ITCZ position in comparison to the I_{pr} in JJA season (Figure 4.14). The long-term mean positions of the ITCZ by I_{pr} and I_{dmsf} in observation (MMM) are 7.99°N (8.08°N) and 8.07°N (8.39°N), respectively (Figure 4.14). Half of the CMIP6 models locate the ITCZ to the north of the observational position and the other half to the south (Figure 4.14).

Figure 4.15 illustrates the ITCZ position to the south of the equator across all CMIP6 models, and it is consistent with the reanalysis. For the DJF season, except for EC-Earth3 and MIROC6, all other models display a strong and statistically significant ($P\text{-value} \leq 0.04$) relationship between the I_{pr} and I_{dmsf} metrics (Figure 4.15). However, the RMSE is comparatively larger in the DJF season than the JJA season, which may arise from the variability of

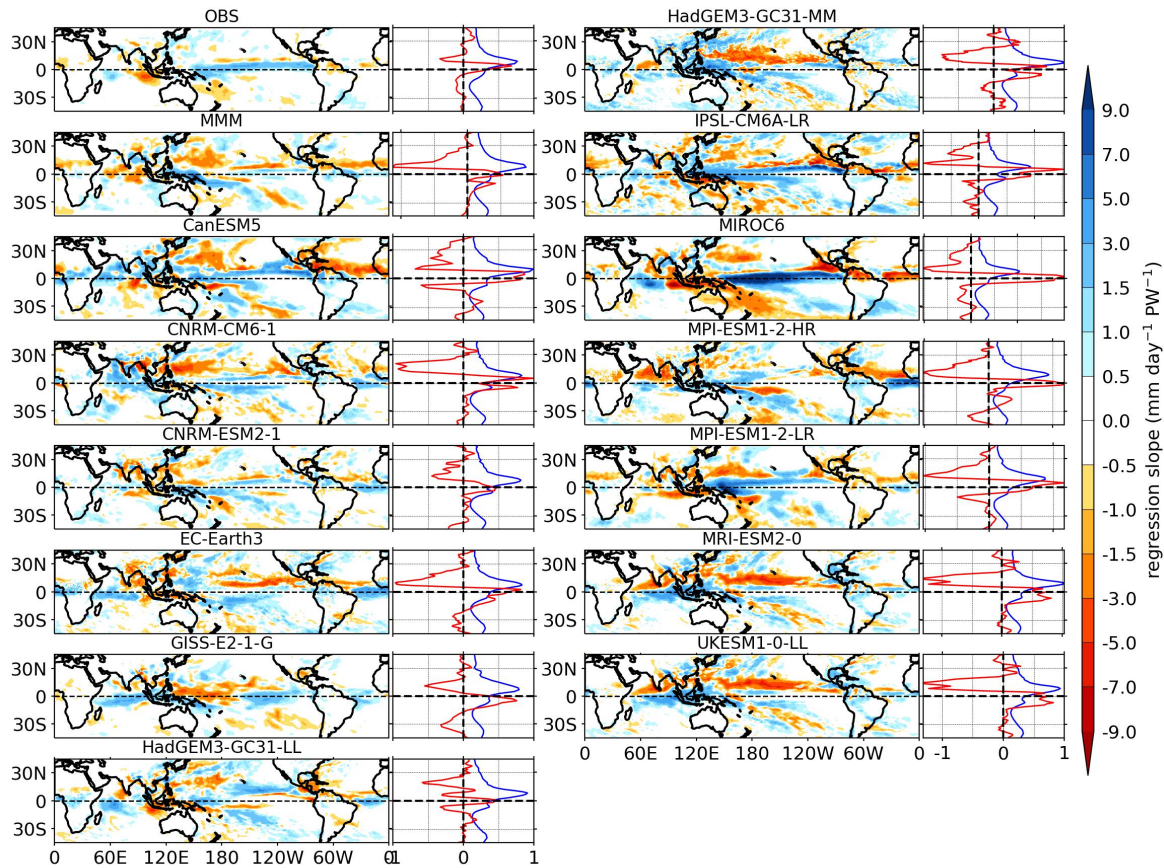


Figure 4.19: The left panel of each model is the inter-annual precipitation regression onto CE-AHT during JJA on an inter-annual time scale for the period 1979–2020 (colour shading in $\text{mm day}^{-1} \text{PW}^{-1}$). The right panel is the zonal mean of climatological precipitation (blue; scaled down by 10; mm day^{-1}) and the regressed precipitation slope onto CE-AHT (red; $\text{mm day}^{-1} \text{PW}^{-1}$) for the JJA season. MMM refers to the multi-model mean.

the Hadley circulation in the DJF season (Huang et al., 2018). In half of the CMIP6 models, the I_{dmsf} displays a northward tendency for the ITCZ position compared to the I_{pr} in the DJF season. In the long-term mean, the I_{pr} and I_{dmsf} metrics estimate the ITCZ positions in observation (MMM) at 7.41°S (7.93°S) and 7.79°S (8.06°S), respectively (Figure 4.15). The majority of the CMIP6 models tend to place the ITCZ south of the observed position (Figure 4.15).

In the earlier chapter (Chapter 3), the movement of the ITCZ with CE-AHT and CE-OHT anomalies during JJA and DJF seasons was studied using I_{dmsf} on an inter-annual time scale in reanalysis data. The I_{dmsf} metric, in comparison to I_{pr} , effectively identifies the ITCZ location across all CMIP6 models, as demonstrated in Figure 4.14 and Figure 4.15. Further

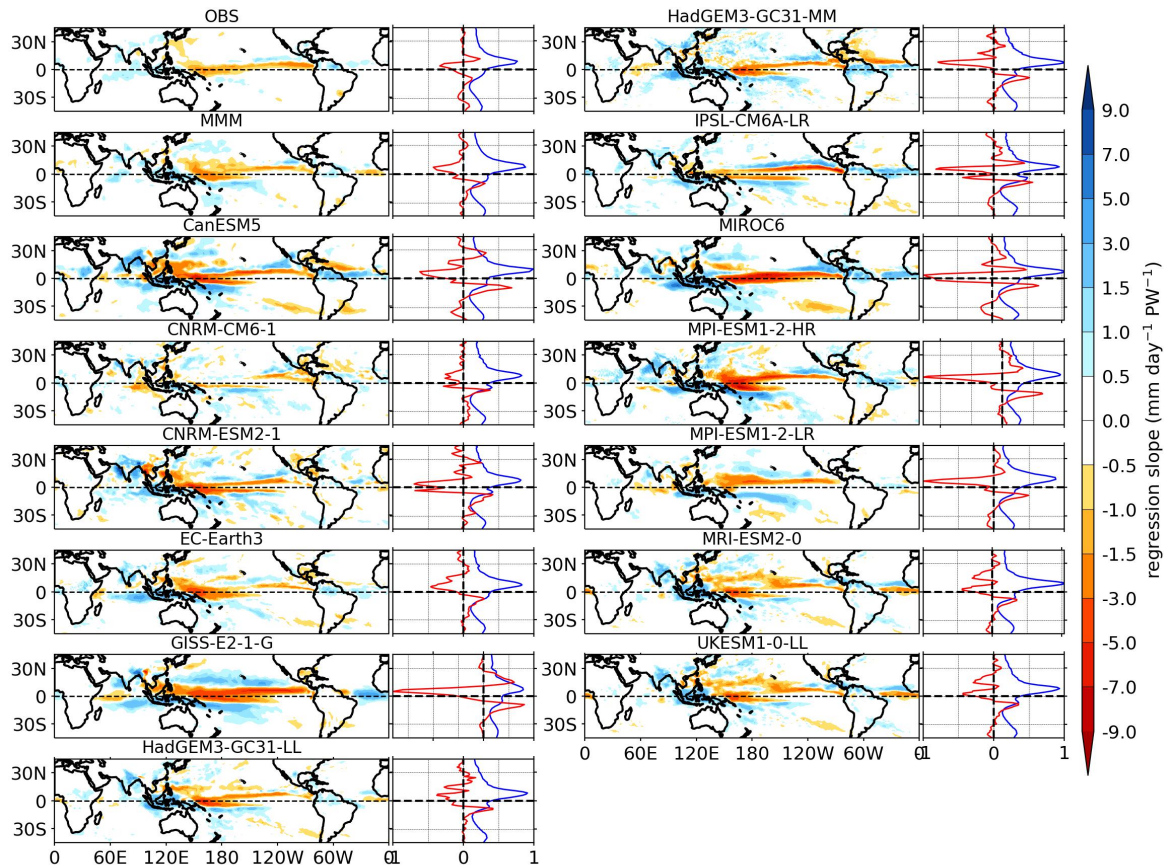


Figure 4.20: Same as in Figure 4.19 but for the CE-OHT.

investigation into the behaviour of the ITCZ movement from the stream-function responses to CE-AHT and CE-OHT across all CMIP6 models would provide valuable insights. Given the consistent behaviour across all CMIP6 models on an inter-annual time scale, we present stream-function responses to changes in CE-AHT and CE-OHT during the JJA and DJF seasons only for the MIROC6 model (Figure 4.16).

In the JJA season, the historical rising and subsiding branches lie to the north and south of the equator across all the CMIP6 models (for example, Figure 4.16(i)a), respectively, consistent with reanalysis (Seo et al., 2023; Quan et al., 2004; Hoskins et al., 2020; Feng et al., 2018). In all CMIP6 models for the JJA season, the rising branch of the Hadley cell undergoes a shift towards the Equator in response to northward CE-AHT anomalies (for example, Figure 4.16(i)b), while the shift occurs in the opposite direction for southward anomalies (for example, Figure 4.16(i)c). However, the displacement of the core occurs to the south and north of its climatological position for northward and southward CE-AHT anomalies,

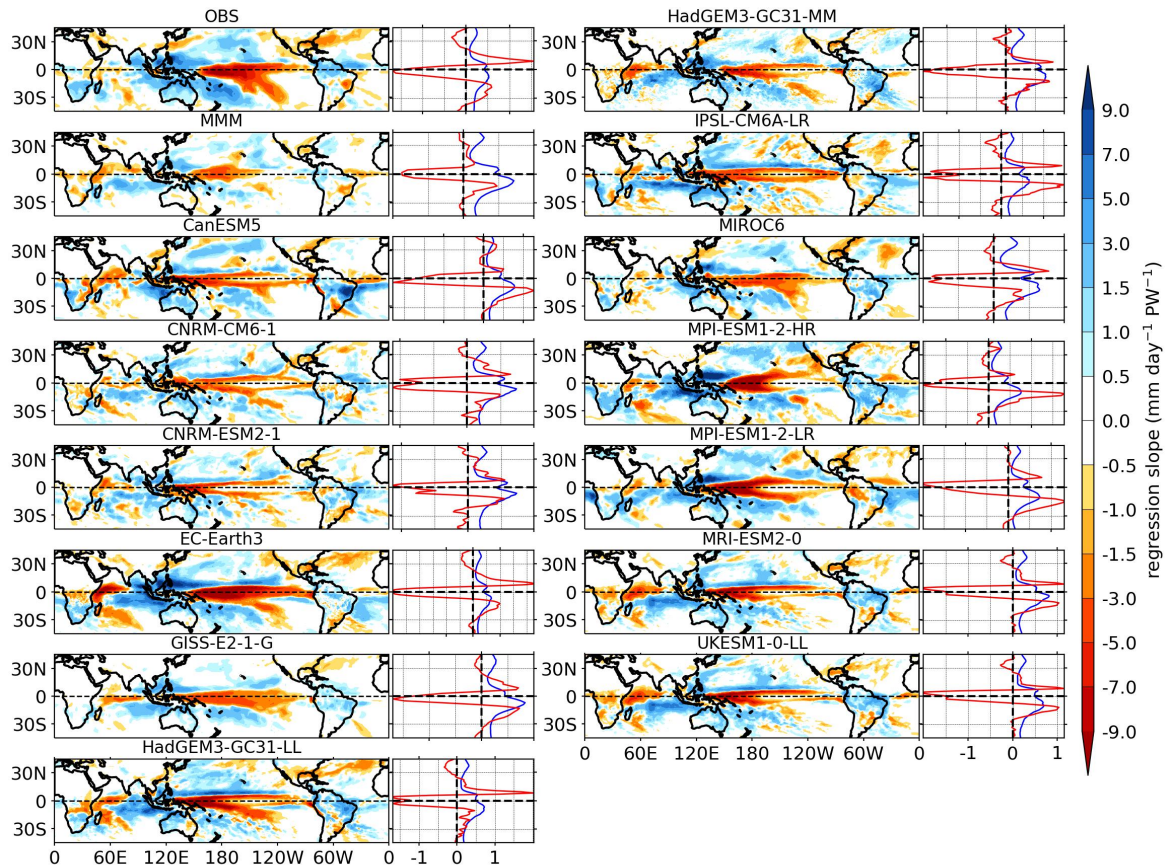


Figure 4.21: Same as Figure 4.19 except for DJF season.

respectively, in the majority of the CMIP6 models during the JJA season. The meridional shifting of the rising branch is either from the displacement of the core or contraction of the winter-Hadley cell in association with El Niño (Quan et al., 2004; Nguyen et al., 2013) by weakening the Walker circulation (Oort and Yienger, 1996).

In relation to the interaction between oceanic and atmospheric heat transports, the CE-OHT anomalies clearly oppose the responses in the Hadley circulation arising from CE-AHT anomalies in all the CMIP6 models for the JJA season (for example, Figure 4.16(i & iii)). The rising branch shifts away from the equator for northward CE-OHT anomalies, while southward anomalies shift towards the equator across all the CMIP6 models (for example, Figure 4.16(iii)(b & c)), resembling the reanalysis. In most CMIP6 models, the displacement of the Hadley circulation core tends to occur northward and southward from its climatological position for northward and southward CE-OHT anomalies, respectively, during the JJA season. Figure 4.16(i)(b & c) and 4.16(iii)(b & c) delineate the latitudinal displacement of the rising branch and highlight the intricate interaction between the ocean and atmosphere.

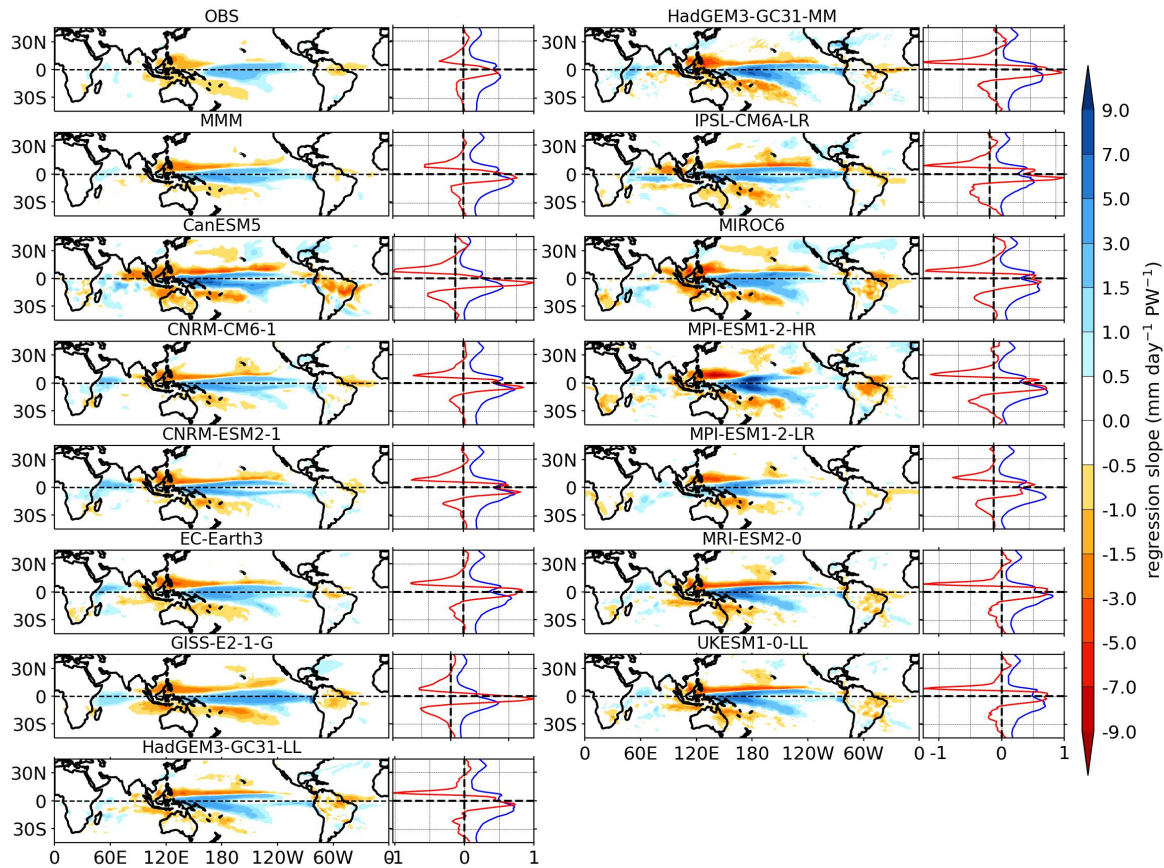


Figure 4.22: Same as Figure 4.20 except for DJF season.

In contrast to the JJA season, Figures 4.16(ii) and 4.16(iv) elucidate the relationship between stream-function and CE-AHT or CE-OHT for the DJF season. In the mean Hadley circulation in DJF season, the rising and subsiding branches are coherent with reanalysis by lying in the south and north of the equator (Seo et al., 2023; Quan et al., 2004; Feng et al., 2018), respectively, in all the CMIP6 models (for example, Figure 4.16(ii)a). Analogous to reanalysis, the rising branch is dislocated towards the pole for northward CE-AHT and southward CE-OHT anomalies across all the CMIP6 models (for example, Figures 4.16(ii)b & (iv)c). In the presence of northward CE-AHT or southward CE-OHT anomalies, an anti-clockwise (from east) circulation is observed within the winter-Hadley cell, predominantly in the lower branch of the Hadley cell near the equator. An anomalous ascent develops in the southern hemisphere, while another forms at approximately 5-10°N. Consequently, a distinctive double ITCZ pattern emerges, accompanied by a noticeable widening of the winter-Hadley cell. The double ITCZ pattern is notably more pronounced for northward

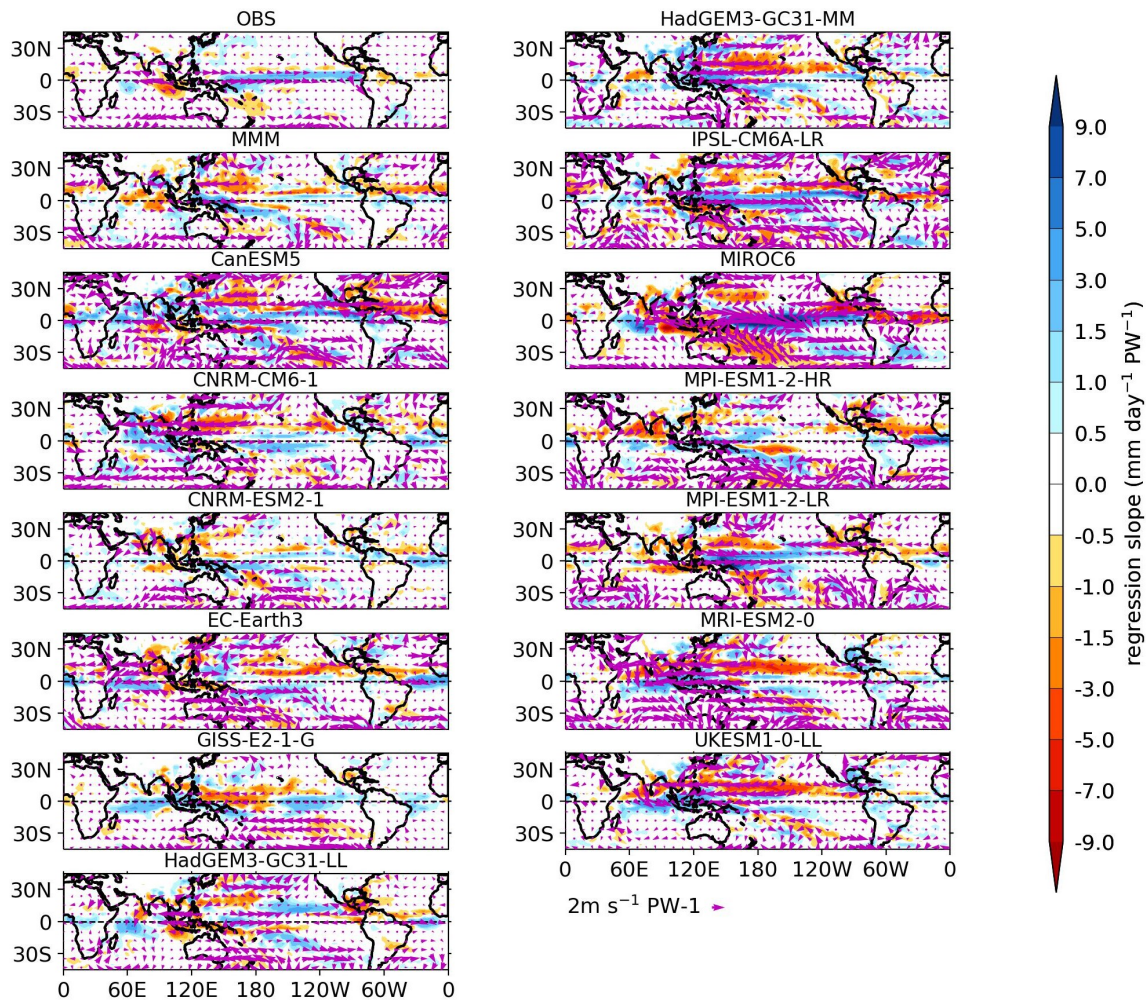


Figure 4.23: The inter-annual regression slope of lower-tropospheric (850 hPa) winds onto CE-AHT is delineated in vectors for the JJA season during the period 1979–2020 ($\text{ms}^{-1} \text{PW}^{-1}$). The colour shading is the inter-annual regression slope of precipitation onto CE-AHT for the same period. MMM refers to the multi-model mean.

CE-AHT and southward CE-OHT anomalies in the DJF season. During the DJF season, the northward anomalies in CE-AHT and southward anomalies in CE-OHT may be linked to the El Niño-Southern Oscillation (ENSO), particularly to La Niña-like states. In La Niña-like conditions during DJF season, an anomalous anti-clockwise circulation develops along the equator, and this circulation pattern disrupts the typical clockwise winter-Hadley cell circulation and results in a split or bifurcated winter-Hadley cell (Oort and Yienger, 1996; Quan et al., 2004).

However, the double-ITCZ bias still prevails in the state-of-the-art released CMIP6 models due to the equatorial Pacific cold tongue bias (Tian and Dong, 2020), coarse resolution,

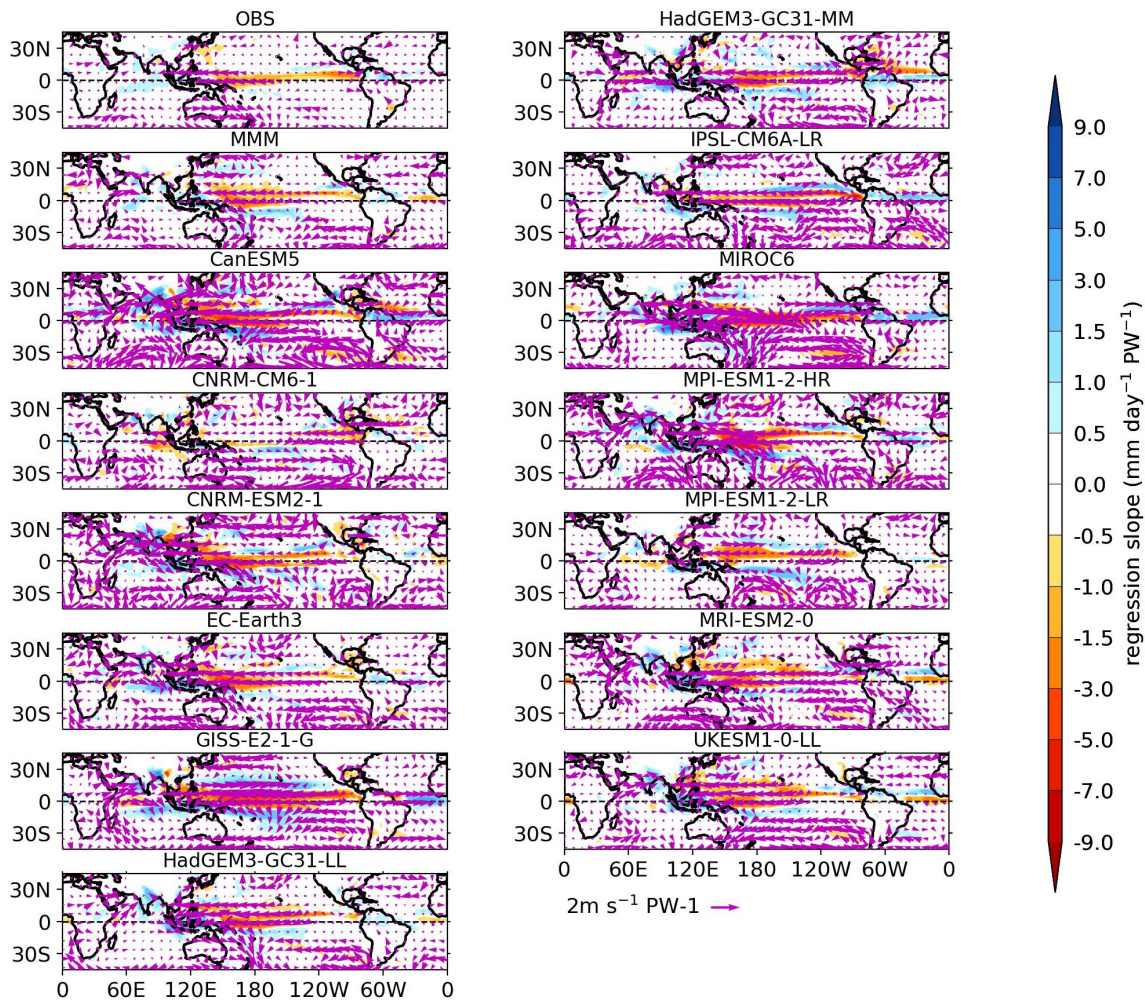


Figure 4.24: Same as Figure 4.23 but for the CE-OHT.

and strong convection over the south-eastern Pacific (Ma et al., 2023). Additionally, the poor simulation of southeastern Pacific marine stratus clouds and convective parametrization contribute to this bias (Zhang et al., 2019a). Therefore, (Zhang et al., 2019a) stated that the double ITCZ arises from a chain of complex interactions among convection, atmospheric large-scale circulation, SST, surface turbulent fluxes, upper ocean circulation, and heat transport.

Conversely, when southward CE-AHT or northward CE-OHT anomalies prevail, the double-ITCZ phenomenon dissipates as the rising branches of the Hadley cell converge during the DJF season (Figures 4.16(ii)c & (iv)b). This convergence during the DJF season can be explained from the perspective of the equatorward movement of the acpstj for southward CE-AHT or northward CE-OHT anomalies (Manney et al., 2021). Moreover, El Niño-like conditions prevail for southward CE-AHT or northward CE-OHT anomalies, which induce

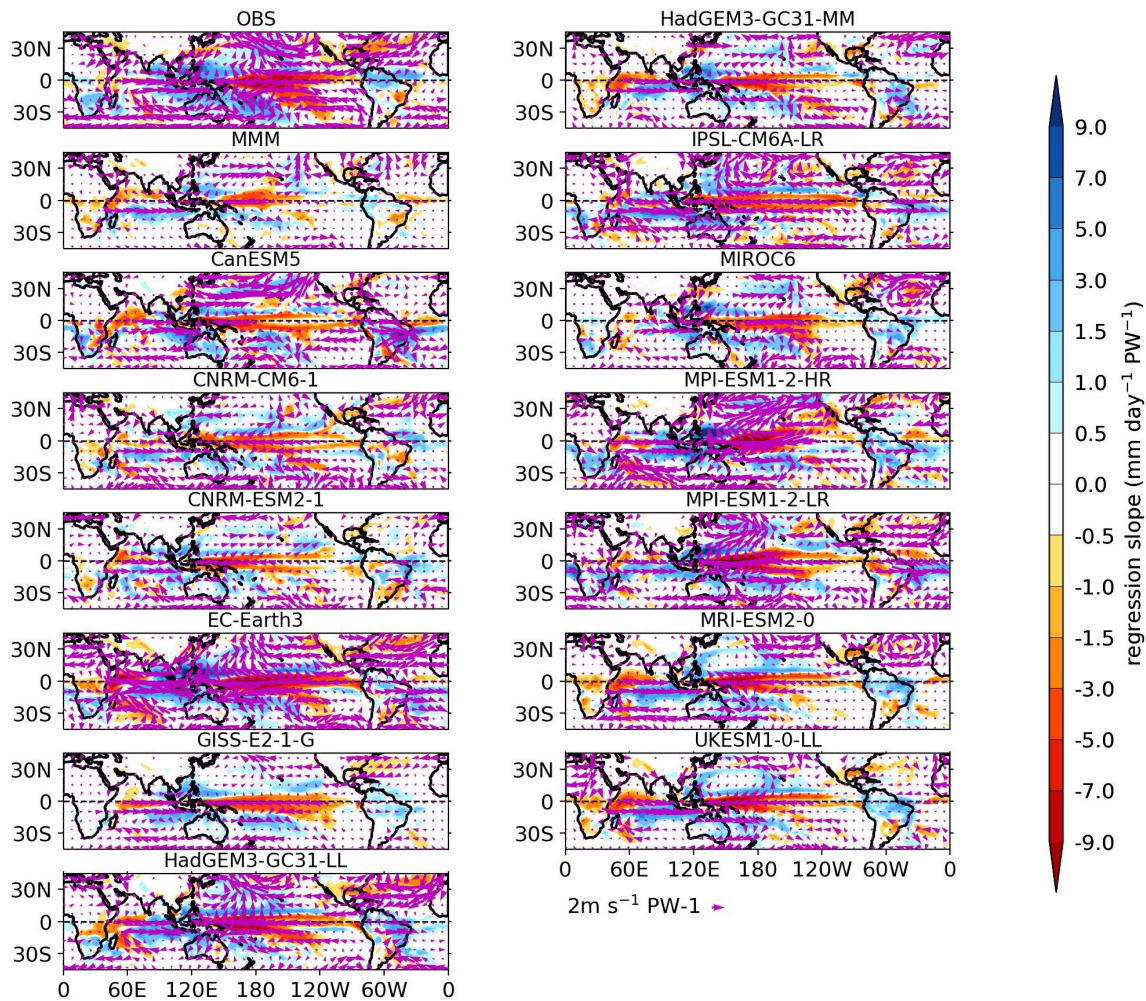


Figure 4.25: Same as Figure 4.23 except for the DJF season.

two anomalous anti-clockwise (from east) circulations on either side of the equator, leading to a squeezed winter-Hadley cell (Quan et al., 2004). In this scenario, the rising branch has an equatorward shift, and this behaviour is consistent in all CMIP6 models and agrees with reanalysis.

For understanding the zonal mean movement of the ITCZ in response to CE-AHT and CE-OHT anomalies, the I_{dmsf} metric is employed in CMIP6.

Figures 4.17a and 4.17b illustrate the meridional movement of the ITCZ in the JJA season for each Petta Watt CE-AHT and CE-OHT anomalies, respectively. In agreement with the reanalysis and above discussion of the stream function, the ITCZ moves northward up to 1° (except for GISS-E2-1-G: $\approx 2.1^\circ$) from its mean location for 1 PW negative (southward) CE-AHT anomaly and positive (northward) CE-OHT anomaly during the JJA season (Byrne et al., 2018). In response to positive CE-AHT anomalies and negative CE-OHT anomalies,

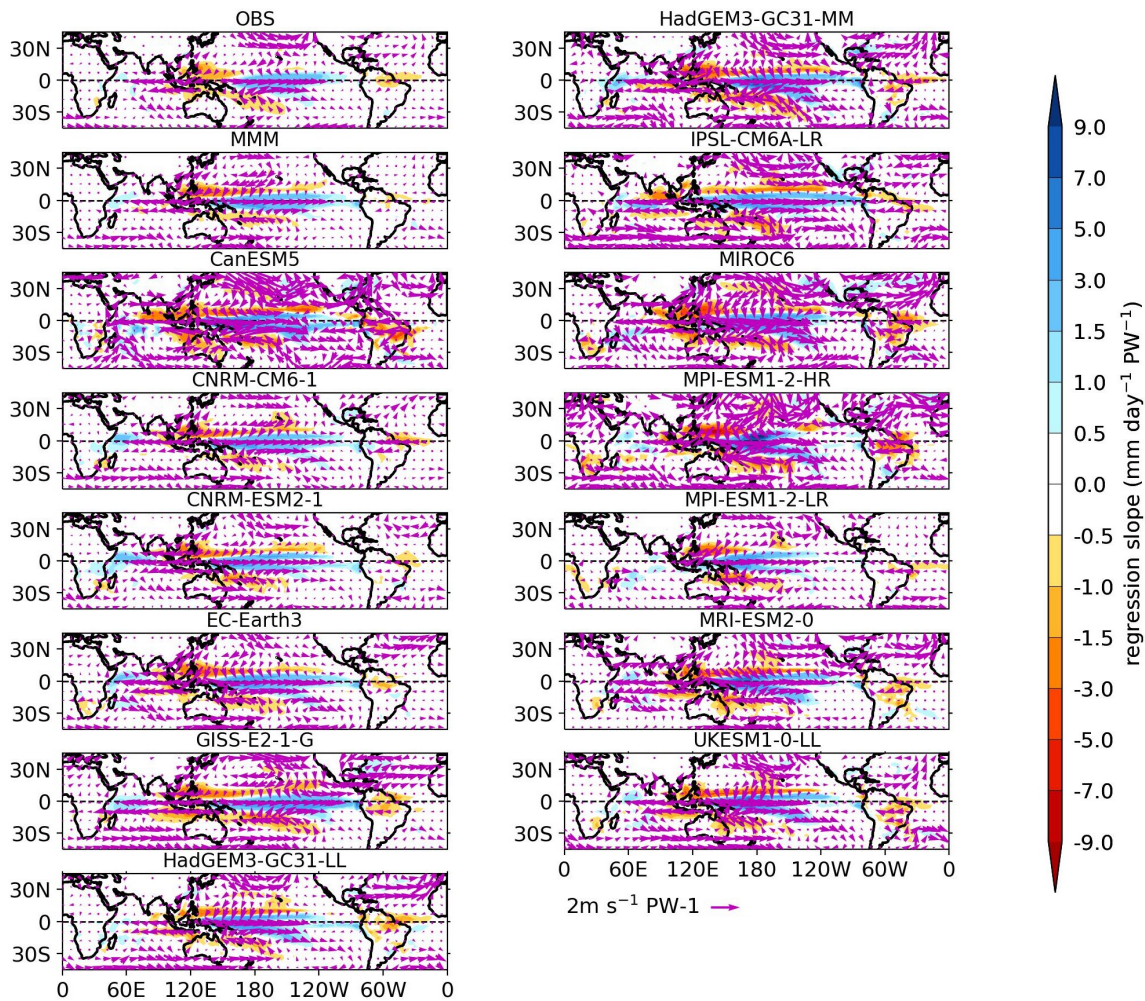


Figure 4.26: Same as Figure 4.24 except for the DJF season.

the ITCZ appears to be shifted towards the equator up to $1.4^{\circ} \text{PW}^{-1}$. The movement of the ITCZ is relatively strong for positive CE-AHT anomalies and negative CE-OHT anomalies.

In contrast to JJA season, Figures 4.18a and 4.18b depict the latitudinal displacement of the ITCZ in the DJF season corresponding to each Petta Watt CE-AHT and CE-OHT anomaly, respectively. The ITCZ is shifted in the poleward direction for 1 PW positive CE-AHT anomaly and negative CE-OHT anomaly across all CMIP6 models. The equatorward movement of the ITCZ occurs for negative CE-AHT or positive CE-OHT anomalies. All the movements of the ITCZ are consistent with the reanalysis.

Overall, the increase in cross-equatorial heat transport (CE-AHT or CE-OHT), whether northward or southward, is offset by the latitudinal movement of the Hadley cell's rising branch during the JJA or DJF season, both within the CMIP6 framework and in reanalysis. The northward CE-AHT and southward CE-OHT anomalies favour the equatorward move-

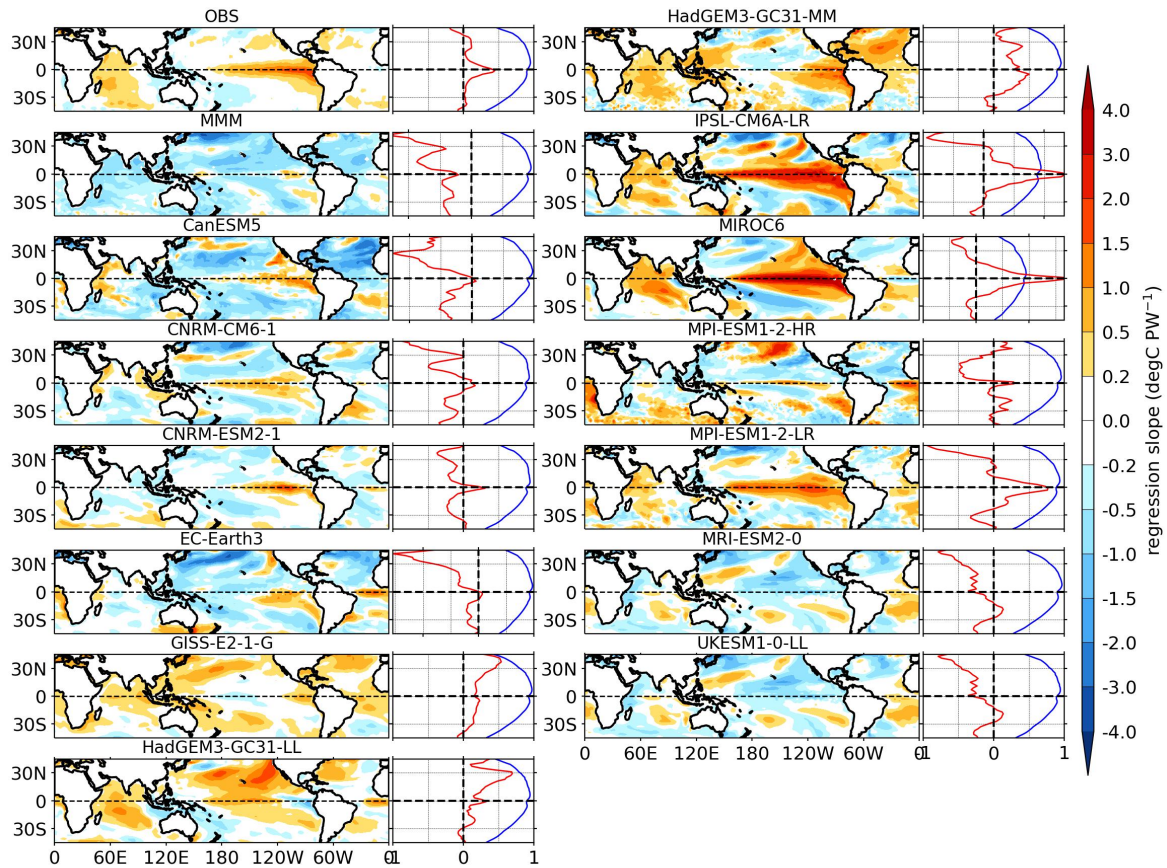


Figure 4.27: The inter-annual SST regression onto CE-AHT is displayed in colour shading for the JJA season over 1979–2020 in CMIP6 models ($^{\circ}\text{C PW}^{-1}$). The right panel shows the zonal mean SST (scaled down by 30; blue) and regressed SST (red curve) for the JJA season.

ment of the ITCZ in the JJA season, and they contribute to the poleward displacement of the ITCZ in the DJF season. Conversely, the movement of the ITCZ is inverse for southward CE-AHT and northward CE-OHT anomalies. The equatorward and poleward movements of the ITCZ (rising branch) arise either from contraction and expansion or from the meridional movement of the dominant winter-Hadley cell, respectively. The double-ITCZ phenomenon emerges from northward CE-AHT and southward CE-OHT anomalies in the DJF season, due to the poleward shift of the STJs and corresponding La Niña-like conditions over the Pacific Ocean (Zhang, 2001; Manney et al., 2021). It may also arise from biases in simulations and parametrizations of global coupled models, as described by (Zhang et al., 2019a).

The meridional movement of the ITCZ across the equator influences monsoonal precipitation (Wang et al., 2014), where monsoon-induced precipitation mainly occurs at the rising branch of the Hadley cell during the solstitial seasons (JJA and DJF). The fluctuations of the

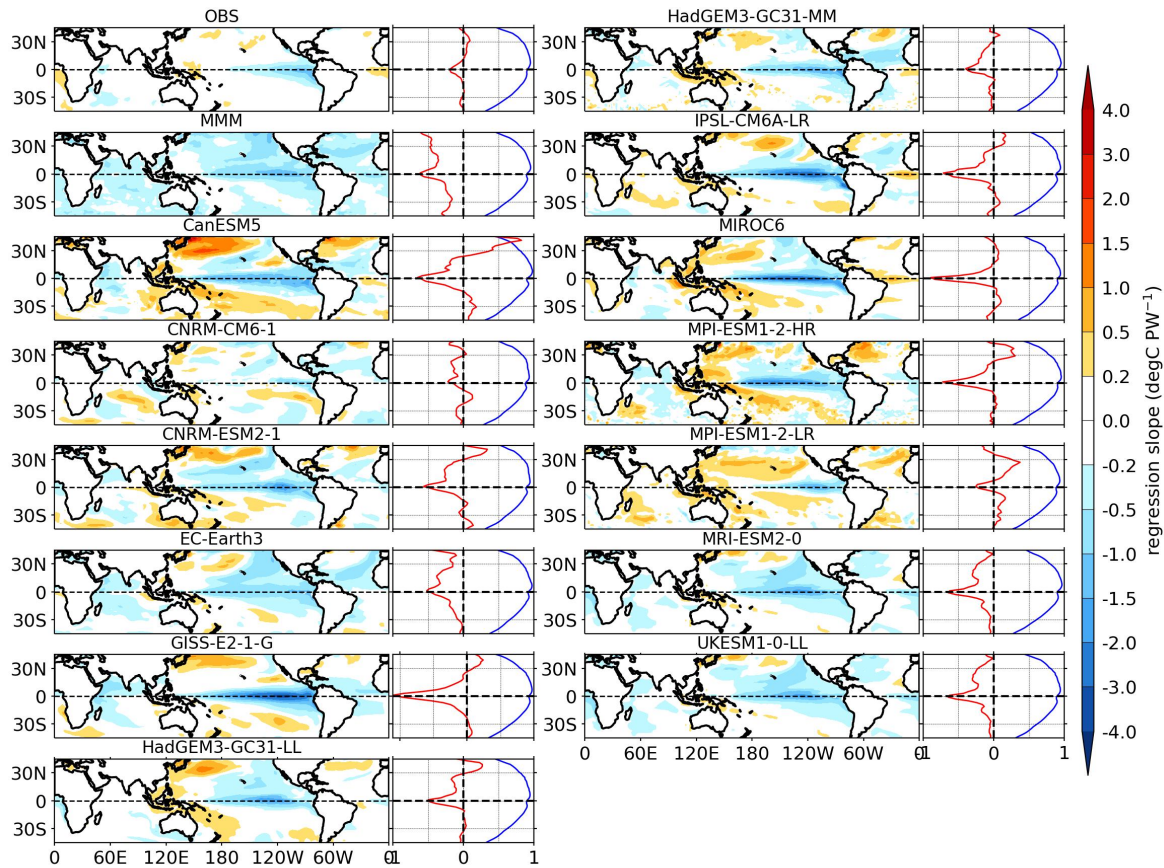


Figure 4.28: Same as in Figure 4.27 but for the CE-OHT.

ITCZ across the equator with cross-equatorial heat transport are consistent and expected for both the JJA and DJF seasons. Consequently, conducting regression analysis of precipitation onto cross-equatorial heat transport on an inter-annual time scale serves as a complementary component to the earlier stream-function results.

As depicted in Figure 4.19, when the zonal mean precipitation is regressed onto CE-AHT for the JJA season, a shift of the ITCZ emerges towards the equator across all CMIP6 models and the observations, as illustrated in the right panel of each map in Figure 4.19. This shift is consistent with the output obtained from the stream-function analysis coupled with the CE-AHT, as shown in Figure 4.17a. A notable increase in precipitation is observed towards the equatorial regions, particularly over the Pacific Ocean, when a northward CE-AHT anomaly occurs during the JJA season, consistent with the result from Chapter 3. Additionally, many models display a positive IOD-like precipitation pattern over the equatorial Indian Ocean, similar to observations. Conversely, a decrease in precipitation, as observed in observations, is noticeable over the Indian monsoon domain, with specific impact areas including

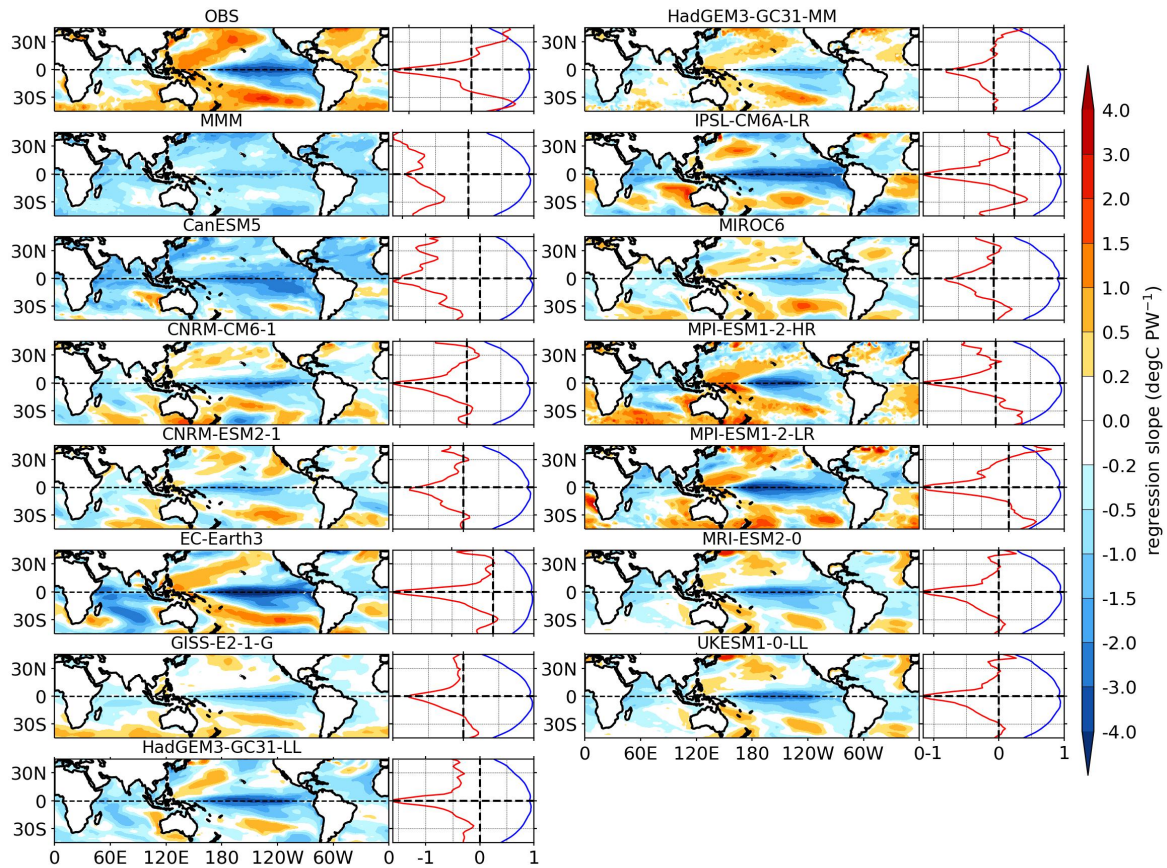


Figure 4.29: Same as Figure 4.27 except for the DJF season.

the Western-Ghats (in all models) and the southern flanks of the Himalaya (in some models). Significantly reduced precipitation is evident over the Maritime Continent (Sumatra, Java, Borneo, Sulawesi, Papua New Guinea, and the Philippines) in several CMIP6 models. The suppressed precipitation over the Maritime Continent and Indian monsoon region is consistent with the weakened Walker-like circulation (Athira et al., 2023) from upper tropospheric winds analysis. Additionally, West African monsoonal precipitation is reduced in most models, while precipitation over the North American monsoon domain is suppressed in all CMIP6 models (except CanESM5) and observations. However, in opposition to observations, most of the CMIP6 models exhibit a strong reduction and increase in precipitation over the north-western Pacific Ocean and equatorial Atlantic Ocean, respectively. In contrast to observations, a strong precipitation signal is noted along the Gulf of Guinea coast in the majority of the CMIP6 models. Moreover, the magnitude of the intensity of regressed precipitation is larger in all CMIP6 models. All these deviations may be linked to the bias in model simulations.

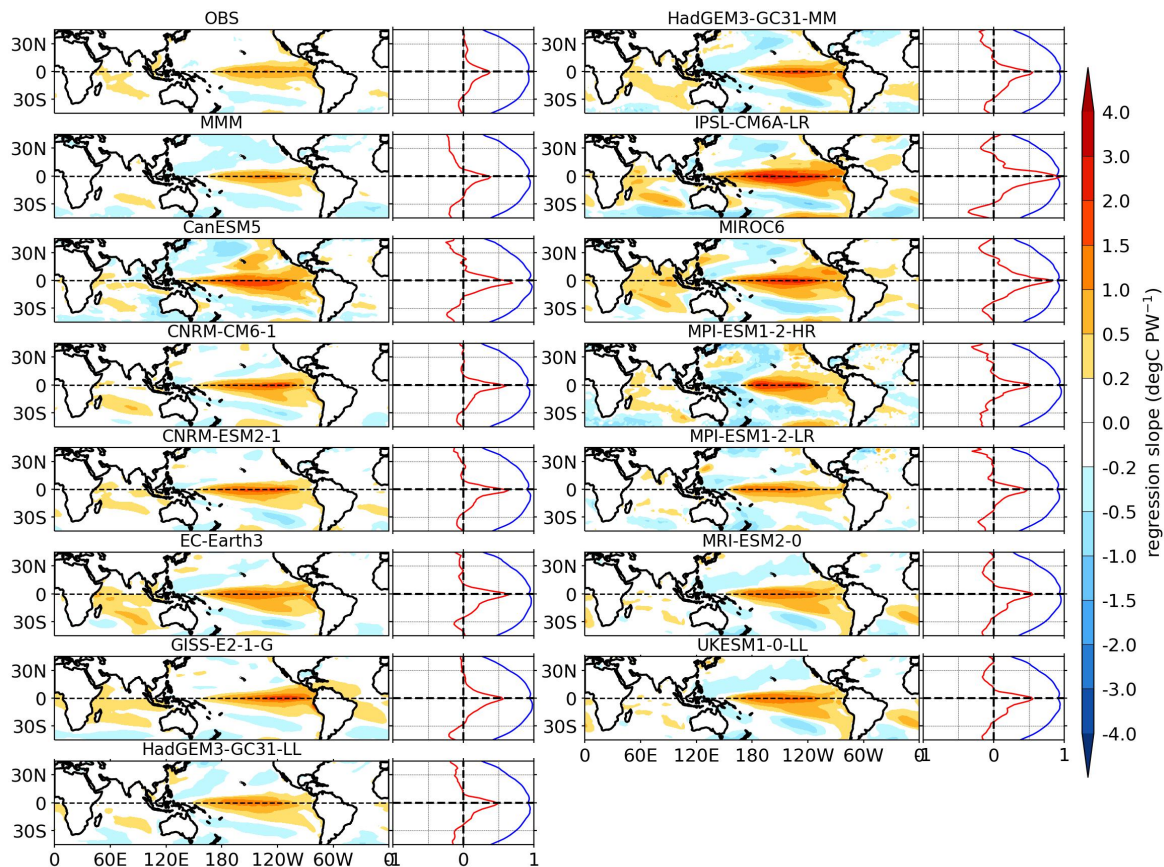


Figure 4.30: Same as Figure 4.28 except for the DJF season.

Unlike the CE-AHT, the zonal mean of regressed precipitation for CE-OHT in the JJA season, as displayed in the right panel of each map in Figure 4.20, emphasises the poleward displacement of the ITCZ in the CMIP6 models. The ITCZ moves away from the equator to compensate for the increase in CE-OHT anomaly, consistent with observations and the earlier result displayed in Figure 4.17b. However, an anomalous double-peak precipitation phenomenon exists only in a few of the CMIP6 models, which may be due to precipitation bias in models. But the analysis of stream function with the CE-OHT in the JJA season does not exhibit the spurious ITCZ. A northward increase in the CE-OHT anomaly during the JJA season results in reduced precipitation along the equator, mainly over the Pacific Ocean, in all CMIP6 models, consistent with observational results. This leads to the emergence of two distinct east-west bands of heavy precipitation away from the equator, as illustrated by the left panel of each map in Figure 4.20. Precipitation intensifies over the Indian monsoon domain and the Maritime continent, with a few exceptions such as Borneo (CNRM-CM6-

1 and IPSL-CM6A-LR), northern Sumatra (CanESM5, CNRM-CM6-1, MPI-ESM1-2-LR, and MRI-ESM2-0), and the Philippines in all models. From an upper tropospheric perspective, heavy precipitation over the Maritime Continent and the Indian monsoon domain results from strong TEJ-like and La Niña-like (strong Walker circulation) phenomena (Abish et al., 2013; Athira et al., 2023) (Figure 4.11). The changes in North American and West African monsoonal precipitation are consistent with the observations in the majority of models.

Figure 4.21 illustrates the impact of a northward CE-AHT anomaly during the DJF season on precipitation. In agreement with observations, the ITCZ shifts away from the equator. However, the double-ITCZ phenomenon is distinctly captured in the zonal mean of regressed precipitation, with the extra ITCZ in the northern hemisphere, as shown in the right panel of each map in Figure 4.21. Notably, a significant reduction in precipitation is observed along the equatorial region, particularly over the Pacific Ocean, resulting in the emergence of a double ITCZ-like pattern, similar to the observations. Moreover, half of the models, aligning with reanalysis, exhibit an increase in precipitation over the Maritime Continent, the Eastern Indian Ocean, including the Bay of Bengal, the North-Western Pacific Ocean, and the SPCZ (Southern Pacific Convergence Zone). The northern part of Australia experiences increased precipitation, consistent with observations, although certain models, including CNRM-ESM2-1, HadGEM3-GC31-MM, MMM, and MIROC6, exhibit the opposite trend. Regarding the upper-level winds, pronounced precipitation over the Maritime Continent and Australian monsoon region is attributed to a strong Walker-like circulation, as depicted in Figure 4.12 (Power et al., 2006; Cai et al., 2010; King et al., 2015). Additionally, the decrease in precipitation over the SACZ (South Atlantic Convergence Zone) in observations is captured by a few models (CNRM-CM6-1, CNRM-ESM2-1, and MMM). However, positive signals, in contrast to observations, are noted for the South American monsoon domain in most of the CMIP6 models.

In contrast, the impact of northward CE-OHT anomalies during the DJF season is depicted in Figure 4.22. The ITCZ shifts notably towards the equator, as clearly depicted in the zonal mean of regressed precipitation (the right panel of each map in Figure 4.22). The CE-OHT anomaly leads to a reduction in precipitation over the Australian, South African, and

South American monsoon domains across all models, which is consistent with observations. In connection to the upper level winds, a weak Walker-like circulation reduces precipitation over the Maritime Continent and Australian monsoon domain, as displayed in Figure 4.13 (Power et al., 2006; Cai et al., 2010; King et al., 2015). A negative precipitation signal over the North-Western Pacific Ocean, SPCZ, and equatorial Atlantic Ocean is noticed across all CMIP6 models, which is coherent with the observations. Conversely, a distinct and strong signal of precipitation, matching the observation, is evident along the equatorial regions of the Pacific Ocean. This, in turn, results in a unified ITCZ observed in most of the models.

In short, in all CMIP6 models, the movements of the ITCZ using precipitation in response to CE-AHT and CE-OHT anomalies are in agreement with observations and earlier findings from the stream-function for both JJA and DJF seasons. The ITCZ moves equatorward and poleward for northward CE-AHT and CE-OHT anomalies, respectively, in the JJA season. On the other hand, for the DJF season, the displacement of the ITCZ is inverse for northward CE-AHT and CE-OHT anomalies. The CE-AHT anomaly in JJA contributes to: strong precipitation along the equatorial Pacific Ocean with an equatorward shift; a decline in precipitation over the Indian monsoon domain, including Western Ghats and southern flanks of Himalaya; a positive IOD-like precipitation pattern over the Indian Ocean; a decline in precipitation over the Maritime continent; and a weakening of West African and North American monsoonal precipitation. The responses of the northward CE-OHT anomaly in JJA are: reduced precipitation over the Pacific Ocean along the equator; intensified precipitation over the Indian monsoon domain; and the Maritime Continent, in all CMIP6 models and coherent with the observations. In agreement with observations, the northward increase of CE-AHT in DJF season causes: a reduction in precipitation along the equatorial Pacific Ocean in all CMIP6 models; an increase in precipitation over the Maritime continent, Bay of Bengal, North-Western Pacific Ocean, SPCZ, northern part of Australia, and South African monsoon domain in half of the models. The CE-OHT anomaly in DJF season leads to an increase in precipitation along the equatorial Pacific Ocean and a reduction over the SPCZ, North-Western Pacific Ocean, equatorial Atlantic Ocean, Australian, South African, and South American monsoon domains across all models.

For a comprehensive analysis of the meridional movement of the rising branch and spatial variations in precipitation associated with cross-equatorial heat transport, I conducted regression analyses of 850-hPa winds (u , v) with respect to CE-AHT or CE-OHT on an inter-annual time scale. Most importantly, a connection with upper-level winds will be established through this analysis. Also, It will explain whether changes in precipitation relative to CE-AHT or CE-OHT arise from the convergence, divergence, and convection of lower-level air masses.

As captured in Figure 4.23, the increase of northward CE-AHT in the JJA season induces an equatorward shift in the convergence of trade winds. An anomalous divergence appears as a descent over the Maritime Continent, leading to strong and weak trade winds over the equatorial Indian Ocean and Pacific Ocean, respectively. The wind pattern over the Pacific Ocean indicates an El Niño associated weak Walker circulation, consistent with the reanalysis and upper-level winds (Sandeep and Ajayamohan, 2015; Pattanaik and Satyan, 2000). As a result, resembling the observations, precipitation is suppressed over the Maritime Continent, as demonstrated in most of the CMIP6 models. A positive IOD-like pattern in wind and precipitation also appears through convergence and divergence over the western and eastern equatorial Indian Ocean, respectively, in a few models, coherent with the observations. However, in other models, an anomalous convergence of winds causes heavy precipitation anomalies over the Maritime Continent, with easterly wind anomalies dominating the equatorial Pacific and Indian Oceans. South-westerly winds weaken, reducing moisture transport towards the Indian monsoon domain, leading to decreased precipitation in all models, as in observations. Meanwhile, north-easterly wind anomalies increase over the North African and American monsoon domains, contributing to reduced precipitation. When compared with the findings presented in Chapter 3, the majority of CMIP6 models fail to capture the anomalous convergence and divergence over the western and eastern equatorial Indian Ocean, respectively, and it may be linked to bias in models.

As described in Figure 4.24, for the northward CE-OHT anomaly in JJA season, the trade winds strengthen over the Pacific Ocean in all models except for CNRM-CM61. The wind

pattern behaves like it is the lower branch of a strong Walker circulation, as in upper-level winds and reanalysis. South-westerly winds follow the path of reanalysis and prevail over the Indian monsoon domain and the Maritime Continent. Convergence and convection over the Maritime Continent lead to substantial precipitation. Moisture transport through strong south-westerly winds towards the Indian monsoon domain increases, contributing to significant precipitation. The wind patterns identified in these models align with the findings presented in Chapter 3.

On the other hand, Figure 4.25 reveals that during the DJF season with a northward CE-AHT anomaly, easterly and westerly winds are strengthened along the equator over the Pacific and Indian Oceans, respectively. In all models, westerly winds from the Indian Ocean converge with easterly winds from the Pacific Ocean over the Maritime continent and the Australian monsoon domain, leading to enhanced precipitation anomalies, as observed in reanalysis (Wang et al., 2017). The wind pattern agreeing with the upper tropospheric winds behaves as a La Niña-like condition prevails over the Pacific Ocean, leading to a negative IOD-like phenomenon over the Indian Ocean. Despite wind convergence, in contrast to the reanalysis, reduced precipitation over the Maritime Continent is attributed to the southward shift of westerly wind anomalies over the Indian Ocean as well as an intrusion of northerly wind anomalies in a few models. In opposition to reanalysis, an anomalous convergence either from the north and south easterly winds or anti-cyclonic circulation forms over the SACZ and South American monsoon domains and results in increased precipitation in most of the CMIP6 models. The southern African monsoon domain, particularly the southern parts, including the coastal regions, exhibits a significant increase in precipitation due to the anomalous convergence, similar to reanalysis. As in reanalysis, an anomalous cyclonic circulation forms over the North-Western Pacific Ocean across all models. However, most of the CMIP6 models fail to capture the anomalous anti-cyclonic circulation over the Southern Pacific Ocean, as observed in reanalysis.

During the DJF season, a positive CE-OHT anomaly induces a divergence of low-level winds across all models over the southern African, south American, and Australian (includ-

ing Maritime Continent) monsoon domains, as illustrated in Figure 4.26. As a result, moisture transport decreases over there, and a reduction in precipitation is found. In agreement with the reanalysis, it seems an anomalous subsidence from a weak Walker-like circulation, as found in upper-level winds, occurs over the Maritime Continent and moves eastward and westward over the equatorial Pacific Ocean and Indian Ocean, respectively. Thus, the wind pattern indicates an El Niño-like anomaly over the Pacific Ocean, leading to a positive IOD-like anomaly over the Indian Ocean. Therefore, trade winds strengthen and weaken over the Indian and Pacific Oceans, respectively. The anomalous westerly winds from both sides of the equator meet along the equator and develop a convergence zone over the Pacific Ocean, resulting in heavy precipitation anomalies. Most of the models capture a cyclonic circulation anomaly over the North-Western Pacific Ocean and an anti-cyclonic circulation anomaly over the Southern Pacific Ocean, as consistent with reanalysis.

Briefly, for the northward CE-AHT anomalies during JJA season, anomalous divergence (convergence) in the lower (upper) troposphere occurs over the Maritime Continent as a part of the El Niño associated weak Walker circulation over the equatorial Pacific Ocean and suppresses precipitation. In addition, a positive IOD-like anomaly is noticed over the Indian Ocean. Due to south-westerly wind anomalies, moisture transport is reduced towards the Indian monsoon domain, resulting in decreased precipitation. However, the northward CE-OHT anomalies are linked to a strong Walker circulation supported by both upper and lower winds and negative IOD-like anomalies over the equatorial Pacific Ocean and Indian Ocean, respectively. As a result, heavy precipitation over the maritime continent is noticed across all models. Anomalous north-westerly winds prevail and increase moisture transport towards the Indian monsoon domain; consequently, heavy precipitation anomalies are noted. In contrast to JJA season, when the CE-AHT anomalies are positive in DJF season, the wind pattern behaves as a strong Walker circulation over the Pacific Ocean and negative IOD-like anomalies over the Indian Ocean. As a consequence, a positive precipitation signal prevails over the Maritime Continent and Australian monsoon domains. Anomalous convergence over the Southern African monsoon region causes increased precipitation during DJF season. In opposition to CE-AHT in DJF, positive CE-OHT anomalies facilitate a divergent

wind anomaly over the Maritime Continent that helps to form a weak Walker circulation. As a result, precipitation reduces over the Maritime Continent and Australian monsoon domain.

The winds, serving as dynamic indicators, have provided valuable insights into the atmospheric circulation patterns with the inter-annual increases of the CE-AHT and CE-OHT. Oceans act as a thermal reservoir and influence atmospheric conditions and circulation patterns. To bridge between dynamic and thermal effects for the CE-AHT or CE-OHT anomalies, regression analysis of SST is performed on CE-AHT and CE-OHT on an inter-annual time scale.

For a northward CE-AHT anomaly in JJA season, Figure 4.27 shows that an El Niño-like pattern appears over the Pacific Ocean in most models, as noted in upper and lower tropospheric winds and consistent with the observations. The El Niño-like state corresponds to the existence of westerly wind anomalies over that region. A positive IOD-like condition exists over the Indian Ocean in half of the models. As expected from the upper and lower level winds, the rise of northward CE-OHT in JJA season leads to a La Niña-like condition in most models (Figure 4.28). Positive SST anomalies are noted on the north-western and south-western boundaries of the Pacific Ocean. Wind analysis has also shown convergences on both sides of the equator, resulting in two zonal bands of positive precipitation signals.

Conversely, a negative SST anomaly is captured in the Eastern Pacific and Western Indian Oceans along the equator for northward CE-AHT anomalies in DJF (Figure 4.29), as expected from the upper and low-level winds analysis. SST increases in the south-eastern part of the Indian Ocean, specifically in the vicinity of the western Australian coast, which agrees with the cyclonic (clockwise) circulation over the Indian Ocean as observed in wind analysis. The SST of the western Pacific Ocean also goes up with an eastward extension of latitude, resulting from two circulation patterns across the equator.

The positive CE-OHT anomaly in DJF exhibits a rise in SST of the Eastern Pacific Ocean and Western Indian Ocean across all models, as shown in Figure 4.30. It is consistent with the earlier winds analysis, which shows divergence of low-level winds and suppression of precipitation over the Maritime Continent and northern Australia, while precipitation increases

over the equatorial middle-eastern Pacific Ocean and western Indian Ocean, including Somalia. The SST anomalies are negative off the equator with north-eastward and south-eastward extensions over the Pacific Ocean. The SST changes over the Atlantic Ocean are not strong, though the precipitation is reduced in the South American monsoon domain across all models.

In brief, northward CE-AHT and CE-OHT anomalies in the JJA season favour La Niña-like and Ea Niño-like states, respectively, while during the DJF season, the opposite occurs. These findings are consistent with lower and upper tropospheric wind analysis and reanalysis.

4.3.3 Model Performance Based on Pattern Correlation

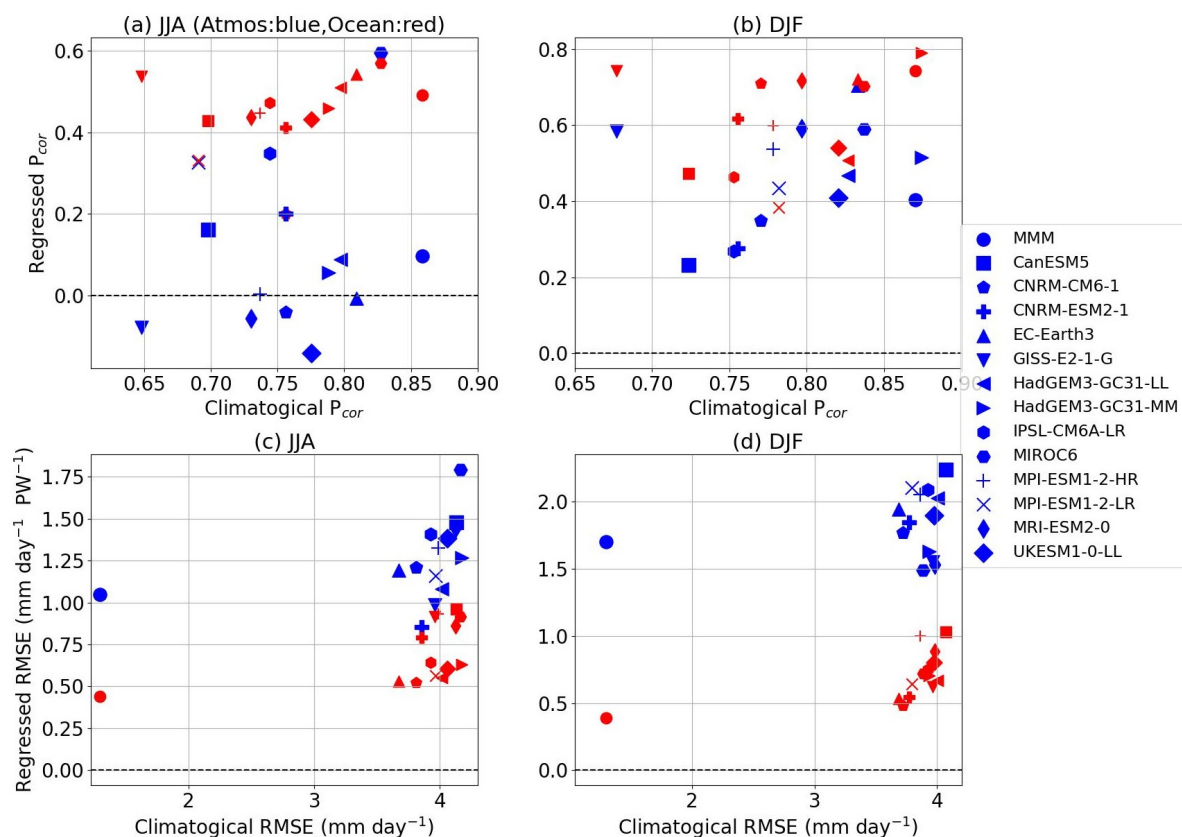


Figure 4.31: The pattern correlation between reanalysis and CMIP6 models is shown for JJA (a) and DJF (b), with climatological mean precipitation along the horizontal axis and regressed precipitation (onto CE-AHT in blue and CE-OHT in red) along the vertical axis on an inter-annual time scale for the period 1979–2020. Similarly, the RMSE is displayed in panels (c) and (d).

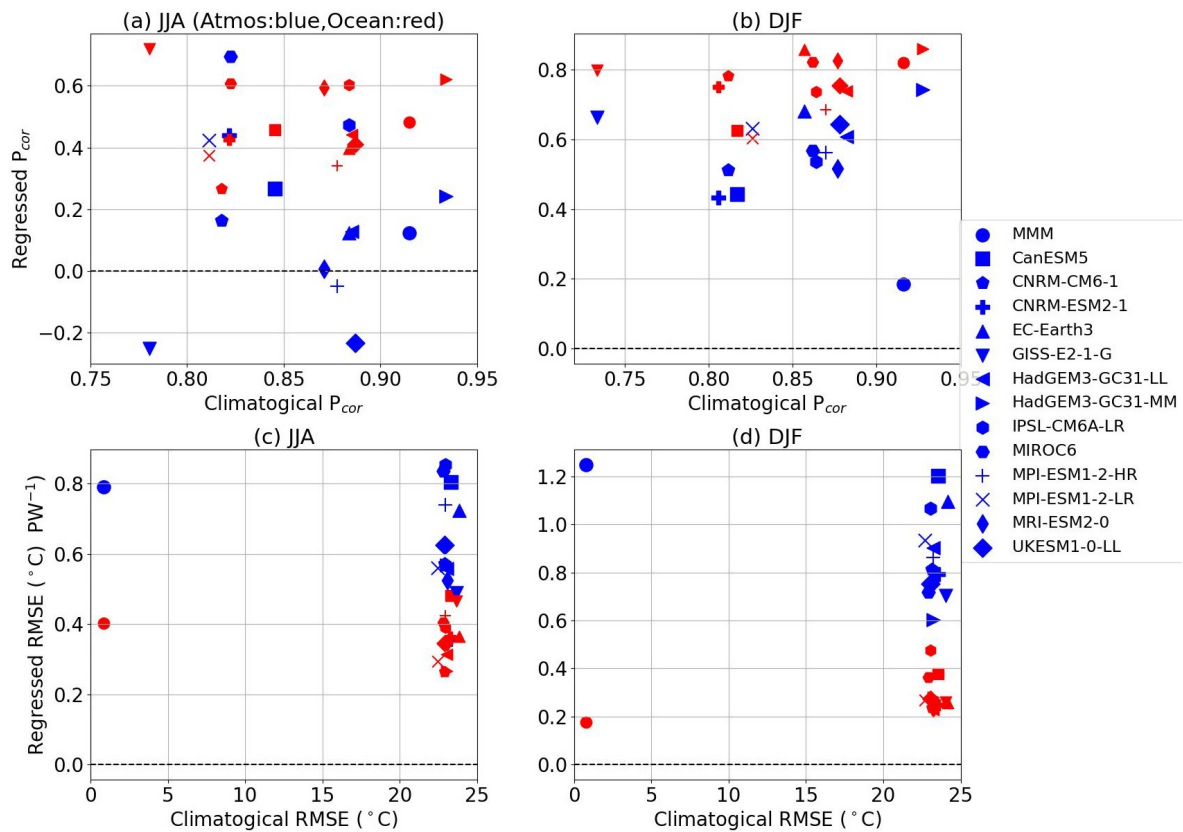


Figure 4.32: Same as in Figure 4.31 but for the SST.

For validating the accuracy and reliability of CMIP6 climate models, a crucial aspect is investigating the agreement between monsoon-associated reanalysis datasets and model simulations. Pattern correlation serves as a quantitative metric to assess how well the model replicates observed spatial patterns in both the climatological version and the regressed version with cross-equatorial heat transport. High pattern correlations imply that a model is adept at reproducing observed spatial structures, enhancing our confidence in its ability to simulate realistic monsoonal precipitation and its relationship with cross-equatorial heat transport. The horizontal and vertical axes (JJA in ‘a’ & DJF in ‘b’) represent the climatological and regressed pattern correlations between observations and CMIP6 models, respectively, as displayed in Figures 4.31, and 4.32. Similarly, the RMSE is displayed in ‘c’ and ‘d’ in these figures.

Figure 4.31(i) demonstrates that all CMIP6 models efficiently simulate time-averaged observational precipitation during the JJA (a) and DJF (b) seasons. For the seasonal mean precipitation from subtropical to subtropical (45° S– 45° N), P_{cor} ranges from 0.65 to 0.88 and

shows higher values denoting better simulation for DJF season for the period 1979-2020. For the climatological precipitation field, the MMM (multi-model mean) has the highest P_{cor} value for both JJA and DJF seasons. Apart from MMM, the MIROC6 and HadGEM3-GC31-MM models have peak P_{cor} in JJA and DJF, respectively, for climatological precipitation fields. In JJA season, P_{cor} values are suppressed for precipitation regressed onto CE-AHT than CE-OHT in both JJA and DJF seasons. Notably, the MIROC6 model excels with a pattern correlation of 0.6 (0.58) for regressed precipitation on CE-AHT (CE-OHT) for JJA, whereas the EC-Earth3 (CE-AHT) and HadGEM3-GC31-MM (CE-OHT) model excels in DJF season. On the other hand, UKESM1-0-LL (JJA) and CanESM5 (DJF) perform worst for regressed precipitation.

The RMSE of precipitation is depicted in Figure 4.31(i)c and Figure 4.31(i)d for the JJA and DJF seasons, respectively, for climatological and regressed fields. The RMSE is comparatively smaller when precipitation is regressed onto CE-OHT in both JJA and DJF, indicating better performance in capturing the observed relationship. The RMSE is larger in DJF than in the JJA season for regressed precipitation. This indicates that the simulations of the CMIP6 models for regressed precipitation are less accurate or have larger deviations from the observed values in the DJF season compared to the JJA season (Huang et al., 2023).

Figure 4.32(ii) illustrates the efficacy of the CMIP6 model simulation in terms of P_{cor} and RMSE for the SST. For the JJA (Figure 4.32a) and DJF (Figure 4.32b) climatological mean SST simulation, the P_{cor} ranges between 0.73 and 0.93, and HadGEM3-GC31-MM has the peak value in both seasons. For the SST regressed onto CE-AHT and CE-OHT, the maximum P_{cor} occurs for the MIROC6 and GISS-E2-1-G models in JJA, respectively, whereas it happens for the HadGEM3-GC31-MM model for both CE-AHT and CE-OHT regression cases in the DJF season.

Figure 4.32(ii)c and Figure 4.32(ii)d represent the RMSE for the SST in JJA and DJF seasons, respectively. The same pattern, as noted in precipitation, prevails in RMSE for the SST, with smaller RMSE values in both seasons when SST is regressed onto CE-OHT.

Hence, the CMIP6 models show high pattern correlation in simulating the mean precipitation (Du et al., 2022) and SST (Li et al., 2023) for both JJA and DJF seasons. In JJA, the

MIROC6 model performs well in reproducing regressed precipitation and SST patterns for both CE-AHT and CE-OHT, whereas the HadGEM3-GC31-MM is for the DJF season. The MIROC6 also shows consistency for the DJF season. Overall, the MIROC6 appears to be the best model, while the UKESM1-0-LL and CanESM5 are the worst.

The variation in the performance of CMIP6 models may arise from several factors. Differences in model resolution, such as atmospheric and oceanic grid scales, influence the ability to resolve fine-scale processes like convection and ocean eddies, with higher-resolution models often performing better in regional simulations. HadGEM3-GC31-MM has the highest resolution, suitable for fine-scale regional studies. MIROC6, UKESM1-0-LL, and HadGEM3-GC31-LL share a coarser resolution, while CanESM5 has the coarsest atmospheric resolution.

Differences in the inclusion or exclusion of Earth system feedback, such as the representation of interactive or prescribed aerosols, can impact radiative forcing and cloud properties, leading to differences in climate responses. UKESM1-0-LL and CanESM5 include fully interactive biogeochemical cycles, while MIROC6 has limited biogeochemical interactions, and HadGEM3 variants lack biogeochemical components. UKESM1-0-LL and CanESM5 include interactive aerosol modelling, while MIROC6 and HadGEM3 models use prescribed aerosols. The choice of ocean and sea ice models is also different across models. For example, the MIROC6 uses the COCO ocean and sea ice model, while the others use variants of the NEMO ocean model with different sea ice schemes.

Variations in numerical methods and parameterization schemes for processes like cloud formation, convection, and radiation can also contribute significantly. MIROC6 uses a horizontal spectral transformation scheme combined with a semi-implicit time integration method and a mass-flux-based single-plume convection model following Park and Bretherton (2009) (Tatebe et al., 2019). Its bulk cloud microphysics scheme provides a flexible representation of cloud liquid/ice partitioning and describes atmospheric water using four components: vapour, liquid-phase cloud droplets, raindrops, and frozen water (Ando et al., 2021; Watanabe et al., 2009; Cesana et al., 2015). In the UKESM1-0-LL and HadGEM3-GC31-MM models, a semi-implicit, semi-Lagrangian scheme is used for solving the primitive equations, and a mass-flux convection is based on the Gregory and Rowntree (1990)

scheme. The model incorporates a prognostic condensate scheme that includes three prognostic water mixing ratios (vapour, liquid, ice) and three cloud fractions (liquid, ice, mixed-phase) (UKESM Team, 2022; Wilson et al., 2008a,b).

All the above factors highlight the complexity and diversity in CMIP6 models and underscore the need for careful interpretation of their outputs in climate studies.

4.4 Conclusion

During the JJA season, the CE-AHT and CE-OHT exhibit a southward export of heat, while the export is northward in DJF. Notably, there is a negative correlation on an inter-annual scale between CE-AHT and CE-OHT, with the correlation being particularly pronounced in DJF in all CMIP6 models.

In most of the models, during the JJA season, northward CE-AHT anomalies cause a divergence in upper-level winds over the Maritime, strengthening easterly wind anomalies over the equatorial Pacific Ocean, shifting the STJs equatorward, and weakening the TEJ, resulting in a weak Walker-like circulation that leads to the contraction of the winter Hadley cell and a shift of the ITCZ towards the equator. A weak Walker-like circulation, characterized by divergence in the lower troposphere and convergence in the upper troposphere over the Maritime Continent, contributes to a positive IOD pattern. Consequently, precipitation decreases over the Maritime Continent, Indian, and West African monsoon domains. Conversely, CE-OHT anomalies in the JJA season expand the winter Hadley cell and push the ITCZ away from the equator, as all the responses stemming from northward CE-AHT anomalies are in the opposite direction. A strong Walker-like circulation develops and causes heavy precipitation over the Indian monsoon domain and Maritime Continent, while it reduces precipitation over the equatorial Pacific Ocean. El Niño-like and La Niña-like conditions prevail in SST as well for northward CE-AHT and CE-OHT anomalies in the JJA season, respectively.

On the other hand, during the DJF season, the northward CE-AHT anomalies push the STJs poleward, widen the dominant winter-Hadley cell, and dislocate the ITCZ in a poleward direction. A strong Walker-like circulation comes into existence, and it is characterized by low-level convergence and upper-level divergence, which leads to pronounced precipita-

tion over the Australian, South American, and South African monsoon domains. In contrast, the northward CE-OHT anomalies contract the dominant winter-Hadley cell and relocate the ITCZ near the equator. A weak Walker circulation emerges, which suppresses precipitation over the Australian, South American, and South African monsoon domains. The El Niño-like conditions over the Pacific Ocean are evident. Moreover, there exist La Niña-like and El Niño-like conditions in SST as well over the Pacific Ocean for positive CE-AHT and CE-OHT anomalies, respectively.

However, in precipitation analysis, the double-ITCZ is identified for both CE-AHT and CE-OHT in both JJA and DJF seasons, especially strong for northward CE-AHT in the DJF season. This implies that the model-simulated precipitations are prone to creating spurious ITCZ by reducing precipitation over the Pacific Ocean along the equator. The poleward movements of the STJs and La Niña conditions in the Pacific Ocean are consistently found for the double-ITCZ pattern. Furthermore, the double-ITCZ pattern appears across all the models showing its minimal association with the horizontal resolution of the models.

Considering the regressed precipitation and SST aspects, the MIROC6 model exhibits better and more consistent performance during the JJA and DJF seasons. In contrast, the UKESM1-0-LL and CanESM5 models show relatively poorer performance, with greater inconsistencies in capturing the seasonal variations in regressed precipitation and SST patterns.

Thus, monsoons are intrinsically linked to cross-equatorial atmospheric and oceanic heat transport through global energy budget constraints. Changes in the magnitude and direction of cross-equatorial heat transport can lead to shifts in the ITCZ and associated monsoon rainfall patterns by influencing the STJs followed by the Hadley and Walker circulations. Therefore, it would be worthwhile to investigate whether the relationships documented here change in the future as the climate warms. Furthermore, insights drawn from the discrepancies between good and bad models of warming climates will shape our understanding of future monsoon behaviour and help identify the key processes driving monsoon variability in a warming climate. These questions will be explored further in the next chapter.

5

Climate Change effects on the Relationship between Cross-Equatorial Heat Transports and the Monsoons

5.1 Introduction

The current state of the atmosphere around us, characterized by the temperature, wind, humidity, precipitation, clouds, atmospheric pressure, and other weather elements that are fluctuating rapidly, is defined as the weather. Climate, on the other hand, refers to the long-term patterns and averages of weather conditions in a particular region over extended periods, typically decades to centuries. Unlike weather, which can change rapidly and is highly variable, climate changes gradually over time. The variations in the mean state of the climate or

its variability that typically persist for decades or longer and are statistically significant are referred to as ‘climate change’ (Abbass et al., 2022). A condition that is warmer or colder, wetter or drier than normal over a mesoscale, synoptic-scale, continental-scale, or global-scale region for several decades or longer is generally attributed to climate change.

Under the SSP5-8.5 scenario, increasing greenhouse gases cause the widening and weakening of both the northern hemisphere and southern hemisphere Hadley cells in the annual mean (Xia et al., 2020). Similar widening and weakening trends are found for both the JJA and DJF seasons in the CMIP6 models (Xia et al., 2020). In a warming climate, subtropical static stability increases and drives the baroclinic instability zone poleward, consequently expanding the Hadley cell’s outer boundary poleward (Lu et al., 2007). The HC widens as both the SST gradient and global mean temperature rise (Frierson et al., 2007). Therefore, the hypothesis is that the CE-AHT will decrease in both the JJA and DJF seasons in a greenhouse gas-dominated future climate. This implies that the CE-AHT will be more northward in JJA and less northward in DJF.

However, in a warming climate, the annual mean OHT increases in a southward direction due to decreased northward heat transport over the Atlantic Ocean basin (Mecking and Drijfhout, 2023). The Atlantic meridional overturning circulation (AMOC) strength is projected to decline in the CMIP6 model (Weijer et al., 2020), resulting in northern cooling attributed to reduced northward oceanic heat transport from the tropics to the high latitudes (Mecking and Drijfhout, 2023). So, it remains to be explored how the CE-OHT will change in the future climate, likely due to a decrease in northward transport during both the JJA and DJF seasons, driven by the weakening of the AMOC.

The changes in cross-equatorial heat transport are closely linked to the ITCZ in a warming climate. For instance, the seasonal cycle of the ITCZ location is strongly anti-correlated with the CE-AHT, with a regression coefficient of $-3.2^{\circ} \text{PW}^{-1}$ under doubled CO_2 climate conditions (Donohoe et al., 2013). The annual mean ITCZ shift is less than 1° per PW CE-AHT in a warming climate (Byrne et al., 2018). In CMIP6 models under the SSP3-7.0 scenario, the annual mean ITCZ shifts southward ($-0.5 \pm 1.2^{\circ}\text{N}$) (Mamalakis et al., 2021).

The projected weak Hadley circulation (Xia et al., 2020) might have contributed to the reduction of the CE-AHT. Conversely, it is reported that the decrease of oceanic heat transport is associated with a southward shift of the ITCZ (Mecking and Drijfhout, 2023). Hence, a knowledge gap lies between the movement of the ITCZ with respect to cross-equatorial heat transport during JJA and DJF under the SSP5-8.5 scenario.

The location of the ITCZ greatly impacts monsoonal precipitation. Under the SSP5-8.5 scenario, the global land monsoon precipitation will increase (Du et al., 2022) in both near (2021–2040) and long (2080–2099) terms (Chen et al., 2020). A rise in moisture convergence resulting from high surface evaporation and increased water vapour in the atmospheric column causes the expected rise in global monsoon rainfall (Kitoh et al., 2013). The CMIP6 model projection shows significantly increased precipitation for the northern hemisphere monsoon (NHM), southern hemisphere monsoon (SHM), and Asian monsoon with a 1°C warming (Moon and Ha, 2020). Additionally, under SSP2–4.5, the total northern hemisphere land monsoon rainfall is projected to increase by approximately 2.8% per degree Celsius of global warming (Wang et al., 2020). However, this increase is moderate compared to predictions based on the Clausius-Clapeyron approximation (Held and Soden, 2006), partly due to strengthened static stability leading to weaker vertical motion and resulting in reduced precipitation in a warmer atmosphere (Moon and Ha, 2020), as well as the weakening of the monsoon circulation (Kitoh et al., 2013; Chen et al., 2020).

In a warming climate, near-surface specific humidity increases with temperature at a rate of around $6.5\%K^{-1}$ following the Clausius-Clapeyron relationship. However, global mean precipitation increases more slowly, at approximately $2\%K^{-1}$ in climate models (Held and Soden, 2006). Despite this slower increase, global (Du et al., 2022) and regional, such as Asian-Australian (Chevuturi et al., 2018; Ueda et al., 2006) monsoonal precipitation is projected to rise, compensating for a decrease in monsoonal circulation (Sooraj et al., 2015). In a warmed climate, the availability of moisture and its convergence increase and strengthen monsoonal precipitation (Chevuturi et al., 2018; Ueda et al., 2006). A significant driver for changes in monsoon patterns is greenhouse gas (GHG) concentrations, particularly CO₂ (Doblas-Reyes et al., 2021). For the Indian monsoon, the changes in GHG concentration af-

fect the meridional temperature contrast that drives monsoon circulation (Ueda et al., 2006) and influence monsoon winds in the lower troposphere (Krishnan et al., 2013). So, it would be worthy of investigating how cross-equatorial heat transports impact monsoons in a warming climate when greenhouse gas emissions dominate.

In previous chapters, we investigated the relationship between cross-equatorial heat transports (CE-AHT and CE-OHT) and monsoons (both regional and global) using reanalysis (Chapter 3) and CMIP6 (Chapter 4) datasets for the historical period (1979-2020). Expanding on this analysis, our study now shifts its focus to assessing the effects of climate change, with the objective of understanding how it modifies the intricate relationship between cross-equatorial heat transport and monsoonal patterns for the JJA and DJF seasons. This chapter seeks to provide valuable insights into the future forecasts of monsoonal precipitation, Hadley circulation, CE-AHT, CE-OHT, and the ITCZ as projected by CMIP6 models. Hence, all the questions to be examined in Chapter 5 include:

- ▶ What are the patterns of cross-equatorial heat transport in the CMIP6 projected climate? The hypothesis is that the northward CE-AHT increase in JJA and the northward CE-AHT decrease in DJF seasons are due to a greenhouse gas-dominated future climate. For CE-OHT, a northward decrease in both the JJA and DJF seasons is due to the decline of the AMOC if the AMOC is not compensated by transport in the Pacific and Indian Oceans.
- ▶ How will climate change affect the cross-equatorial heat transports, the monsoons, and the interplay between them?

The CMIP6 model projected datasets and methodologies are detailed in Section 5.2, with results discussed in Section 5.3 and conclusions drawn in Section 5.4.

5.2 Data and Methodology

The ScenarioMIP projections forecast the future global climate under various scenarios of greenhouse gas emissions and socio-economic development until the late 21st century,

which are important for societal concerns regarding climate change mitigation, adaptation, or impacts (O'Neill et al., 2016). As described in Chapter 4, table 1, we utilize the data from 13 CMIP6 (after dropping the FGOALS-g3) models to explore the impacts of climate change under the SSP5-8.5 scenario. The SSP5-8.5 scenario is chosen for its representation of a high-emission future, when greenhouse gas concentrations rise significantly due to continued reliance on fossil fuels and energy-consuming lifestyles. This scenario helps in understanding the potential extreme impacts on the climate system, including shifts in the ITCZ and changes in monsoon patterns. By the period 2080-2100, this scenario is dominated by GHG effects, with CO₂ concentrations and other GHGs driving substantial changes in temperature and atmospheric dynamics. Aerosol effects will be relatively weaker compared to the overwhelming influence of GHGs. The selection of SSP5-8.5 thus highlights the upper bound of climate impacts, offering insights into the severe consequences of unmitigated emissions. Long-term changes are estimated for the period 2080–2100, using the base period from 1995 to 2014 (Lee et al., 2023).

The computation of CE-AHT, CE-OHT, stream-function, and the ITCZ location, identified by metric I_{dmsf} and I_{pr} , has been described with detailed information in Chapter 3 (section 3.2) and Chapter 4 (section 4.2). To explore the relationship between cross-equatorial heat transports and the monsoons in the projected climate, regression analysis is performed for the period 2060–2100 as discussed in Chapter 3. I employ the boxplot technique described in Chapter 4 and elaborated upon in Section 4.2.

Different indexes, such as the monsoon precipitation index (MPI) and the monsoon westerly index, are used to identify the global monsoon domain based on precipitation and 850 hPa zonal winds, respectively (Wang and Ding, 2008; Zhou et al., 2008a,b; Wang et al., 2012a, 2013a; Kitoh et al., 2013; Wang et al., 2014; Yim et al., 2014; Geen et al., 2020). The monsoon precipitation index (MPI) assesses the global monsoon domain using the annual range of precipitation relative to the mean precipitation, expressed as follows:

$$\text{MPI} = \frac{\text{Annual range of precipitation}}{\text{Annual mean precipitation}} \quad (5.1)$$

The annual range can be characterized by the difference between summer and winter

precipitation: JJA precipitation minus DJF precipitation in the Northern Hemisphere, and DJF minus JJA in the Southern Hemisphere (Wang and Ding, 2006; Masson-Delmotte et al., 2021). We employ MPI to define the global monsoon domain as regions where the MPI exceeds 0.55, i.e., at least 55% of the annual rainfall falls within the summer season, and the annual precipitation range is greater than 180 mm or 2 mm/day.

5.3 Results

Initially, we analyse the projected CE-AHT and CE-OHT under the SSP5-8.5 scenario. Subsequently, the reliability of the metric I_{dmsf} compared with I_{pr} is demonstrated. Later, potential changes in monsoonal precipitation distribution, Hadley circulation, and ITCZ in response to CE-AHT and CE-OHT changes in a warm climate are discussed. After that, the relationship between the cross-equatorial heat transports and the monsoons in the projected climate is described.

Hence, the climate change effect on heat transports and the monsoons is in subsection 5.3.1. The projected cross-equatorial heat transport are discussed in subsection 5.3.2, and the ITCZ metric I_{dmsf} and I_{pr} in subsection 5.3.3. Lastly, the linkage of heat transports and the monsoons in projected future climate is provided in subsection 5.3.4.

5.3.1 Climate Change Effects on Heat Transports and the Monsoons

Understanding how precipitation, CE-AHT, and CE-OHT evolve under climate change scenarios is crucial for assessing the potential shifts in atmospheric circulation and precipitation regimes, particularly across monsoon domains. Therefore, the changes in precipitation, CE-AHT, and CE-OHT are investigated for future projections spanning 2080–2100, considering 1995–2014 as a base period. For precipitation, long-term changes are shown only for good (MIROC6) and bad (CanESM5 and UKESM1-0-LL) models, while all the models are included in the rest of the analysis.

Figure 5.1 shows the long-term changes in precipitation for the JJA season. In MIROC6, a positive signal of precipitation over the Indian and West African monsoon domains indicates either a strong monsoon or increased local convection due to warming. The signal is

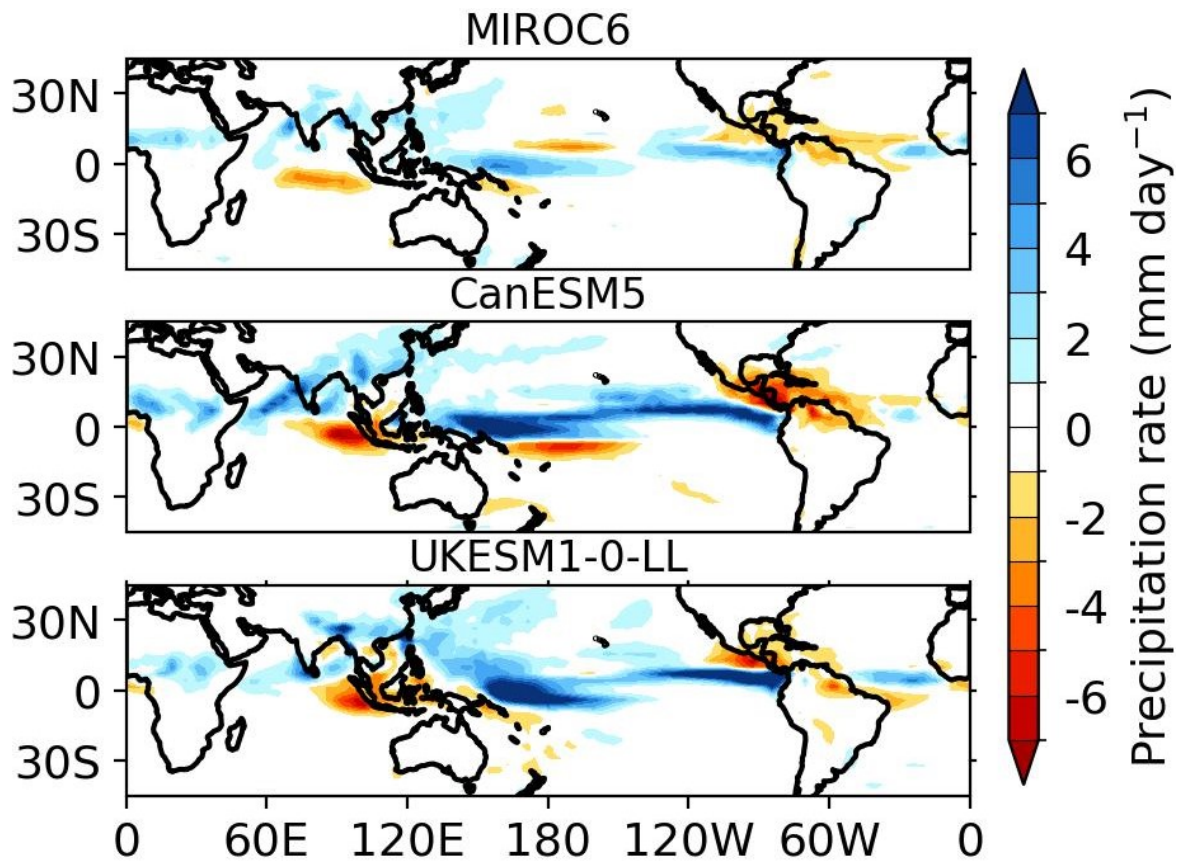


Figure 5.1: Long-term changes in precipitation for good (MIROC6) and bad (CanESM5 and UKESM1-0-LL) models during the JJA season, computed for 2080–2100 with respect to the base period 1995–2014.

comparatively stronger in rest of the two models. Stronger signal of precipitation exists also over the equatorial Pacific Ocean for the bad models. North American monsoon precipitation is stronger MIROC6.

Conversely, Figure 5.1 displays the long-term changes in precipitation for the DJF season. In MIROC6, precipitation over all the southern hemisphere regional monsoon domains are weaker.

To explore how CE-AHT and CE-OHT are changing in the future compared to the base period, box plots are used.

Figure 5.3(i) and 5.3(ii) depict the distribution of projected CE-AHT and CE-OHT, respectively, in a boxplot for the JJA season. Most of the models show an increase and decrease in CE-AHT and CE-OHT in comparison to the historical values, respectively, consistent with the trends. The average CE-AHT rises from 1995–2014 to 2080–2100, while the CE-OHT decreases across all models and amounts to 0.07 ± 0.13 PW in JJA and -0.49 ± 0.26 PW in

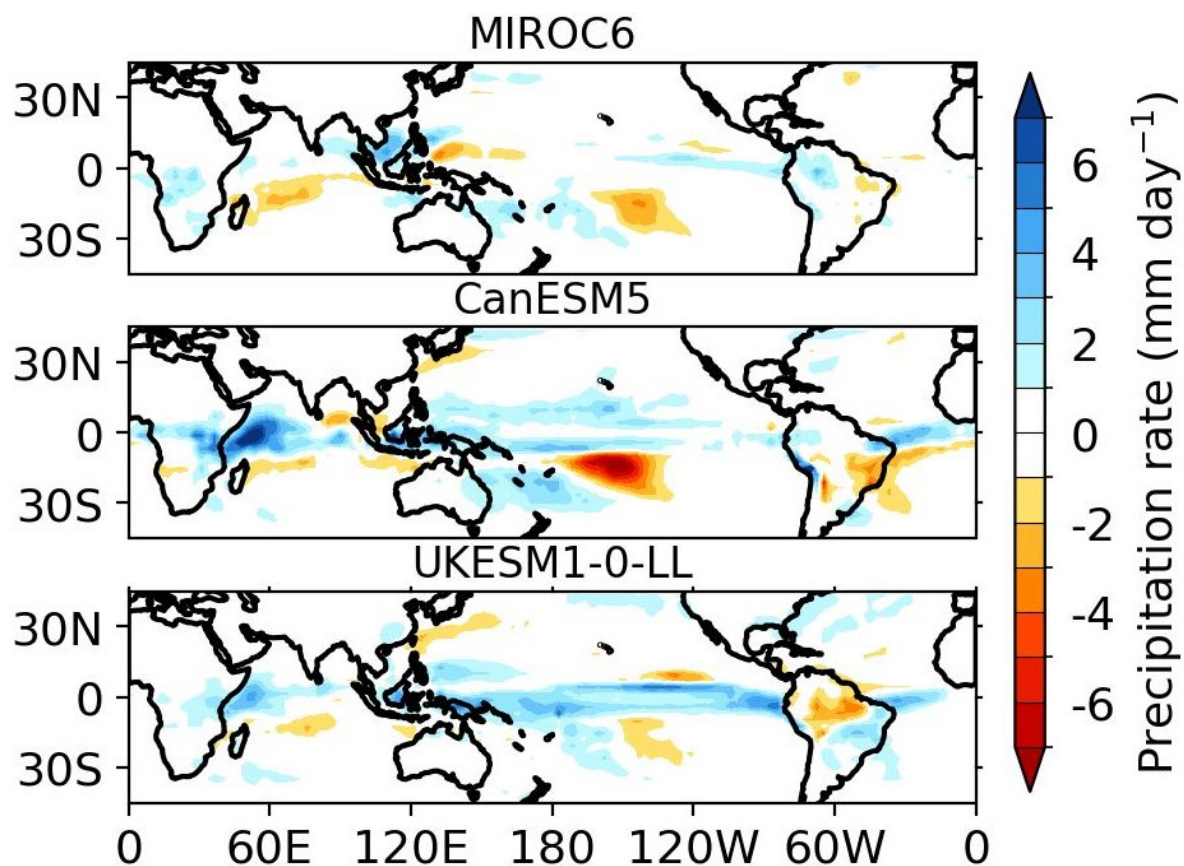


Figure 5.2: Same as Figure 5.1 but for the DJF season.

DJF. The increase of CE-AHT indicates less southward heat transport by the atmospheric circulation, particularly the weak winter Hadley cell (Xia et al., 2020), and the magnitude ranges from 0.03-0.38 PW in future warmer climates. On the other hand, the decrease of CE-OHT, ranging from 0.33-0.81 PW, implies strong southward heat transport via the oceanic circulation.

Unlike the JJA season, Figure 5.5(i) and 5.5(ii) present the projected distribution of CE-AHT and CE-OHT, respectively, using boxplots for the DJF season. CE-AHT and CE-OHT demonstrate a decrease across the majority of models, indicating a reduction in heat export across the equator due to weakened atmospheric (Xia et al., 2020) and oceanic circulation. On average, CE-AHT reduces by -0.14 PW with a standard deviation of 0.16 PW, while CE-OHT decreases by -0.23 PW with a standard deviation of 0.25 PW across all models. The magnitude of decreased CE-AHT values varies between 0.02 and 0.45 PW, and between 0.01–0.63 PW for CE-OHT values.

In relation to the decreases of CE-AHT, Figure 5.4 explains the strengths of stream-

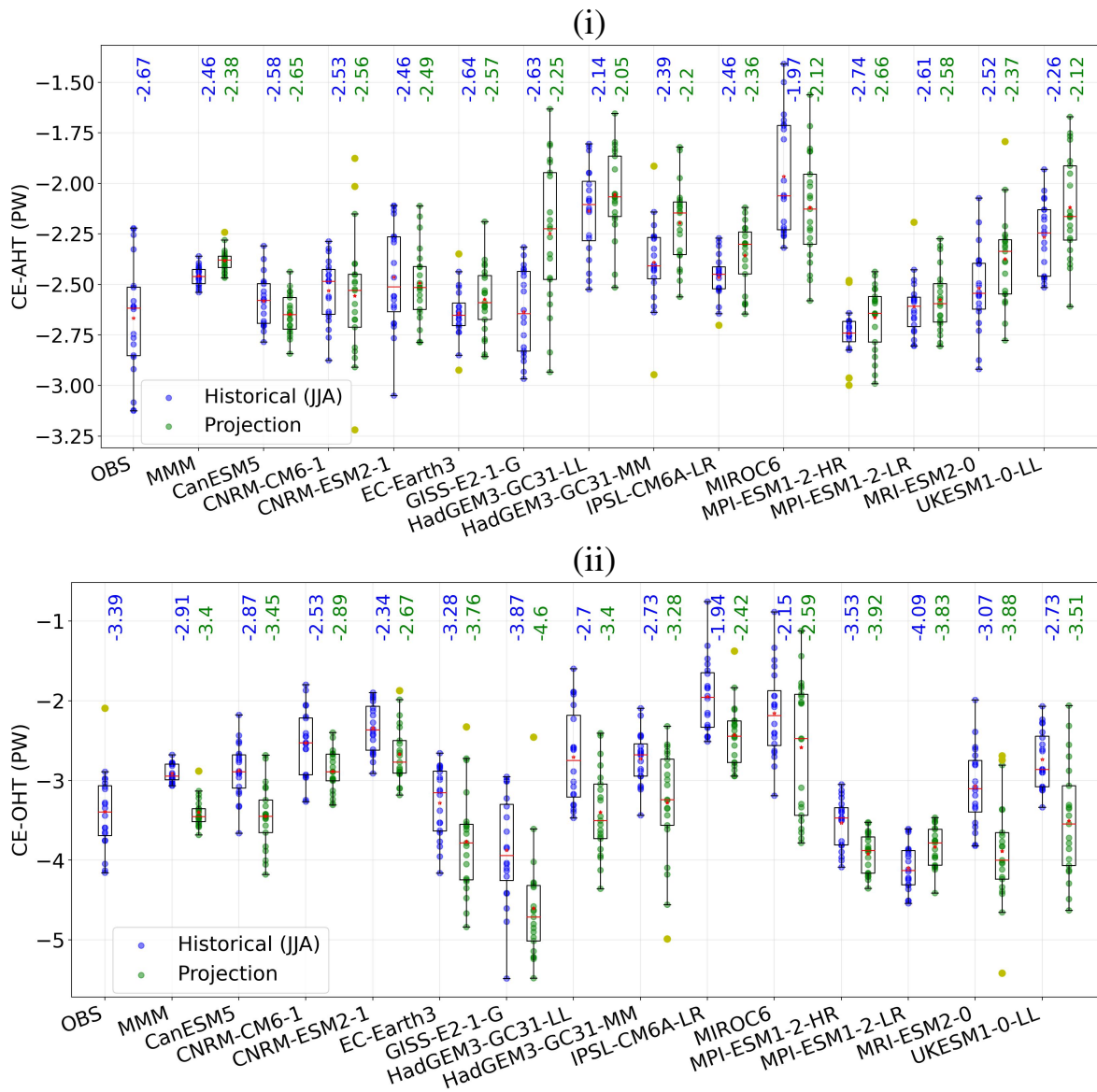


Figure 5.3: (i) CE-AHT during the JJA season is represented utilizing reanalysis and CMIP6 model datasets for the historical periods (1995–2014; blue) and future projections (2080–2100; green). Whiskers denote the data range, excluding outliers, while the lower and upper edges of the box signify the first quartile (Q1) and the third quartile (Q3), respectively. The median is depicted by a red line, the mean by a red star, and the outliers by yellow points. MMM refers to the multi-model mean, and OBS represents ERA-5. (ii) Same as ‘(i)’ but for the CE-OHT, and OBS represents ORAS-5.

function for JJA and DJF seasons spanning 1995–2014 and 2080–2100. Analogous to CE-AHT decreases, the stream-function strength weakens in both JJA (Figure 5.4 (i)) and DJF (Figure 5.4 (ii)) seasons in projected future climates, consistent with the earlier findings of (Xia et al., 2020). The strength of the stream function is calculated, and it shows that the stream function weakens by $0.11 \times 10^{11} \text{ kg s}^{-1}$ in JJA and $-0.2 \times 10^{11} \text{ kg s}^{-1}$ in DJF, with a standard deviation of $0.06 \times 10^{11} \text{ kg s}^{-1}$ and $0.1 \times 10^{11} \text{ kg s}^{-1}$, respectively, across all mod-

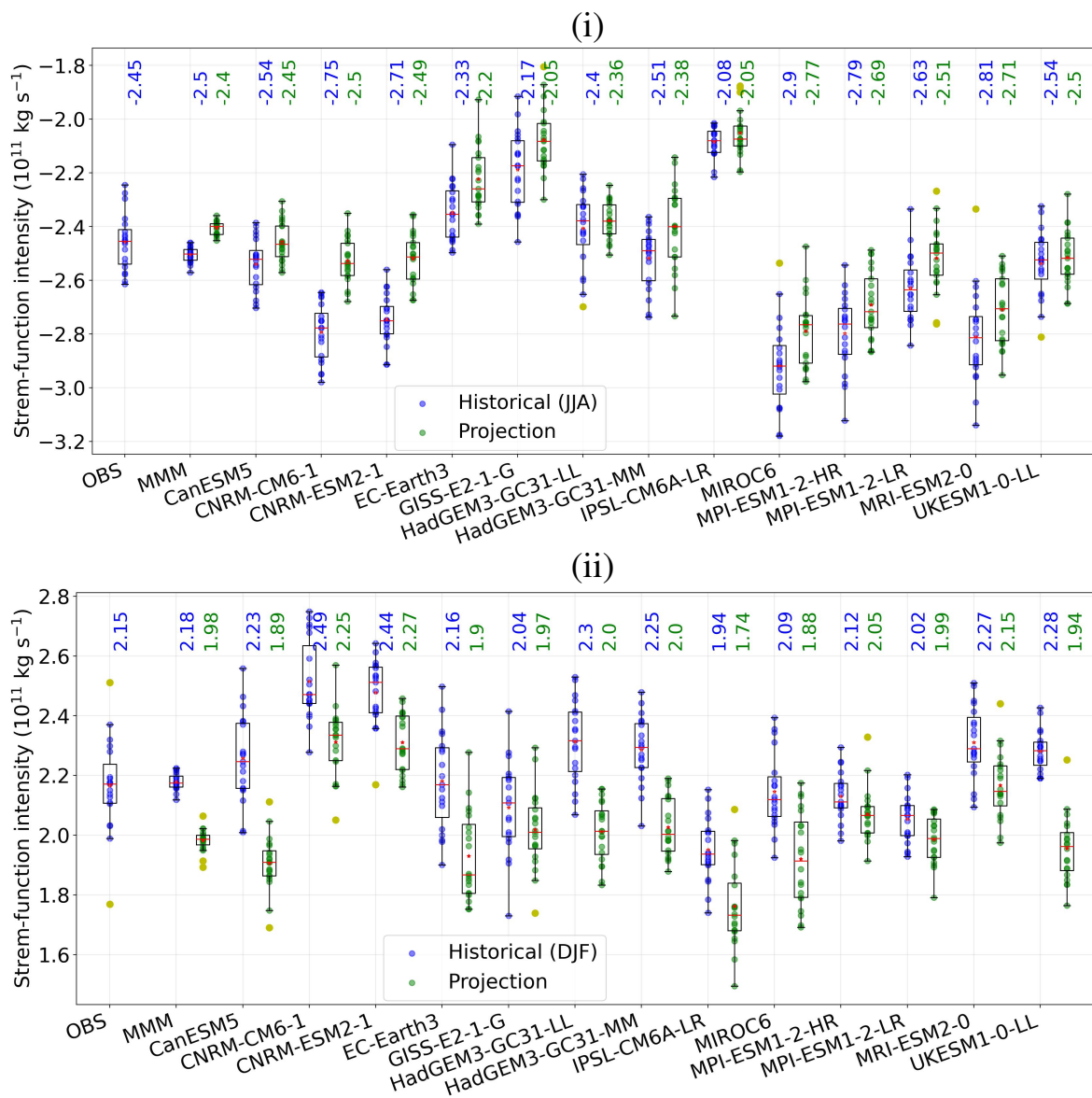


Figure 5.4: Same as Figure 5.3 except for the stream-function strength.

els. The weakening and variability are stronger in DJF season than JJA season, as found in CE-AHT.

It would be worthwhile to explore how the ITCZ shifts in warmer climates compared to the present day.

Figure 5.6 displays the inter-annual latitudinal position of the ITCZ (by I_{pr}) for the JJA season spanning 2080–2100 and 1995–2014. All the CMIP6 models exhibit an equatorward shift of the ITCZ in the projected warmer climate. The equatorward movement of the ITCZ agrees with the increase of CE-AHT and decrease of CE-OHT in the JJA season, as established in Chapter 3 and Chapter 4. Across all models, the average southward shift of

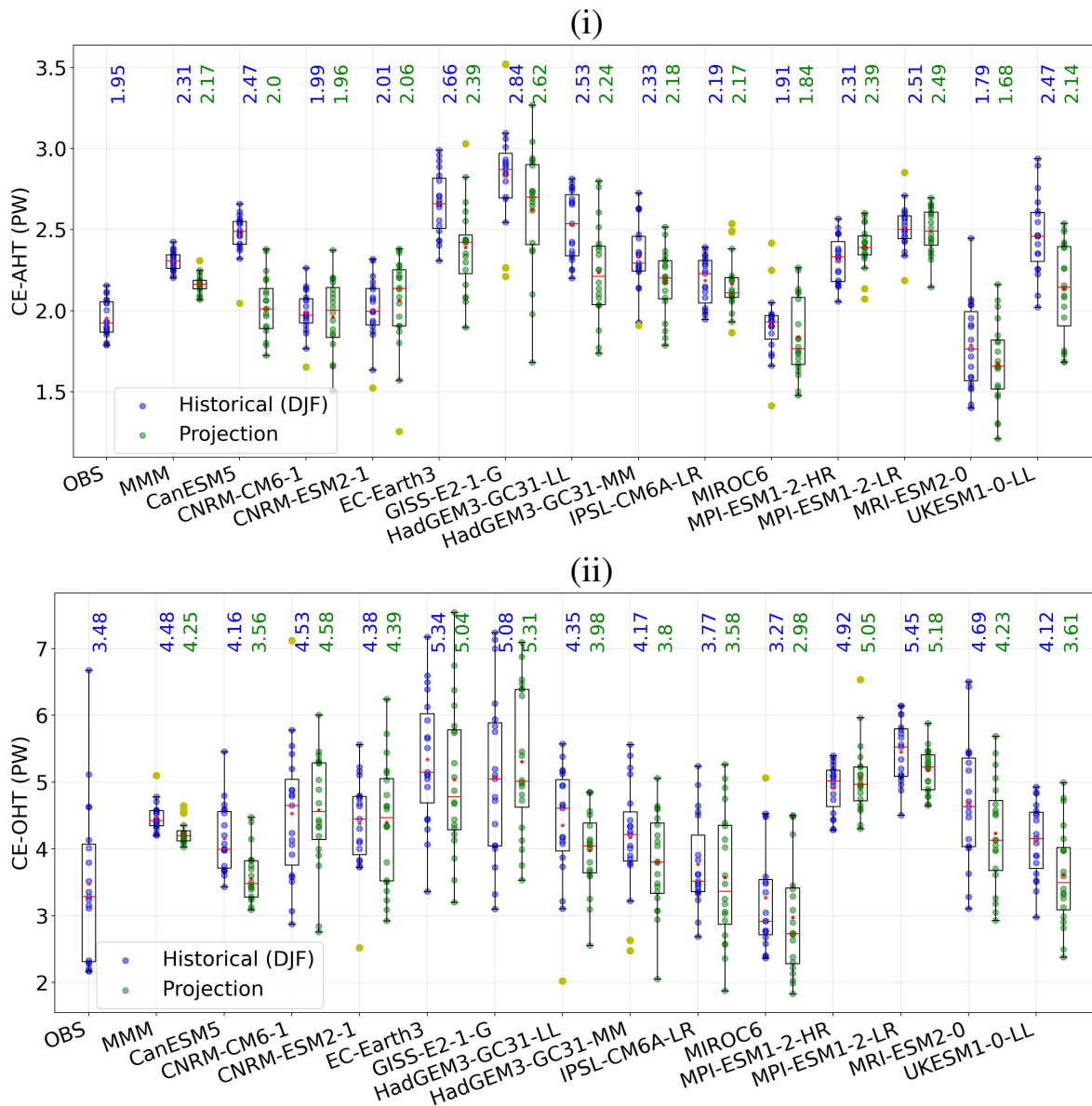


Figure 5.5: Same as in Figure 5.3, but for the DJF season.

the ITCZ is $-0.3 \pm 0.25^\circ\text{N}$, and the mean location is 7.94°N in JJA season under the SSP5-8.5 scenario. In JJA, the ITCZ lying north of the equator has very little movement under a warming climate, similar to the annual case (Byrne et al., 2018).

In contrast to the JJA season, Figure 5.7 illustrates the inter-annual latitudinal position of the ITCZ (by I_{pr}) for the DJF season for the periods 2080–2100 and 1995–2014. Across all CMIP6 models, there is a consistent shift of the ITCZ towards the equator in the projected warmer climate. A decrease in CE-AHT (Figure 5.5(i)) relative to the historical period in DJF indicates an equatorward shift of the ITCZ, which evidences the domination of CE-AHT in the meridional movement of the ITCZ in warmer climates. Under the SSP5-8.5 scenario

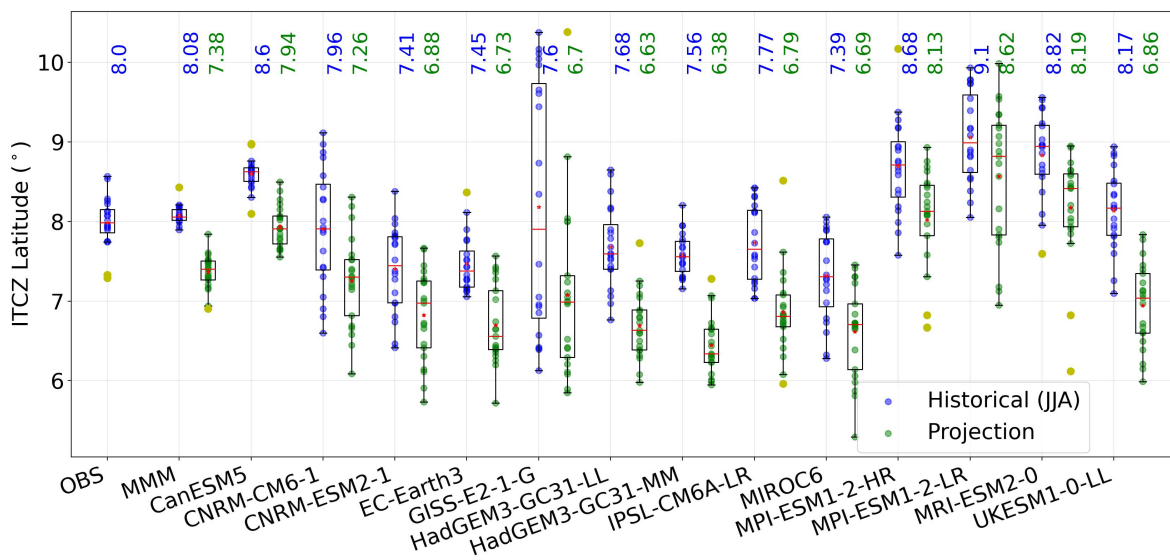


Figure 5.6: The ITCZ location during the JJA season is represented using reanalysis and CMIP6 model datasets for historical (1995–2014; blue) and future projections (2080–2100; green). Whiskers denote the data range, excluding outliers, while the lower and upper edges of the box signify the first quartile (Q1) and the third quartile (Q3), respectively. The median is depicted by a red line, the mean by a red star, and the outliers by yellow points. MMM refers to the multi-model mean.

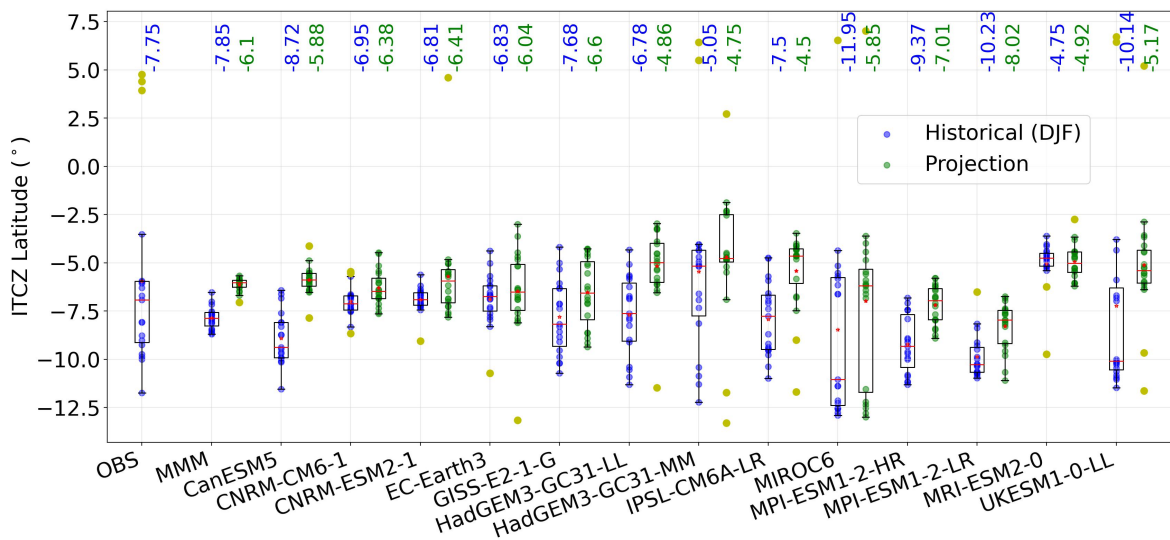


Figure 5.7: Same as Figure 5.6 except for the DJF season.

during DJF, the mean ITCZ lies at approximately 6.1°S, with a typical southward shift of $1.7 \pm 1.8^\circ\text{S}$.

The zonal mean maximum precipitation indicates the strength of the ITCZ. Therefore, understanding how this precipitation changes in the future climate relative to the present day is crucial. Figure 5.8 outlines the zonal mean maximum precipitation intensity for the

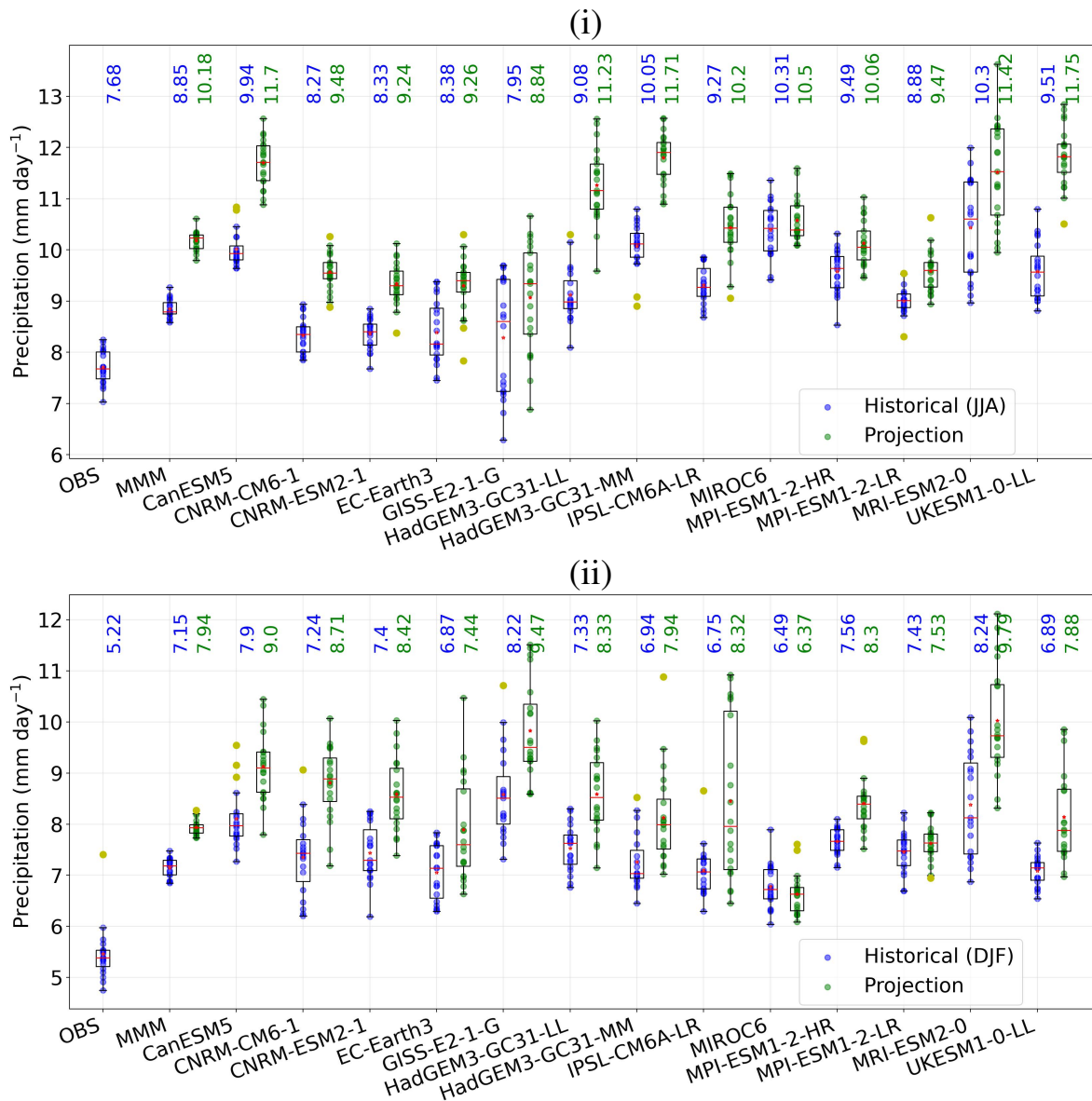


Figure 5.8: (i) The zonal mean precipitation intensity during the JJA season is represented by utilizing reanalysis and CMIP6 model datasets for historical (1995–2014; blue) and future projections (2080–2100; green). Whiskers denote the data range, excluding outliers, while the lower and upper edges of the box signify the first quartile (Q1) and the third quartile (Q3), respectively. The median is depicted by a red line, the mean by a red star, and the outliers by yellow points. MMM refers to the multi-model mean. (ii) Same as ‘(i)’ except for the DJF season.

JJA and DJF seasons, respectively, for the periods 2080–2100 and 1995–2014. In both seasons, the intensity increases across all models (except in MIROC6 in DJF) in warmer climates. The multi-model mean intensity peaks at 10.18 mm day⁻¹ and 7.99 mm day⁻¹ in JJA (Figure 5.8(i)) and DJF (Figure 5.8(ii)) seasons, respectively. The intensity is stronger in the JJA season than in the DJF season. Across all models, there is an average increase of 1.16 ± 0.6 mm day⁻¹ during JJA season, whereas in DJF season, there is an average increase

of $0.94 \pm 0.5 \text{ mm day}^{-1}$.

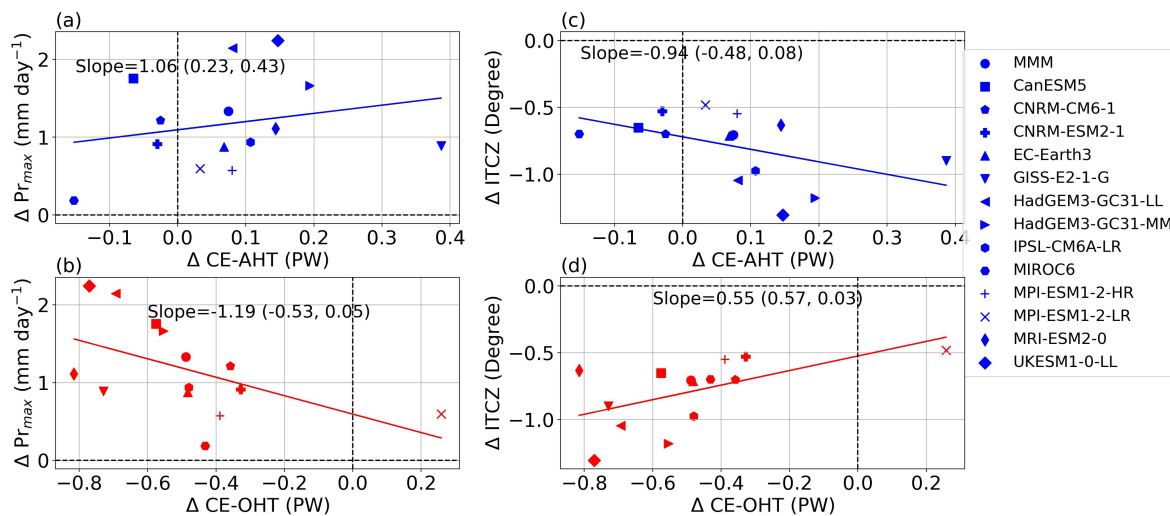


Figure 5.9: (a) Inter-model correlation between zonal mean maximum precipitation changes and CH-AHT changes during the JJA season, computed for 2080–2100 with respect to the base period 1995–2014. The first and second entries in parenthesis represent correlation coefficient and p-value, respectively. (b) Similar analysis for the ITCZ position and CE-AHT. (c) and (d) represent analogous investigations to (a) and (b), respectively, but for CE-OHT. MMM refers to the multi-model mean.

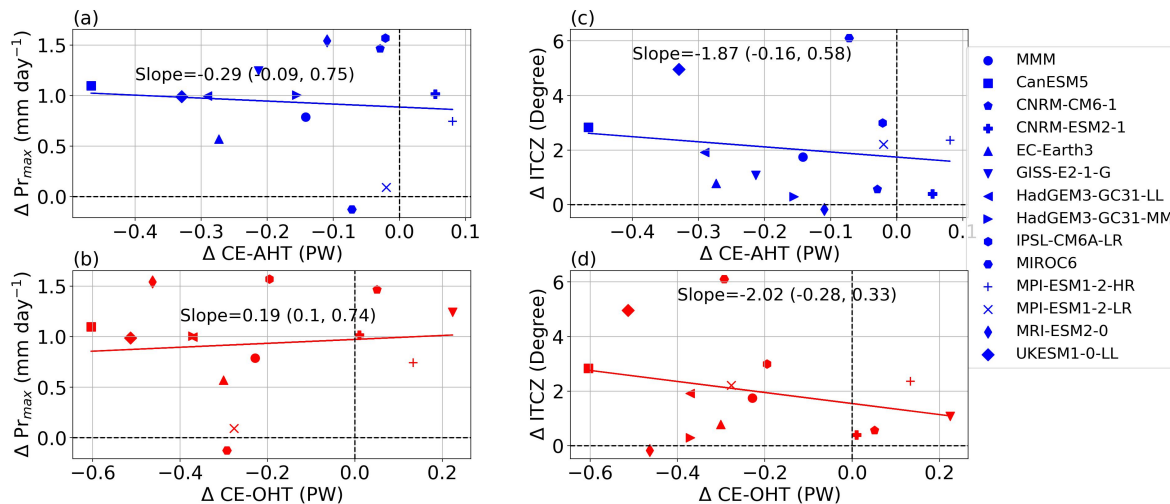


Figure 5.10: Same as Figure 5.9 except for the DJF season.

Figure 5.9 illustrates the changes in zonal mean maximum precipitation, ITCZ position, CE-AHT, and CE-OHT for the period 2080–2100 using the base period 1995–2014 for the JJA season. The increase in precipitation intensity exhibits a strong negative correlation at 95% confidence level with CE-OHT (Figure 5.9(b)), whereas it is weak and insignificant for CE-AHT across all models (Figure 5.9(a)). For each peta Watt CE-OHT increase, the inten-

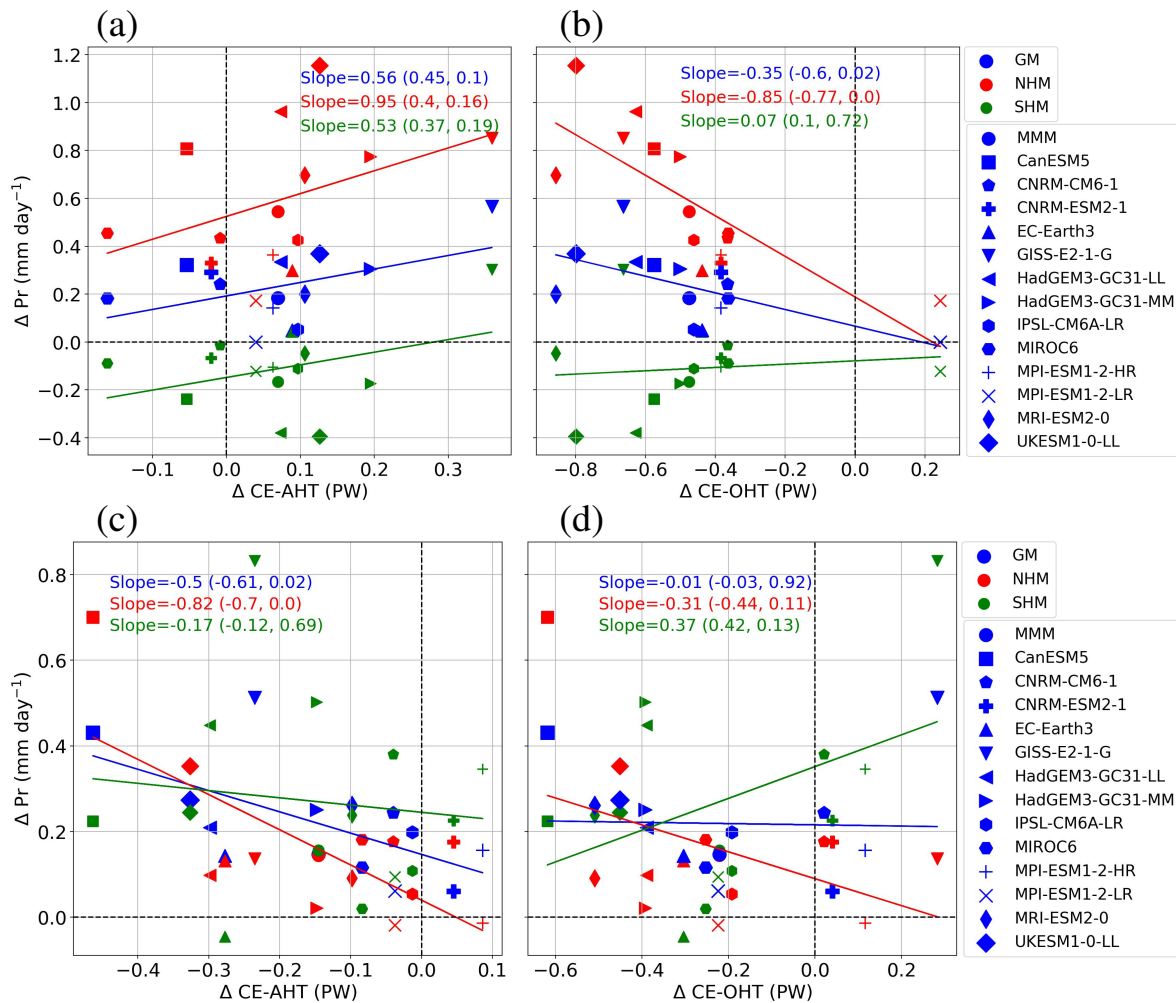


Figure 5.11: (a) Inter-model correlation between global monsoon mean precipitation (45°S – 45°N) changes and CH-AHT changes (blue), northern-hemisphere monsoon mean precipitation (0 – 45°N) changes and CH-AHT changes (red), and southern-hemisphere monsoon mean precipitation (45°S – 0) changes and CH-AHT changes (green), during the JJA season, computed for 2080–2100 with respect to the base period 1995–2014. The first and second entries in parenthesis represent the correlation coefficient and p-value, respectively. (b) Similar analysis for the precipitation and CE-OHT during the JJA season. (c) and (d) represent analogous investigations to (a) and (b), respectively, but for the DJF season. MMM refers to the multi-model mean.

sity of peak precipitation changes by $-1.19 \text{ mm day}^{-1}$ (Figure 5.9(b)). However, the correlation coefficient between the ITCZ position changes and CE-AHT changes is -0.48 with a confidence level of 92% (Figure 5.9(c)). Conversely, the changes in the ITCZ position show a significant positive correlation ($\text{cor} = 0.57$; $p\text{-value} < 0.05$) with CE-OHT (Figure 5.9(d)). The increase of CE-AHT and CE-OHT causes equatorward and poleward movement of the ITCZ relative to the equator and its historical position, as obtained in the previous chapter. In a warmer climate during the JJA season, the increase in precipitation intensity and meridional movement of the ITCZ will be highly influenced by CE-OHT.

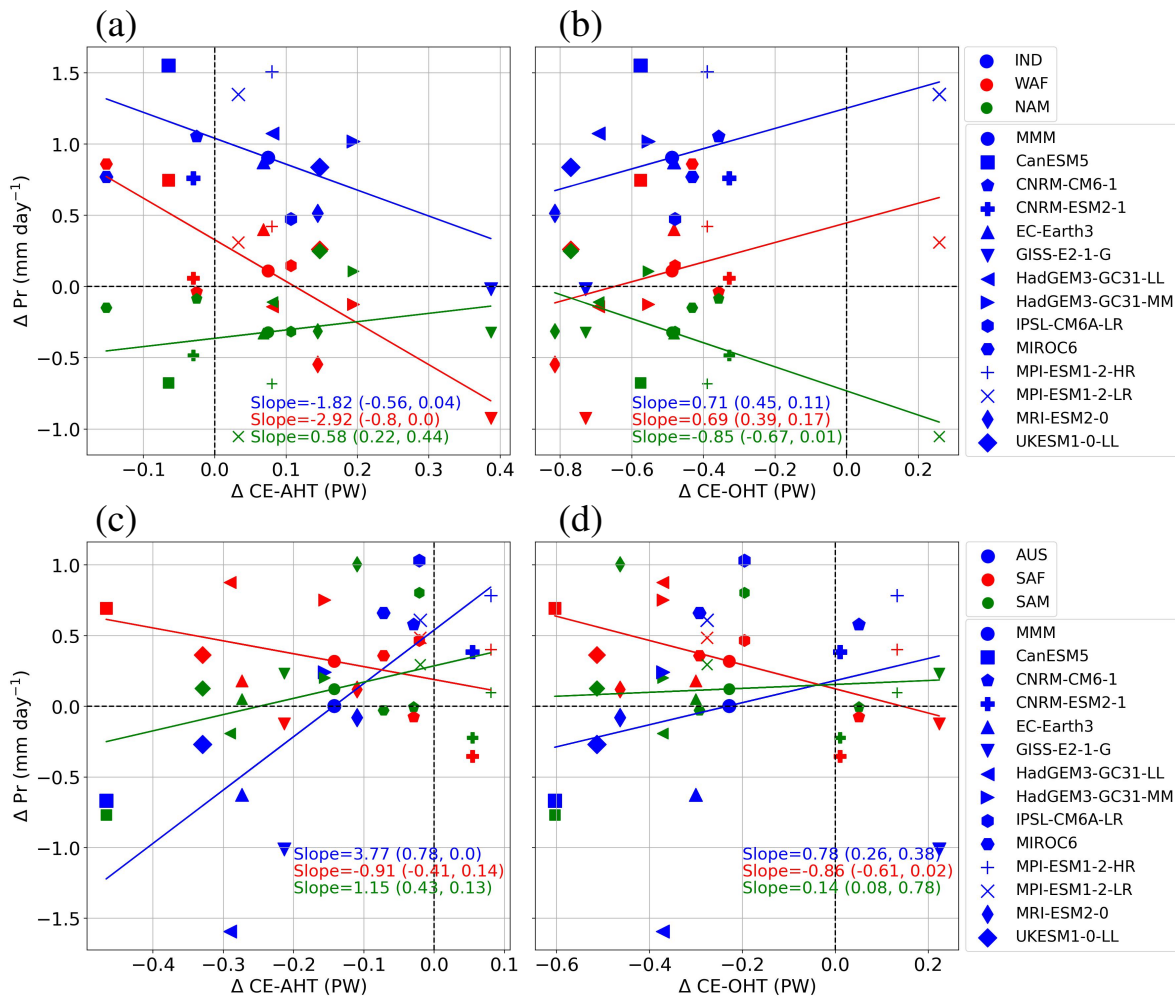


Figure 5.12: (a) Inter-model correlation between Indian monsoon mean precipitation (45°S–45°N) changes and CH-AHT changes (blue), West-African monsoon mean precipitation (0–45°N) changes and CH-AHT changes (red), and North-American monsoon mean precipitation (45°S–0) changes and CH-AHT changes (green), during the JJA season, computed for 2080–2100 with respect to the base period 1995–2014. The first and second entries in parenthesis represent the correlation coefficient and p-value, respectively. (b) Similar analysis for precipitation and CE-OHT during the JJA season. (c) and (d) represent analogous investigations to (a) and (b), respectively, but for the DJF season. MMM refers to the multi-model mean.

In contrast to the JJA season, Figure 5.10 highlights the changes in zonal mean maximum precipitation, ITCZ position, CE-AHT, and CE-OHT for the period 2080–2100 using the base period 1995–2014 for the DJF season. In each case for both precipitation intensity and ITCZ position with CE-AHT and CE-OHT, a nonlinear relationship is noted in Figure 5.10(a), Figure 5.10(b), Figure 5.10(c), and Figure 5.10(d), across all models.

The changes in precipitation in a warmer climate relative to the historical period for global monsoon precipitation, northern-hemisphere precipitation, and southern-hemisphere

precipitation are presented in Figure 5.11, along with the changes in CE-AHT and CE-OHT. During the JJA season, comparing Figure 5.11(a) and Figure 5.11(b), a negative correlation exists between global monsoon precipitation and CE-OHT ($\text{cor} = -0.6$, $\text{p-value} < 0.05$), as well as between northern hemisphere precipitation and CE-OHT ($\text{cor} = -0.77$, $\text{p-value} < 0.05$). Therefore, global monsoon precipitation and northern-hemisphere precipitation decrease with an increase in CE-OHT. Southern-hemisphere precipitation changes are insignificant. However, the correlation is positive for CE-AHT but statistically insignificant for every case.

On the contrary, during DJF season, global monsoon precipitation, northern-hemisphere precipitation, and southern-hemisphere precipitation decrease with the increase of CE-AHT (Figure 5.11(c)). Similar patterns are noticed for CE-OHT, except for southern-hemisphere precipitation (Figure 5.11(d)). Specifically, a negative correlation is found between global monsoon precipitation and CE-AHT ($\text{cor} = -0.61$; $\text{p-value} < 0.02$) (Figure 5.11(c)) and between northern-hemisphere precipitation and CE-AHT ($\text{cor} = -0.82$; $\text{p-value} < 0.001$), whereas it is insignificant for southern-hemisphere precipitation (Figure 5.11(c)). However, for every case, a negative and insignificant correlation is found for the CE-OHT (Figure 5.11(d)).

Figure 5.12(a) and Figure 5.12(b) display the changes in JJA mean precipitation for the Indian, West African, and North American monsoons compared to historical periods, alongside variations in CE-AHT and CE-OHT. Across all models in JJA season, the Indian monsoon precipitation is strong in a warmer climate (Katzenberger et al., 2021), whereas West-African and North American monsoonal precipitation increases and decreases, respectively, in the majority of models (Figure 5.12(a)). In the JJA season, when comparing Figure 5.12(a) and Figure 5.12(b), there is a negative correlation found between Indian monsoon precipitation and CE-AHT ($\text{cor} = -0.56$, $\text{p-value} < 0.05$), as well as between West African monsoon precipitation and CE-AHT ($\text{cor} = -0.80$, $\text{p-value} < 0.05$), whereas the correlation is positive but insignificant for CE-OHT. The increase of CE-AHT moves the ITCZ equatorward, resulting in reduced precipitation over the Indian and West African monsoon domains. The North American monsoonal precipitation decreases with the increase of CE-OHT, with a correlation coefficient of -0.67 ($\text{p-value} < 0.05$) (Figure 5.12(b)). Despite a decrease in CE-AHT

(Figure 5.3), the increase in Indian monsoon precipitation may be linked to heat transport by regional atmospheric and oceanic circulation. (Lutsko et al., 2019) reported that a southward increase in northern Indian Ocean heat transport during JJA strengthens the monsoon but reduces CE-AHT by modulating the surface SST gradient and moist static energy.

On the other hand, Figure 5.12(c) and Figure 5.12(d) illustrate the changes in DJF mean precipitation for the Australian, South African, and South American monsoons compared to historical periods, alongside variations in CE-AHT and CE-OHT. The magnitude and direction of precipitation change exhibit disagreement across models for the Australian (Narsey et al., 2020), South African, and South American monsoons. The Australian monsoonal precipitation increases with the increase of CE-AHT ($\text{cor}=0.78$; $\text{p-value} < 0.05$), and the correlation is not significant for South African and South American monsoons (Figure 5.12(c)). However, the increase of CE-OHT exhibits a significant decrease in South African monsoon precipitation, with a correlation coefficient of -0.61 and $\text{p-value} < 0.05$ (Figure 5.12(c)).

5.3.2 Projected Cross-Equatorial Heat Transport

As discussed in Chapter 3 and Chapter 4, CE-AHT and CE-OHT play crucial roles in redistributing heat between hemispheres, affecting the Hadley circulation and ITCZ and, ultimately, regional monsoon rainfall patterns. Therefore, at first, projections of CE-AHT and CE-OHT are examined.

Figure 5.13(a) and Figure 5.13(b) depict the seasonal cycles of CE-AHT and CE-OHT, respectively. Maximum northward and southward CE-AHT occur in February and August, respectively, in most of the CMIP6 models (Figure 5.13(a)). In contrast, northward CE-OHT peaks in February across all CMIP6 models, while southward CE-OHT peaks in September in most models (Figure 5.13(b)).

Figure 5.14 and Figure 5.15 illustrate the time series of CE-AHT and CE-OHT, respectively, for the JJA season. The projected CE-AHT exhibits a southward transport in all chosen CMIP6 models (Figure 5.14(a)), whereas the future trend is significant and positive in the majority of the models (Figure 5.14(b)). The positive trend indicates a decrease in CE-AHT transport by the Hadley circulation from the northern hemisphere to the southern hemisphere in the JJA season. The weakening trend of the projected Hadley circulation in

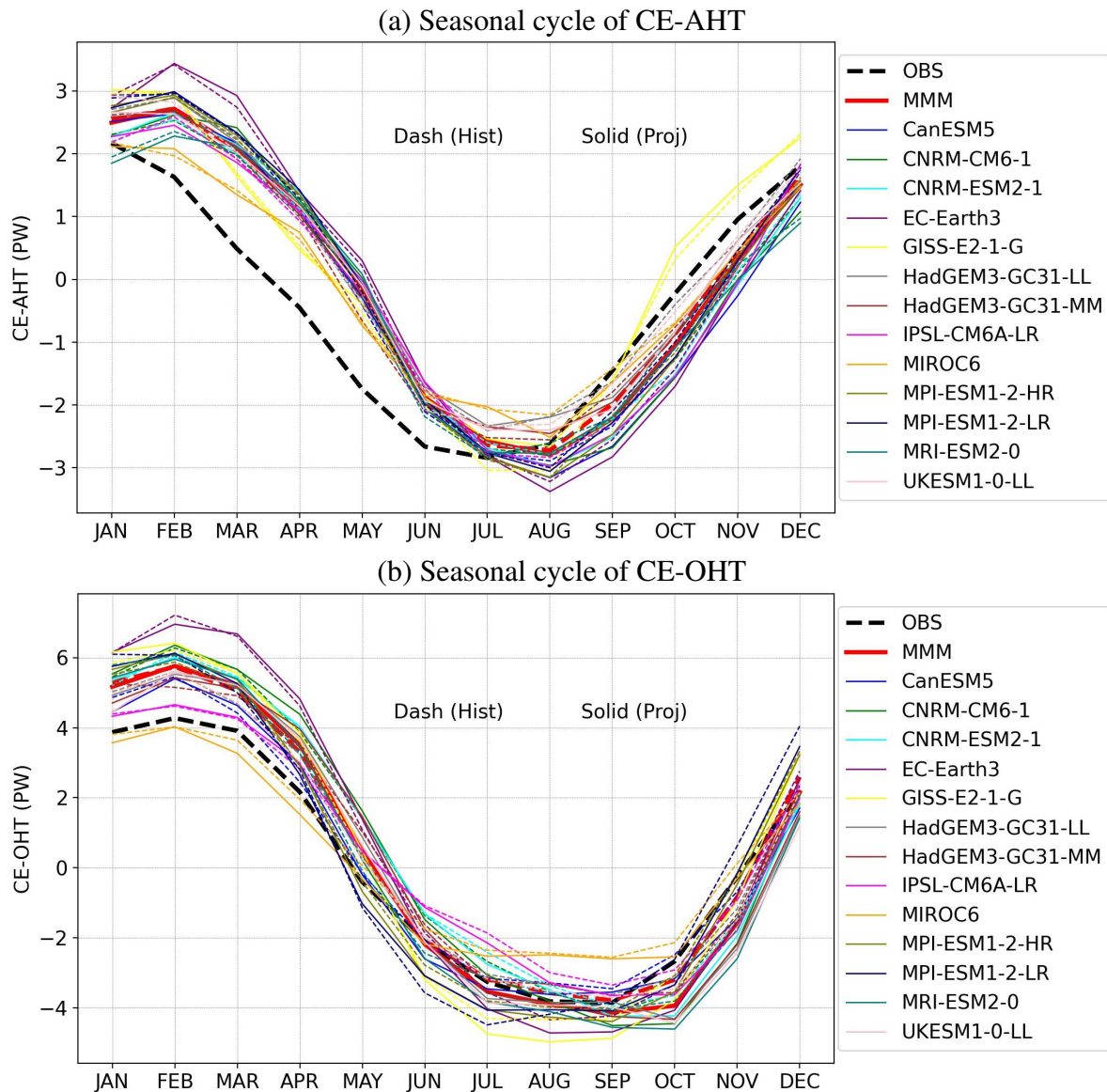


Figure 5.13: (a) The seasonal cycle of the CE-AHT (PW) for various CMIP6 models for the period 2021–2100. Positive and negative denote northward and southward transport, respectively. (b) Same as ‘a’ except for CE-OHT. Here, OBS indicates ERA-5 in (a) and ORAS-5 in (b), and MMM refers to the multi-model mean.

JJA season (Xia et al., 2020) is consistent with the decrease of CE-AHT.

Similarly, the CE-OHT also demonstrates a southward transport in future projection for JJA (Figure 5.15(a)), but the trend is negative and statistically significant across all CMIP6 models, except for the HadGEM3-GC31-MM, MIROC6, and MPI-ESM1-2-LR (Figure 5.15(b)). The negative trend denotes an increase in CE-OHT in a southward direction, that is, a strengthening, across the equator.

In contrast to the southward export in the JJA season, both CE-AHT and CE-OHT show-

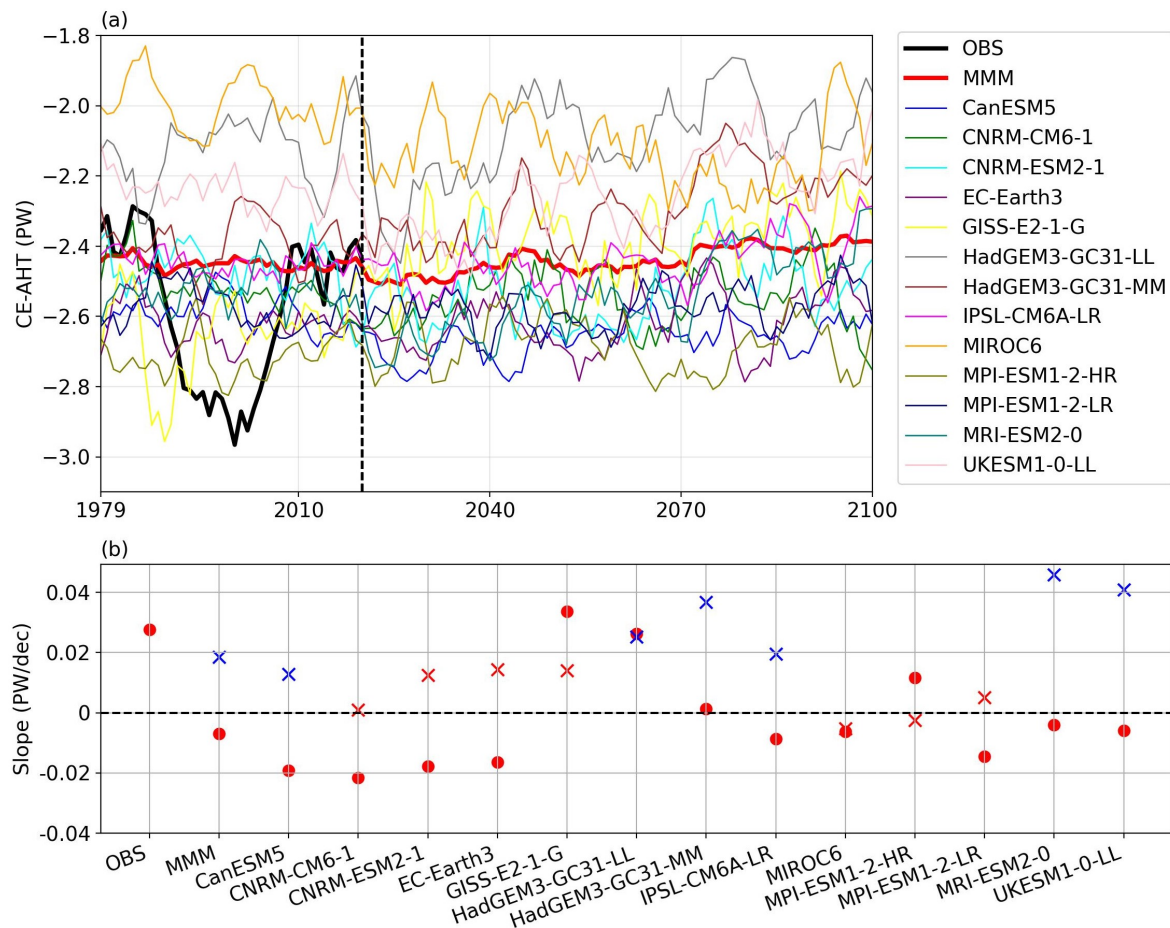


Figure 5.14: (a) The time series of five-year running mean CE-AHT (PW) for various CMIP6 models for the JJA season. (b) The slopes, calculated using linear regression, of the corresponding CE-AHT time series for the period 1960–2020 in dots and 2021–2100 in cross markers (blue: statistical significance at the 95% confidence level or higher; red color markers: statistically insignificant at the 95% confidence level), measured in PW per decade. Positive and negative denote northward and southward transport, respectively. Here, OBS indicates ERA-5, and MMM refers to the multi-model mean.

case a northward export, as displayed in Figure 5.16(a) and Figure 5.17(a), respectively, for the DJF season. The trend of CE-AHT is negatively significant only in a few models in a warming climate (Figure 5.16(b)). In DJF season, the negative trend implies a decrease in CE-AHT by the Hadley circulation from the southern hemisphere to the northern hemisphere. The weakening CE-AHT trend aligns with the projected decrease in the Hadley circulation during the DJF season, as noted in (Xia et al., 2020). On the other hand, the trend of CE-OHT is negative and statistically significant only in CanESM5, and represents a reduction by ocean circulation (Figure 5.17(b)).

Figure 5.18 depicts the BJC, a climate phenomenon where changes in heat transport by

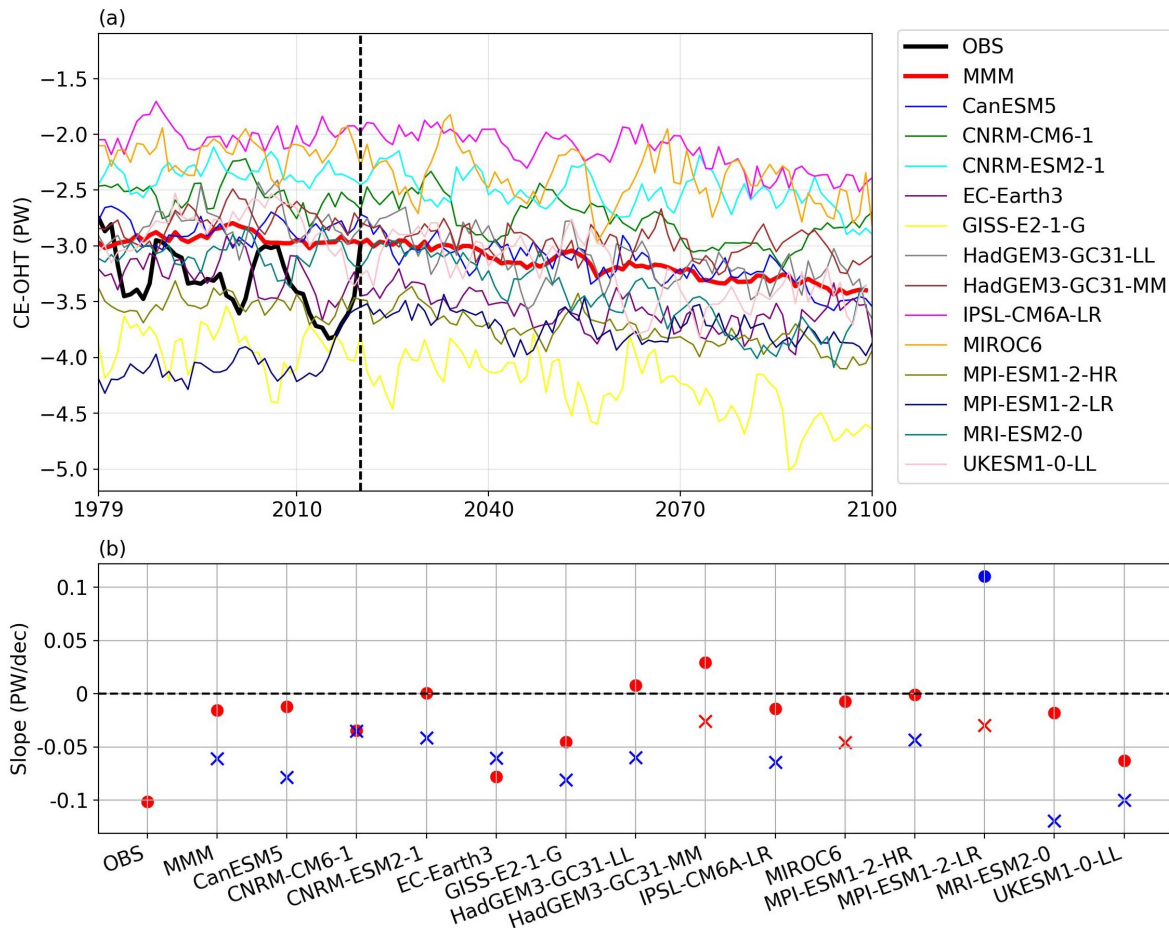


Figure 5.15: As in Figure 5.14 but for CE-OHT, and OBS refers to ORAS-5.

the atmosphere and ocean tend to balance each other out, between CE-AHT and CE-OHT in the future projected climate. This compensation signifies how the atmosphere and ocean will interact with each other in the future projection. In JJA season, the BJC prevails in most of the CMIP6 models, but it is statistically significant and relatively stronger in the MMM, IPSL-CM6A-LR, and MIROC6 models on an inter-annual time scale. Similarly, in DJF season, the statistically significant negative relationship between CE-AHT and CE-OHT is present in most of the CMIP6 models.

In non-equilibrium climates, BJC relies on factors such as energy conservation and local climate feedback. When the climate is influenced by both heat and freshwater flux perturbations, the occurrence of BJC largely depends on the interactions among meridional temperature gradients, salinity gradients, and the strength of thermohaline circulation (Yang et al., 2016). During transient climate change, BJC remains well-established when variations in ocean heat storage are slow and significantly smaller than changes in net heat flux at the ocean surface (Yang et al., 2017). However, greenhouse-gas forcing fails BJC by violating

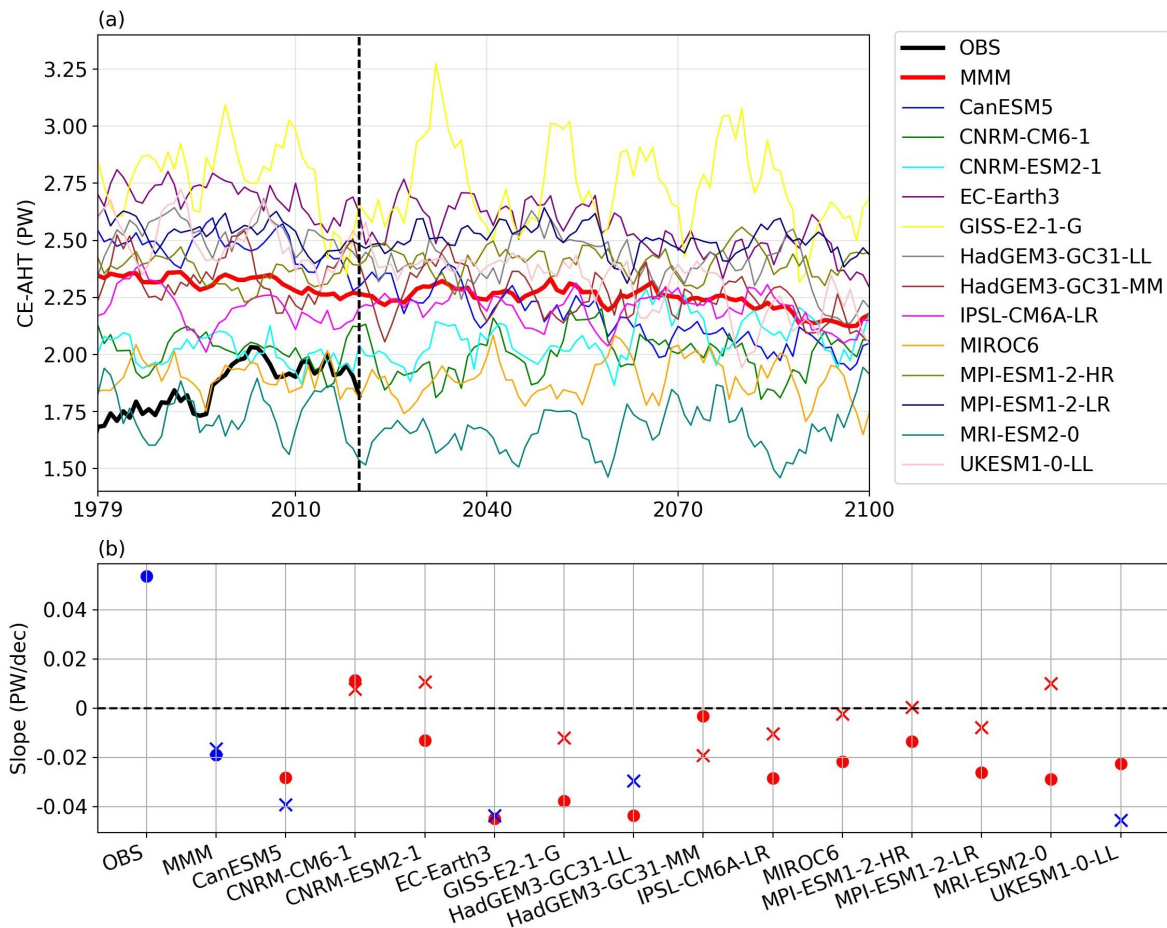


Figure 5.16: Same as Figure 5.14 except for the DJF season.

global energy conservation (Yang et al., 2016).

If Bjerknes compensation does not occur at the equator, it is possible for the compensation to manifest at another latitude, as the mechanism is influenced by regional energy fluxes and dynamic feedback processes. However, this remains an open question that requires further study to determine the conditions under which BJC may occur at a different latitude and the processes that govern such shifts.

Figure 5.19(a) and Figure 5.19(b) illustrate the long-term mean inter-model relationship between CE-AHT and CE-OHT for the JJA and DJF seasons, respectively. In the JJA season, 1 PW CE-AHT change is compensated by 0.77 PW CE-OHT, but it is statistically insignificant. In DJF season in turn, it is stronger and statistically significant, and 1 PW CE-AHT change is compensated by 1.45 PW CE-OHT (Figure 5.19(b)). The multi-model relationship demonstrates weak associations among the models during JJA and strong associations during DJF, with each model representing cross-equatorial heat transport (CE-AHT along the x-axis and CE-OHT along the y-axis). It provides insights into how different models simu-

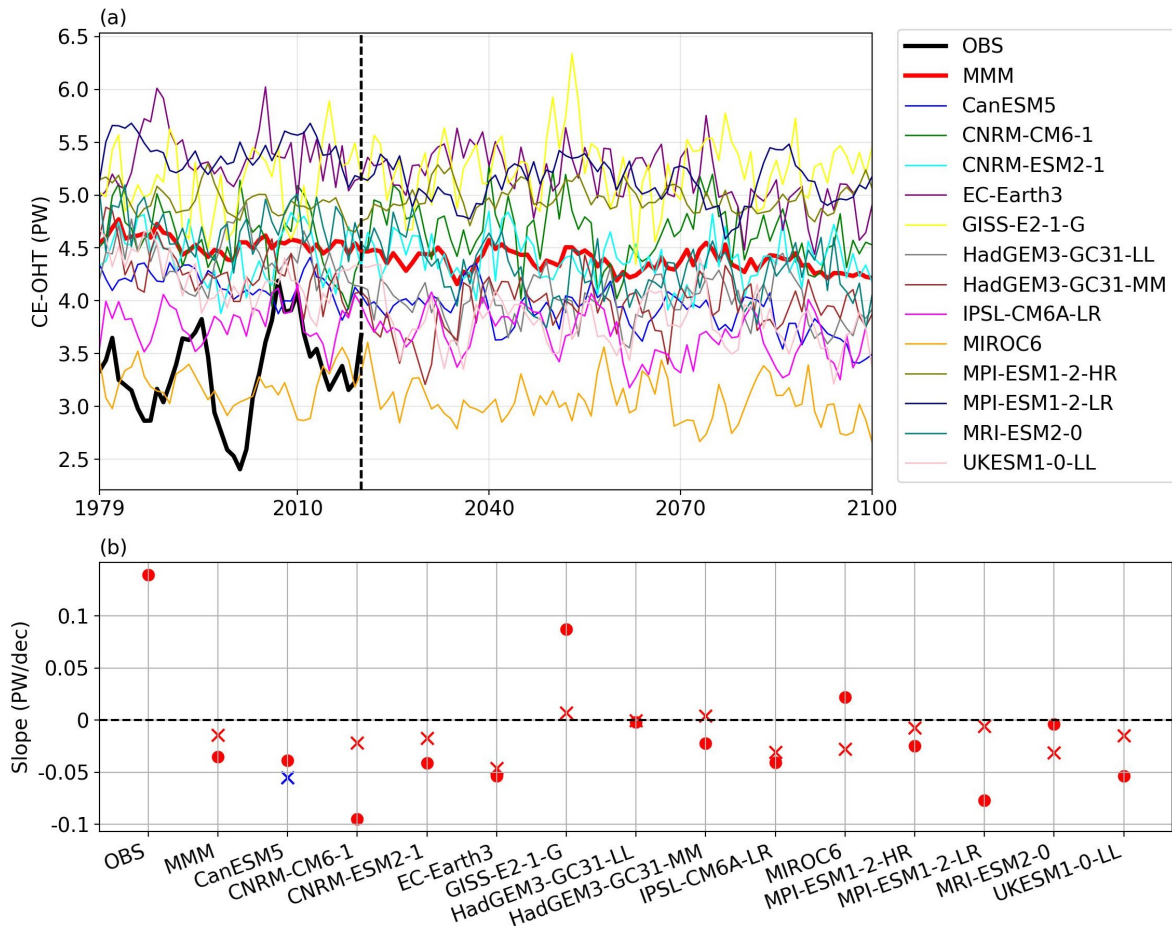


Figure 5.17: Same as Figure 5.15 except for the DJF season

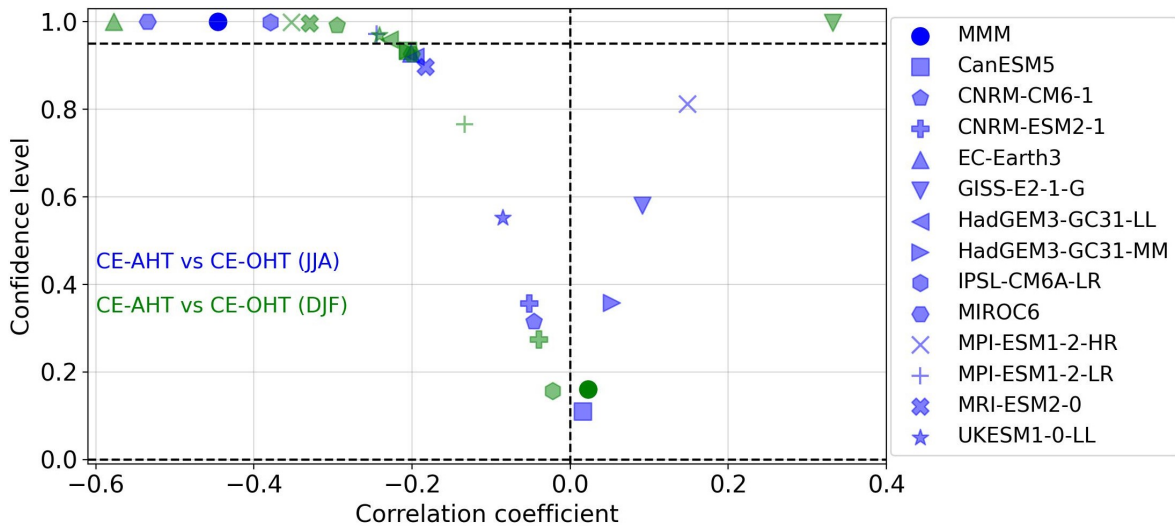


Figure 5.18: The inter-annual correlation coefficient between CE-AHT and CE-OHT for JJA (blue markers) and DJF (green markers) for 2021–2100 for each CMIP6 model. The vertical axis represents the confidence level. MMM refers to the multi-model mean. The dashed horizontal line (at 0.95) indicates the 95% confidence level.

late heat transport processes, which could be influenced by their design, parameterizations, or resolution.

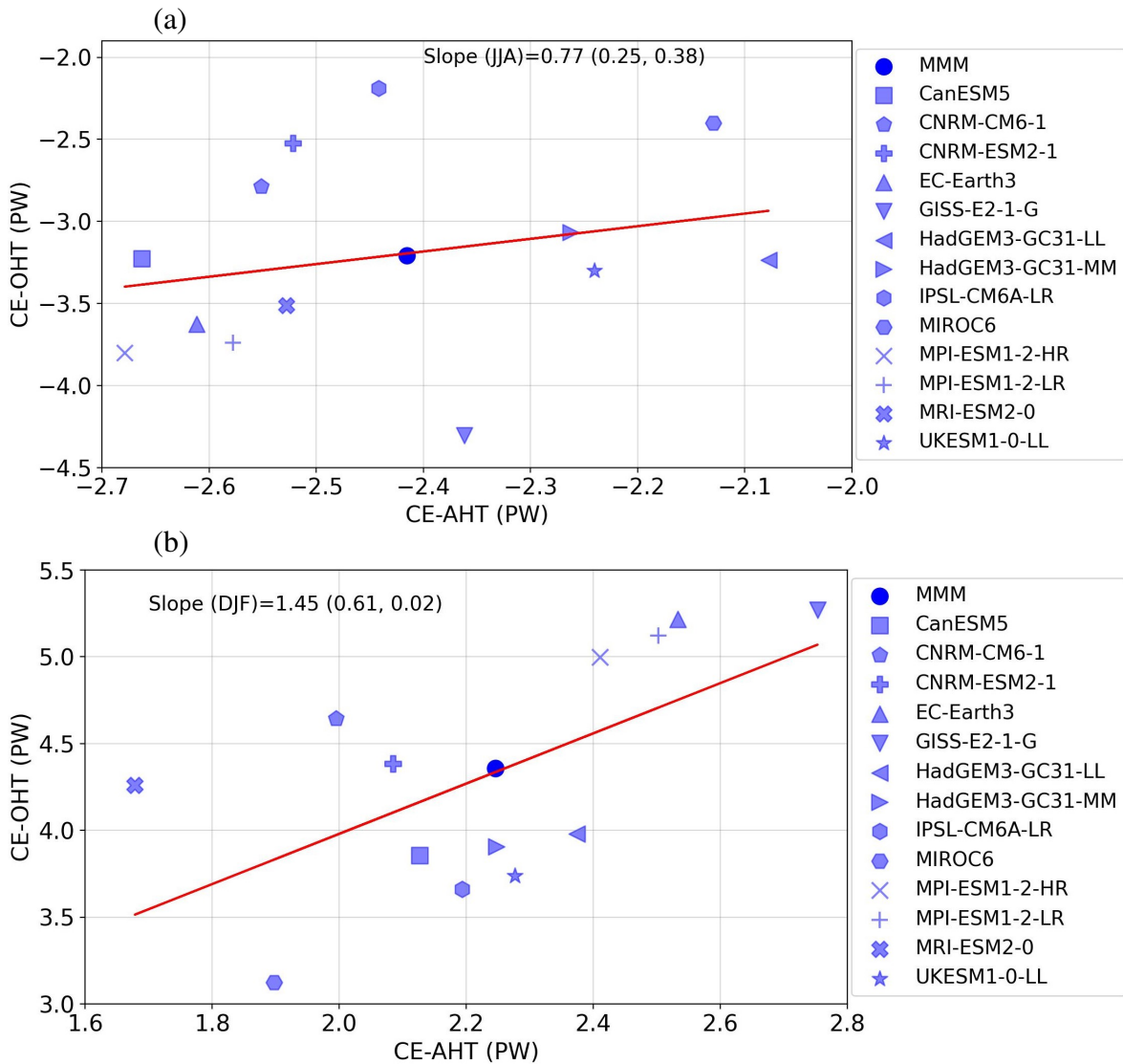


Figure 5.19: (a) The inter-model relationship between CE-AHT and CE-OHT for the time-averaged JJA season spanning 2021–2100. The correlation coefficient and p-value from linear regression are provided as the first and second entries inside the parenthesis. (b) Same as ‘a’ except for the DJF season. MMM refers to the multi-model mean.

Therefore, under SSP5-8.5, the CE-AHT exhibits a significant increasing trend and the CE-OHT a decreasing trend in most of the models in the future projection for the JJA season. In DJF, both the CE-AHT and CE-OHT display a decreasing trend in both JJA and DJF seasons but are not statistically significant, particularly for the CE-OHT. The coupled relationship between the atmosphere and ocean in terms of Berknes compensation is noticeable in a few models in the future projection. The inter-model relationship between CE-AHT and CE-OHT is significant and strong, i.e. if the mean AHT increases, the mean OHT also increases, in the DJF seasons, but the compensation pattern is absent in both seasons.

5.3.3 Reliability of the ITCZ metric I_{msf}

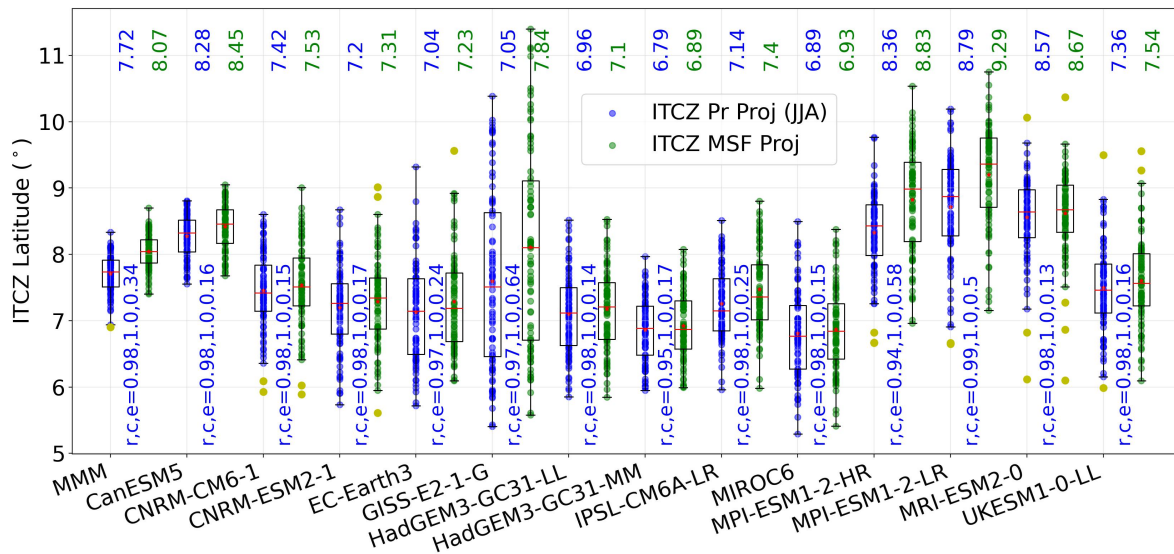


Figure 5.20: The latitudinal position of the ITCZ using zonal mean precipitation (I_{pr} , blue dots) and mid-tropospheric stream function (I_{dmsf} , green dots) for the inter-annual JJA season in the CMIP6 model datasets for the period 2021–2100. The whiskers indicate the range of the data, excluding outliers. The lower and upper edges of the box represent the first quartile (Q1) and the third quartile (Q3), respectively. The median is shown as a red line, and the mean is shown as a red star. Outliers are indicated by yellow dots. At the bottom, ‘r’, ‘c’, and ‘e’ refer to the inter-annual correlation coefficient, confidence level, and RMSE error, respectively, between inter-annual I_{pr} and I_{dmsf} . For JJA mean, the latitudes of the ITCZ by I_{pr} and I_{dmsf} are given by the top blue and green numbers, respectively. MMM refers to the multi-model mean. The I_{pr} and I_{dmsf} metrics are discussed in Chapter 3 and Section 3.2.

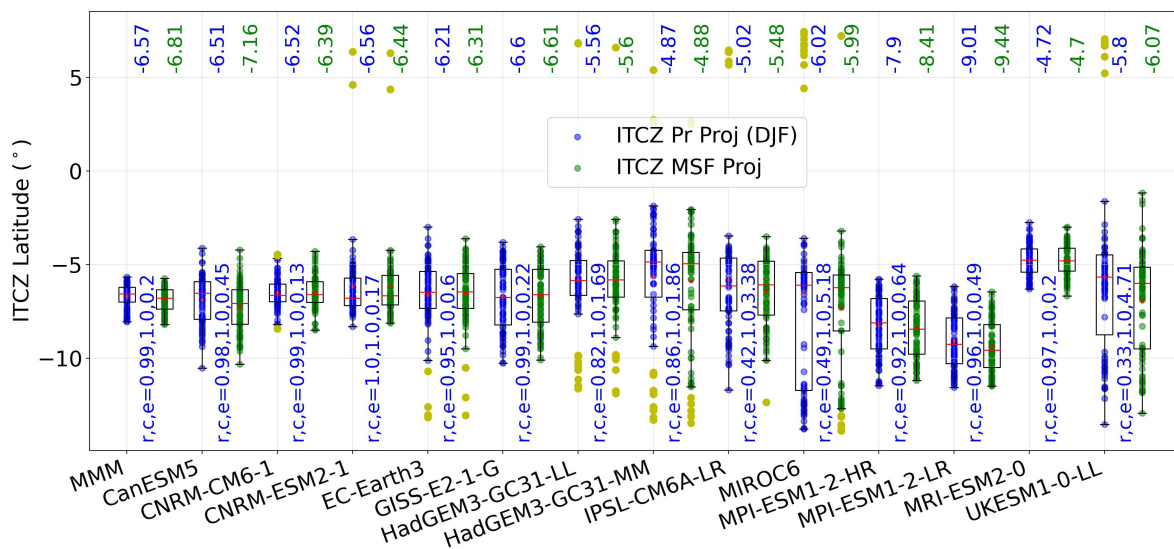


Figure 5.21: Same as Figure 5.20 except for the DJF season.

The position of the ITCZ in future projections provides an idea of precipitation distribution. The ITCZ position can be found using the precipitation-based I_{pr} metric and the stream

function-based I_{dmsf} metric. Since the metric I_{dmsf} is also used in this chapter to identify the position of the ITCZ, it is necessary to verify whether I_{dmsf} is capable of determining the ITCZ latitude in comparison to the I_{pr} metric. Figure 5.20 and Figure 5.21 depict the zonal mean ITCZ position as estimated by the I_{pr} and I_{dmsf} metrics for the JJA and DJF seasons, respectively, spanning the period 2021–2100. These metrics exhibit a strong positive correlation (p -value <0.001) in identifying the ITCZ on an inter-annual scale for both seasons. During JJA, the ITCZ resides north of the equator, with each CMIP6 model's estimation falling between 6.8°N – 8.8°N (I_{pr}) and 6.9°N – 9.3°N (I_{dmsf}). Conversely, in DJF, the ITCZ shifts south of the equator, displaying variations across models, ranging from 4.7°S – 9.0°S (I_{pr}) to 4.7°S – 9.4°S (I_{dmsf}). The root mean square error (RMSE) ranges from 0.13° to 0.64° in JJA and from 0.13° to 5.2° in DJF. Notably, the I_{dmsf} metric effectively locates the ITCZ, as determined by I_{pr} , for both seasons, demonstrating a tendency towards the north and south poles in the JJA and DJF seasons, respectively. Hence, the position of the ITCZ determined by the I_{dmsf} metric is a good approximation of I_{pr} .

5.3.4 Heat Transport and the Monsoons in the future Climate

The relationship between cross-Equatorial heat transport (CE-AHT and CE-OHT) and monsoons has been investigated in reanalysis in Chapter 3 and in CMIP6 models for the historical period in Chapter 4. It is also explored whether the relationship changes in the projected climate under the SSP5-8.5 scenario.

In the projected climate under the SSP5-8.5 scenario, the established relationships in historical periods between northward CE-AHT and CE-OHT anomalies and their consequent effects on atmospheric circulation patterns and precipitation regimes persist. Considering the consistent patterns found across all CMIP6 models over inter-annual time scales in the future projections, only the movement of the ITCZ (winter-Hadley cell rising branch) in response to future changes in CE-AHT and CE-OHT during both the JJA and DJF seasons is discussed below.

Figure 5.22(a) and Figure 5.22(b) illustrate the latitudinal fluctuation of the ITCZ in a warming climate with the increase of CE-AHT and CE-OHT, respectively, for the JJA

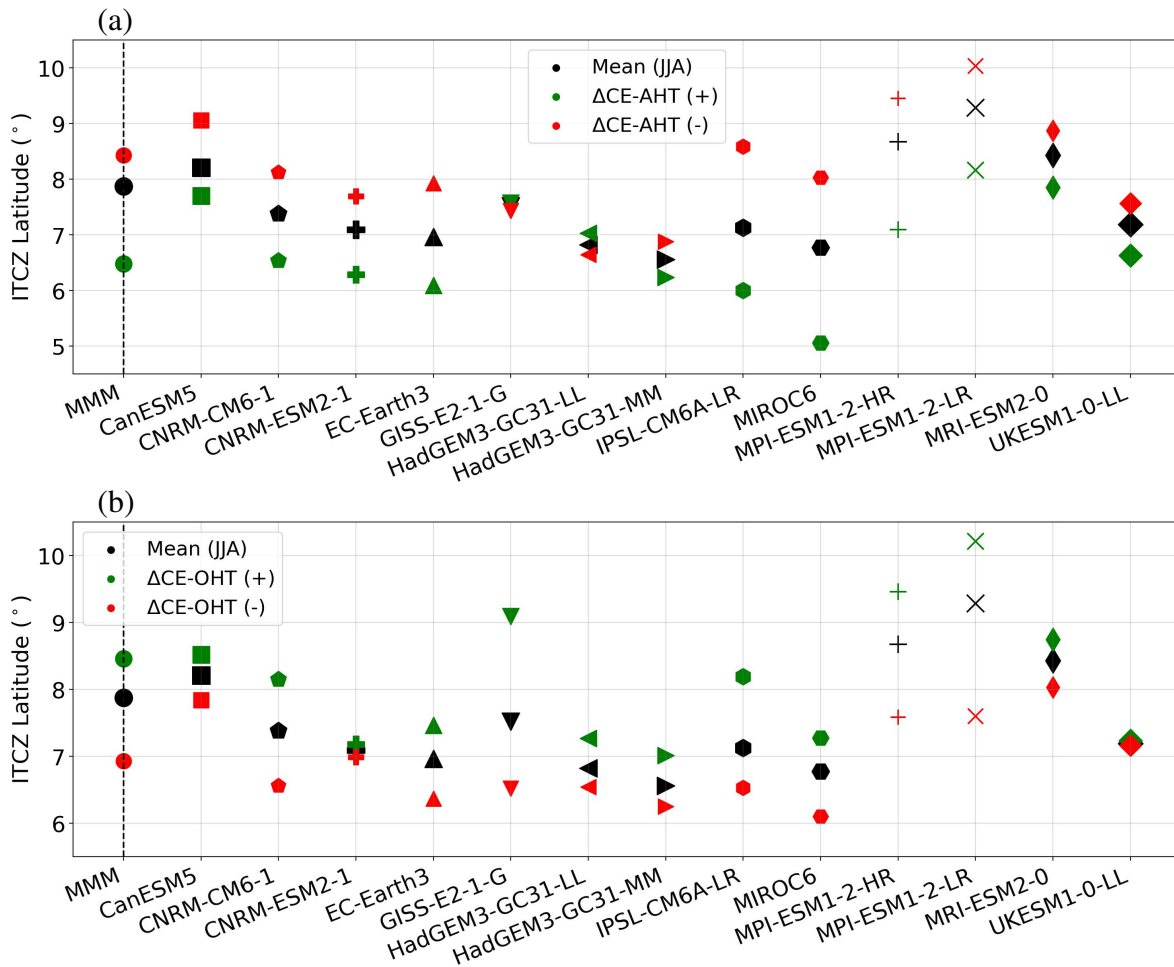


Figure 5.22: (a) The latitudinal position of the Hadley Cell rising branch in the JJA season: regression of the stream-function onto CE-AHT in CMIP6 models data for the period 2060–2100. Marker points are used to indicate the rising branch’s position for the climatological mean (black), positive CE-AHT anomaly (red), and negative CE-AHT anomaly (blue). (b) Same as ‘a’ but for the CE-OHT. MMM refers to the multi-model mean.

season. The ITCZ moves towards the equator for northward CE-AHT (Figure 5.22(a)) and southward CE-OHT (Figure 5.22(b)) anomalies, as expected, whereas the movement is poleward for southward CE-AHT and northward CE-OHT anomalies in the majority of models. In contrast to JJA, during DJF season, the ITCZ is pushed away from the equator and its mean position with the increase of northward CE-AHT (Figure 5.23(a)) and southward CE-OHT (Figure 5.23(b)) and vice versa.

In a warming climate, the relationship between cross-equatorial heat transport and the ITCZ movement exhibits notable consistency with historical patterns. The patterns of all other variables, such as winds (850 hPa and 200 hPa), stream-function, precipitation, and SST, in response to cross-equatorial heat transport under the SSP5-8.5 scenario are summarized below.

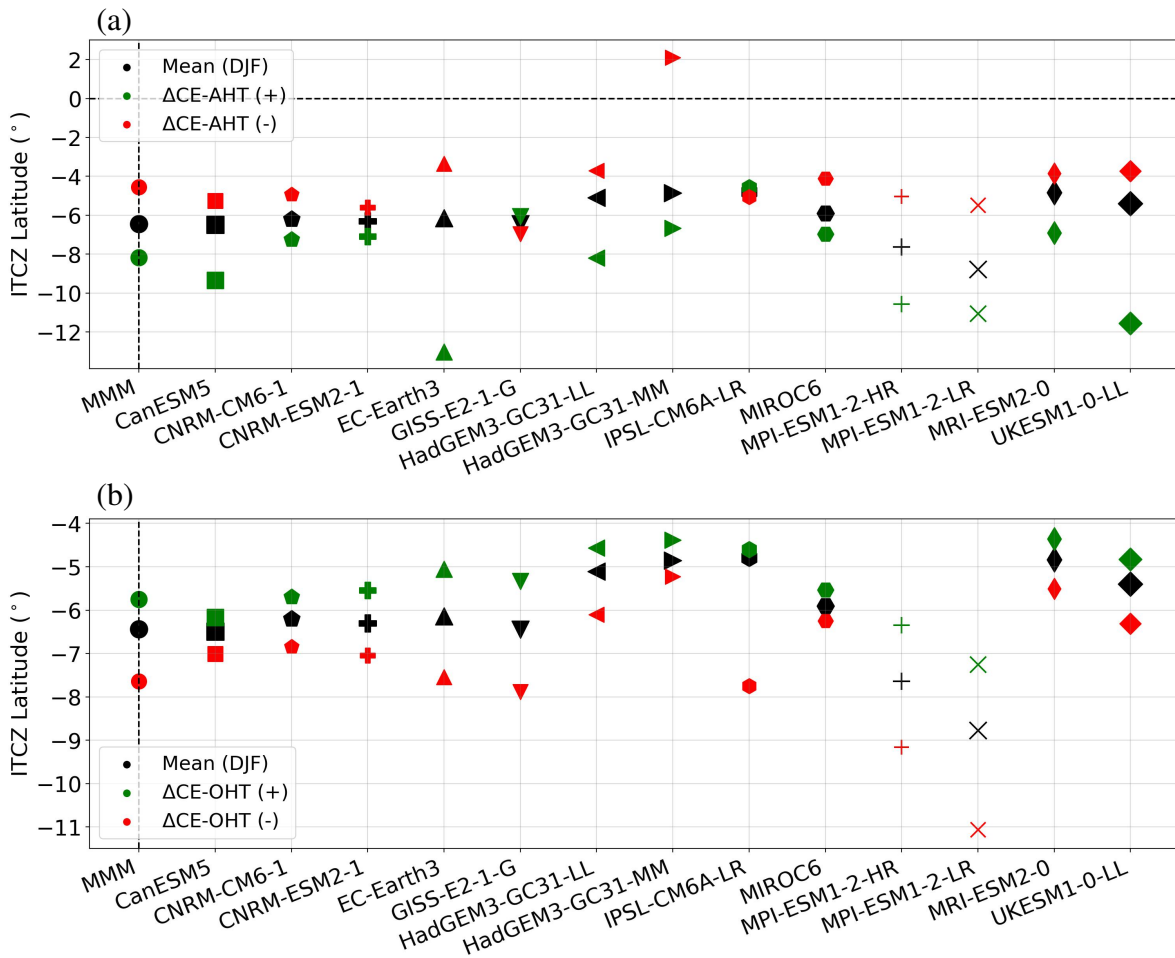


Figure 5.23: Same as Figure 5.22 except for the DJF season

During the JJA season, northward CE-AHT anomalies continue to shift the subtropical jet stream equatorward and induce a weakening of the Walker circulation, resulting in a contraction of the winter Hadley cell and a shift of the ITCZ towards the equator. Conversely, positive CE-OHT anomalies lead to an expansion of the winter-Hadley cell and a poleward displacement of the ITCZ. These dynamics manifest in altered precipitation patterns across various monsoon domains and changes in sea surface temperatures reflective of El Niño and La Niña-like conditions.

Similarly, during the DJF season, northward CE-AHT anomalies drive the poleward shift of the subtropical jet stream, widening of the winter Hadley cell, and displacement of the ITCZ towards higher latitudes, while CE-OHT anomalies contract the winter Hadley cell and shift the ITCZ equatorward. These shifts in atmospheric circulation patterns correspond to changes in precipitation distribution and are accompanied by distinct SST anomalies indicative of El Niño and La Niña conditions.

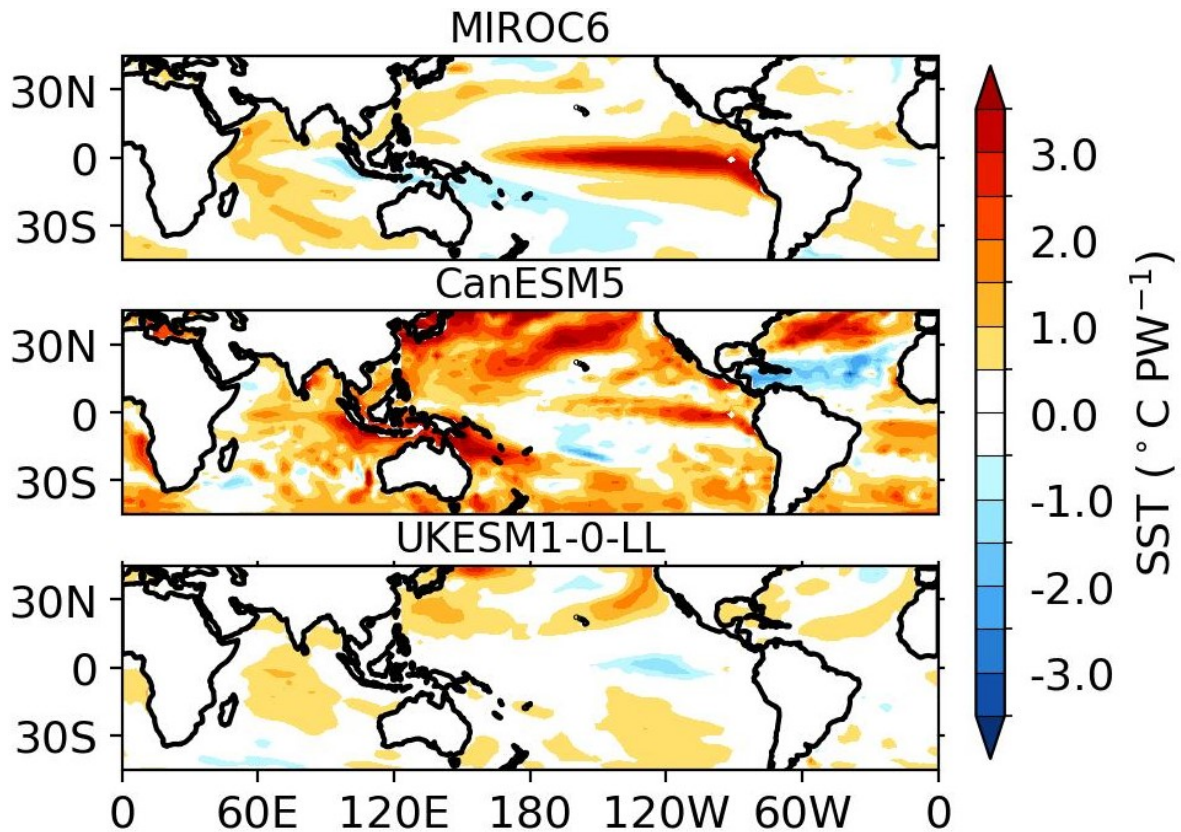


Figure 5.24: The inter-annual SST regression onto CE-AHT ($^{\circ}\text{C PW}^{-1}$) is displayed in colour shading during the JJA season over 2080–2100 for good (MIROC6) and bad (CanESM5 and EKESM1-0-LL) models.

For example, Figure 5.24 and Figure 5.25 display the changes of SST when it is regressed onto CE-AHT for the JJA and DJF seasons spanning the period 2080-2100. El Niño-like conditions in JJA and La Niña-like conditions in DJF appear, aligning with the relationship found for the historical periods. Furthermore, the results found for the CE-OHT are similar to the results of historical periods for both seasons (the figure is not shown since patterns are consistent with historical analysis). So, the link found for the future is also projecting on ENSO-congruent patterns.

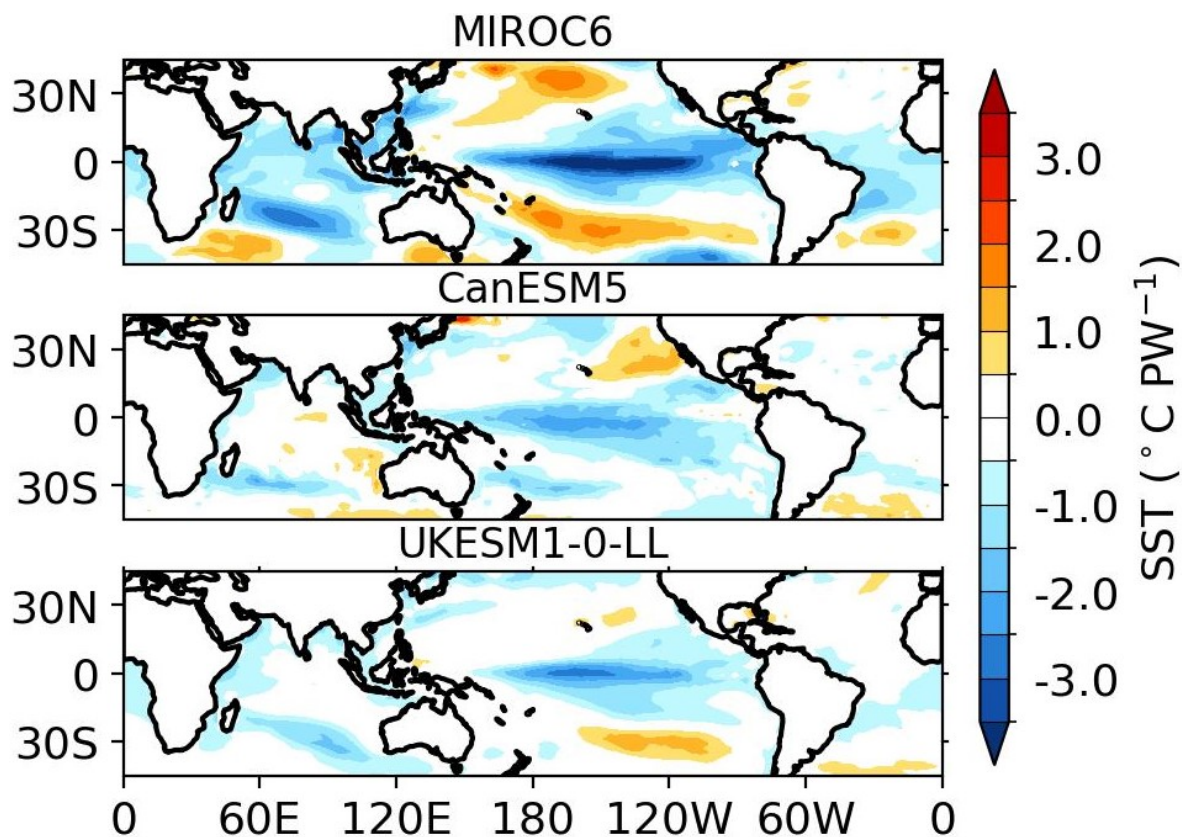


Figure 5.25: The inter-annual SST regression onto CE-AHT ($^{\circ}\text{C PW}^{-1}$) is displayed in colour shading during the JJA season over 2080–2100 for good (MIROC6) and bad (CanESM5 and EKESM1-0-LL) models.

5.4 Conclusion

In the future climate under SSP5-8.5 during the JJA season, the export of heat at the equator is southward in both the atmosphere and ocean, but the trend is positive and negative for CE-AHT and CE-OHT, respectively, in the majority of models. In contrast to the JJA season, during the DJF season, the export of heat at the equator is northward in both the atmosphere and ocean. The trend is decreasing but insignificant in the majority of models, particularly for CE-OHT.

In future climates, an inter-annual regression analysis for the period 2060–2100 reveals that an equatorward and poleward movement of the ITCZ prevails for northward CE-AHT and CE-OHT anomalies, respectively, in most of the models, as found in historical simulation and observation-based reanalysis. For the DJF season, the ITCZ movement mirrors the pattern found in the reanalysis and historical simulation: poleward for increased CE-AHT

and equatorward for increased CE-OHT.

In JJA, the northward CE-AHT increase is consistent with the decrease of southward mass flux by the Hadley circulation. The increase in zonal mean precipitation intensity and equatorward shift of the ITCZ is strongly correlated with the CE-OHT. Similarly, the global and northern-hemisphere monsoonal precipitations are also strongly correlated (p-value < 0.05) with the CE-OHT, having a correlation coefficient of -0.6 ($-0.35 \text{ mm day}^{-1} \text{ PW}^{-1}$) and -0.77 ($-0.85 \text{ mm day}^{-1} \text{ PW}^{-1}$), respectively. The changes in Indian monsoonal precipitation are positive in all models, whereas the directions of changes disagree with each other for West-African and North-American monsoons. Indian and West African monsoon precipitation both show negative correlations with increasing CE-AHT, while for the North American monsoon, this trend occurs with increasing CE-OHT.

During DJF, CE-AHT and CE-OHT decrease (weakly northward) in the majority of models. The northward reduction of CE-AHT is consistent with the decrease in northward mass flux caused by the Hadley circulation. In future climates, the ITCZ will move towards the equator, and the intensity of zonal mean precipitation will increase across all models. No significant correlation is noted for the intensity changes and the ITCZ position changes with the CE-AHT and CE-OHT among the models. Similarly, the southern-hemisphere monsoon displays an insignificant correlation with CE-AHT and CE-OHT, but the global monsoonal precipitation significantly weakens with the increase of CE-AHT. However, both Australian and South African monsoon precipitation are influenced differently by CE-AHT and CE-OHT. Specifically, Australian monsoonal precipitation strengthens and South African monsoonal precipitation weakens with increasing CE-AHT, and vice versa with CE-OHT. Additionally, the South American monsoon precipitation has a positive correlation with CE-AHT, with a correlation coefficient of 0.43 and a confidence level of 83%.

Hence, in JJA, Indian monsoon precipitation increases and is significantly linked to CE-OHT. During DJF, global monsoonal precipitation weakens with increased CE-AHT, while the Australian monsoon strengthens with CE-AHT, and the South African monsoon weakens with CE-OHT.

The conclusions drawn from this study should be interpreted in light of certain limitations and caveats inherent in the models utilized. One notable aspect is the discrepancy in the direction of changes among different models, particularly evident in the West African and North American monsoons during the JJA season and Australian, South African, and South American monsoons in DJF. These discrepancies underscore the uncertainty associated with model simulations and highlight the need for caution when interpreting the results. Furthermore, while the CMIP6 models offer valuable insights into future climate scenarios, they are subject to inherent biases. Variability in model resolution, representation of physical processes, and treatment of uncertainties can lead to inconsistencies in simulated monsoonal behaviours. Additionally, uncertainties in future greenhouse gas emissions scenarios and aerosol forcing further contribute to the uncertainty in model projections. It is imperative to consider these limitations when interpreting the findings and to exercise caution when extrapolating them to real-world scenarios. Addressing these challenges through ongoing research efforts will be essential for improving the reliability of climate projections and informing effective decision-making processes.

These results underscore the importance of understanding cross-equatorial heat transport dynamics to predict future monsoonal behaviours accurately. In the following chapter, I will synthesise all the findings, discuss their broader implications, and outline potential pathways for future research to address the limitations and uncertainties identified in this study.

6

Conclusion

6.1 Recap of Scientific Questions

The preceding chapters have delved into the intricate relationship between cross-equatorial heat transport and the monsoon system. Through a comprehensive analysis of observation-based data and the CMIP6 model simulations, this study has shed light on the mechanisms driving the interplay of CE-AHT and CE-OHT with monsoons from the perspective of low- and upper-level winds, stream-function, the ITCZ, precipitation, and SST. I investigated the projections of the CMIP6 models to understand potential changes in the relationship under the SSP5-8.5 scenario. In this concluding chapter, I summarize the key insights obtained from the investigation and discuss their implications for understanding monsoon dynamics and their response to climate change.

This chapter summarizes all the results in the context of the following scientific research

questions, as also stated in Chapter 1 Section 1.3.

- ▶ What relationships exist between cross-equatorial transports of heat in the atmosphere/ocean and the monsoons using reanalysis products?
- ▶ How do the CMIP6 climate models simulate the relationship between cross-equatorial heat transports and monsoons?
- ▶ How do future climate projections alter the cross-equatorial transports, and can this be related to the monsoon response?

6.2 Discussion of Results

6.2.1 What relationships exist between cross-equatorial transports of heat in the atmosphere/ocean and the monsoons using reanalysis products?

In reanalysis, the increase in CE-AHT and CE-OHT during JJA results in the weakening and strengthening of regional and global monsoonal precipitations and their circulations, respectively, manifested through various atmospheric processes. The relationships between cross-equatorial heat transports and the monsoons are explained in Section 6.2.1 and Section 6.2.1 for the JJA and DJF seasons, respectively.

JJA

Firstly, for an increase in CE-AHT in the JJA season, the anomalous STJ strengthens in both the northern and southern hemispheres and shifts equatorward, while the TEJ weakens. Consequently, the HC contracts, leading to a southward movement of the ITCZ. The southern hemisphere STJ usually lies near $\approx 32^\circ\text{S}$ (Zolotov et al., 2018; Maher et al., 2020), whereas its counterpart is at $\approx 40^\circ\text{N}$ (Du et al., 2016; Maher et al., 2020) in the northern hemisphere in the climatological mean of the JJA season. The angular momentum-conserving and poleward-flowing upper tropospheric branch of the tropical Hadley circulation drives the STJs (Held and Hou, 1980; Schneider, 1977). So, the equatorward movement of the STJs

is in agreement with a contraction of the HC. An anomalous convergence and divergence of upper-level winds over the Maritime Continent and Eastern Pacific Ocean are observed, respectively. This convergence and divergence pattern implies a weaker Walker-like circulation associated with El Niño-like conditions. The anomalous upper-level convergence over the Maritime Continent aligns with decreased rainfall (Wang et al., 2017). However, the contraction of the HC and El Niño-like conditions are complementary, as found in previous studies (Hu et al., 2018; Nguyen et al., 2013; Lau et al., 2006; Stachnik and Schumacher, 2011). The weakening of the TEJ signifies a decrease in Indian monsoon (Madhu et al., 2014), and it occurs typically when anomalously warm surface water appears over the eastern and central equatorial Pacific (Chen and van Loon, 1987; Pattanaik and Satyan, 2000).

Secondly, for the CE-AHT increase in JJA, anomalous low-level winds diverge from the Maritime Continent and converge over the Eastern and Central Pacific Oceans, which supports upper-level wind patterns and a weaker Walker-like circulation. The weakening of trade winds is observed over the Pacific Ocean, with a descent over the Maritime Continent implying a decrease in precipitation (Wang et al., 2017). As a result, the low-level Somali jet weakens, and anomalous north-easterly winds prevail over the Arabian Sea and Bay of Bengal. Consequently, moisture transport decreases towards the Indian monsoon domain, and precipitation is reduced. The weakening of the low-level jet and suppression of Indian monsoon precipitation are associated with El Niño (Sandeep and Ajayamohan, 2015; Pattanaik and Satyan, 2000). Usually, an anti-cyclone over the north-western Pacific Ocean supplies moisture towards the East Asian monsoon domain (Yang et al., 2007; Wang et al., 2013b), which is diminished and contributes to the decrease of precipitation, and it is also related to El Niño (Wang et al., 2013b).

Thirdly, the ITCZ shifts towards the equator due to the CE-AHT increase in the JJA season, consistent with findings on the annual mean inter-annual time scale (Schneider et al., 2014; Bischoff and Schneider, 2014; Liu et al., 2021). This shift leads to a decrease in regional monsoonal precipitation over the Indian, West African, and North American domains, resulting in a decline in global and northern hemisphere monsoonal precipitations. This shift

aligns with the contraction of the HC (Oort and Yienger, 1996; Trenberth and Stepaniak, 2003a; Change, 2007). A positive IOD-like pattern in precipitation over the Indian Ocean is observed. Due to the decrease in regional monsoon precipitation, a decline in global and northern hemisphere monsoonal precipitation is also observed, and it is linked to El Niño (Zhou et al., 2008a; Wang et al., 2017, 2012a).

Conversely, an increase in CE-OHT results in the opposite relationship during the JJA season. The anomalous STJ weakens in both hemispheres and shifts poleward, while the TEJ strengthens. As a result, the HC expands, causing a northward shift of the ITCZ. Anomalous upper-level wind divergence occurs over the Maritime Continent, and an anomalous convergence occurs over the Eastern Pacific Ocean. This pattern resembles a strong Walker-like circulation associated with La Niña-like conditions. The anomalous upper-level divergence over the Maritime Continent is an indication of a strong rainy season (Wang et al., 2017). The expansion of the HC and La Niña-like conditions are linked together (Hu et al., 2018; Nguyen et al., 2013; Lau et al., 2006; Stachnik and Schumacher, 2011). The strengthening of the TEJ indicates an increase in the Indian monsoon (Madhu et al., 2014) and is commonly associated with anomalously cold surface water appearing over the eastern and central equatorial Pacific (Chen and van Loon, 1987; Pattanaik and Satyan, 2000).

Additionally, the Maritime Continent and the Central-Eastern Pacific Ocean experience anomalous low-level convergence and divergence, respectively, for the increase of CE-OHT in JJA. Trade winds strengthen over the Pacific Ocean, with an anomalous ascent over the Maritime Continent. This is consistent with the upper-level wind patterns and a strong Walker-like circulation. The anomalous convergence of low-level winds over the Maritime Continent causes heavy precipitation in those regions (Wang et al., 2017). The low-level Somali jet strengthens, and anomalous south-westerly winds bring a large amount of moisture towards the Indian monsoon domain. The strengthening of the low-level jet and Indian monsoon precipitation are linked to La Niña (Sandeep and Ajayamohan, 2015; Pattanaik and Satyan, 2000). Furthermore, the anti-cyclone over the North-Western Pacific Ocean becomes stronger and increases moisture supply towards the Asian monsoon domain (Yang

et al., 2007; Wang et al., 2013b), leading to an increase in precipitation (Wang et al., 2013b).

In contrast to CE-AHT, the CE-OHT increase in the JJA season pushes the ITCZ away from the equator, similar to the result of the yearly mean inter-annual time scale (Marshall et al., 2014; Lu and Dong, 2008; Vellinga and Wood, 2002). The northward shift of the ITCZ induces increased precipitation over the Indian, West African, and North American regional monsoon domains. As a result, global and northern hemisphere monsoonal precipitations increase. The increase in precipitation in both global and regional monsoon domains is linked to La Niña in other studies (Zhou et al., 2008a; Wang et al., 2017, 2012a).

Hence, the increase of CE-AHT in the JJA season shifts the STJs towards the equator, weakens the TEJ and Walker circulation, and diminishes the anti-cyclone over the north-western Pacific Ocean. These changes lead to decreased precipitation across all regional monsoon domains, particularly in the Indian, West African, and North American monsoon regions, resulting in a decline in global and northern hemispheric monsoonal precipitation. The analysis of SST with the increase in CE-AHT is associated with a positive IOD and an El Niño-like pattern during the JJA season and supports the response of precipitation. Conversely, when CE-OHT increases in the JJA season, the STJs move towards the pole, and the TEJ, Walker circulation, and anti-cyclone over the North-Western Pacific Ocean strengthen. As a consequence, a positive precipitation anomaly occurs across all regional monsoon domains, particularly in the Indian, West African, and North American monsoon regions, resulting in a positive signal in global and northern hemispheric monsoonal precipitation. The strengthening of regional and global monsoons corresponds to La Niña conditions in the Pacific Ocean, which occur at the same time with the increase in CE-OHT during the JJA season, according to SST analysis.

DJF

The regional, global, and southern hemispheric monsoonal precipitations strengthen with the increase of CE-AHT and weaken with the decrease of CE-OHT during the DJF season.

These changes are reflected in various atmospheric phenomena, which illustrate their impact on the monsoon system.

In the DJF climatological mean, the position of the southern hemisphere STJ is usually near $\approx 44^{\circ}\text{S}$ (Yang and Webster, 1990; Zolotov et al., 2018; Maher et al., 2020), whereas it appears at $\approx 30^{\circ}\text{N}$ (Yang and Webster, 1990; Luna-Niño et al., 2021; Maher et al., 2020) in the northern hemisphere. With an increase in CE-AHT in the DJF season, both the STJs weaken and shift poleward, leading to an expansion of the HC and a shift of the ITCZ away from the equator. Strong easterly upper-level wind anomalies dominate over the Indian Ocean, while strong westerly upper-level wind anomalies prevail over the Pacific Ocean. A strong Walker-like circulation, implying La Niña-like conditions, is evident through diverging upper-level winds from the Maritime Continent, an indication of strong monsoonal precipitation (Wang et al., 2017), and converging over the central-eastern Pacific Ocean. The expansion of the HC and the La Niña-like conditions during the DJF season agree with the result of Hu et al. (2018).

In the lower levels, the increase of CE-AHT in the DJF season induces anomalous westerly and easterly winds over the equatorial Indian and Pacific Oceans, leading to convergence over the Maritime Continent and consequently heavy precipitation (Wang et al., 2017). This pattern of winds resembles a strong Walker-like circulation as found in the upper-level for increasing CE-AHT. Anomalous cyclonic features over the South Indian, South Atlantic, and north-western Pacific Oceans supply moisture towards the Australian, South African, and Maritime Continent monsoons, respectively. Additionally, an anti-cyclonic feature over the south-western Pacific Ocean brings moisture towards the SPCZ. As a result, a pronounced positive precipitation signal is found over the Maritime Continent, South African monsoon domain, Australian monsoon domain, and SPCZ, and reduced precipitation over the South American monsoon domain. The increased precipitation in regional monsoon domains contributes to the increase of global and southern hemisphere monsoonal precipitations. An extra zonal band of precipitation is observed to the north of the equator in this case, which is evident in the HC analysis as well. The double zonal band feature of precipitation during La Niña-like conditions was found in earlier studies as well (Brown et al., 2020). The regression

analysis of SST shows that an increase in CE-AHT induces La Niña-like conditions over the central-eastern Pacific Ocean. This pattern agrees with earlier findings in upper- and lower-level winds.

In contrast to CE-AHT, the increase of CE-OHT strengthens and moves the STJs towards the equator, resulting in the contraction of the HC and a movement of the ITCZ towards the equator. Strong westerly and easterly upper-level wind anomalies prevail over the Indian and Pacific Oceans, respectively. An anomalous convergence over the Maritime Continent, a token for weak monsoon (Wang et al., 2017), is observed, whereas a divergence over the central-eastern Pacific Ocean is observed, indicating weakened Walker-like circulation or El Niño-like conditions. The contraction of the HC and the El Niño-like conditions during the DJF season align with earlier studies (Hu et al., 2018).

Moreover, opposite responses to CE-AHT are observed in the low-level winds due to the increase of CE-OHT during the DJF season. Low-level easterly and westerly anomalies dominate over the Indian and Pacific Oceans, respectively. Anomalous anti-cyclonic features lie over the Southern Indian, Southern Atlantic, and North-Western Pacific Oceans and suppress moisture transports towards the Australian, South African, and Maritime Continents, respectively. Moreover, a cyclonic feature is evident over the south-central Pacific Ocean and reduces the export of moisture towards the SPCZ. As a consequence, precipitation decreases in the Maritime Continent, South African monsoon domain, Australian monsoon domain, and SPCZ but increases over the equatorial Indian and Pacific Oceans due to low-level convergence. The decline of regional monsoon domains sums to a reduction in global and southern hemisphere monsoonal precipitations. A single zonal band of precipitation is observed to the south of the equator in this case, as observed in the HC analysis as well. The single zonal band of precipitation feature is consistent with El Niño-like conditions (Brown et al., 2020). El Niño-like conditions in SST also appear with the increase of CE-OHT in the DJF season, which agrees with the upper-level and lower-level wind analyses.

Therefore, when the CE-AHT increases in the DJF season, the STJs shift away from

the equator, and the Walker-like circulation or La Niña-like conditions strengthen. The winter-Hadley cell expands, and the ITCZ moves towards the pole. Anomalous cyclonic features appear over the Southern Indian, South Atlantic, and north-western Pacific Oceans, which supply moisture towards the Australian, South African, and Maritime Continent monsoons, respectively, whereas an anti-cyclonic feature appearing over the South-Western Pacific Ocean brings moisture towards the SPCZ. As a result, positive precipitation anomalies occur over the Maritime Continent, South African monsoon domain, Australian monsoon domain, and SPCZ, and negative precipitation anomalies occur over the South American monsoon domain. Consequently, there has been an increase in precipitation in the global and northern hemisphere monsoon domains.

On the contrary, the increase of CE-OHT strengthens and relocates the STJs towards the equator and induces a weak Walker-like circulation or an El Niño-like condition. The HC shrinks, leading to an equatorward movement of the ITCZ. Anomalous anti-cyclonic features over the southern Indian Ocean, South Atlantic Ocean, and northwestern Pacific Ocean reduce moisture transport to the Australian, South African, and Maritime Continent regions, respectively. Consequently, negative precipitation anomalies dominate the Maritime Continent, South African monsoon domain, Australian monsoon domain, SPCZ, and South American monsoon domain, but a positive anomaly dominates the equatorial Indian and Pacific Oceans. The decrease in regional precipitation results in the decline of global and northern hemisphere monsoons.

6.2.2 How do the CMIP6 climate models simulate the relationship between cross-equatorial heat transports and monsoons?

The CMIP6 models are employed to investigate their capability in simulating the observed relationship between cross-equatorial heat transport and monsoons. The CMIP6 historical simulations show only a few of the models capture the trends of CE-AHT and CE-OHT as in reanalysis. In nearly all CMIP6 models, the trends are not significant. Nevertheless, the analyses of CMIP6 data display results similar to those observed in the reanalysis,

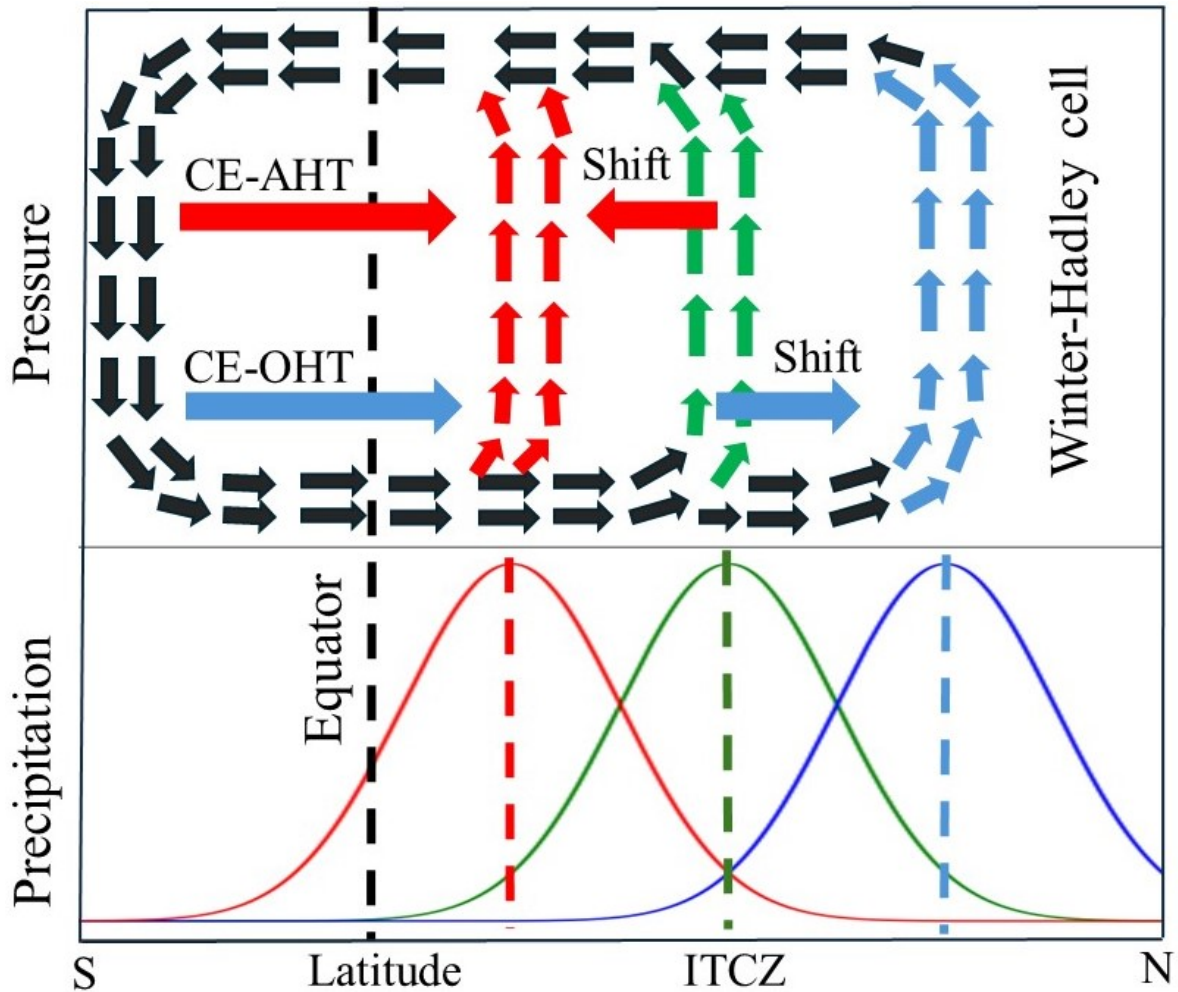


Figure 6.1: A schematic illustration of outcomes for northward CE-AHT and CE-OHT anomalies in JJA is displayed, showing the winter-Hadley cell (top panel) and zonal mean precipitation (bottom panel). The mean position of the rising branch of the HC is shown by green vectors, while red and blue vectors denote its shift for northward CE-AHT and CE-OHT anomalies, respectively. Similarly, the green dashed line indicates the ITCZ location by zonal mean precipitation, with red and blue dashed lines representing the ITCZ location for northward CE-AHT and CE-OHT anomalies. The black vertical dashed line refers to the equator.

particularly in terms of key atmospheric features such as the STJ, TEJ, Walker circulation, Somali jet, HC, ITCZ, and ENSO.

However, a few of the CMIP6 models indicate a meridional shift of the STJs, consistent with patterns seen in reanalysis data for both CE-AHT and CE-OHT during solstice seasons. Similarly, a few models are also in agreement with the reanalysis in displaying the strengthening and weakening of the TEJ and Walker-like circulation. However, all the CMIP6 models capture the corresponding expansion and contraction of the HC, reinforc-

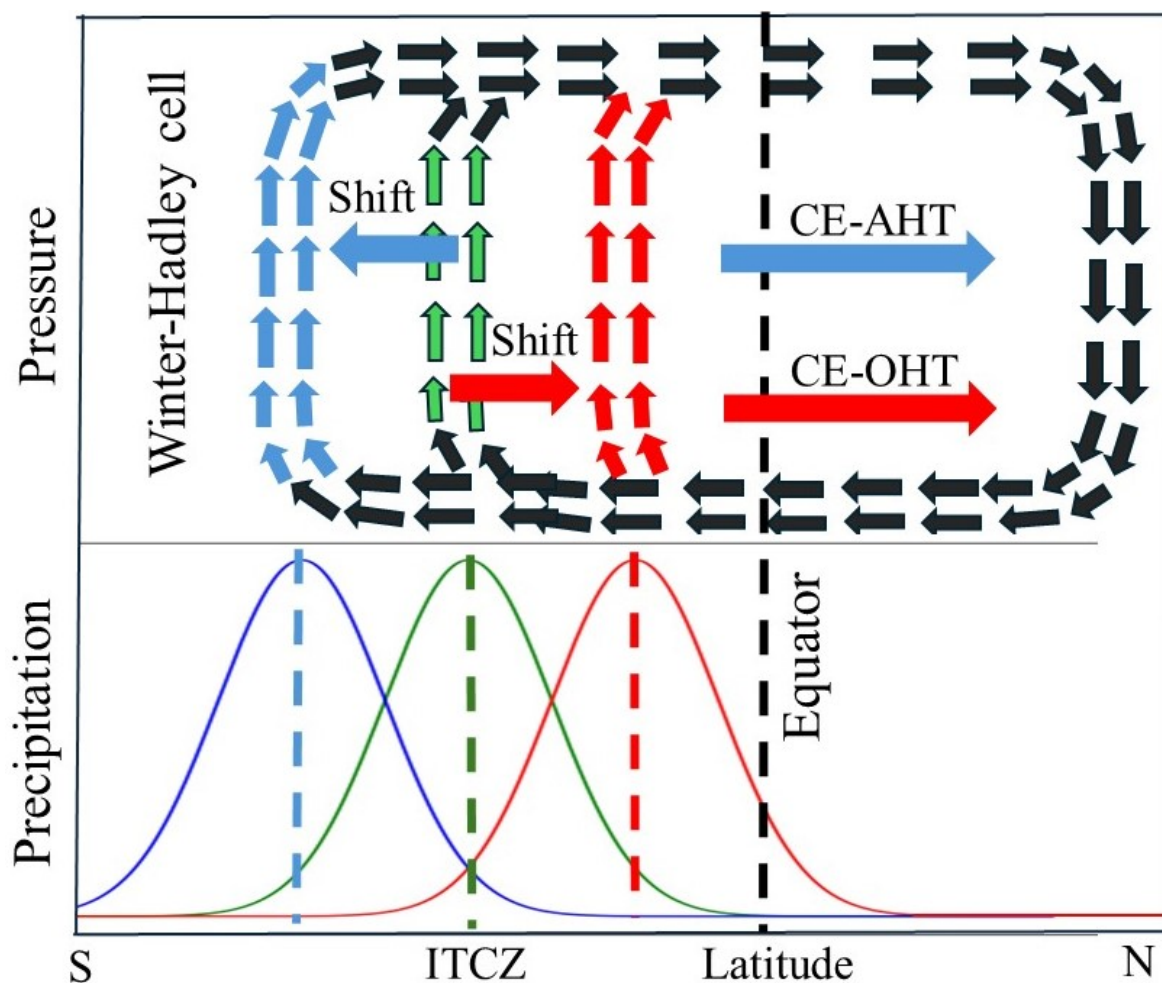


Figure 6.2: Same as Figure 6.1, but for the DJF season.

ing the findings from the reanalysis data and confirming their ability to simulate the key processes involved. Additionally, these models show corresponding meridional shifts in the ITCZ, which align with observations for each type of cross-equatorial heat transport in solstice seasons. Low-level anomalous wind patterns and SST anomalies are well captured by the majority of the models. Furthermore, anomalous precipitation signals in different regional and global monsoon domains agree with the observations for each solstice season and each type of cross-equatorial heat transport in the majority of the CMIP6 models.

The similarities mentioned earlier underscore the robustness of the CMIP6 models in simulating critical aspects of atmospheric circulation and variability, although dissimilarities also indicate areas where improvements are needed. For each variable analysis, a different group of models seems to perform well, which highlights the discrepancies among the CMIP6 models. Therefore, it has been difficult to identify a group of good and bad models

across all analyses. However, the MPI-ESM1-2-LR outperforms other models in both the JJA and DJF seasons.

For northward CE-AHT and CE-OHT anomalies, Figure 6.1 illustrates the responses of the HC and the ITCZ for the JJA season, while Figure 6.2 demonstrates those responses for the DJF season.

6.2.3 How do future climate projections alter the cross-equatorial transports, and can this be related to the monsoon response?

In examining future climate projections under the SSP5-8.5 scenario, significant seasonal variations are observed in the patterns of heat export at the equator. These variations highlight the different behaviours of atmospheric and oceanic heat transport across seasons. Specifically, the projections reveal how heat distribution mechanisms are expected to change in response to intensified greenhouse gas emissions and associated climate changes.

During the JJA season, on an inter-annual time scale, both the atmosphere and ocean exhibit southward heat export at the equator for the period 2021-2100. The trends are significant (95% confidence level) in the majority of the CMIP6 models, but positive for CE-AHT and negative for CE-OHT. Conversely, during the DJF season, heat export at the equator is northward in both the atmosphere and ocean. However, the trends for both CE-AHT and CE-OHT are negative but significant in a very few of the models.

Most of the CMIP6 models in future projections show an equatorward shift of the ITCZ during both the JJA and DJF seasons, as consistent with the annual and zonal-mean southward shift of the ITCZ under the SSP3-7.0 scenario in CMIP6 (Mamalakis et al., 2021). Additionally, the intensity of zonal mean precipitation increases in both JJA and DJF seasons across all models.

To explore the mean changes in precipitation over various regional and global monsoon domains, the time-averaged JJA and DJF means for the period 1995–2014 were subtracted

from those for 2080–2100. Similarly, the changes in CE-AHT and CE-OHT were determined, and a multi-model regression was conducted between the changes in cross-equatorial heat transport with the ITCZ and monsoonal precipitation for each season.

Models exhibit greater disagreement about the direction of changes in CE-AHT and CE-OHT for the JJA and DJF seasons, respectively. In most of the models, under unabated climate change in scenario SSP5-8.5, changes in CE-AHT are positive, indicating an increase of northward CE-AHT in future climate in the JJA season, whereas they are negative for the DJF season, implying a decrease of northward CE-AHT. In contrast, changes in CE-OHT are negative in both the JJA and DJF seasons, denoting an overall northward decrease in the future in the majority of models. However, almost all models display good agreement about the direction of changes in the maximum zonal mean precipitation and in the ITCZ for both seasons.

In inter-model space, changes in the ITCZ are negatively correlated with changes in CE-AHT in JJA ($\text{cor} = -0.48$; confidence level 92%), which supports earlier results of equatorward movement of the ITCZ with the increasing northward CE-AHT. However, during the JJA season, in inter-model space, variations in the zonal mean maximum precipitation intensity and in the shift of the ITCZ are significant and closely linked to CE-OHT. The correlation coefficients are significantly positive for precipitation and significantly negative for the ITCZ, which again highlights the movement of the ITCZ away from the equator with the rise of CE-OHT, leading to a decrease in zonal mean precipitation. However, no significant relationship is found for the DJF season, which might be related to the poor capability displayed by the CMIP6 models in simulating precipitation for the DJF season (Huang et al., 2023).

The changes in global, southern-hemisphere, and northern-hemisphere monsoonal precipitation are consistent among models. In inter-model space, during the JJA season, the global monsoonal precipitation increases with CE-AHT (confidence level of 90%). However, global monsoonal precipitation is suppressed with CE-OHT, leading to a reduction in northern-hemisphere monsoon precipitation with CE-OHT as well. The correlation coefficients are -0.6 ($p\text{-value} < 0.05$; $-0.35 \text{ mm day}^{-1} \text{ PW}^{-1}$) for global monsoonal precipitation

and -0.77 (p -value < 0.05 ; $-0.85 \text{ mm day}^{-1} \text{ PW}^{-1}$) for northern-hemisphere monsoonal precipitation. Conversely, during the DJF season, the increase of CE-AHT reduces the global monsoonal precipitation ($\text{cor} = -0.61$; $-0.5 \text{ mm day}^{-1} \text{ PW}^{-1}$), under the SSP5-8.5 high emission scenario.

In JJA, all models indicate increases in Indian monsoonal precipitation (Wang et al., 2021; Katzenberger et al., 2021). However, there is disagreement among models regarding signs of changes for the West African and North American monsoons. Most of the models exhibit reductions in North American monsoon precipitation (Wang et al., 2021; Hernandez and Chen, 2022) and increases in the West African monsoon (Wang et al., 2021). In the inter-model relationship, Indian and West African monsoonal precipitation changes decrease with CE-AHT ($\text{cor} = -0.56$; p -value < 0.05 ; $-1.82 \text{ mm day}^{-1} \text{ PW}^{-1}$ and $\text{cor} = -0.8$; p -value < 0.05 ; $-2.92 \text{ mm day}^{-1} \text{ PW}^{-1}$, respectively). On the other hand, the multi-model relationship shows that increased CE-OHT strengthens Indian monsoon precipitation ($\text{cor} = 0.45$; confidence level 89%). However, increased CE-OHT reduces North American monsoon precipitation ($\text{cor} = -0.67$; p -value < 0.05 ; $-0.85 \text{ mm day}^{-1} \text{ PW}^{-1}$).

On the other hand, during the DJF season, the direction of changes in the Australian, South African, and South American monsoonal precipitation exhibits a significant discrepancy across all the models. In future climate, the changes in Australian monsoon precipitation is related to the increase of CE-AHT ($\text{cor} = 0.78$; p -value < 0.05 ; $3.77 \text{ mm day}^{-1} \text{ PW}^{-1}$). The increase of CE-OHT reduces the South African monsoonal precipitation ($\text{cor} = -0.61$; p -value < 0.05 ; $-0.86 \text{ mm day}^{-1} \text{ PW}^{-1}$). However, the correlation is not significant for South American monsoon precipitation.

6.3 Limitations and Constraints

In investigating the relationship between cross-equatorial heat transport and monsoons, the very first attempt was to calculate the CE-AHT and CE-OHT accurately using both observation-based and CMIP6 datasets. The CMIP6 models also exhibit limitations in sim-

ulating the observed relationship in reanalysis.

However, the accurate estimation of CE-AHT and CE-OHT relies heavily on maintaining mass and energy conservation. Initially, considerable effort was required to achieve this balance, revealing certain constraints. Firstly, temperature, winds (u , v), geopotential, surface pressure, and specific humidity must be interpolated to a common location across grid cells. The choice of integration lower limit for each column is critical, with surface pressure used for the atmosphere (Trenberth, 1991; Trenberth and Solomon, 1994; Trenberth et al., 1995; Trenberth, 1997; Trenberth et al., 2002) and bathymetry for the ocean. Additionally, enhancing horizontal and vertical resolution improves accuracy and reduces energy imbalances, while the non-linear nature of integral terms underscores the importance of time resolution (Boer, 1982; Trenberth, 1991; Trenberth et al., 2002, 1995; Trenberth, 1997; Trenberth et al., 2002; Liu et al., 2020b).

A violation of mass convergence can affect the energy budget and the representation of key processes like the ITCZ, which is tightly linked to the global distribution of precipitation (Vannière et al., 2019). However, mass is conserved in model coordinates because the omega fields are derived to ensure conservation that is disrupted by interpolation onto pressure surfaces (Trenberth, 1991; Trenberth and Solomon, 1994; Trenberth et al., 1995; Trenberth, 1997; Trenberth et al., 2002). Interpolating model coordinates to pressure coordinates suggests that the values are the most accurate at a fixed level, but they do not accurately represent layers. Apart from that, the post-processing of variables onto pressure surfaces introduces an artificial atmosphere below ground level (Trenberth and Fasullo, 2018; Liu et al., 2015; Mayer et al., 2017; Liu et al., 2020b). All these together contribute to the violation of mass convergence. Moreover, at least four-times-daily analyses are required to capture the semidiurnal tide effect on mass (Boer, 1982; Trenberth, 1991; Trenberth et al., 2002, 1995). However, the existing database is insufficient to properly capture the semidiurnal tide in the analyses, resulting in it being largely model-generated. The lack of proper resolution of tidal variations raises the possibility of them being aliased onto other variations (Trenberth, 1991).

Reanalyses can sometimes be affected by spurious temporal variability, and their ac-

curacy may be compromised due to a lack of sufficient observations. This deficiency in observational data can lead to reanalysis fields that are heavily influenced by the underlying models, raising questions about their reliability (Wang et al., 2014). Additionally, at higher model resolutions, the simulated global precipitation and southward transport of moist static energy towards the poles tend to increase compared to coarse resolutions (Vannière et al., 2019). Among reanalyses, discrepancies can arise due to variations in the assimilated data streams, occurring both before and during the satellite era. These discrepancies suggest that trends previously considered genuine in other studies may actually be spurious (Fasullo, 2012).

Additionally, the uncertainties in atmospheric and oceanic energy transport stem from uncertainties in both the TOA and surface energy exchanges (Zhang and Rossow, 1997). Moreover, the energy imbalance at the surface and top of the atmosphere impacts the heat transport estimation process (Wild, 2020). No model is perfect, and uncertainty exists in each model due to factors such as model physics, initial conditions, boundary conditions, assimilation of observational data, computational resources, numerical methods, resolution, parameterization schemes, and systematic bias. For instance, cloud physics impacts atmospheric and oceanic energy transport by influencing the radiation budget (Zhang and Rossow, 1997). Regional physical factors such as extensive irrigation practices, which contribute to increased local soil moisture over the Asian monsoon region (Ha et al., 2020), may contribute negatively to the performance of the model.

Discrepancies among CMIP6 models are found in simulating the relationship between cross-equatorial heat transport and monsoons for the historical period (1979-2020). Each variable analysis reveals that different groups of models tend to perform well, underscoring the inconsistencies among the CMIP6 models. This variation in model performance for different variables indicates that no single group of models can be consistently classified as good or bad across all analyses. Consequently, the task of identifying universally reliable models remains challenging. This highlights the importance of careful model selection and evaluation tailored to specific variables or scenarios in climate studies.

6.4 Future Avenues

Several key areas of research can be identified in this study, which could yield further insight into the relationship between cross-equatorial heat transport and monsoons through investigation. Aerosol and greenhouse gas forcing influences the climate response in the Indo-Pacific and eastern equatorial Pacific sectors, respectively. Asian anthropogenic aerosol emissions significantly contributed to the rise in Australian summer monsoon (AUSM) rainfall from 1930 to 2014 (Fahrenbach et al., 2024). Sulfate aerosol emissions induced regional cooling and strengthened the Siberian high over eastern China, altering temperature and pressure gradients across the Indian Ocean. This led to intensified and southward-shifted Australian monsoonal westerlies and the local Hadley cell, augmenting precipitation over northern Australia. However, aerosol emissions results in a diminished temperature contrast between the northern and southern hemispheres, ultimately leading to a decrease in Asian summer monsoon (ASM) rainfall during second of the 20th century (Bollasina et al., 2011; Liu et al., 2019; Ha et al., 2020; Masson-Delmotte et al., 2021).

In a future of continued global warming, the combined effects of ENSO and ITCZ shifts could worsen regional differences in rainfall and water availability in ASM areas (Xu et al., 2019). Previous studies using CMIP5 and CMIP6 climate models highlighted an increase in the ASM-ENSO relationship under anthropogenic global warming, reflecting the enhanced ENSO teleconnection regardless of potential changes in ENSO dynamics (Xu et al., 2023). Additionally, the correlations between simulated ASM and AUSM display a notable upward trend due to greenhouse gas forcing. This finding corroborates the observations and provides further evidence for the potential impact of global warming on the increasingly synchronized inter-annual variability of the two monsoons, despite their distinct seasonal patterns. **ENSO, as a global climate driver, by modulating the ocean currents and winds, may alter the atmospheric and oceanic heat transport regionally and globally. Therefore, what are the impacts of greenhouse gas forcing on the relationship between cross-equatorial heat transports (both atmospheric and oceanic) and monsoon systems on inter-annual and decadal time scales?**

The climatic changes in the multi-decadal AMOC are extensive, and a few notable im-

pacts linked to monsoon systems include shifts in the ITCZ; variations in the Sahel and Indian monsoons; influences on the ENSO; Pacific Decadal Variability; surface air temperature; and variations in global surface temperatures (Srokosz et al., 2012; McCarthy et al., 2015; Zhang et al., 2019b). When the multidecadal AMOC is in a positive phase, it leads to increased temperatures in the northern Atlantic and a greater temperature contrast between hemispheres (Xu et al., 2023). As a result, the ITCZ shifts to the heated hemisphere (Schneider et al., 2014; Tan et al., 2019; Green et al., 2019). This northward shift in the ITCZ results in increased precipitation for the AUSM and decreased precipitation for the ASM. It is reported that AMOC is declining (Send et al., 2011; Smeed et al., 2014; Sandeep et al., 2020), which implies a reverse teleconnective impact on ASM and AUSM.

Moreover, a long-term climate variability pattern in the Pacific Ocean known as the Interdecadal Pacific Oscillation (IPO) may have contributed to the increased correlation between ASM and AUSM since 1850 (Xu et al., 2023). The IPO can modulate ocean currents, SST gradients, and trade winds, and alter heat transport across the ocean and atmosphere. On a decadal time scale, monsoonal precipitation, particularly global and northern hemispheric, is influenced by the mega El Niño (Wang et al., 2013a). Regional monsoons could be impacted as well, since they belong to the planetary-scale monsoon. Therefore, it would be worthwhile to investigate: how are the multi-decadal Atlantic Meridional Overturning Circulation (AMOC) and IPO, along with their corresponding heat transports, associated with the ASM and AUSM?

The increase in atmospheric CO₂ concentrations can significantly impact the CE-AHT and the position of the ITCZ. During periods of elevated CO₂ forcing, the poleward atmospheric heat transport increases in both hemispheres, driven by an increase in latent heat transport due to higher specific humidity (An et al., 2022). This counteracts the reduction in poleward oceanic heat transport from a weakened meridional overturning circulation. However, in the CO₂ doubling simulation, each petawatt (PW) increase in CE-AHT results in a 4.2° southward shift of the ITCZ in annual mean (McGee et al., 2014). The relationship between the ITCZ and CE-AHT is consistent in both the seasonal cycle and the annual mean response. After returning to original CO₂ levels, the hemispheric thermal contrast reverses,

enhancing northward energy transport in the atmosphere while further weakening deep ocean heat transport southward due to changes in the AMOC (An et al., 2022). Consequently, a southward shift of the ITCZ occurs (Mecking and Drijfhout, 2023).

Additionally, during the CO₂ ramp-up period, South Asian summer monsoon rainfall gradually intensifies, but it reverses slowly during the ramp-down phase (Zhang et al., 2023). The reason is that the lower-tropospheric monsoonal circulation weakens due to the strengthening of near-surface poleward land-sea moist static energy contrast driven by long-term Sea surface temperature (SST) changes (Zhang et al., 2024). Additionally, during the ramp-down period, the tropical Pacific and Indian Ocean experience stronger warming, displaying enhanced El Niño-like and IOD-like patterns, respectively. This intensified warming weakens the monsoon circulation by reducing the thermal gradient, causing sinking over the monsoon region, weakening the Walker circulation, and generating anomalous easterlies over the tropical Indian Ocean (Zhang et al., 2023). Similarly, in a doubled CO₂ scenario, the Australian summer monsoon circulation intensifies, leading to a roughly 20% increase in precipitation (Suppiah, 1995).

Considering the significant influence of CO₂ forcing on global climate patterns, it is crucial to understand its effects and the corresponding mechanisms on the relationship between cross-equatorial heat transport and monsoon systems. So, how does CO₂ forcing impact the relationship between cross-equatorial heat transport (CE-AHT and CE-OHT) and monsoon circulation?

By pursuing these research avenues, the impacts of climate variability and changes on monsoonal precipitation can be better predicted, and areas prone to climate change can be identified. Ultimately, it will contribute to improving climate resilience and adaptation strategies for affected communities.

Bibliography

Abbass, K., Qasim, M. Z., Song, H., Murshed, M., Mahmood, H. and Younis, I. (2022) A review of the global climate change impacts, adaptation, and sustainable mitigation measures. *Environmental Science and Pollution Research*, **29**, 42539–42559.

Abish, B., Joseph, P. and Johannessen, O. M. (2013) Weakening trend of the tropical easterly jet stream of the boreal summer monsoon season 1950–2009. *Journal of Climate*, **26**, 9408–9414.

Adam, O., Bischoff, T. and Schneider, T. (2016a) Seasonal and interannual variations of the energy flux equator and ITCZ. Part I: Zonally averaged ITCZ position. *Journal of Climate*, **29**, 3219–3230.

— (2016b) Seasonal and interannual variations of the energy flux equator and ITCZ. Part II: Zonally varying shifts of the ITCZ. *Journal of Climate*, **29**, 7281–7293.

Adler, R. F., Huffman, G. J., Chang, A., Ferraro, R., Xie, P.-P., Janowiak, J., Rudolf, B., Schneider, U., Curtis, S., Bolvin, D. et al. (2003) The version-2 global precipitation climatology project (GPCP) monthly precipitation analysis (1979–present). *Journal of Hydrometeorology*, **4**, 1147–1167.

Adler, R. F., Sapiano, M. R., Huffman, G. J., Wang, J.-J., Gu, G., Bolvin, D., Chiu, L., Schneider, U., Becker, A., Nelkin, E. et al. (2018) The Global Precipitation Climatology Project (GPCP) monthly analysis (new version 2.3) and a review of 2017 global precipitation. *Atmosphere*, **9**, 138.

Li et al., Y. (2023) Relationships between the Hadley circulation and tropical sea surface temperature with different meridional structures simulated in CMIP6 models. URL: <https://www.frontiersin.org/articles/10.3389/fmars.2023.1145509>.

An, S.-I., Park, S.-E., Shin, J., Yang, Y.-M., Yeh, S.-W., Son, S.-W. and Kug, J.-S. (2022) General circulation and global heat transport in a quadrupling CO₂ pulse experiment. *Scientific reports*, **12**, 11569.

Ando, T., Higuchi, T., Hotta, H., Iwakiri, T., Jinno, T., Kino, K., Takano, Y., Toda, M., Yamazaki, K., Suzuki, K. S. et al. (2021) Description of MIROC6 AGCM. *The University of Tokyo: Chiba, Japan*.

Athira, K., Roxy, M. K., Dasgupta, P., Saranya, J., Singh, V. K. and Attada, R. (2023) Regional and temporal variability of Indian summer monsoon rainfall in relation to El Niño southern oscillation. *Scientific Reports*, **13**, 12643.

Babaousmail, H., Hou, R., Ayugi, B., Ojara, M., Ngoma, H., Karim, R., Rajasekar, A. and Ongoma, V. (2021) Evaluation of the performance of CMIP6 models in reproducing rainfall patterns over North Africa. *Atmosphere*, **12**, 475.

Bischoff, T. and Schneider, T. (2014) Energetic constraints on the position of the intertropical convergence zone. *Journal of Climate*, **27**, 4937–4951.

— (2016) The equatorial energy balance, ITCZ position, and double-ITCZ bifurcations. *Journal of Climate*, **29**, 2997–3013.

Bjerknes, J. (1964) Atlantic air-sea interaction. In *Advances in geophysics*, vol. 10, 1–82. Elsevier.

Boer, G. J. (1982) Diagnostic equations in isobaric coordinates. *Monthly Weather Review*, **110**, 1801–1820.

Bollasina, M. A., Ming, Y. and Ramaswamy, V. (2011) Anthropogenic aerosols and the weakening of the South Asian summer monsoon. *science*, **334**, 502–505.

- Böning, C. W. and Herrmann, P. (1994) Annual cycle of poleward heat transport in the ocean: Results from high-resolution modeling of the North and equatorial Atlantic. *Journal of Physical Oceanography*, **24**, 91–107.
- Bordoni, S. and Schneider, T. (2008) Monsoons as eddy-mediated regime transitions of the tropical overturning circulation. *Nature Geoscience*, **1**, 515–519.
- Boucher, O., Denvil, S., Levassasseur, G., Cozic, A., Caubel, A., Foujols, M.-A., Meurdesoif, Y., Cadule, P., Devilliers, M., Ghattas, J., Lebas, N., Lurton, T., Mellul, L., Musat, I., Mignot, J. and Cheruy, F. (2018) IPSL IPSL-CM6A-LR model output prepared for CMIP6 CMIP historical. URL: <https://doi.org/10.22033/ESGF/CMIP6.5195>.
- Brown, J. R., Brierley, C. M., An, S.-I., Guarino, M.-V., Stevenson, S., Williams, C. J., Zhang, Q., Zhao, A., Abe-Ouchi, A., Braconnot, P. et al. (2020) Comparison of past and future simulations of ENSO in CMIP5/PMIP3 and CMIP6/PMIP4 models. *Climate of the Past*, **16**, 1777–1805.
- Bryan, K. (1962) Measurements of meridional heat transport by ocean currents. *Journal of Geophysical Research*, **67**, 3403–3414.
- Bryden, H. L. (1993) Ocean Heat Transport Across 24°N Latitude. *GEOPHYSICAL MONOGRAPH-AMERICAN GEOPHYSICAL UNION*, **75**, 65–65.
- Bryden, H. L., Johns, W. E., King, B. A., McCarthy, G., McDonagh, E. L., Moat, B. I. and Smeed, D. A. (2020) Reduction in ocean heat transport at 26 N since 2008 cools the eastern subpolar gyre of the North Atlantic Ocean. *Journal of Climate*, **33**, 1677–1689.
- Bryden, H. L., Longworth, H. R. and Cunningham, S. A. (2005) Slowing of the Atlantic meridional overturning circulation at 25°N. *Nature*, **438**, 655–657.
- Byrne, M. P., Pendergrass, A. G., Rapp, A. D. and Wodzicki, K. R. (2018) Response of the intertropical convergence zone to climate change: Location, width, and strength. *Current climate change reports*, **4**, 355–370.

Caesar, L., McCarthy, G., Thornalley, D., Cahill, N. and Rahmstorf, S. (2021) Current Atlantic meridional overturning circulation weakest in last millennium. *Nature Geoscience*, **14**, 118–120.

Caesar, L., Rahmstorf, S., Robinson, A., Feulner, G. and Saba, V. (2018) Observed fingerprint of a weakening Atlantic Ocean overturning circulation. *Nature*, **556**, 191–196.

Cai, W., Van Rensch, P., Cowan, T. and Sullivan, A. (2010) Asymmetry in ENSO teleconnection with regional rainfall, its multidecadal variability, and impact. *Journal of Climate*, **23**, 4944–4955.

Cesana, G., Waliser, D., Jiang, X. and Li, J.-L. (2015) Multimodel evaluation of cloud phase transition using satellite and reanalysis data. *Journal of Geophysical Research: Atmospheres*, **120**, 7871–7892.

Change, I. (2007) Climate change 2007: The physical science basis. *Agenda*, **6**, 333.

Chao, W. C. (2000) Multiple quasi equilibria of the ITCZ and the origin of monsoon onset. *Journal of the atmospheric sciences*, **57**, 641–652.

Chao, W. C. and Chen, B. (2001) The origin of monsoons. *Journal of the Atmospheric Sciences*, **58**, 3497–3507.

Chemke, R. (2022) Large hemispheric differences in the Hadley cell strength variability due to ocean coupling. *npj Climate and Atmospheric Science*, **5**, 1.

Chen, T.-C. and van Loon, H. (1987) Interannual variation of the tropical easterly jet. *Monthly Weather Review*, **115**, 1739–1759.

Chen, Z., Zhou, T., Zhang, L., Chen, X., Zhang, W. and Jiang, J. (2020) Global land monsoon precipitation changes in CMIP6 projections. *Geophysical Research Letters*, **47**, e2019GL086902.

Chevuturi, A., Klingaman, N. P., Turner, A. G. and Hannah, S. (2018) Projected changes in the Asian-Australian monsoon region in 1.5° C and 2.0° C global-warming scenarios. *Earth's Future*, **6**, 339–358.

- Chiodo, G. and Haimberger, L. (2010) Interannual changes in mass consistent energy budgets from ERA-Interim and satellite data. *Journal of Geophysical Research: Atmospheres*, **115**.
- Chou, C. and Neelin, J. D. (2003) Mechanisms limiting the northward extent of the northern summer monsoons over North America, Asia, and Africa. *Journal of climate*, **16**, 406–425.
- Choudhury, B. A., Rajesh, P., Zahan, Y. and Goswami, B. (2022) Evolution of the Indian summer monsoon rainfall simulations from CMIP3 to CMIP6 models. *Climate Dynamics*, 1–26.
- Cohen, I., Huang, Y., Chen, J., Benesty, J., Benesty, J., Chen, J., Huang, Y. and Cohen, I. (2009) Pearson correlation coefficient. *Noise reduction in speech processing*, 1–4.
- Dima, I. M. and Wallace, J. M. (2003) On the seasonality of the Hadley cell. *Journal of the atmospheric sciences*, **60**, 1522–1527.
- Dixit, Y. (2020) Regional character of the “global monsoon”. *Oceanography*, **33**, 56–64.
- Doblas-Reyes, F. J., Sorensson, A., Almazroui, M., Dosio, A., Gutowski, W., Haarsma, R., Hamdi, R., Hewitson, B., Kwon, W.-T., Lamptey, B. et al. (2021) Linking global to regional climate change.
- Donohoe, A., Fajber, R., Cox, T., Armour, K., DBattisti, D. and Roe, G. (2023) Model biases in the atmosphere-ocean partitioning of poleward heat transport are persistent across three CMIP generations. *Authorea Preprints*.
- Donohoe, A., Marshall, J., Ferreira, D. and Mcgee, D. (2013) The relationship between ITCZ location and cross-equatorial atmospheric heat transport: From the seasonal cycle to the Last Glacial Maximum. *Journal of Climate*, **26**, 3597–3618.
- Du, Y., Li, T., Xie, Z. and Zhu, Z. (2016) Interannual variability of the Asian subtropical westerly jet in boreal summer and associated with circulation and SST anomalies. *Climate dynamics*, **46**, 2673–2688.

Du, Y., Wang, D., Zhu, J., Wang, D., Qi, X. and Cai, J. (2022) Comprehensive assessment of CMIP5 and CMIP6 models in simulating and projecting precipitation over the global land. *International Journal of Climatology*, **42**, 6859–6875.

Dutta, U., Hazra, A., Chaudhari, H. S., Saha, S. K., Pokhrel, S. and Verma, U. (2022) Unraveling the global teleconnections of Indian summer monsoon clouds: expedition from CMIP5 to CMIP6. *Global and Planetary Change*, **215**, 103873.

EC-Earth Consortium (EC-Earth) (2019) EC-Earth-Consortium EC-Earth3 model output prepared for CMIP6 CMIP historical. URL: <https://doi.org/10.22033/ESGF/CMIP6.4700>.

Eyring, V., Bony, S., Meehl, G. A., Senior, C. A., Stevens, B., Stouffer, R. J. and Taylor, K. E. (2016) Overview of the Coupled Model Intercomparison Project Phase 6 (CMIP6) experimental design and organization. *Geoscientific Model Development*, **9**, 1937–1958.

Eyring, V., Cox, P. M., Flato, G. M., Gleckler, P. J., Abramowitz, G., Caldwell, P., Collins, W. D., Gier, B. K., Hall, A. D., Hoffman, F. M. et al. (2019) Taking climate model evaluation to the next level. *Nature Climate Change*, **9**, 102–110.

Fahrenbach, N. L., Bollasina, M. A., Samset, B. H., Cowan, T. and Ekman, A. M. (2024) Asian Anthropogenic Aerosol Forcing Played a Key Role in the Multidecadal Increase in Australian Summer Monsoon Rainfall. *Journal of Climate*, **37**, 895–911.

Fajber, R., Donohoe, A., Ragen, S., Armour, K. C. and Kushner, P. J. (2023) Atmospheric heat transport is governed by meridional gradients in surface evaporation in modern-day Earth-like climates. *Proceedings of the National Academy of Sciences*, **120**, e2217202120.

Fasullo, J. (2012) A mechanism for land–ocean contrasts in global monsoon trends in a warming climate. *Climate Dynamics*, **39**, 1137–1147.

Fasullo, J. T. and Trenberth, K. E. (2008a) The annual cycle of the energy budget. Part I: Global mean and land–ocean exchanges. *Journal of Climate*, **21**, 2297–2312.

— (2008b) The annual cycle of the energy budget. Part II: Meridional structures and poleward transports. *Journal of Climate*, **21**, 2313–2325.

- Faulk, S., Mitchell, J. and Bordoni, S. (2017) Effects of rotation rate and seasonal forcing on the ITCZ extent in planetary atmospheres. *Journal of the Atmospheric Sciences*, **74**, 665–678.
- Feng, J., Li, J., Jin, F., Zhao, S. and Zhu, J. (2018) Relationship between the Hadley circulation and different tropical meridional SST structures during boreal summer. *Journal of Climate*, **31**, 6575–6590.
- Ferrari, R. and Ferreira, D. (2011) What processes drive the ocean heat transport? *Ocean Modelling*, **38**, 171–186.
- Fichefet, T. and Maqueda, M. M. (1997) Sensitivity of a global sea ice model to the treatment of ice thermodynamics and dynamics. *Journal of Geophysical Research: Oceans*, **102**, 12609–12646.
- Forget, G. and Ferreira, D. (2019) Global ocean heat transport dominated by heat export from the tropical Pacific. *Nature Geoscience*, **12**, 351–354.
- Frierson, D. M., Hwang, Y.-T., Fučkar, N. S., Seager, R., Kang, S. M., Donohoe, A., Maroon, E. A., Liu, X. and Battisti, D. S. (2013) Contribution of ocean overturning circulation to tropical rainfall peak in the Northern Hemisphere. *Nature Geoscience*, **6**, 940–944.
- Frierson, D. M., Lu, J. and Chen, G. (2007) Width of the Hadley cell in simple and comprehensive general circulation models. *Geophysical Research Letters*, **34**.
- Fu, Q., Johanson, C. M., Wallace, J. M. and Reichler, T. (2006) Enhanced mid-latitude tropospheric warming in satellite measurements. *Science*, **312**, 1179–1179.
- Gadgil, S. (2018) The monsoon system: Land–sea breeze or the ITCZ? *Journal of Earth System Science*, **127**, 1–29.
- Ganachaud, A. and Wunsch, C. (2003) Large-scale ocean heat and freshwater transports during the World Ocean Circulation Experiment. *Journal of Climate*, **16**, 696–705.
- Geen, R., Bordoni, S., Battisti, D. S. and Hui, K. (2020) Monsoons, ITCZs, and the concept of the global monsoon. *Reviews of Geophysics*, **58**, e2020RG000700.

— (2021) Summer Monsoons: Regional Manifestations of a Global System. *EOS (Transactions, American Geophysical Union)*, 102.

Geen, R., Lambert, F. and Vallis, G. (2018) Regime change behavior during Asian monsoon onset. *Journal of Climate*, **31**, 3327–3348.

Geen, R., Lambert, F. H. and Vallis, G. K. (2019) Processes and timescales in onset and withdrawal of "aquaplanet monsoons". *Journal of the Atmospheric Sciences*, **76**, 2357–2373.

Gill, A. E. (1980) Some simple solutions for heat-induced tropical circulation. *Quarterly Journal of the Royal Meteorological Society*, **106**, 447–462.

Graversen, R. G., Källén, E., Tjernström, M. and Körnich, H. (2007) Atmospheric mass-transport inconsistencies in the ERA-40 reanalysis. *Quarterly Journal of the Royal Meteorological Society: A journal of the atmospheric sciences, applied meteorology and physical oceanography*, **133**, 673–680.

Green, B., Marshall, J. and Campin, J.-M. (2019) The 'sticky' ITCZ: Ocean-moderated ITCZ shifts. *Climate dynamics*, **53**, 1–19.

Gregory, D. and Rowntree, P. (1990) A mass flux convection scheme with representation of cloud ensemble characteristics and stability-dependent closure. *Monthly Weather Review*, **118**, 1483–1506.

Gruber, A. (1972) Fluctuations in the position of the ITCZ in the Atlantic and Pacific Oceans. *Journal of Atmospheric Sciences*, **29**, 193–197.

Gusain, A., Ghosh, S. and Karmakar, S. (2020) Added value of CMIP6 over CMIP5 models in simulating Indian summer monsoon rainfall. *Atmospheric Research*, **232**, 104680.

Ha, K.-J., Kim, B.-H., Chung, E.-S., Chan, J. C. and Chang, C.-P. (2020) Major factors of global and regional monsoon rainfall changes: Natural versus anthropogenic forcing. *Environmental Research Letters*, **15**, 034055.

Hadley, G. (1735) VI. Concerning the cause of the general trade-winds. *Philosophical Transactions of the Royal Society of London*, **39**, 58–62.

- Haigh, J. D., Blackburn, M. and Day, R. (2005) The response of tropospheric circulation to perturbations in lower-stratospheric temperature. *Journal of Climate*, **18**, 3672–3685.
- Hall, M. M. and Bryden, H. L. (1982) Direct estimates and mechanisms of ocean heat transport. *Deep Sea Research Part A. Oceanographic Research Papers*, **29**, 339–359.
- Halley, E. (1686) An historical account of the trade winds, and monsoons, observable in the seas between and near the Tropics, with an attempt to assign the physical cause of the said winds. *Philosophical Transactions of the Royal Society of London*, **16**, 153–168.
- Hari, V., Villarini, G., Karmakar, S., Wilcox, L. J. and Collins, M. (2020) Northward propagation of the intertropical convergence zone and strengthening of Indian summer monsoon rainfall. *Geophysical Research Letters*, **47**, e2020GL089823.
- Hartmann, D. L. (2016) *Global physical climatology (2nd ed.)*. Amsterdam: Elsevier Press.
- He, C., Liu, Z. and Hu, A. (2019) The transient response of atmospheric and oceanic heat transports to anthropogenic warming. *Nature Climate Change*, **9**, 222–226.
- Heaviside, C. and Czaja, A. (2013) Deconstructing the Hadley cell heat transport. *Quarterly Journal of the Royal Meteorological Society*, **139**, 2181–2189.
- Held, I. M. and Hou, A. Y. (1980) Nonlinear axially symmetric circulations in a nearly inviscid atmosphere. *Journal of the Atmospheric Sciences*, **37**, 515–533.
- Held, I. M. and Soden, B. J. (2006) Robust responses of the hydrological cycle to global warming. *Journal of climate*, **19**, 5686–5699.
- Hernandez, M. and Chen, L. (2022) Future land precipitation changes over the North American monsoon region using CMIP5 and CMIP6 simulations. *Journal of Geophysical Research: Atmospheres*, **127**, e2021JD035911.
- Hersbach, H., Bell, B., Berrisford, P., Hirahara, S., Horányi, A., Muñoz-Sabater, J., Nicolas, J., Peubey, C., Radu, R., Schepers, D. et al. (2020) The ERA5 global reanalysis. *Quarterly Journal of the Royal Meteorological Society*, **146**, 1999–2049.

Hoskins, B., Yang, G.-Y. and Fonseca, R. (2020) The detailed dynamics of the June–August Hadley cell. *Quarterly Journal of the Royal Meteorological Society*, **146**, 557–575.

Hu, Y., Huang, H. and Zhou, C. (2018) Widening and weakening of the Hadley circulation under global warming. *Science Bulletin*, **63**, 640–644.

Huang, B., Liu, Z., Liu, S. and Duan, Q. (2023) Investigating the performance of CMIP6 seasonal precipitation predictions and a grid based model heterogeneity oriented deep learning bias correction framework. *Journal of Geophysical Research: Atmospheres*, **128**, e2023JD039046.

Huang, B., Thorne, P. W., Banzon, V. F., Boyer, T., Chepurin, G., Lawrimore, J. H., Menne, M. J., Smith, T. M., Vose, R. S. and Zhang, H.-M. (2017) Noaa extended reconstructed sea surface temperature (ersst), version 5. URL: <https://cir.nii.ac.jp/crid/1882553967453261184>.

Huang, R., Chen, S., Chen, W. and Hu, P. (2018) Interannual variability of regional Hadley circulation intensity over Western Pacific during boreal winter and its climatic impact over Asia-Australia region. *Journal of Geophysical Research: Atmospheres*, **123**, 344–366.

Huang, X., Zhou, T., Turner, A., Dai, A., Chen, X., Clark, R., Jiang, J., Man, W., Murphy, J., Rostron, J. et al. (2020) The recent decline and recovery of Indian summer monsoon rainfall: relative roles of external forcing and internal variability. *Journal of Climate*, **33**, 5035–5060.

Hwang, Y.-T. and Frierson, D. M. (2010) Increasing atmospheric poleward energy transport with global warming. *Geophysical Research Letters*, **37**.

Jafari, M. and Lashkari, H. (2020) Study of the relationship between the intertropical convergence zone expansion and the precipitation in the southern half of Iran. *Atmospheric and Solar-Terrestrial Physics*, **210**, 1–13.

Jiang, J. and Zhou, T. (2019) Global monsoon responses to decadal sea surface temperature variations during the twentieth century: Evidence from AGCM simulations. *Journal of Climate*, **32**, 7675–7695.

- Johanson, C. M. and Fu, Q. (2009) Hadley cell widening: Model simulations versus observations. *Journal of Climate*, **22**, 2713–2725.
- Johns, W. E., Baringer, M. O., Beal, L., Cunningham, S., Kanzow, T., Bryden, H. L., Hirschi, J., Marotzke, J., Meinen, C., Shaw, B. et al. (2011) Continuous, array-based estimates of Atlantic Ocean heat transport at 26.5°N. *Journal of Climate*, **24**, 2429–2449.
- Jungclaus, J., Bittner, M., Wieners, K.-H., Wachsmann, F., Schupfner, M., Legutke, S., Giorgetta, M., Reick, C., Gayler, V., Haak, H., de Vrese, P., Raddatz, T., Esch, M., Mauritsen, T., von Storch, J.-S., Behrens, J., Brovkin, V., Claussen, M., Crueger, T., Fast, I., Fiedler, S., Hagemann, S., Hohenegger, C., Jahns, T., Kloster, S., Kinne, S., Lasslop, G., Kornblueh, L., Marotzke, J., Matei, D., Meraner, K., Mikolajewicz, U., Modali, K., Müller, W., Nabel, J., Notz, D., Peters-von Gehlen, K., Pincus, R., Pohlmann, H., Pongratz, J., Rast, S., Schmidt, H., Schnur, R., Schulzweida, U., Six, K., Stevens, B., Voigt, A. and Roeckner, E. (2019) MPI-M MPI-ESM1.2-HR model output prepared for CMIP6 CMIP historical. URL: <https://doi.org/10.22033/ESGF/CMIP6.6594>.
- Kang, S. M., Held, I. M., Frierson, D. M. and Zhao, M. (2008) The response of the ITCZ to extratropical thermal forcing: Idealized slab-ocean experiments with a GCM. *Journal of Climate*, **21**, 3521–3532.
- Kang, S. M. and Lu, J. (2012) Expansion of the Hadley cell under global warming: Winter versus summer. *Journal of Climate*, **25**, 8387–8393.
- Karl, T. R. and Trenberth, K. E. (2003) Modern global climate change. *Science*, **302**, 1719–1723.
- Katzenberger, A., Schewe, J., Pongratz, J. and Levermann, A. (2021) Robust increase of Indian monsoon rainfall and its variability under future warming in CMIP6 models. *Earth System Dynamics*, **12**, 367–386.
- King, A. D., Donat, M. G., Alexander, L. V. and Karoly, D. J. (2015) The ENSO–Australian rainfall teleconnection in reanalysis and CMIP5. *Climate Dynamics*, **44**, 2623–2635.

Kishore, P., Jyothi, S., Basha, G., Rao, S., Rajeevan, M., Velicogna, I. and Sutterley, T. C. (2016) Precipitation climatology over India: validation with observations and reanalysis datasets and spatial trends. *Climate dynamics*, **46**, 541–556.

Kitoh, A., Endo, H., Krishna Kumar, K., Cavalcanti, I. F., Goswami, P. and Zhou, T. (2013) Monsoons in a changing world: A regional perspective in a global context. *Journal of Geophysical Research: Atmospheres*, **118**, 3053–3065.

Klinger, B. A. and Marotzke, J. (2000) Meridional heat transport by the subtropical cell. *Journal of physical oceanography*, **30**, 696–705.

Knietzsch, M.-A., Schröder, A., Lucarini, V. and Lunkeit, F. (2015) The impact of oceanic heat transport on the atmospheric circulation. *Earth System Dynamics*, **6**, 591–615.

Koteswaram, P. (1958) The easterly jet stream in the tropics. *Tellus*, **10**, 43–57.

Krishnan, R., Sabin, T., Ayantika, D., Kitoh, A., Sugi, M., Murakami, H., Turner, A., Slingo, J. and Rajendran, K. (2013) Will the South Asian monsoon overturning circulation stabilize any further? *Climate dynamics*, **40**, 187–211.

Kushner, P. J., Held, I. M. and Delworth, T. L. (2001) Southern Hemisphere atmospheric circulation response to global warming. *Journal of Climate*, **14**, 2238–2249.

Lashkari, H. and Jafari, M. (2021) Annual displacement and appropriate index to determine ITCZ position in East Africa and the Indian Ocean regions. *Meteorology and Atmospheric Physics*, **133**, 1111–1126.

Latif, M., Anderson, D., Barnett, T., Cane, M., Kleeman, R., Leetmaa, A., O'Brien, J., Rosati, A. and Schneider, E. (1998) A review of the predictability and prediction of ENSO. *Journal of Geophysical Research: Oceans*, **103**, 14375–14393.

Lau, N.-C., Leetmaa, A. and Nath, M. J. (2006) Attribution of atmospheric variations in the 1997–2003 period to SST anomalies in the Pacific and Indian Ocean basins. *Journal of Climate*, **19**, 3607–3628.

Lee, H., Calvin, K., Dasgupta, D., Krinner, G., Mukherji, A., Thorne, P., Trisos, C., Romero, J., Aldunce, P., Barrett, K. et al. (2023) *Climate change 2023: synthesis report. Contribution of working groups I, II and III to the sixth assessment report of the intergovernmental panel on climate change*. The Australian National University.

Li, D., Folini, D. and Wild, M. (2023) Assessment of top of atmosphere, atmospheric and surface energy budgets in CMIP6 models on regional scales. *Earth and Space Science*, **10**, e2022EA002758.

Li, L. (2019) CAS FGOALS-g3 model output prepared for CMIP6 CMIP historical. URL: <https://doi.org/10.22033/ESGF/CMIP6.3356>.

Li, L., Dong, L., Xie, J., Tang, Y., Xie, F., Guo, Z., Liu, H., Feng, T., Wang, L., Pu, Y. et al. (2020) The GAMIL3: Model description and evaluation. *Journal of Geophysical Research: Atmospheres*, **125**, e2020JD032574.

Lindzen, R. S. and Hou, A. V. (1988) Hadley circulations for zonally averaged heating centered off the equator. *Journal of Atmospheric Sciences*, **45**, 2416–2427.

Lionello, P., D'Agostino, R., Ferreira, D., Nguyen, H. and Singh, M. S. (2024) The Hadley circulation in a changing climate. *Annals of the New York Academy of Sciences*.

Liu, C., Allan, R. P., Berrisford, P., Mayer, M., Hyder, P., Loeb, N., Smith, D., Vidale, P.-L. and Edwards, J. M. (2015) Combining satellite observations and reanalysis energy transports to estimate global net surface energy fluxes 1985–2012. *Journal of Geophysical Research: Atmospheres*, **120**, 9374–9389.

Liu, C., Allan, R. P., Mayer, M., Hyder, P., Desbruyères, D., Cheng, L., Xu, J., Xu, F. and Zhang, Y. (2020a) Variability in the global energy budget and transports 1985–2017. *Climate Dynamics*, **55**, 3381–3396.

Liu, C., Allan, R. P., Mayer, M., Hyder, P., Loeb, N. G., Roberts, C. D., Valdivieso, M., Edwards, J. M. and Vidale, P.-L. (2017a) Evaluation of satellite and reanalysis-based global net surface energy flux and uncertainty estimates. *Journal of Geophysical Research: Atmospheres*, **122**, 6250–6272.

Liu, F., Luo, Y., Lu, J. and Wan, X. (2021) The role of ocean dynamics in the cross-equatorial energy transport under a thermal forcing in the Southern Ocean. *Advances in Atmospheric Sciences*, **38**, 1737–1749.

Liu, X., Battisti, D. S. and Donohoe, A. (2017b) Tropical precipitation and cross-equatorial ocean heat transport during the mid-Holocene. *Journal of Climate*, **30**, 3529–3547.

Liu, Y., Attema, J., Moat, B. and Hazeleger, W. (2020b) Synthesis and evaluation of historical meridional heat transport from midlatitudes towards the Arctic. *Earth System Dynamics*, **11**, 77–96.

Liu, Y., Cai, W., Sun, C., Song, H., Cobb, K. M., Li, J., Leavitt, S. W., Wu, L., Cai, Q., Liu, R. et al. (2019) Anthropogenic aerosols cause recent pronounced weakening of Asian Summer Monsoon relative to last four centuries. *Geophysical Research Letters*, **46**, 5469–5479.

Liu, Z., Yang, H., He, C. and Zhao, Y. (2016) A theory for Bjerknes compensation: The role of climate feedback. *Journal of Climate*, **29**, 191–208.

Loeb, N., Su, W., Doelling, D., Wong, T., Minnis, P., Thomas, S. and Miller, W. (2018) Earth's top-of-atmosphere radiation budget. *Comprehensive remote sensing*, **5**, 67–84.

Loeb, N. G., Wang, H., Allan, R. P., Andrews, T., Armour, K., Cole, J. N., Dufresne, J.-L., Forster, P., Gettelman, A., Guo, H. et al. (2020) New generation of climate models track recent unprecedented changes in Earth's radiation budget observed by CERES. *Geophysical Research Letters*, **47**, e2019GL086705.

Loeb, N. G., Wang, H., Cheng, A., Kato, S., Fasullo, J. T., Xu, K.-M. and Allan, R. P. (2016) Observational constraints on atmospheric and oceanic cross-equatorial heat transports: revisiting the precipitation asymmetry problem in climate models. *Climate Dynamics*, **46**, 3239–3257.

Lorenz, D. J. and DeWeaver, E. T. (2007) Tropopause height and zonal wind response to global warming in the IPCC scenario integrations. *Journal of Geophysical Research: Atmospheres*, **112**.

- Lu, J., Vecchi, G. A. and Reichler, T. (2007) Expansion of the Hadley cell under global warming. *Geophysical Research Letters*, **34**.
- Lu, R. and Dong, B. (2008) Response of the Asian summer monsoon to weakening of Atlantic thermohaline circulation. *Advances in Atmospheric Sciences*, **25**, 723–736.
- Luna-Niño, R., Cavazos, T., Torres-Alavez, J. A., Giorgi, F. and Coppola, E. (2021) Inter-annual variability of the boreal winter subtropical jet stream and teleconnections over the CORDEX-CAM domain during 1980–2010. *Climate Dynamics*, **57**, 1571–1594.
- Lutsko, N. J., Marshall, J. and Green, B. (2019) Modulation of monsoon circulations by cross-equatorial ocean heat transport. *Journal of Climate*, **32**, 3471–3485.
- Ma, X., Zhao, S., Zhang, H. and Wang, W. (2023) The double-ITCZ problem in CMIP6 and the influences of deep convection and model resolution. *International Journal of Climatology*, **43**, 2369–2390.
- Madhu, V. et al. (2014) Variation of zonal winds in the upper troposphere and lower stratosphere in association with deficient and excess Indian summer monsoon scenario. *Atmospheric and Climate Sciences*, **4**, 685.
- Magnusdottir, G. and Saravanan, R. (1999) The response of atmospheric heat transport to zonally-averaged SST trends. *Tellus A: Dynamic Meteorology and Oceanography*, **51**, 815–832.
- Maher, P., Kelleher, M. E., Sansom, P. G. and Methven, J. (2020) Is the subtropical jet shifting poleward? *Climate Dynamics*, **54**, 1741–1759.
- Mamalakis, A., Randerson, J. T., Yu, J.-Y., Pritchard, M. S., Magnusdottir, G., Smyth, P., Levine, P. A., Yu, S. and Foufoula-Georgiou, E. (2021) Zonally contrasting shifts of the tropical rain belt in response to climate change. *Nature climate change*, **11**, 143–151.
- Manney, G. L., Hegglin, M. I. and Lawrence, Z. D. (2021) Seasonal and regional signatures of ENSO in upper tropospheric jet characteristics from reanalyses. *Journal of Climate*, **34**, 9181–9200.

Marshall, J., Donohoe, A., Ferreira, D. and McGee, D. (2014) The ocean's role in setting the mean position of the Inter-Tropical Convergence Zone. *Climate Dynamics*, **42**, 1967–1979.

Masson-Delmotte, V., Zhai, P., Pirani, A., Connors, S., Péan, C., Berger, S., Caud, N., Chen, Y., Goldfarb, L., Gomis, M., Huang, M., Leitzell, K., Lonnoy, E., Matthews, J., Maycock, T., Waterfield, T., Yelekçi, O., Yu, R. and Zhou, B. (2021) *IPCC, 2021: Annex V: Monsoons [Cherchi, A., A. Turner (eds.)]. In Climate Change 2021: The Physical Science Basis. Contribution of Working Group I to the Sixth Assessment Report of the Intergovernmental Panel on Climate Change*. Cambridge University Press.

Masuda, K. (1988) Meridional heat transport by the atmosphere and the ocean: analysis of FGGE data. *Tellus A*, **40**, 285–302.

Matthes, K., Funke, B., Andersson, M. E., Barnard, L., Beer, J., Charbonneau, P., Clilverd, M. A., Dudok de Wit, T., Haberreiter, M., Hendry, A. et al. (2017) Solar forcing for CMIP6 (v3. 2). *Geoscientific Model Development*, **10**, 2247–2302.

Mayer, J., Haimberger, L. and Mayer, M. (2023) A quantitative assessment of air-sea heat flux trends from ERA5 since 1950 in the North Atlantic basin. *Earth System Dynamics Discussions*, **2023**, 1–36.

Mayer, J., Mayer, M. and Haimberger, L. (2021) Consistency and homogeneity of atmospheric energy, moisture, and mass budgets in ERA5. *Journal of Climate*, **34**, 3955–3974.

Mayer, M. and Haimberger, L. (2012) Poleward atmospheric energy transports and their variability as evaluated from ECMWF reanalysis data. *Journal of climate*, **25**, 734–752.

Mayer, M., Haimberger, L., Edwards, J. M. and Hyder, P. (2017) Toward consistent diagnostics of the coupled atmosphere and ocean energy budgets. *Journal of Climate*, **30**, 9225–9246.

McCarthy, G. D., Haigh, I. D., Hirschi, J. J.-M., Grist, J. P. and Smeed, D. A. (2015) Ocean impact on decadal Atlantic climate variability revealed by sea-level observations. *Nature*, **521**, 508–510.

- McGee, D., Donohoe, A., Marshall, J. and Ferreira, D. (2014) Changes in ITCZ location and cross-equatorial heat transport at the Last Glacial Maximum, Heinrich Stadial 1, and the mid-Holocene. *Earth and Planetary Science Letters*, **390**, 69–79.
- Mecking, J. V. and Drijfhout, S. S. (2023) The decrease in ocean heat transport in response to global warming. *Nature Climate Change*, **13**, 1229–1236.
- Meehl, G. A. (1992) Effect of tropical topography on global climate. *Annual Review of Earth and Planetary Sciences*, **20**, 85–112.
- Meinshausen, M., Vogel, E., Nauels, A., Lorbacher, K., Meinshausen, N., Etheridge, D. M., Fraser, P. J., Montzka, S. A., Rayner, P. J., Trudinger, C. M. et al. (2017) Historical greenhouse gas concentrations for climate modelling (CMIP6). *Geoscientific Model Development*, **10**, 2057–2116.
- Mitra, A. (2021) A comparative study on the skill of CMIP6 models to preserve daily spatial patterns of monsoon rainfall over India. *Frontiers in Climate*, **3**, 654763.
- Mogensen, K., Balmaseda, M. A., Weaver, A. et al. (2012) The NEMOVAR ocean data assimilation system as implemented in the ECMWF ocean analysis for System 4.
- Moon, S. and Ha, K.-J. (2020) Future changes in monsoon duration and precipitation using CMIP6. *npj Climate and Atmospheric Science*, **3**, 45.
- Moreno-Chamarro, E., Arsouze, T., Acosta, M., Bretonnière, P.-A., Castrillo, M., Ferrer, E., Frigola, A., Kuznetsova, D., Martin-Martinez, E., Ortega, P. et al. (2024) The very-high resolution configuration of the EC-Earth global model for HighResMIP. *Geoscientific Model Development Discussions*, **2024**, 1–49.
- Narsey, S., Brown, J., Colman, R., Delage, F., Power, S., Moise, A. and Zhang, H. (2020) Climate change projections for the Australian monsoon from CMIP6 models. *Geophysical Research Letters*, **47**, e2019GL086816.
- NASA Goddard Institute for Space Studies (NASA/GISS) (2018) NASA-GISS GISS-E2.1G model output prepared for CMIP6 CMIP historical. URL: <https://doi.org/10.22033/ESGF/CMIP6.7127>.

Nguyen, H., Evans, A., Lucas, C., Smith, I. and Timbal, B. (2013) The Hadley circulation in reanalyses: Climatology, variability, and change. *Journal of Climate*, **26**, 3357–3376.

Nishant, N., Di Virgilio, G., Ji, F., Tam, E., Beyer, K. and Riley, M. L. (2022) Evaluation of Present-Day CMIP6 Model Simulations of Extreme Precipitation and Temperature over the Australian Continent. *Atmosphere*, **13**, 1478.

Nogueira, M. (2020) Inter-comparison of ERA-5, ERA-interim and GPCP rainfall over the last 40 years: Process-based analysis of systematic and random differences. *Journal of Hydrology*, **583**, 124632.

O'Neill, B. C., Tebaldi, C., Van Vuuren, D. P., Eyring, V., Friedlingstein, P., Hurtt, G., Knutti, R., Kriegler, E., Lamarque, J.-F., Lowe, J. et al. (2016) The scenario model intercomparison project (ScenarioMIP) for CMIP6. *Geoscientific Model Development*, **9**, 3461–3482.

Oort, A. H. (1971) The observed annual cycle in the meridional transport of atmospheric energy. *J. Atmos. Sci.*, **28**, 325–339.

Oort, A. H. and Peixóto, J. P. (1983) Global angular momentum and energy balance requirements from observations. In *Advances in geophysics*, vol. 25, 355–490. Elsevier.

Oort, A. H. and Vonder Haar, T. H. (1976) On the observed annual cycle in the ocean-atmosphere heat balance over the Northern Hemisphere. *Journal of Physical Oceanography*, **6**, 781–800.

Oort, A. H. and Yienger, J. J. (1996) Observed interannual variability in the Hadley circulation and its connection to ENSO. *Journal of Climate*, 2751–2767.

Outten, S., Esau, I. and Otterå, O. H. (2018) Bjerknes compensation in the CMIP5 climate models. *Journal of Climate*, **31**, 8745–8760.

O'Neill, B. C., Kriegler, E., Riahi, K., Ebi, K. L., Hallegatte, S., Carter, T. R., Mathur, R. and Van Vuuren, D. P. (2014) A new scenario framework for climate change research: the concept of shared socioeconomic pathways. *Climatic change*, **122**, 387–400.

- Palter, J. B. (2015) The role of the Gulf Stream in European climate. *Annual review of marine science*, **7**, 113–137.
- Park, S. and Bretherton, C. S. (2009) The University of Washington shallow convection and moist turbulence schemes and their impact on climate simulations with the Community Atmosphere Model. *Journal of Climate*, **22**, 3449–3469.
- Pattanaik, D. and Satyan, V. (2000) Fluctuations of tropical easterly jet during contrasting monsoons over India: A GCM study. *Meteorology and Atmospheric Physics*, **75**, 51–60.
- Philander, S., Gu, D., Lambert, G., Li, T., Halpern, D., Lau, N. and Pacanowski, R. C. (1996) Why the ITCZ is mostly north of the equator. *Journal of climate*, **9**, 2958–2972.
- Polvani, L. M. and Kushner, P. J. (2002) Tropospheric response to stratospheric perturbations in a relatively simple general circulation model. *Geophysical Research Letters*, **29**, 18–1.
- Power, S., Haylock, M., Colman, R. and Wang, X. (2006) The predictability of interdecadal changes in ENSO activity and ENSO teleconnections. *Journal of Climate*, **19**, 4755–4771.
- Quan, X.-W., Diaz, H. F. and Hoerling, M. P. (2004) Change in the tropical Hadley cell since 1950. In *The Hadley circulation: present, past and future*, chap. Chapter 3, 85–120. Springer.
- Rabier, F. and Liu, Z. (2003) Variational data assimilation: theory and overview. In *Proc. ECMWF Seminar on Recent Developments in Data Assimilation for Atmosphere and Ocean, Reading, UK, September 8–12*, 29–43.
- Rajendran, K., Surendran, S., Varghese, S. J. and Sathyanath, A. (2022) Simulation of Indian summer monsoon rainfall, interannual variability and teleconnections: evaluation of CMIP6 models. *Climate Dynamics*, **58**, 2693–2723.
- Raju, P., Mohanty, U., Rao, P. and Bhatla, R. (2002) The contrasting features of Asian summer monsoon during surplus and deficient rainfall over India. *International Journal of Climatology: A Journal of the Royal Meteorological Society*, **22**, 1897–1914.

Rayner, N., Parker, D. E., Horton, E., Folland, C. K., Alexander, L. V., Rowell, D., Kent, E. C. and Kaplan, A. (2003) Global analyses of sea surface temperature, sea ice, and night marine air temperature since the late nineteenth century. *Journal of Geophysical Research: Atmospheres*, **108**.

Ridley, J., Menary, M., Kuhlbrodt, T., Andrews, M. and Andrews, T. (2019a) MOHC HadGEM3-GC31-LL model output prepared for CMIP6 CMIP historical. URL: <https://doi.org/10.22033/ESGF/CMIP6.6109>.

— (2019b) MOHC HadGEM3-GC31-MM model output prepared for CMIP6 CMIP historical. URL: <https://doi.org/10.22033/ESGF/CMIP6.6112>.

Rodwell, M. J. and Hoskins, B. J. (1996) Monsoons and the dynamics of deserts. *Quarterly Journal of the Royal Meteorological Society*, **122**, 1385–1404.

Rose, B. E. and Ferreira, D. (2012) Ocean heat transport and water vapor greenhouse in a warm equable climate: A new look at the low gradient paradox. *Journal of Climate*, **26**, 2117–2136.

Saji, N., Goswami, B. N., Vinayachandran, P. and Yamagata, T. (1999) A dipole mode in the tropical Indian Ocean. *Nature*, **401**, 360–363.

Sandeep, N., Swapna, P., Krishnan, R., Farneti, R., Prajeesh, A., Ayantika, D. and Manmeet, S. (2020) South Asian monsoon response to weakening of Atlantic meridional overturning circulation in a warming climate. *Climate dynamics*, **54**, 3507–3524.

Sandeep, S. and Ajayamohan, R. (2015) Poleward shift in Indian summer monsoon low level jetstream under global warming. *Climate Dynamics*, **45**, 337–351.

Schneider, E. K. (1977) Axially symmetric steady-state models of the basic state for instability and climate studies. Part II. Nonlinear calculations. *Journal of Atmospheric Sciences*, **34**, 280–296.

Schneider, T. (2017) Feedback of atmosphere-ocean coupling on shifts of the Intertropical Convergence Zone. *Geophysical Research Letters*, **44**, 11–644.

- Schneider, T., Bischoff, T. and Haug, G. H. (2014) Migrations and dynamics of the intertropical convergence zone. *Nature*, **513**, 45–53.
- Seager, R., Ting, M., Held, I., Kushnir, Y., Lu, J., Vecchi, G., Huang, H.-P., Harnik, N., Leetmaa, A., Lau, N.-C. et al. (2007) Model projections of an imminent transition to a more arid climate in southwestern North America. *Science*, **316**, 1181–1184.
- Seferian, R. (2018) CNRM-CERFACS CNRM-ESM2-1 model output prepared for CMIP6 CMIP historical. URL: <https://doi.org/10.22033/ESGF/CMIP6.4068>.
- Seidel, D. J., Fu, Q., Randel, W. J. and Reichler, T. J. (2008) Widening of the tropical belt in a changing climate. *Nature geoscience*, **1**, 21–24.
- Send, U., Lankhorst, M. and Kanzow, T. (2011) Observation of decadal change in the Atlantic meridional overturning circulation using 10 years of continuous transport data. *Geophysical Research Letters*, **38**.
- Seo, K.-H., Yoon, S.-P., Lu, J., Hu, Y., Staten, P. W. and Frierson, D. M. (2023) What controls the interannual variation of Hadley cell extent in the Northern Hemisphere: physical mechanism and empirical model for edge variation. *npj Climate and Atmospheric Science*, **6**, 204.
- Shi, J. and Yang, H. (2021) Bjerknes compensation in a coupled global box model. *Climate Dynamics*, **57**, 3569–3582.
- Simmons, A., Hersbach, H., Muñoz-Sabater, J., Nicolas, J., Vamborg, F., Berrisford, P., de Rosnay, P., Willett, K. and Woollen, J. (2021) *Low frequency variability and trends in surface air temperature and humidity from ERA5 and other datasets*. European Centre for Medium-Range Weather Forecasts.
- Simpkins, G. (2017) Progress in climate modelling. *Nature Climate Change*, **7**, 684–685.
- Smeed, D. A., McCarthy, G., Cunningham, S. A., Frajka-Williams, E., Rayner, D., Johns, W., Meinen, C. S., Baringer, M. O., Moat, B. I., Duchez, A. et al. (2014) Observed decline of the Atlantic meridional overturning circulation 2004–2012. *Ocean Science*, **10**, 29–38.

- Song, F. and Zhang, G. J. (2020) The impacts of horizontal resolution on the seasonally dependent biases of the northeastern Pacific ITCZ in coupled climate models. *Journal of Climate*, **33**, 941–957.
- Sooraj, K., Terray, P. and Mujumdar, M. (2015) Global warming and the weakening of the Asian summer monsoon circulation: assessments from the CMIP5 models. *Climate Dynamics*, **45**, 233–252.
- Srokosz, M., Baringer, M., Bryden, H., Cunningham, S., Delworth, T., Lozier, S., Marotzke, J. and Sutton, R. (2012) Past, present, and future changes in the Atlantic meridional overturning circulation. *Bulletin of the American Meteorological Society*, **93**, 1663–1676.
- Stachnik, J. P. and Schumacher, C. (2011) A comparison of the Hadley circulation in modern reanalyses. *Journal of Geophysical Research: Atmospheres*, **116**.
- Stephens, G. L., Hakuba, M. Z., Hawcroft, M., Haywood, J. M., Behrangi, A., Kay, J. E. and Webster, P. J. (2016) The curious nature of the hemispheric symmetry of the Earth's water and energy balances. *Current Climate Change Reports*, **2**, 135–147.
- Stone, P. H. (1978) Constraints on dynamical transports of energy on a spherical planet. *Dynamics of atmospheres and oceans*, **2**, 123–139.
- Sun, Y. and Zhou, T. (2014) How does El Niño affect the interannual variability of the boreal summer Hadley circulation? *Journal of Climate*, **27**, 2622–2642.
- Suppiah, R. (1992) The Australian summer monsoon: a review. *Progress in Physical Geography*, **16**, 283–318.
- (1995) The Australian summer monsoon: CSIRO9 GCM simulations for $1 \times \text{CO}_2$ and $2 \times \text{CO}_2$ conditions. *Global and Planetary Change*, **11**, 95–109.
- Van der Swaluw, E., Drijfhout, S. and Hazeleger, W. (2007) Bjerknes compensation at high northern latitudes: The ocean forcing the atmosphere. *Journal of climate*, **20**, 6023–6032.
- Swart, N. C., Cole, J. N., Kharin, V. V., Lazare, M., Scinocca, J. F., Gillett, N. P., Anstey, J., Arora, V., Christian, J. R., Jiao, Y., Lee, W. G., Majaess, F., Saenko, O. A., Seiler, C., Seinen,

- C., Shao, A., Solheim, L., von Salzen, K., Yang, D., Winter, B. and Sigmond, M. (2019) CCCma CanESM5 model output prepared for CMIP6 CMIP historical. URL: <https://doi.org/10.22033/ESGF/CMIP6.3610>.
- Tan, L., Shen, C.-C., Löwemark, L., Chawchai, S., Edwards, R. L., Cai, Y., Breitenbach, S. F., Cheng, H., Chou, Y.-C., Duerrast, H. et al. (2019) Rainfall variations in central Indo-Pacific over the past 2,700 y. *Proceedings of the National Academy of Sciences*, **116**, 17201–17206.
- Tanaka, H. L., Ishizaki, N. and Kitoh, A. (2004) Trend and interannual variability of Walker, monsoon and Hadley circulations defined by velocity potential in the upper troposphere. *Tellus A: Dynamic Meteorology and Oceanography*, **56**, 250–269.
- Tang, Y., Rumbold, S., Ellis, R., Kelley, D., Mulcahy, J., Sellar, A., Walton, J. and Jones, C. (2019) MOHC UKESM1.0-LL model output prepared for CMIP6 CMIP historical. URL: <https://doi.org/10.22033/ESGF/CMIP6.6113>.
- Tatebe, H., Ogura, T., Nitta, T., Komuro, Y., Ogochi, K., Takemura, T., Sudo, K., Sekiguchi, M., Abe, M., Saito, F. et al. (2019) Description and basic evaluation of simulated mean state, internal variability, and climate sensitivity in MIROC6. *Geoscientific Model Development*, **12**, 2727–2765.
- Tatebe, H. and Watanabe, M. (2018) MIROC MIROC6 model output prepared for CMIP6 CMIP historical. URL: <https://doi.org/10.22033/ESGF/CMIP6.5603>.
- Taylor, K., Crucifix, M., Braconnot, P., Hewitt, C., Doutriaux, C., Broccoli, A., Mitchell, J. and Webb, M. (2007) Estimating shortwave radiative forcing and response in climate models. *Journal of Climate*, **20**, 2530–2543.
- Tian, B. and Dong, X. (2020) The double-ITCZ bias in CMIP3, CMIP5, and CMIP6 models based on annual mean precipitation. *Geophysical Research Letters*, **47**, e2020GL087232.
- Timmermann, A., An, S., Krebs, U. and Goosse, H. (2005) ENSO suppression due to weakening of the North Atlantic thermohaline circulation. *Journal of Climate*, **18**, 3122–3139.

Trenberth, K. E. (1991) Climate diagnostics from global analyses: Conservation of mass in ECMWF analyses. *Journal of Climate*, **4**, 707–722.

— (1997) Using atmospheric budgets as a constraint on surface fluxes. *Journal of climate*, **10**, 2796–2809.

Trenberth, K. E. and Caron, J. M. (2001) Estimates of meridional atmosphere and ocean heat transports. *Journal of Climate*, **14**, 3433–3443.

Trenberth, K. E. and Fasullo, J. T. (2018) Applications of an updated atmospheric energetics formulation. *Journal of Climate*, **31**, 6263–6279.

Trenberth, K. E., Hurrell, J. W. and Solomon, A. (1995) Conservation of mass in three dimensions in global analyses. *Journal of climate*, **8**, 692–708.

Trenberth, K. E. and Solomon, A. (1994) The global heat balance: Heat transports in the atmosphere and ocean. *Climate Dynamics*, **10**, 107–134.

Trenberth, K. E. and Stepaniak, D. P. (2003a) Covariability of components of poleward atmospheric energy transports on seasonal and interannual timescales. *Journal of climate*, **16**, 3691–3705.

— (2003b) Seamless poleward atmospheric energy transports and implications for the Hadley circulation. *Journal of Climate*, **16**, 3706–3722.

— (2004) The flow of energy through the Earth's climate system. *Quarterly Journal of the Royal Meteorological Society: A journal of the atmospheric sciences, applied meteorology and physical oceanography*, **130**, 2677–2701.

Trenberth, K. E., Stepaniak, D. P. and Caron, J. M. (2000) The global monsoon as seen through the divergent atmospheric circulation. *Journal of Climate*, **13**, 3969–3993.

— (2002) Accuracy of atmospheric energy budgets from analyses. *Journal of Climate*, **15**, 3343–3360.

- Trenberth, K. E., Zhang, Y., Fasullo, J. T. and Cheng, L. (2019) Observation-based estimates of global and basin ocean meridional heat transport time series. *Journal of Climate*, **32**, 4567–4583.
- Turner, A. G. and Annamalai, H. (2012) Climate change and the South Asian summer monsoon. *Nature Climate Change*, **2**, 587–595.
- Ueda, H., Iwai, A., Kuwako, K. and Hori, M. E. (2006) Impact of anthropogenic forcing on the Asian summer monsoon as simulated by eight GCMs. *Geophysical Research Letters*, **33**.
- UKESM Team (2022) Ukesm1.0-ll model description. URL: <https://ukesm.ac.uk/wp-content/uploads/2022/06/UKESM1-0-LL.html>. Accessed: 2025-01-03.
- Váňa, F., Düben, P., Lang, S., Palmer, T., Leutbecher, M., Salmond, D. and Carver, G. (2017) Single precision in weather forecasting models: An evaluation with the IFS. *Monthly Weather Review*, **145**, 495–502.
- Vannière, B., Demory, M.-E., Vidale, P. L., Schiemann, R., Roberts, M. J., Roberts, C. D., Matsueda, M., Terray, L., Koenigk, T. and Senan, R. (2019) Multi-model evaluation of the sensitivity of the global energy budget and hydrological cycle to resolution. *Climate dynamics*, **52**, 6817–6846.
- Vellinga, M. and Wood, R. A. (2002) Global climatic impacts of a collapse of the Atlantic thermohaline circulation. *Climatic change*, **54**, 251–267.
- Vellinga, M. and Wu, P. (2008) Relations between northward ocean and atmosphere energy transports in a coupled climate model. *Journal of Climate*, **21**, 561–575.
- Voltaire, A. (2019) CNRM-CERFACS CNRM-CM6-1-HR model output prepared for CMIP6 CMIP historical. URL: <https://doi.org/10.22033/ESGF/CMIP6.4067>.
- Von Schuckmann, K., Cheng, L., Palmer, M. D., Hansen, J., Tassone, C., Aich, V., Adusumilli, S., Beltrami, H., Boyer, T., Cuesta-Valero, F. J. et al. (2020) Heat stored in the Earth system: where does the energy go? *Earth System Science Data*, **12**, 2013–2041.

Von Schuckmann, K., Minière, A., Gues, F., Cuesta-Valero, F. J., Kirchengast, G., Adusumilli, S., Straneo, F., Ablain, M., Allan, R. P., Barker, P. M. et al. (2023) Heat stored in the Earth system 1960–2020: where does the energy go? *Earth System Science Data*, **15**, 1675–1709.

Wallace, J. M. and Hobbs, P. V. (2006) Introduction to atmospheric science. In *Atmospheric Science: An Introductory Survey*, 1–22. Academic Press, 2 edn.

Wang, B. (1994) Climatic regimes of tropical convection and rainfall. *Journal of Climate*, **7**, 1109–1118.

Wang, B., Biasutti, M., Byrne, M. P., Castro, C., Chang, C.-P., Cook, K., Fu, R., Grimm, A. M., Ha, K.-J., Hendon, H., Kitoh, A., Krishnan, R., Lee, J.-Y., Li, J., Liu, J., Moise, A., Pascale, S., Roxy, M. K., Seth, A., Sui, C.-H., Turner, A., Yang, S., Yun, S., Yun, K.-S., Zhang, L. and Zhou, T. (2021) Monsoons climate change assessment. *Bulletin of the American Meteorological Society*, **102**, E1–E19.

Wang, B. and Ding, Q. (2006) Changes in global monsoon precipitation over the past 56 years. *Geophysical Research Letters*, **33**.

— (2008) Global monsoon: Dominant mode of annual variation in the tropics. *Dynamics of Atmospheres and Oceans*, **44**, 165–183.

Wang, B., Ding, Q. and Liu, J. (2011) Concept of global monsoon. In *The global monsoon system: research and forecast*, chap. 1, 3–14. World Scientific.

Wang, B., Jin, C. and Liu, J. (2020) Understanding future change of global monsoons projected by CMIP6 models. *Journal of Climate*, **33**, 6471–6489.

Wang, B., Liu, J., Kim, H.-J., Webster, P. J. and Yim, S.-Y. (2012a) Recent change of the global monsoon precipitation (1979–2008). *Climate Dynamics*, **39**, 1123–1135.

Wang, B., Liu, J., Kim, H.-J., Webster, P. J., Yim, S.-Y. and Xiang, B. (2013a) Northern Hemisphere summer monsoon intensified by mega-El Niño/southern oscillation and Atlantic multidecadal oscillation. *Proceedings of the National Academy of Sciences*, **110**, 5347–5352.

- Wang, B., Xiang, B. and Lee, J.-Y. (2013b) Subtropical high predictability establishes a promising way for monsoon and tropical storm predictions. *Proceedings of the National Academy of Sciences*, **110**, 2718–2722.
- Wang, P., Wang, B., Cheng, H., Fasullo, J., Guo, Z., Kiefer, T. and Liu, Z. (2014) The global monsoon across timescales: coherent variability of regional monsoons. *Climate of the Past*, **10**, 2007–2052.
- Wang, P., Wang, B. and Kiefer, T. (2012b) Global Monsoon across timescales.
- Wang, P. X., Wang, B., Cheng, H., Fasullo, J., Guo, Z., Kiefer, T. and Liu, Z. (2017) The global monsoon across time scales: Mechanisms and outstanding issues. *Earth-Science Reviews*, **174**, 84–121.
- Wang, S., Feng, J., Liu, X. and Ji, X. (2023) Simulation of the long-term variability of the Hadley circulation in CMIP6 models. *Atmospheric Research*, **287**, 106716.
- Watanabe, M., Emori, S., Satoh, M. and Miura, H. (2009) A PDF-based hybrid prognostic cloud scheme for general circulation models. *Climate Dynamics*, **33**, 795–816.
- Watt-Meyer, O. and Frierson, D. M. (2019) ITCZ width controls on Hadley cell extent and eddy-driven jet position and their response to warming. *Journal of Climate*, **32**, 1151–1166.
- Webster, P. J. (1987) The variable and interactive monsoon. *Monsoons*.
- (1994) The role of hydrological processes in ocean-atmosphere interactions. *Reviews of Geophysics*, **32**, 427–476.
- (2004) The elementary hadley circulation. 9–60.
- Webster, P. J., Magana, V. O., Palmer, T., Shukla, J., Tomas, R., Yanai, M. and Yasunari, T. (1998) Monsoons: Processes, predictability, and the prospects for prediction. *Journal of Geophysical Research: Oceans*, **103**, 14451–14510.
- Weijer, W., Cheng, W., Garuba, O. A., Hu, A. and Nadiga, B. (2020) CMIP6 models predict significant 21st century decline of the Atlantic meridional overturning circulation. *Geophysical Research Letters*, **47**, e2019GL086075.

Wieners, K.-H., Giorgetta, M., Jungclaus, J., Reick, C., Esch, M., Bittner, M., Legutke, S., Schupfner, M., Wachsmann, F., Gayler, V., Haak, H., de Vrese, P., Raddatz, T., Mauritsen, T., von Storch, J.-S., Behrens, J., Brovkin, V., Claussen, M., Crueger, T., Fast, I., Fiedler, S., Hagemann, S., Hohenegger, C., Jahns, T., Kloster, S., Kinne, S., Lasslop, G., Kornbluh, L., Marotzke, J., Matei, D., Meraner, K., Mikolajewicz, U., Modali, K., Müller, W., Nabel, J., Notz, D., Peters-von Gehlen, K., Pincus, R., Pohlmann, H., Pongratz, J., Rast, S., Schmidt, H., Schnur, R., Schulzweida, U., Six, K., Stevens, B., Voigt, A. and Roeckner, E. (2019) MPI-M MPI-ESM1.2-LR model output prepared for CMIP6 CMIP historical. URL: <https://doi.org/10.22033/ESGF/CMIP6.6595>.

Wild, M. (2020) The global energy balance as represented in CMIP6 climate models. *Climate Dynamics*, **55**, 553–577.

Williams, G. (2006) Circulation sensitivity to tropopause height. *Journal of the atmospheric sciences*, **63**, 1954–1961.

Wilson, D. R., Bushell, A. C., Kerr-Munslow, A. M., Price, J. D. and Morcrette, C. J. (2008a) PC2: A prognostic cloud fraction and condensation scheme. I: Scheme description. *Quarterly Journal of the Royal Meteorological Society: A journal of the atmospheric sciences, applied meteorology and physical oceanography*, **134**, 2093–2107.

Wilson, D. R., Bushell, A. C., Kerr-Munslow, A. M., Price, J. D., Morcrette, C. J. and Bodas-Salcedo, A. (2008b) PC2: A prognostic cloud fraction and condensation scheme. II: Climate model simulations. *Quarterly Journal of the Royal Meteorological Society: A journal of the atmospheric sciences, applied meteorology and physical oceanography*, **134**, 2109–2125.

Xia, Y., Hu, Y. and Liu, J. (2020) Comparison of trends in the Hadley circulation between CMIP6 and CMIP5. *Science Bulletin*, **65**, 1667–1674.

Xian, T., Xia, J., Wei, W., Zhang, Z., Wang, R., Wang, L.-P. and Ma, Y.-F. (2021) Is Hadley cell expanding? *Atmosphere*, **12**, 1699.

Xu, C., Wang, S.-Y. S., Borhara, K., Buckley, B., Tan, N., Zhao, Y., An, W., Sano, M., Nakatsuka, T. and Guo, Z. (2023) Asian-Australian summer monsoons linkage to ENSO strengthened by global warming. *npj Climate and Atmospheric Science*, **6**, 8.

- Xu, H., Song, Y., Goldsmith, Y. and Lang, Y. (2019) Meridional ITCZ shifts modulate tropical/subtropical Asian monsoon rainfall. *Sci. Bull*, **64**, 1737–1739.
- Yanai, M. and Wu, G.-X. (2006) Effects of the Tibetan Plateau, in: *The Asian Monsoon*, edited by: Wang, B. *Springer*, 513–549.
- Yang, H., Li, Q., Wang, K., Sun, Y. and Sun, D. (2015) Decomposing the meridional heat transport in the climate system. *Climate Dynamics*, **44**, 2751–2768.
- Yang, H., Wen, Q., Yao, J. and Wang, Y. (2017) Bjerknes compensation in meridional heat transport under freshwater forcing and the role of climate feedback. *Journal of Climate*, **30**, 5167–5185.
- Yang, H., Zhao, Y. and Liu, Z. (2016) Understanding Bjerknes compensation in atmosphere and ocean heat transports using a coupled box model. *Journal of Climate*, **29**, 2145–2160.
- Yang, J., Liu, Q., Xie, S.-P., Liu, Z. and Wu, L. (2007) Impact of the Indian Ocean SST basin mode on the Asian summer monsoon. *Geophysical Research Letters*, **34**.
- Yang, S. and Webster, P. J. (1990) The effect of summer tropical heating on the location and intensity of the extratropical westerly jet streams. *Journal of Geophysical Research: Atmospheres*, **95**, 18705–18721.
- Yim, S.-Y., Wang, B., Liu, J. and Wu, Z. (2014) A comparison of regional monsoon variability using monsoon indices. *Climate dynamics*, **43**, 1423–1437.
- Yukimoto, S., Koshiro, T., Kawai, H., Oshima, N., Yoshida, K., Urakawa, S., Tsujino, H., Deushi, M., Tanaka, T., Hosaka, M., Yoshimura, H., Shindo, E., Mizuta, R., Ishii, M., Obata, A. and Adachi, Y. (2019) MRI MRI-ESM2.0 model output prepared for CMIP6 CMIP historical. URL: <https://doi.org/10.22033/ESGF/CMIP6.6842>.
- Zhang, C. (2001) Double ITCZs. *Journal of Geophysical Research: Atmospheres*, **106**, 11785–11792.
- Zhang, G. J., Song, X. and Wang, Y. (2019a) The double ITCZ syndrome in GCMs: A coupled feedback problem among convection, clouds, atmospheric and ocean circulations. *Atmospheric Research*, **229**, 255–268.

Zhang, H., Ma, X., Zhao, S. and Kong, L. (2021) Advances in research on the ITCZ: Mean position, model bias, and anthropogenic aerosol influences. *Journal of Meteorological Research*, **35**, 729–742.

Zhang, R. and Delworth, T. L. (2005) Simulated tropical response to a substantial weakening of the Atlantic thermohaline circulation. *Journal of climate*, **18**, 1853–1860.

Zhang, R., Sutton, R., Danabasoglu, G., Kwon, Y.-O., Marsh, R., Yeager, S. G., Amrhein, D. E. and Little, C. M. (2019b) A review of the role of the Atlantic meridional overturning circulation in Atlantic multidecadal variability and associated climate impacts. *Reviews of Geophysics*, **57**, 316–375.

Zhang, S., Qu, X., Huang, G. and Hu, P. (2023) Asymmetric response of South Asian summer monsoon rainfall in a carbon dioxide removal scenario. *npj Climate and Atmospheric Science*, **6**, 10.

Zhang, S., Qu, X., Huang, G., Hu, P., Zhou, S. and Wu, L. (2024) Delayed onset of Indian summer monsoon in response to CO₂ removal. *Earth's Future*, **12**, e2023EF004039.

Zhang, Y. and Rossow, W. (1997) Estimating meridional energy transports by the atmospheric and oceanic general circulations using boundary fluxes. *Journal of climate*, **10**, 2358–2373.

Zhao, Y., Yang, H. and Liu, Z. (2016) Assessing Bjerknes compensation for climate variability and its time-scale dependence. *Journal of Climate*, **29**, 5501–5512.

Zheng, Y. and Giese, B. S. (2009) Ocean heat transport in simple ocean data assimilation: Structure and mechanisms. *Journal of Geophysical Research: Oceans*, **114**.

Zhou, S., Huang, G. and Huang, P. (2020) Excessive ITCZ but negative SST biases in the tropical Pacific simulated by CMIP5/6 models: The role of the meridional pattern of SST bias. *Journal of Climate*, **33**, 5305–5316.

Zhou, T., Yu, R., Li, H. and Wang, B. (2008a) Ocean forcing to changes in global monsoon precipitation over the recent half-century. *Journal of Climate*, **21**, 3833–3852.

Zhou, T., Zhang, L. and Li, H. (2008b) Changes in global land monsoon area and total rainfall accumulation over the last half century. *Geophysical Research Letters*, **35**.

Zhu, Y.-Y. and Yang, S. (2020) Evaluation of CMIP6 for historical temperature and precipitation over the Tibetan Plateau and its comparison with CMIP5. *Advances in Climate Change Research*, **11**, 239–251.

Zolotov, S. Y., Ippolitov, I., Loginov, S. and Kharyutkina, E. (2018) Variability of the Southern Hemisphere subtropical jet stream in the second half of the 20th century and early 21st century. *Izvestiya, Atmospheric and Oceanic Physics*, **54**, 430–438.

Zuo, H., Balmaseda, M. A., Tietsche, S., Mogensen, K. and Mayer, M. (2019) The ecmwf operational ensemble reanalysis–analysis system for ocean and sea ice: a description of the system and assessment. *Ocean science*, **15**, 779–808.